

DIMUON PRODUCTION BY HIGH ENERGY NEUTRINO AND
ANTINEUTRINO NUCLEON COLLISIONS

BY

DAVID ROBERTS WINN

A thesis submitted in partial fulfillment of the
requirements for the degree of

DOCTOR OF PHILOSOPHY

(Physics)

at the

UNIVERSITY OF WISCONSIN--MADISON

1979

ACKNOWLEDGMENTS

To my major professor, Don Reeder, I owe a special debt of gratitude for his patience, encouragements, hard and creative work, insights, and many kindnesses which have been both my good fortune and my pleasure to receive. Indeed, it is an honor to be his student.

I would like to thank the collaborators from Wisconsin and from Fermilab, Harvard and Penn on experiment E310: Ben, Furio, Dave, Peter, Gil, Richard, T-Y, Dick, Al, Peter, Shigeki, Don, Carlo, Ray, and especially my fellow students and co-conspirators Jim, Max and Tom, whose fellowship and good humor are greatly appreciated.

The technical help from Priscilla and all the scanning staff, from Karen and her crew at physics, from Lynwood, Paul, Bob and their crews at PSL was superb under often difficult conditions.

The physics department and High Energy Group in Madison is a lively and stimulating place to work in and with: my thanks to all of the staff; I'm proud to be your student.

I thank Angela Gonzales for her help on the technical drawing and for her refreshing insights. I thank Marilyn Griffin for working far into the night typing with grace and intelligence.

I thank the staff of Fermilab: Scanners Joanne, Robin and Eileen; the computing department, surveyors, riggers, neutrino

crew chiefs, 15' and 30" bubble chamber crews, and a host of other personnel, especially in the neutrino department.

I owe a debt of gratitude to the citizens and taxpayers of this Republic for the freedom and funds to complete this work. I hope that ultimately their investment in the far future represented by this research is proven to be as wise, fruitful and as good an augury for the futures of all people as I believe it to be.

Finally, I thank my dear family, friends, and especially Judy, for their love and support which are a great blessing on me.

TABLE OF CONTENTS

CHAPTER	PAGE
I. NEUTRINO-NUCLEON REACTIONS AND DIMUON	
FINAL STATES	1
1. Introduction	1
2. Inelastic Neutrino-Nucleon Scattering	4
3. Quarks, Leptons, and Weak Currents	12
4. Dimuons from Charm	14
5. Dimuons from Sources Beyond Charm	21
II. APPARATUS	41
1. Introduction	41
2. Experiment Design	41
3. Beams	42
4. Calorimeter-Targets	43
5. Muon Spectrometer	44
6. Trigger Counters	44
7. Triggers and Logic	45
8. Data Logging	47
9. Recapitulation	47

	PAGE
III. DIMUON ANALYSIS	53
1. Introduction	53
2. Summary of Data and Running	53
3. Triggers and Counter Efficiency	54
4. Dimuon Scan	58
5. Event Processing	59
6. Efficiency	63
7. Dimuon Backgrounds	67
IV. DIMUON CHARACTERISTICS	110
1. Introduction	110
2. Charm Monte Carlo	110
3. Characteristics of Dimuon Events and Charm	113
4. Dimuons from other Sources and Charm	123
5. Conclusions and Summary	130
REFERENCES CHAPTERS I - IV	181
APPENDIX	
I. BEAMS	190
II. CALORIMETER CONSTRUCTION AND ELECTRONICS	195
III. SPARK CHAMBERS	203
IV. MUON SPECTROMETER CONSTRUCTION	208

	PAGE
V. OPTICS	214
VI. RECONSTRUCTION IN SPACE	224
VII. MOMENTUM FITTING	228
VIII. TRIGGERS AND ACQUISITION	233
IX. CALORIMETER CALIBRATION AND EH	252
X. SPECTROMETER CALIBRATION	267
XI. SINGLE MUON DATA	270
XII. DIMUON BACKGROUNDS	282

CHAPTER I

Neutrino-Nucleon Reactions and Dimuon Final States

1.1 Introduction

The neutrino was first hypothesized by Pauli¹ in 1933 in order to conserve energy-momentum in beta decay. About twenty years later, reactor neutrinos were used to directly observe the inverse processes:²

$$\nu_e + (A, Z) \rightarrow e^+ + (A, Z-1)$$

The existence of a second type of neutrino, the muon neutrino, was demonstrated in the first accelerator neutrino experiment using a neutrino beam generated from pion and kaon decay:³

$$\nu_\mu(\bar{\nu}_\mu) + N \rightarrow \mu(\mu^+) + \text{hadrons.}$$

The absence of electrons in the final state of the reaction provided evidence for the existence of two neutrino types, the electron and muon neutrinos. Subsequently the neutrino-nucleon reaction has become an important tool in the study of nucleon structures, weak interactions, and the fundamental quantities characterizing matter.

In the early 1970s and continuing to this day, neutrino nucleon together with electron and muon-nucleon scattering revealed evidence for hard scattering from point-like constituents by the phenomena called scaling, whereby the shapes of the differential cross sections become independent of energy.⁴ This was consonant with the developments of the quark model of hadrons and its evolution into the

quark-parton constituent model,⁶ and finally to a proposed field theory of quarks and gluons currently being studied (quantum chromodynamics, or QCD).⁷

Concurrent with nucleon structures were a series of discoveries about lepton final states in neutrino scattering. The first was the discovery of a neutral current reaction:

$$\nu_{\mu}(\bar{\nu}_{\mu}) + N \rightarrow \nu_{\mu}(\bar{\nu}_{\mu}) + \text{hadrons}^8$$

which was predicted by a gauge theory that attempted to unite weak and electromagnetic interactions by a common spontaneously broken symmetry.⁹ Secondly was the discovery of opposite sign dimuons in the reaction:¹⁰

$$\nu(\bar{\nu}) + N \rightarrow \mu\bar{\mu} + \text{hadrons} \quad (1)$$

In addition events of the form:¹¹

$$\nu(\bar{\nu}) + N \rightarrow \mu^{\pm} + e^{\pm} + k + \text{hadrons} \quad (2)$$

were discovered. In the bulk of these events, the extra μ or e occur from the production of a charm meson and decay:¹²

$$D \rightarrow \mu + \nu + \text{hadrons}$$

$$\rightarrow e + \nu + \text{hadrons}$$

Following the discovery of dileptons, other multilepton channels were searched for. Events with three muons in the final state:¹³

$$\nu + N \rightarrow \mu\mu\mu + \text{hadrons} \quad (3)$$

were found, followed by evidence for promptly produced same-sign

dimuon events:¹⁴

$$\nu(\bar{\nu}) + N \rightarrow \mu^{\pm}\mu^{\pm} + \text{hadrons} \quad (4)$$

and tetralepton events:¹⁵

$$\nu + N \rightarrow \ell^+\ell^+\ell^+\ell^- + \text{hadrons} \quad (5)$$

This study will thus be devoted to measuring and comparing the rates and properties of opposite sign dimuon events with the mechanisms hypothesized to explain them. In particular, the existence of the reactions (3)-(5) would imply multilepton production mechanisms different from (1)-(2), which may also cause some component of dimuon production.

Sections 1.2 and 1.3 of this chapter will be a digression describing the general features of inelastic neutrino nucleon scattering, of nucleon structure, and of models of quarks, leptons, and the weak interactions which are necessary for a discussion of sources of dimuon events. Using the background and language of sections 1.2 and 1.3, section 1.4 will then describe the primary source of dimuon events, namely weak charm production and decay, followed by section 1.5 which will discuss other possibilities for opposite sign dimuons production and their relationships to other multilepton topologies. Sections 1.4 and 1.5 thus constitute a theoretical basis for a search for dimuon events, and a measurement of their properties. Section 1.5 in particular provides a motivation to search for dimuon sources beyond single charm production as described in section 1.4.

Chapter II discusses comparisons of data and predictions, followed by a conclusion.

1.2 Inelastic Neutrino-Nucleon Scattering

1.2.1 Kinematics

The diagram in figure 1.21a describes the dynamics of the reaction:

$$\nu + N \rightarrow \mu + x \quad [k + p \rightarrow k' + p' \text{ (four-vectors)}]$$

via the weak charged current W (W -propagator). Three Lorentz scalars can be defined from these variables:

$$Q^2 = -q^2 = -(k-k')^2 = 4E_\nu E_\mu \sin^2 \theta / 2 \quad (\text{lab})$$

$$\nu = p \cdot q \approx M(E_\nu - E_\mu) = ME_H \quad (\text{lab})$$

where E_ν , E_μ , E_H , are the neutrino, muon and hadron energies in the lab, θ the muon polar angle, and m the nucleon mass (figure 1.2.1b).

In the (Q^2, ν) plane, $Q^2 < 2\nu + m^2$. Note that

$$Q^2 = \text{mass of propagator}$$

$$W^2 = \text{mass of hadronic system}$$

$$\nu = \text{energy transfer in lab}$$

Instead of Q^2, ν the equivalent dimensionless (scaling) variables can be defined:

$$x = Q^2/2\nu \approx \frac{2(E_\mu + E_H)}{ME_H} \sin^2\theta/2 \quad (\text{lab})$$

$$y = \nu/k \cdot p \approx (E_H - m)/(E_H + E_\mu) \quad (\text{lab})$$

Note that x is the fraction of nucleon momentum struck, while in the C.M. of xP and the neutrino

$$y = (1 - \cos\theta^*)/2$$

or, in the lab, y is the inelasticity,

$$y = \frac{E_\nu - E_\mu}{E_\nu} = \nu/E_\nu$$

(figures 1.2.1b,c). Two useful relations are:

$$xy = Q^2/s \quad (1 - x)y \approx w^2/s$$

1.2.2 Nucleon Structure Functions

For the charged weak current reaction (figure 1.2.1a) the most general form for the inclusive cross section can be found from requirements of Lorentz invariance and from assuming an effective current-current weak interaction with a V-A structure for the lepton current.¹⁶

In terms of 3 dimensionless structure functions this is:

$$\begin{aligned} \frac{d^2\sigma^\nu}{dx dy} &= \frac{G_F^2 2mE}{2\pi} \left\{ F_L + F_R (1-y)^2 + 2F_S (1-y) \right\} \\ \frac{d^2\sigma^{\bar{\nu}}}{dx dy} &= \frac{G_F^2 2mE}{2\pi} \left\{ F_L (1-y)^2 + F_R + 2F_S (1-y) \right\} \end{aligned} \quad (1.2.1)$$

G_F is the Fermi weak coupling constant (10^{-5} GeV^2). The structure functions F are functions of (x, Q^2) and the subscripts L, R, S refer to left, right and scalar couplings. These cross sections are in the high energy limit where m/E goes to zero. Since mE is approximately $s/2$, the cross section rises as the square of the invariant energy (point-like coupling limit). Table 1.2.1 constitutes a review of deep inelastic neutrino scattering, listing various relations among the kinematic quantities and structure functions including the usual connection with the structure functions F_i of electromagnetic scattering (in the neutrino case there is an extra parity violating F_3).¹⁷

1.2.3 Scaling and Scale Violations

It has been conjectured that the neutrino scattering is the incoherent sum of scattering from point-like centers (partons) in the nucleon, and thus by dimensional arguments the structure functions are independent of energy.¹⁸ The more precise statement of this is that x remains finite as Q^2 and $\nu \rightarrow \infty$, and the structure functions become functions only of x , and not x, Q^2 . The structure functions thus have an interpretation as the momentum fraction density functions of the quark-partons which comprise the nucleon:

$$F(x, Q^2) \approx xq(x, Q^2) \approx xq(x)$$

where $q(x, Q^2)$ is the number density of a quark of momentum fraction x . Referring to figures 1.2.1c and d, scattering by like-helicity particles is allowed for all θ^* ($\nu + q, \bar{\nu} + \bar{q}$), and scattering by

opposite helicity particles at $\theta = \pi$ is forbidden ($\nu + \bar{q}, \bar{\nu} + q$) by angular momentum conservation. Thus, in this picture of neutrino nucleon scattering the following is equivalent to relation 1.2.1:

$$\frac{d^2\sigma^{\nu N}}{dx dy} = \frac{G_F^2}{2\pi} 2mx E \left\{ q(x, Q^2) + (1-y)^2 \bar{q}(x, Q^2) + 2(1-y) \ell(x, Q^2) \right\}$$

where q refers to left-handed currents and charge $-1/3$ quarks, \bar{q} refers to right-handed currents and charge $-2/3$ antiquarks and ℓ refers to possible longitudinal (scalar) constituents. For $\bar{\nu}$, q and \bar{q} interchange, and with charge $+2/3$ quarks and charge $+1/3$ anti-quarks. In the scaling limit (free quarks) $q(x, Q^2) \rightarrow q(x)$ and $\ell(x) \rightarrow 0$. Note that $2mx E$ is s of ν - q subprocess.

The quantity R is defined as the ratio of longitudinal (transversely aligned or scalar boson propagator) to transverse (longitudinally aligned propagator) cross sections:

$$R = \sigma_L / \sigma_T \quad \text{for } q^2 \rightarrow \infty$$

(see table 1.2.1). R is non-zero only if there are apparent non-spinor scattering centers in the nucleon, which could be, for example, spinors with a momentum component transverse to the nucleon momentum.¹⁹ In other words, $R \neq 0$ implies $\ell(x, Q) \neq 0$. Experimentally, the following relations in terms of the standard $F_1 - F_3$ are true to about 10 - 20%:

$$2xF_1 \approx F_2, R \approx 0 \quad (\text{Callan-Gross})$$

$$-2xF_1 \approx F_3 \quad (\text{maximal V-A interference}),$$

the q content of the nucleon is about 10%-15% at 100 GeV (refer to table 1.2.1).

Up to this point in the discussion quarks are considered to be free, and the nucleon is composed only of massless quarks and $q\bar{q}$ pairs. None of these statements are completely correct. The quarks are neither free (?)²⁰ nor massless (?)²¹, and simple sum rules compared to data have shown that it is inconsistent to require that quarks carry all the momentum of the nucleon (only about 50%).²² In addition there is a progressive, although gentle, change in the structure functions with E and Q^2 , and $R \approx 0.1 - 0.2$.²²

To explain these objections (deviations) to simple scaling, and hadronic physics in general, there is some evidence (hope) that a non-abelian gauge theory of quarks and gluons may be a theory of hadronic matter (QCD).²³ It is analogous to the QED theory of electrons and photons, except that the photon is charged (gluon). In the case of deep inelastic scattering, this theory presumably explains the logarithmic Q^2 dependence of the structure functions and the presence of antiquarks in the nucleon. At large Q^2 , the current can always "resolve" a quark into a quark and a gluon (the Uncertainty Principle) as in figure 1.2.2, thus sharing the momentum fraction x between the quark and the gluon, and thus causing the quark densities to appear at lower x as Q^2 increases. In addition, the theory has

the property that the effective coupling constant α_s decreases in strength as Q^2 increases, thus explaining the approximate scaling behavior at high energy, since the quarks appear to be quasi-free from the other quarks (asymptotically free).²⁴ (In the low Q^2 limit it is conjectured that this behavior reverses and the quarks are confined: infrared slavery.) A gluon can always be resolved by a current (W-boson) into a pair of quarks (figure 1.2.3) and thus at larger W^2 and Q^2 , the nucleon appears more as $q\bar{q}$ pairs of any flavor at low x since they share the x of the gluon. This explains especially the \bar{q} peaking at $x \rightarrow 0$. The gluons can also be identified as carrying the "missing" momentum of the nucleon not carried by quarks. Finally, the quark-gluon interactions give transverse components to the quark momenta, inducing an effective $R [x]$.

In summary:

1. The nucleon structure functions in deep inelastic scattering scale approximately
2. Charge symmetry ($\nu - \bar{\nu}$ structure function differences) appears to be a valid symmetry, at least at high energy.
3. R is small ≈ 0.2
4. The total cross section rises with energy for $E < 400$ GeV
5. The number of valence quarks is 3 (quarks not pairable in $q\bar{q}$ pairs)
6. F_2 in electromagnetic and weak interactions is similar up to differences in quark charge
7. The quarks carry half of the nucleon momentum

There are systematic QCD effects in Q^2 , E , which effectively change the quark content of the nucleon, causing the structure functions to peak at lower x and allowing gluons to carry nucleon momentum.

However a note of caution should be interjected. Radiative corrections also induce Q^2 effects.²⁴ Massive quark production alters simple scaling behavior with Q^2 due to threshold effects.²⁵ (The whole subject of the role of quark masses as "constituent" quarks, and as "current" quarks in scattering is poorly understood.²⁵ Care must be taken to remove these effects in the study of QCD by deep inelastic scattering.

Finally, one of the beautiful aspects of QCD from a lepton scattering point of view is that it allows the nucleon to serve as a target of quarks of any flavor as the lepton energy increases. The subject of quark flavors is discussed in the next section.

1.3 Quarks and Leptons and the Weak Currents

1.3.1 Weak Currents

The neutrino nucleon cross section for energies small with respect to $G_F^{-1/2}$ can be derived from a current-current V-A interaction, implying a total cross section linear in s , which eventually violates the unitarity bound for s-wave (pointlike) interactions.²⁶ However, this interaction predicts to a high degree of accuracy many of the low energy decay phenomena. Fortunately the effective current-current interaction lagrangian can be derived as a low energy limit of a spontaneously broken gauge theory $SU(2) \times U(1)$ (Weinberg-Salam) of both electromagnetism and the weak interactions.⁹ The point coupling is replaced by heavy propagators (W^\pm, Z^0) which together with the photon acquire their masses from the effects of the symmetry breaking.²⁷ This theory is assumed to be a correct description of the weak interactions for the purposes of this work.

It is the 3 heavy propagators W^\pm, Z^0 connecting the quarks and leptons, and in particular, the neutrino and the quarks, which are the source of the weak interaction. Because the boson masses are

large (more than 75 GeV), the cross section is undamped in Q^2 by propagator effects for the energies under consideration (unlike electromagnetism).

The basic effects of the weak interaction in neutrino scattering can be summarized as follows:

1. undamped by propagator effects, leading to high Q^2 events
2. highly inelastic - flat y - distribution for like helicity particles, and large scattered lepton momenta perpendicular to the beam direction
3. large hadronic masses (W^2 large)
4. non-conservation of some hadronic quantum numbers
5. parity violation terms
6. quarks have equal weak charges

1.3.2 The Fundamental Fermions

Under the charged current, the quarks and leptons are grouped into left-handed mixed doublets. It is believed that there are at least 6 quarks and 6 leptons forming 3 generations²⁸:

$$\begin{pmatrix} u \\ d' \end{pmatrix}_L \quad \begin{pmatrix} c \\ s' \end{pmatrix}_L \quad \begin{pmatrix} t \\ b' \end{pmatrix}_L$$

$$\begin{pmatrix} e \\ \nu_e \end{pmatrix}_L \quad \begin{pmatrix} \mu \\ \nu_\mu \end{pmatrix}_L \quad \begin{pmatrix} \tau \\ \nu_\tau \end{pmatrix}_L$$

The d' , s' , b' are the "Cabbibo" rotated states, each dominated by d ,

s, b quark contributions. (Note that t, ν_τ have not been directly observed.)

The charge changing interaction can be described by the hadronic current:

$$J(u, c, t) A \begin{pmatrix} d \\ s \\ b \end{pmatrix}$$

where A is a 3 x 3 unitary matrix

$$A = \begin{pmatrix} c_1 & -s_1 c_3 & -s_1 s_3 \\ s_1 c_2 & c_1 c_2 c_3 - s_2 s_3 e^{-i\delta} & c_1 c_2 s_3 + s_2 c_3 e^{-i\delta} \\ s_1 s_2 & c_1 s_2 c_3 + c_2 s_3 e^{-i\delta} & c_1 s_2 s_3 - c_2 c_3 e^{-i\delta} \end{pmatrix}$$

and $c_i = \cos\theta_i$, $s_i = \sin\theta_i$ are generalized Cabbibo angles and δ is a complex phase. In principle δ can be adjusted to explain CP violation effects ($K^0 - \bar{K}^0$ system); it is consistent to set $e^{i\delta} \approx \pm 1$. The quark doublets become

$$\begin{pmatrix} u \\ d(c_1) - s(s_1 c_3) - b(s_1 s_3) \end{pmatrix}_L$$

$$\begin{pmatrix} c \\ d(s_1 c_2) + s(c_1 c_2 c_3 - s_2 s_3) + b(c_1 c_2 s_3 + s_2 c_3) \end{pmatrix}$$

$$\begin{pmatrix} t \\ d(s_1 s_2) + s(c_1 s_2 c_3 + c_2 s_3) + b(c_1 s_2 s_3 - c_2 c_3) \end{pmatrix}$$

The angle θ_1 controls the relative strength of $u \leftrightarrow d$ transitions to the strength of $(u, d) \leftrightarrow$ (not d, u) transitions. Angle θ_2 controls the relative strength of $u \leftrightarrow s, b$ while θ_3 controls the relative sharing

of $d \rightarrow c, t$. Since the 4-quark $udsc$ GIM model works well, $\theta_1 \approx \theta_{\text{Cabbibo}}$ and $\cos\theta_2 \approx \cos\theta_3 \approx -1$. A complete discussion on the sizes and properties of the angles can be found in reference 29. The constraints are:

$$\begin{aligned}\theta_1 &\approx \theta_c \quad s_1^2 = .05 \\ s_2^2 &< 0.1 \\ s_3^2 &< 0.3\end{aligned}$$

Making a simple assumption that $\theta_1 = \theta_2 = \theta_3 = \theta_c$, $\sin^2\theta_i = 1/20$, $\cos^2\theta_1 = 1$, $\cos\theta_2 = \cos\theta_3 = -1$, the quark doublets are approximately:

$$\begin{pmatrix} u \\ d \pm s/20 - b/20 \end{pmatrix} \quad \begin{pmatrix} c \\ -d/20 + s - 2b/20 \end{pmatrix} \quad \begin{pmatrix} t \\ d/20 - 2s/20 - b \end{pmatrix}$$

from which the relative transition probabilities can be computed.

Note that the allowed maximum rates for $u \rightarrow b \approx 1\%$, $c \rightarrow b$ 50%, while $s \rightarrow c \approx 1.0$, $d \rightarrow c \approx 5\%$.³³

The lepton doublets are not mixed to any known degree, presumably due to the masslessness of the neutrinos.³⁰ The mass scales for the quarks in some models is taken to be roughly:

$$m(u:d:s:c:b:t) \rightarrow 1:1.2:3:9:27:81, \text{ with } M_c \approx 1.5 \text{ GeV.}^{31}$$

1.4 Dimuons from Charm

In the limit of $c_2 = c_3 \approx -1$, the source yielding the highest rate of dimuons is the direct production and prompt semileptonic decay of

charm particles.^{10 12 17} This occurs for $(\bar{\nu})\nu$ nucleon collisions mainly by $(\bar{d}, \bar{s}) d, s$ transitions to $c(\bar{c})$ quarks as shown in figure 1.4.1a,b. Note that charm dimuons for $\bar{\nu}$ occur only from ocean quarks. In addition, charm quarks in the ocean can lead to dimuons from the "leftover" quark as shown in figure 1.4.1c. This diagram is not expected to contribute significantly to the rate due to the $(1 - y)^2$ factor and the assumed weak energy transfer mechanism to the left-over charm quark, yielding lower energy muons relative to the other diagrams.

In the limit of no quark mass effects and ignoring the effect of $c\bar{c}$ pairs in the ocean, the cross section above threshold in the "fast rescaling" limit are

$$\frac{d^2\sigma^{\nu N}}{dx dy} = \frac{G^2 m E}{\pi} (x) (d \sin^2\theta_c + s \cos^2\theta_c)$$

$$\frac{d^2\sigma^{\bar{\nu} N}}{dx dy} = \frac{G^2 m E}{\pi} (x) (\bar{s} \cos^2\theta_c + \bar{d} \sin^2\theta_c)$$

For practical purposes, the term $\bar{d} \sin^2\theta_c$ can be ignored, relative to $\bar{s} \cos^2\theta_c$. Note that the convention on isoscalar targets is:

$$d = d_p + d_n = d_p + u_p = u$$

$$u = u_p + u_n = u_p + d_p = d$$

$$s = s_p + s_n = 2s_p = 2s_n = \bar{s}$$

$$\bar{u} = \bar{u}_p + \bar{u}_n = 2\bar{u}_p = 2\bar{u}_n = \bar{d}$$

$$c = 2c_p = 2c_n = \bar{c}$$

A more complete model for dimuons includes the following five elements³²:

- I the quark densities $d(x)$, $\bar{d}(x)$, $s(x)$, $\bar{s}(x)$, $c(x)$, $\bar{c}(x)$
- II slow rescaling and threshold effects, with x replaced by $x' = x + M_c^2/(2mEy)$, M_c being the mass of the charm quark
- III fragmentation of the charm quark into a charm meson with momentum fraction z of the quark momentum
- IV transverse momentum distribution of the charm particle with respect to the W boson direction
- V muon kinematics from charm particle semileptonic decay

The quark densities are given by the first article in reference 33 for valence V and sea S as:

$$xV(x) = 3.6^2 x^{1/2} (1-x)^3 - 3.59 x^{1/2} (1-x)^5 + 14.79 x^{0.85} (1-x)^9$$

$$xS(x) = 0.202(1-x)^9 \quad (\text{sea})$$

$$\text{and } \left(\int_0^1 xSdx \right) / \left(\int_0^1 xVdx \right) = 0.06$$

The remaining articles in reference 33 give various parametrizations, approximately as:

$$xV(x) \approx (1-x)^3 x^{1/2}$$

$$xS(x) \approx (1-x)^{6.5}$$

with overall percentages of momentum carried by the ocean quarks varying between 5-20%. For this work, the former densities are used and SU(3) symmetry assumed. Discussion of these densities are also found

in reference 32. The question of flavor symmetry in the ocean is an open and important question. Presumably at infinite energy, the ocean arising from gluon processes is $SU(N)$ symmetric, N = number of flavors. At the energies relevant to this experiment, since the symmetry is broken by the quark masses (?), both kinematic and dynamic suppression of the heavier quarks in the ocean may occur.³⁴

This leads to the rescaling of the cross section for charm production. Since the mass of the quark absorbs a large part of the phase space above threshold the terms in the differential cross section referring to charm quark production are recast by the substitution of x' for x as defined by II above. The differential cross sections for charm quark production become³⁵:

$$\frac{d^2\sigma^V}{dx dy} = \frac{G^2 m E}{\pi} \left\{ 1 - y + \frac{yx}{x'} \right\} (x') (d(x') \sin^2\theta_c + s(x') \cos^2\theta_c)$$

$$\frac{d^2\sigma^{\bar{V}}}{dx dy} = \frac{G^2 m E}{\pi} \left\{ 1 - y + \frac{yx}{x'} \right\} (x') (\bar{s}(x') \cos^2\theta_c)$$

As can be seen from the definition, as $E \rightarrow \infty$, $x' \rightarrow x$. The overall effect of this "slow rescaling" is a more gentle increase of the dimuon rate with neutrino energy.

The "fragmentation" of the charm quark into a charmed particle is described by a probability (or "fragmentation") function $D(z)$ where $z = E_D/E_H$. Here, E_D = energy of a D meson, $E_H = yE_\nu$ is the energy absorbed in the quark transition, and z is thus the fraction of the energy of the charm quark retained by the charmed hadron. In the

production of light particle (pions, Kaons), the probability density $D(z) \approx e^{-5z}$.³⁶ Rather adhoc arguments based on intuition about QCD favor flatter [$D(z) \approx \text{constant}$] or even rising [$D(z) \approx z$]³⁷ z distributions, for charm fragmentation.

The momentum of the D meson perpendicular to the W-direction is taken from the P_t distribution in the production of high mass states in hadronic collisions³⁸ as $\frac{dN}{dP_t^2} \approx e^{-aP_t}$, $a \approx 3-6$ and $m_T = (P_t^2 + m_D^2)^{1/2}$

D-decays are taken as $D \rightarrow K(K^*)\mu\nu$ 50% K, 50% K^* analogous to kaon decay³⁹:

$$\frac{dN}{dE_K dE_\mu} \approx 2E_\mu E_\nu - M_D(W_K - E_K)$$

$$\frac{dN}{dE_{K^*} dE_\mu} \approx 2E_\mu E_\nu - M_D(W_{K^*} - E_{K^*}) + \frac{M_{K^*}^2}{M_D} (W_{K^*} - E_{K^*})$$

where $W_i = (M_D^2 + M_i^2 - M_\mu^2)/2M_D$. The average muon energy for the K^* decay mode is about 20% lower than the K decay mode due to the K, K^* mass difference. The branching ratio of $D \rightarrow \mu$ is between 8% and 15%, with a preferred value of about 10%.⁴⁰

In principle, by comparing the neutrino and anti-neutrino dimuon rates relative to single muons, the fractional momentum carried by the strange ocean (s,s) can be approximately determined relative to valence quarks integrated over x and y as:

$$\frac{S}{D} = \tan^2 \theta_c \frac{R_1}{(R_2 - R_1)}$$

where $R_1 = \frac{\sigma_{\bar{\nu}}}{\sigma_{\nu}}$, $R_2 = \frac{R^{\bar{\nu}}}{R^{\nu}} = \frac{(\sigma_{2\mu}/\sigma_{1\mu})^{\bar{\nu}}}{(\sigma_{2\mu}/\sigma_{1\mu})^{\nu}}$

and $Q = \int x q(x) dx$

The values $\frac{\sigma_{\bar{\nu}}}{\sigma_{\nu}} = 0.48 \pm 0.03$, $\sin^2 \theta_c = 0.054$

are used.⁴¹ This approach will be an underestimate of the strange sea as threshold effects require an x'_{\min} to make D mesons of

$$x'_{\min} = \frac{m_D^2 - m_S^2}{2mE_H}$$

which is not an "automatic" requirement in single muon events. This underestimate can be as large as 50% without slow rescaling.⁴² If charm quarks are included the ratio $S/D \rightarrow (S + C_3)/D$

In addition, by integrating the differential cross sections over x , y and using the previous definitions of R^{ν} , $R^{\bar{\nu}}$

$$R^{\nu} = \frac{S \cos^2 \theta_c + D \sin^2 \theta_c + 1/3 \bar{C}}{(D + S) + 1/3 (\bar{U} + \bar{C})} \cdot \frac{b}{\epsilon}$$

$$R^{\bar{\nu}} = \frac{\bar{S} \cos^2 \theta_c + \bar{D} \sin^2 \theta_c + 1/3 C}{1/3 (U + C) + (\bar{D} + \bar{S})} \cdot \frac{b}{\epsilon}$$

where b = branching ratio $\text{charm} \rightarrow \mu$

ϵ = experimental efficiency factor typically $\approx 1.8 - 2^{43}$

Note that the terms $1/3 C$ and $\bar{D} \sin^2 \theta_c$ can be taken as small. By using the shapes of the y distributions defined by B^{ν} , $B^{\bar{\nu}}$ (table 1.2.1)

and the assumption that $\text{ocean} \cdot \sin^2 \theta_c \approx 0$, the following relations can be derived^{4,3}:

$$\frac{\bar{S} + C/3}{U + C} \approx R^{\bar{\nu}} \left\{ 1/3 + \frac{1-B^{\bar{\nu}}}{1+B^{\bar{\nu}}} \right\} \frac{\epsilon}{b}$$

$$\frac{S + D \sin^2 \theta_c + 1/3 \bar{C}}{D + S} \approx R^{\nu} \left\{ 1/3 + \frac{1-B^{\nu}}{1+B^{\nu}} \right\} \frac{\epsilon}{b}$$

Thus using measurements of the dimuon ratio $R^{\bar{\nu}}$, R^{ν} relative to single muons, information about the relative quark contents of the nucleon can be extracted. It is to be emphasized, however, that energy dependent rescaling modifies these simple predictions by as much as 50%.

In summary, the rate of dimuons given by:

$$\begin{aligned} d\sigma (\nu N \rightarrow \mu^+ \mu^- x) = & \\ d\sigma (\nu N \rightarrow \mu x) & \quad \text{charm quark production} \\ \times D(z) dz & \quad \text{fragmentation} \\ \times P(m_T) dP^2 & \quad P \text{ W-direction} \\ \times \frac{bd\Gamma}{\Gamma} (D \rightarrow \mu x) & \quad \text{D-decay} \end{aligned}$$

This overall rate is about 1-2% asymptotically, with no experimental cuts.

Because of the 3-body D decay and the z-distribution, the muon from the D-decay will be soft relative to the initial muon from the lepton vertex. The second muon will follow the W-boson direction up

to a P_t reflecting M_D and heavy particle production. In an experiment, cuts in momentum are always made to ensure, for example, good acceptance and muon identification. Cuts are described further in Chapter 3. With a 4-5 GeV minimum muon energy cut, typically 40-50% of the events are lost. A detailed comparison of the events expected from a charm Monte Carlo will be presented in Chapter 4.

1.5 Dimuons from Sources Beyond Charm

1.5.1 Sources of dimuon events are basically limited only to the inventiveness of physicists. However, sources of dimuons are constrained by properties of other lepton final states: same sign dileptons, trileptons, tetra leptons, and so forth. Sources for 2 muon events must not yield too large a relative rate for other measured topologies. These rates are:

$$\frac{\mu\mu^{--}}{\mu\mu^{+-}} \approx \frac{\mu\mu^{++}}{\mu\mu^{+-}} \approx (5 \pm 3) \times 10^{-2}, P_{\min} > 5 \text{ GeV}$$

$$\frac{\mu\mu\mu}{\mu} \approx (6 \pm 2) \times 10^{-5}, P_{\min} > 4.5 \text{ GeV}$$

$$\frac{\mu\mu\mu\mu}{\mu} < 10^{-6}, P_{\min} > 3 \text{ GeV}$$

quoted for typical high energy beams with $E_{\text{primary}} > 400 \text{ GeV}$. Conversely sources for other topologies must not create dileptons with high rates, or unusual properties.

For the present purposes, the dimuon signal is classified into 6 categories:

1. weak charm production and decay
2. backgrounds: π, k decay, and accidentals
3. electromagnetic processes
4. hadronic charm pair production
5. weak heavy quark production
6. exotic processes: production of heavy leptons, gauge particles (Higgs), etc.

Process 1 has already been discussed in section 1.4 and process 2, backgrounds, are discussed in Appendix XII and chapter 3 and 4.

1.5.2 Weak-Electromagnetic Processes

Process 3, electromagnetic processes is subdivided into 4 categories.

1. standard trimuons with a missing muon due to acceptance (figure 1.5.1a)
2. neutral current radiative corrections (figure 1.5.1b)
3. neutral current direct muon production (figure 1.5.1c)
4. weak-electromagnetic "coherent" scattering (4-fermion) (figure 1.5.1d)

The standard trimuon mechanisms are discussed in reference 45. The "feed-through" from standard trimuons to dimuons via the loss of a muon through momentum cuts is calculated to give a rate of less than 0.5×10^{-5} per single muon event using the models shown in figure 1.5.1a, and assuming that the lost muon must be less than 4.5 GeV.⁴⁶ (Note that this model scales up the calculated direct pair contribu-

tion by a factor of 3 to explain the trimuon rate.)

The neutral current radiative processes are about a factor of 3 larger per neutral current interaction than the corresponding charged current trimuon processes as there is no interference between diagrams.⁴⁵ However, the neutral current/charged current ratio lowers this relative to single muon events. The neutral current direct muon pair processes should occur at a similar rate per charged current interaction as the corresponding rate in trimuons. Thus the overall dimuon rate per single muon event from neutral current induced electromagnetic processes is similar to or slightly lower than the trimuon rate for events with $P_{\min} > 4.5$ GeV: $\frac{\mu^- \mu^+}{\mu^-} \approx \frac{\mu^+ \mu^-}{\mu^+} < 5 \times 10^{-5}$. These events are characterized by very low invariant masses of the muon pairs, averaging about 750 MeV, and have low E visible due to the missing neutrino.

In addition, direct muons in neutral current events can occur from vector meson production. This dimuon rate is also estimated to be $< 10^{-5}$ per single muon event from vector meson production cross sections and muonic branching ratios.⁴⁷ These events are also characterized by low pair masses and low total energy due to the missing neutrino.

The weak-electromagnetic process is characterized by very low hadronic energy E_H . The signal is also very small, having a rate (proportional to Z^2) of about $2-3 \times 10^{-6}$ per single muon event for an average Z of 20.⁵²

In general, all the electromagnetic and direct muon processes, will not contribute substantially to opposite sign dimuons having rates proportional to $G^2\alpha^2$ implying ratios less than 5×10^{-5} per single muon event or about 1% or less of the expected dimuons from charm.

1.5.3 $c\bar{c}$ Production

From beam-dump results and hadronic collisions with single lepton final states, charm pair production is estimated to be about 50 $\mu\text{b}/\text{nucleon}$ or about 10^{-3} per interaction.⁴⁹ Assuming that the W is like a quark beam, $c\bar{c}$ production in ν reactions may occur at the 10^{-3} level of the total cross section. This gives rise to multi-lepton events as illustrated in figures 1.5.2a-d. A crude estimate of the dimuon rate would be $10^{-3}b/\epsilon$ with $b = 10\%$, ϵ (efficiency) ≈ 2 if c, \bar{c} decay is like direct charm with a 4-5 GeV P_{min} cut.

The $c\bar{c}$ processes gives both a same sign and an opposite sign dimuon rate of 5×10^{-3} per single muon event, compatible with the same sign rate. One diagram of a model for $c\bar{c}$ production by gluon bremsstrahlung is shown in figure 1.5.3. Calculations for this contribution are lower than the observed rate by an order of magnitude or more.⁵⁰ It should be noted that in the hadronic direct muon contribution to the trimuons, a naive calculation using pion beam data for muon pair production is too low by about a factor of 3 if the whole of the 3μ rate is to explained by radiation and direct muon

pair production. Charged current charm pair production causes trimuons at a rate 2×10^{-5} per single muon event from both particles' semileptonic decays (figure 1.5.2d) thus making a three source interpretation of trimuons somewhat more compatible with data and providing a natural explanation of the like-sign dimuon rate. At this time, it appears to be virtually impossible to distinguish $c\bar{c}$ induced opposite sign dimuons from ordinary direct charm production from the characteristics of the events, except if accurate models for $D(z)$ and $F(P_t)$ can be formulated, or if threshold effects can be investigated. Charm pair production by neutral currents probably can be ignored due to low momenta and energies, as well as the low rate.

Several interesting points can be made about $c\bar{c}$ production and direct muon pair production by neutrinos. Both processes involve correlations between quarks in the same hadronic system. Referring to figure 1.5.4a, once a quark of momentum fraction x has absorbed a current producing a quark q' of momentum fraction x' , the \bar{q}' with which it annihilates can only have an \bar{x}' distribution which ranges from 0 to $(1-x)$, since the sum of all x in any hadron is bounded by 1. Similarly (refer to figure 1.5.4b) a c quark of energy fraction z necessarily bounds the \bar{c} to a z of $0 < \bar{z} < (1-z)$. In order to correctly calculate these processes, joint quark probabilities must be known, which is contrary to the foundations of the parton model, namely incoherence. However, it is interesting to

speculate that QCD may provide mechanisms to calculate these effects, since the \bar{q} arise from gluons. Indeed, it may be argued that quark confinement is ultimately a correlation.

1.5.4 Heavy Quark Production

Heavy quarks, b and t, can be produced by the weak current analogously to direct charm production but with an additional phase space suppression estimated to be a factor of 3 for b-quarks over charm.⁵¹ The t quark production, with m_t greater than about 14 GeV, will not be considered here. The b-quark can be produced by the following processes:

$$\bar{\nu}_u \rightarrow \mu^- \bar{b} \quad \bar{\nu}_u \rightarrow \mu^+ b$$

$$\bar{\nu}_c \rightarrow \mu^- \bar{b} \quad \bar{\nu}_c \rightarrow \mu^+ b$$

Both are $(1-y)^2$ distributions. Note that only in the ν case can production occur from valence quarks (reverse of charm). For $\bar{\nu}_u \rightarrow \mu^+ b$, the mixing angle bounds imply a maximum allowable rate of 0.3% of the charged current rate, and for $\bar{\nu}_u \rightarrow \mu^- \bar{b}$, about 0.03 - 0.1% above 100 GeV, implying a maximum contribution to $\bar{\nu}$ dimuons of 3% and to ν dimuons of 0.3 - 1% via semileptonic decay.

(figure 1.5.5a).^{29, 51} (Note that the mixing angles were discussed in section 1.3.) The c-b transition rate may be as large as 50%, implying at high energy a dilepton rate as high as 10-20% of the direct charm production assuming an SU(4) symmetric ocean. This is not likely. The most favored parameters in the literature⁵¹ favor a dimuon rate from b-production of 0.1% of the charm rate. Note that

$b \rightarrow c$ cascades can occur yielding a source of trimuons by an additional semi-leptonic c decay (figure 1.5.5b) with a rate lower than the b -quark dimuons by a factor of at least 20 or more, compatible with the trimuon rate. Both figures 1.5.5a,b can give rise to extra muons by "leftover" charm quark decays which presumably will give inly soft muons. It is interesting to speculate that this "left-over" quark decay may be a source of tetraleptons, as its overall rate

$$\frac{\sigma(\nu N \rightarrow \mu^- b)}{\sigma(\nu N \rightarrow \mu^- + x)} * \frac{b}{\epsilon}^3 \approx 10^{-6} - 10^{-7}$$

roughly like the observed tetralepton rate assuming 5% charm ocean.

Since the contribution to the overall rate of dimuons is small for heavy quark production, the most reasonable tests for b -quark production and decay are by the kinematic properties of the decay muon.⁵¹ These are calculated analogously to direct charm production, requiring $D(z)$, $F(P_t)$ and b -quark decay kinematics. For the purposes of calculation this work uses 50% charm - 50% up quark decays. The decay muon will reflect the mass of the b -quark, causing the second muon to reach larger values of momenta transverse to the W -boson direction than charm decays for equal numbers of events.

1.5.5 Heavy Leptons and Other Exotics

A heavy L^- with masses less than 14 GeV have been tested by several experiments and ruled out to the 1% level.⁵³ However, three experiments have reported weak evidence for an L^0 with a mass between

1.5 - 2 GeV⁵⁴, one by $L^0 \rightarrow \mu\pi$, and 2 by $L^0 \rightarrow \mu e \nu$. Tests for dimuon production by $L^0 \rightarrow \mu\mu\nu$ (figure 1.5.6) would be⁵⁵:

1. a higher probability than charm for the 2 muons to have similar momenta $\frac{1}{2} < P_1 / P_2 < 2$.
2. the second muon not following the apparent w-direction
3. invariant muon pair mass less than m_{L^0}
4. small difference in the azimuthal angles of the 2 muons about the beam direction.

Other sources (Higg's particles , axions, etc) will be ignored in this analysis. A reievew of some of these mechanisms can be found in reference 56.

LIST OF FIGURES

Chapter 1

- 1.2.1a-c Feynman diagram and illustrations of inelastic neutrino nucleon scattering.
- 1.2.2 As Q^2 increases a quark can be resolved into a quark and a gluon by a current q .
- 1.2.3. As Q^2 increases, a gluon can be resolved into a pair of quarks by a current q .
- 1.4.1a-c Weak charm production and decay.
- 1.5.1a-d Weak-electromagnetic dimuon processes; 1.5.1a are trimuons which produce dimuons via a missing muon. The Drell-Yan process is described in the references 45.
- 1.52.2a-d $c\bar{c}$ multilepton production.
- 1.5.3 Gluon bremsstrahlung model of $c\bar{c}$ production.
- 1.5.4 Illustration of intra-nucleon processes.
- 1.5.51,b b-quark production and decay yielding 2 muon and 3 or more muon final states.
- 1.5.6 L^0 production and decay to dimuons.

Table 1.2.1. Formulae for deep inelastic ν scattering.

$$\frac{d^2\sigma^{\nu, \bar{\nu}}}{dx dy} = \frac{GmE}{\pi} \{ (1-y)F_2 + xy^2F_1 \pm x(y-y^2/2)F_3 \}$$

$$F_{L,R} = 2xF_1 \pm xF_3 \quad q, \bar{q} = 2F_1 \mp F_3$$

$$F_S = F_2 - 2xF_1 \quad x = RF_2/(1+R)$$

$$R = \int F_2 dx / \int 2xF_1 dx - 1 = \sigma_L / \sigma_T = \int (F_S / 2(F_R + F_L)) dx$$

$$\rho = -1/(1+R) \quad B = - \int xF_3 dx / \int F_2 dx$$

$$B^\nu - B^{\bar{\nu}} = 2 \int x(s-c) dx / \int x(u+\bar{u}+s+c) dx$$

$$xF_3^\nu = x(d+s-\bar{u}-\bar{c}) \quad F_2^\nu = x(d+s+\bar{u}+\bar{c})$$

$$xF_3^{\bar{\nu}} = x(u+c-\bar{d}-\bar{s}) \quad F_2^{\bar{\nu}} = x(u+c+\bar{d}+\bar{s})$$

$$\text{On an isoscalar target: } u=u_p+u_n=u_p+d_p=d$$

$$\bar{d}=d_p+d_n=d_p+u_p=\bar{u}$$

$$s=\bar{s}=2s_p \quad ; \quad c=\bar{c}=2c_p$$

$$\text{Let } G' = \pi / GmE ;$$

$$\frac{3}{4} G' \left(\frac{d\sigma^\nu}{dx} + \frac{d\sigma^{\bar{\nu}}}{dx} \right) = \frac{3}{4} F_2 + \frac{1}{2} xF_1 - \frac{1}{4} (xF_3^\nu - xF_3^{\bar{\nu}})$$

$$\frac{3}{2} G' \left(\frac{d\sigma^\nu}{dx} - \frac{d\sigma^{\bar{\nu}}}{dx} \right) = -\frac{1}{2} (xF_3^\nu + xF_3^{\bar{\nu}}) = x(u-\bar{u})$$

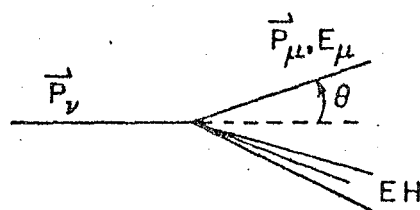
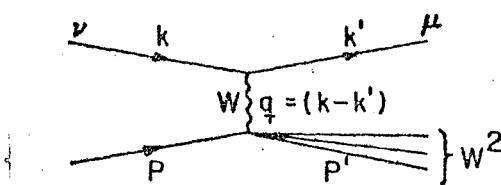
$$\frac{1}{2} G' \left(\frac{d\sigma^\nu}{dy} + \frac{d\sigma^{\bar{\nu}}}{dy} \right) = \int F_2 dx \{ (1-y+y^2/2) + \frac{1}{2} (B^\nu - B^{\bar{\nu}})(y-y^2/2) + \rho y^2/2 \}$$

$$\text{Fractional momentum in quark: } Q+\bar{Q} = \int F_2 dx = \int (q+\bar{q}) dx$$

$$\text{Callan-Gross relation (not assumed): } 2xF_1 \approx F_2$$

$$\text{Gross-Llewellyn Smith sum rule: } \int F_3 dx = 3$$

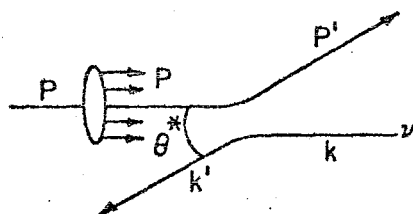
Inelastic Scattering



Lab:

$$y = \frac{E_\nu - E_\mu}{E_\nu} = \frac{EH}{E_\nu}$$

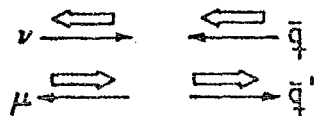
$$x = \frac{Q^2}{2m\nu} = \frac{4E_\mu E_\nu \sin^2 \theta / 2}{2m\nu}$$

C.M. ν -Quark

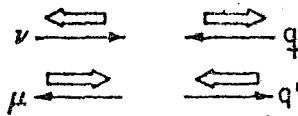
$$p = xP$$

$$y = \frac{1 - \cos \theta^*}{2}$$

(spin)

 $\theta^* = \pi$ forbidden

$$\frac{d\sigma}{dy} \sim (1-y)^2$$

 $\theta^* = \pi$ allowed

$$\frac{d\sigma}{dy} \sim \text{Constant}$$

Figure 1.2.1 a-c

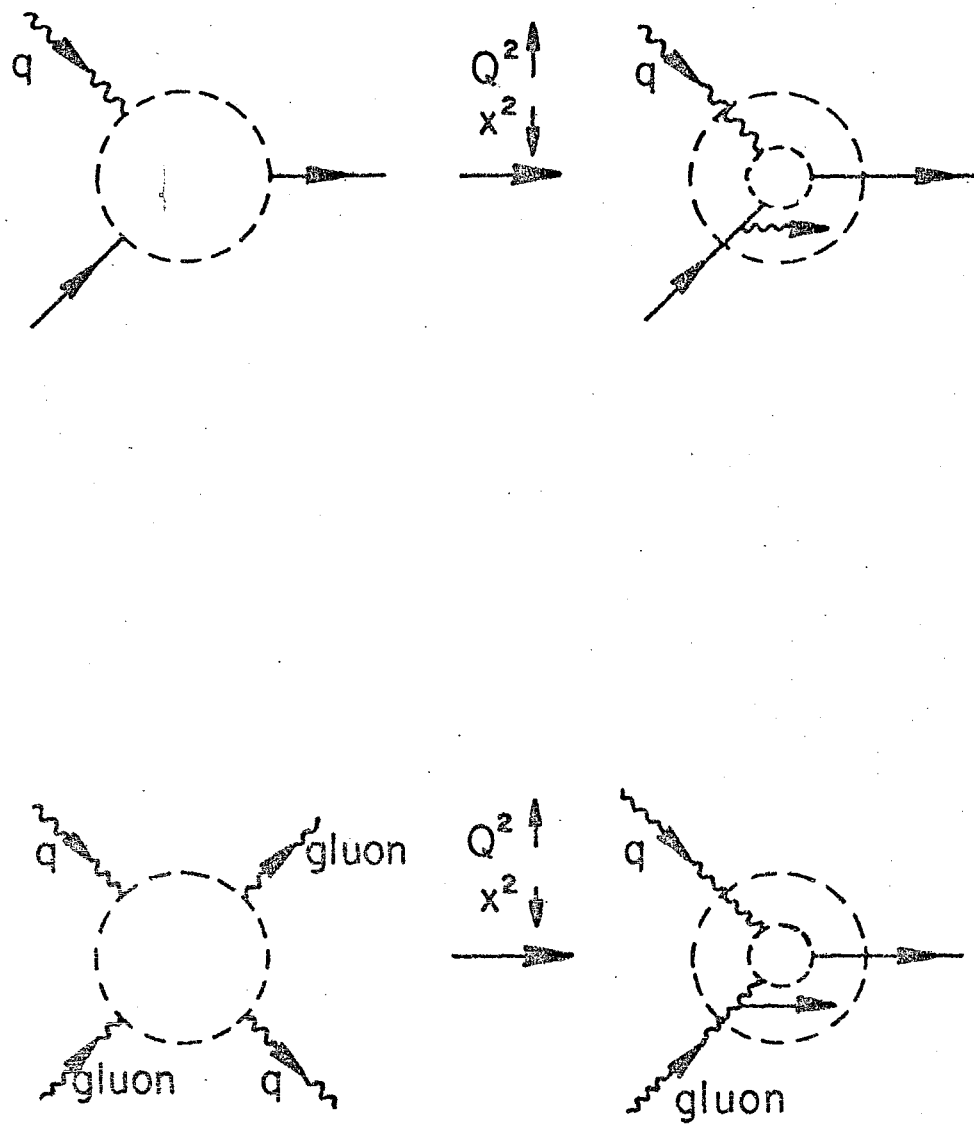


Figure 1.2.3

Dimuons from Charm

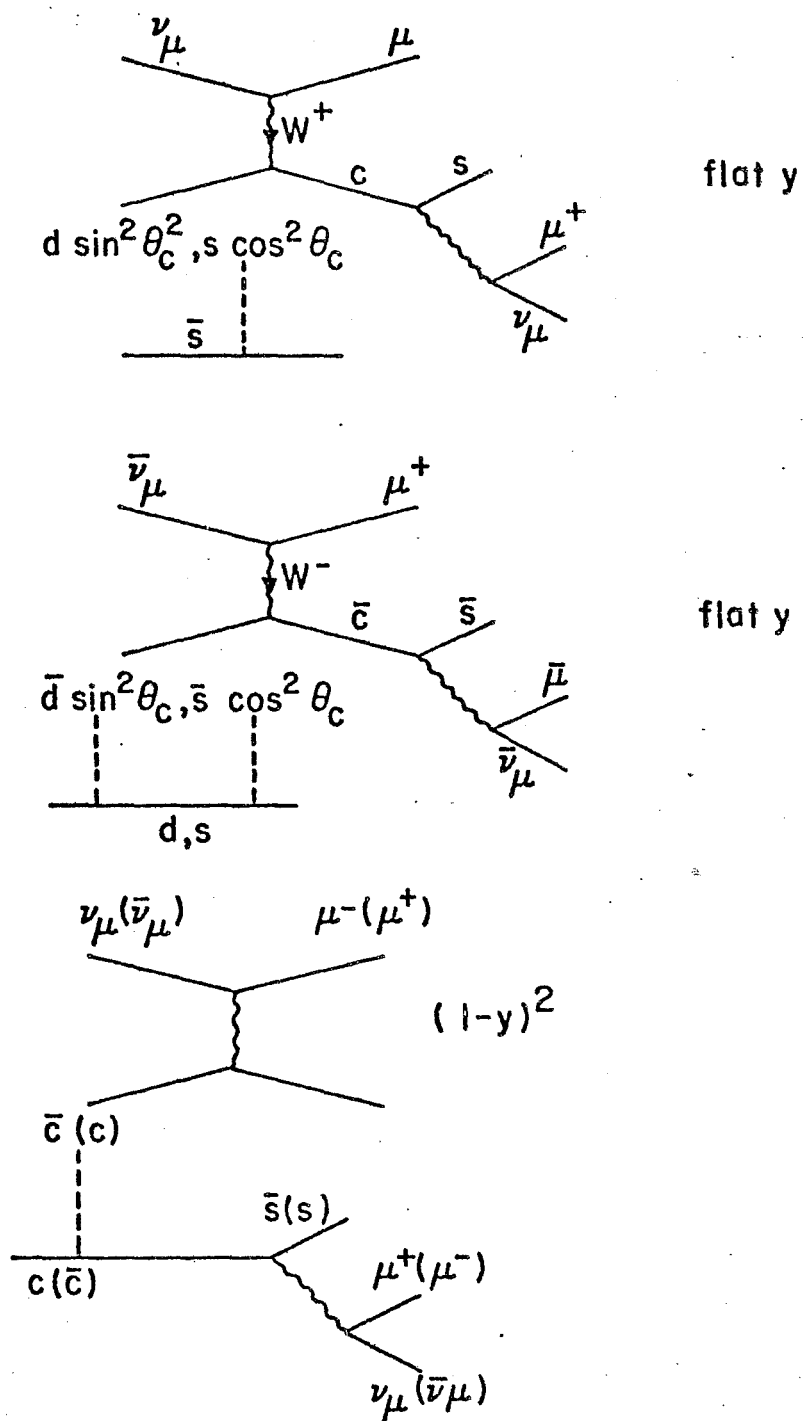
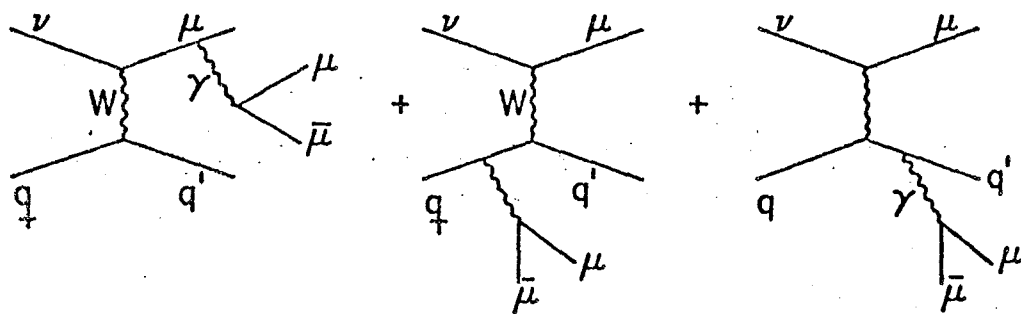


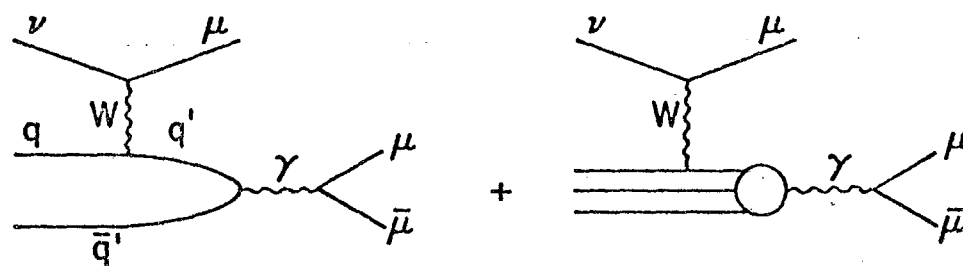
Figure 1.4.1

Electromagnetic Trimuons

Radiative



Hadronic



Drell Yan

Other Direct

Dimuons: $\mu^- (\mu^+)$ lost if $\nu (\bar{\nu})$

Figure 1.5.1 a

Neutral Current Electromagnetic Dimuons Radiative

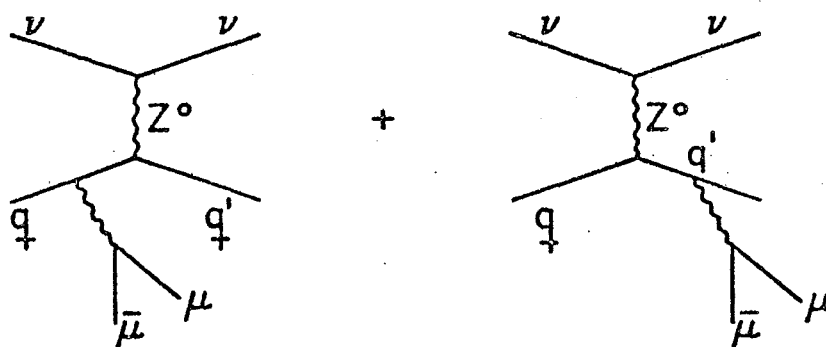


Figure 3.5.1 b

Hadronic

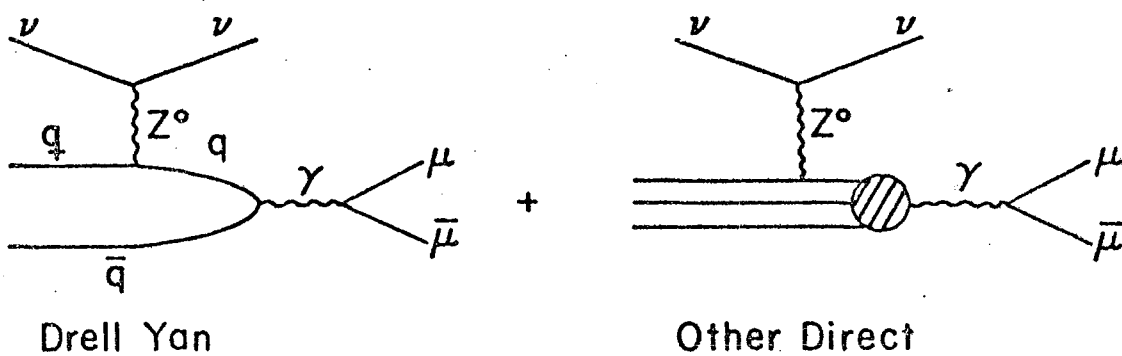


Figure 1.5.1 c

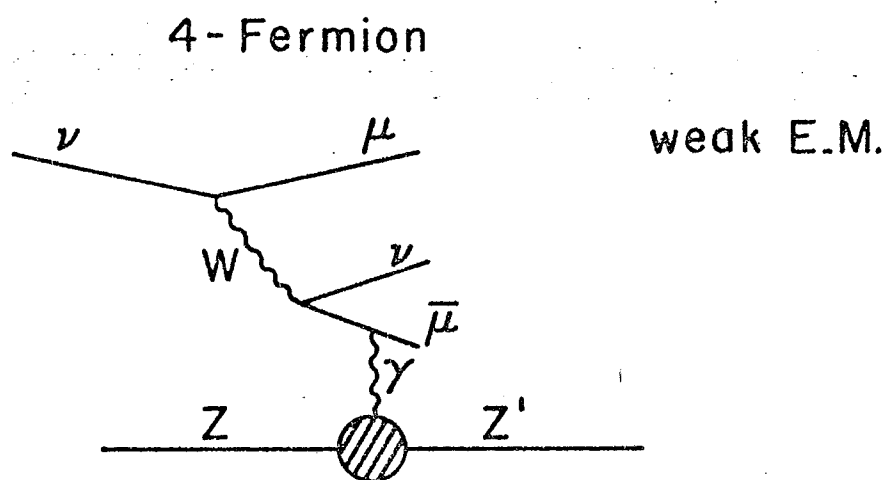
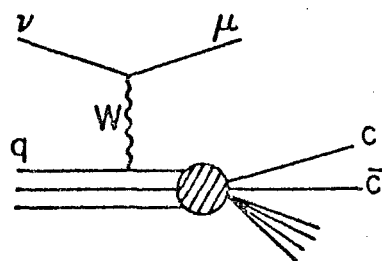


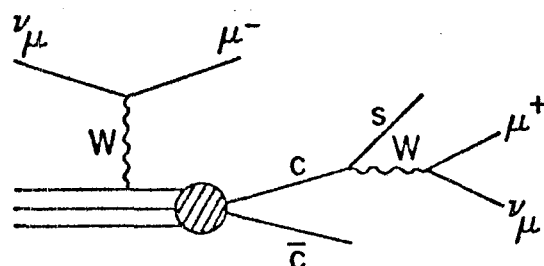
Figure 1.5.1 d

Charm-Anti Charm Multimuons



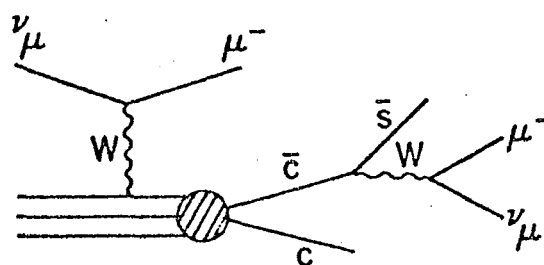
$c\bar{c}$ Production

Figure 1.5.2 a



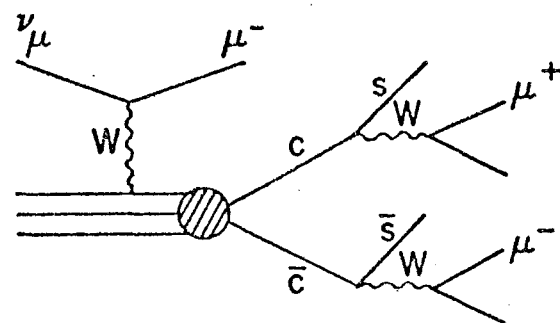
Opposite Sign
Dimuons

Figure 1.5.2 b



Same Sign
Dimuons

Figure 1.5.2 c



Trimuons

Figure 1.5.2 d

Gluon Bremsstrahlung

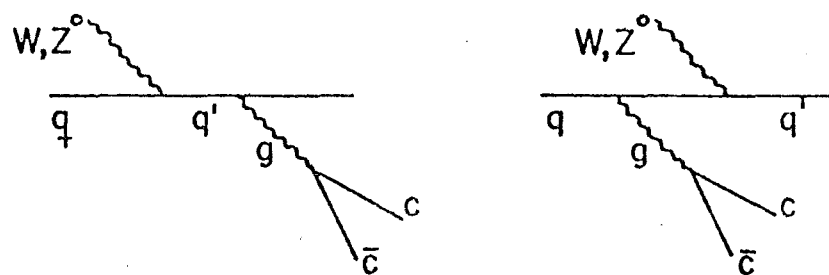
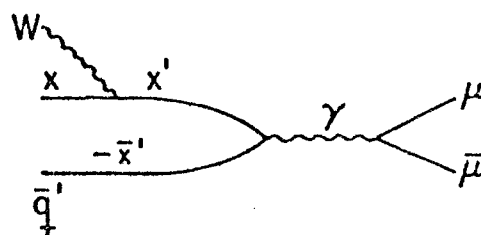


Figure 1.5.3

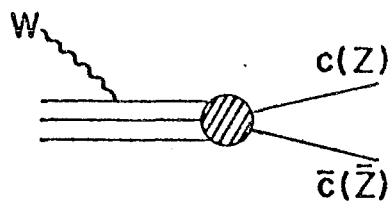
Intra Nucleon Processes



$$x_{\gamma} = x' + \bar{x}'$$

$$x < 1$$

$$\bar{x}' < (1-x)$$



$$Z < 1$$

$$\bar{Z} < (1-Z)$$

Figure 1.5.4

b-Quark Dimuons

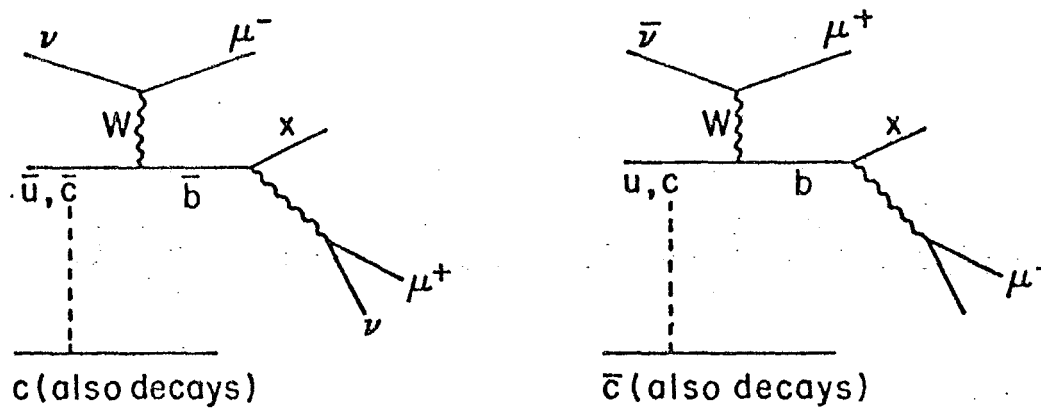


Figure 1.5.5 a

b-Quark Multileptons (Cascade)

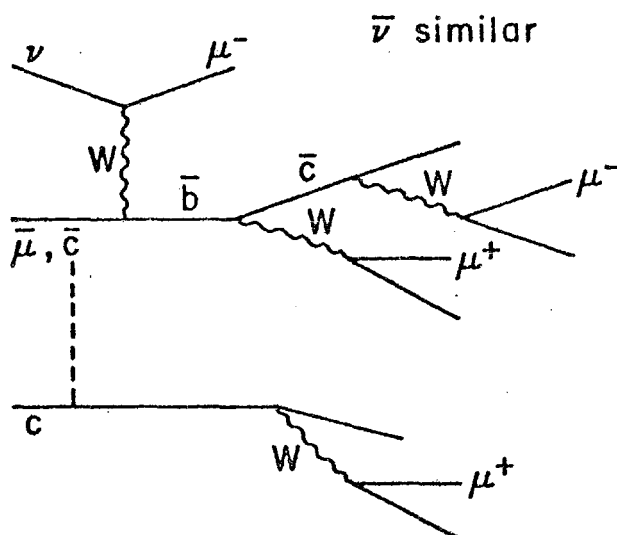


Figure 1.5.5 b

L^0 Production and Decay

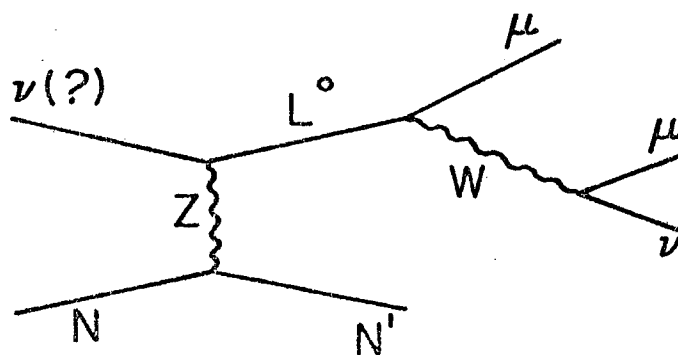


Figure 1.5.6

CHAPTER II

APPARATUS

1. Introduction

This chapter briefly describes the experimental apparatus and terminology pertaining to it for reference on later chapters. Details and expanded descriptions concerning the construction, calibration and use of all phases of the experimental equipment are found in the appendices.

2. Experiment Design

An event is defined by the kinematic variables discussed in chapter I for deep inelastic scattering. These variables imply that measurement of the total hadronic energy E_H , the muon momentum P_1 , and the muon polar angle θ are necessary and sufficient to measure deep inelastic differential cross sections. For multimMuon events all muon momenta $P_2 \dots P_N$ must be measured. Thus highly detailed information about each hadron in the events can be given up in order to obtain large target masses, ensuring a large sample of events and thus the ability to search for and to measure properties of rare multimMuon processes, even though the neutrino total cross section is small ($10^{-38} \text{ Ev cm}^2 \text{ GeV}^{-1}$).

The design philosophy then was to break the requirements of hadron energy and muon momentum measurement into separate parts, but to combine the apparatus into a target - detector. The apparatus thus consists of four basic parts:

1. neutrino beams
2. calorimeter targets
3. muon spectrometer
4. trigger, logic and acquisition systems.

A schematic of the target - detector is shown in figure 2.1. In total it was about 100' long x 24' high x 24' wide, excluding optics and electronics, and weighed about 1,500 tons.

3. Beams

The tertiary muon (anti) neutrino beams were generated from the leptonic decays of the secondary pions and kaons produced by the targetted 400 GeV proton beam extracted from the synchrotron at Fermilab. Two high flux ($\approx 10^9$ neutrinos/burst) broad band beams were employed, where the secondaries traversed one of two magnetic lines: a magnetically focused quadrupole triplet beam (QT) or a bare target magnetically sign selected beam (BTSS). The QT beam provided a beam of neutrino and antineutrino with the event rates in the ratio of 6:1 and average energies of 90 and 60 GeV respectively, with useful neutrino flux past 200 GeV (about 10% of the events). The BTSS beams provided purer beams of either neutrino or antineutrino with energy spectra similar to the QT but lower event rates per incident proton

targetted. Typically the accelerator delivered 10^{13} protons to the target over a 2 msec "spill" with a repetition rate every 10 seconds. Details concerning the beam spectra, the beam lines and other information are found in Appendix I. Figure 2.3 shows a schematic of the beams.

4. Calorimeter - Targets

As can be seen in figure 2.1, there are 3 targets: 1) an upstream solid iron block or iron target (Fe tgt), cleaved into 3 parts separated by scintillator counters, 2) a pure liquid calorimeter (Liq Cal), and 3) a liquid-iron calorimeter sandwich (Fe Cal). The fiducial (total) masses are 198(250), 36(60), and 42(150) metric tons respectively, with hadron absorption lengths of 31, 120, and 61 cm.

The calorimeters measure EH by totally absorbing the hadronic energy and sampling the resulting ionization in liquid scintillator. The total light from the scintillator, measured using photomultiplier, is therefore approximately proportional to EH. The energy resolution for the liquid and iron calorimeters is about 10% and 20% respectively. The iron target was a compromise to obtain large target mass at low cost to search for rare processes; the counters installed are used for monitoring events.

Details concerning the calorimeter construction, calibration, energy resolution and measurement can be found in Appendices II and IX.

5. Muon Spectrometer

The spectrometer consists of track following wide gap optical spark chambers (WGOSC), and solid iron toroidal bending magnets. The muon toroids are built in two sizes: 3 large muon angle 24' diameter toroids, followed by 4 high momentum 12' diameter toroids as shown in figure 2.1. For tracks traversing the entire spectrometer these provided about 30 kG-m and 70 kG-m of bending. The spark chambers are placed in planes behind each toroidal magnet to measure the positions and angles of the bending muon tracks traversing the magnets. The spark chambers are also interspersed throughout the calorimeter to measure the initial muon trajectories and to record event origins from the hadron showers. The sparks are recorded in 3 stereo views using film registration, with the cameras viewing the chambers through a folded mirror optical system. The resolution of the spectrometer is about 12% $\delta p/p$. A complete description of this apparatus, its construction, and its use can be found in Appendices III - VII.

6. Trigger Counters

Planes of liquid scintillator counters were placed in various positions in the apparatus, the information from which was used to tag events and to decide whether to "trigger" the data acquisition sequence (firing the spark chambers and recording the calorimeter and counter data on magnetic tape). These counters are shown

schematically in figure 2.2. Counter A was a veto counter, to ensure that only neutral particles entered the apparatus. Counters F1, F2, F3 monitored the iron target events. Counter T was formed by the logical AND of the last 2 counters in the iron calorimeter I9 · I10, monitoring calorimeter events. In the 24' magnet a multi-muon position hodoscope was installed. It consisted of 2 crossed planes of Horizontal and Vertical counters. Each counter plane provided 20 strips 1.2' wide, 24' long, and were divided into 2 banks each giving 4 counter banks: HU (Horizontal Up), HD (Horizontal Down), VU (Vertical Upstream) and VD (Vertical Downstream). HU, HD, VU were placed in the first gap of the magnet and VD was placed in the second gap as shown in figure 2.2. Counters B and C were placed behind toroids 1 and 2 of the 12' magnet for muon tagging. Construction details for these counters can be found in Appendices II and VIII.

7. Triggers and Logic

This section briefly describes the motivations and essentials for accepting (triggering) an event. The spark chamber dead time, the fiducial flash time and the camera advance time limit the apparatus to one event per accelerator spill. Therefore a trigger system was devised to enhance the multimuon events and at the same time to accept a relatively unbiased sample of neutrino events. Basically 4 elements were used in various combinations for trigger requirements: a beam-on signal, no counts in the veto \bar{A} , hadron energy,

and counts in the muon counters T, H, V, B, C. The beam gate was generated by the accelerator controls group (which also provided information on the targetted proton flux). By knowing the length of time of the "spill" (protons targetted), the spill could be split into two parts. The first part, Spill 1, was used for an enriched sample of multimMuon events, while the second part, Spill 2, was used for relatively unbiased charged current events of all kinds. This was accomplished by switching between the following (simplified) triggers:

$\bar{A} \cdot \bar{F} \cdot H_2V_2$	(Fe tgt Dimuon Trigger)	active full spill
$\bar{A} \cdot \bar{F} \cdot \text{Eliq} \cdot H_2V_2$	(Liq Cal " ")	" $\frac{1}{2}$ "
$\bar{A} \cdot \bar{F} \cdot \text{Efe} \cdot H_2V_2$	(Fe Cal " ")	" " "
$\bar{A} \cdot \bar{F} \cdot \text{Eliq} \cdot HV$	(Liq Cal single muon trigger)	" " "
$\bar{A} \cdot \bar{F} \cdot \text{Efe} \cdot HV$	(Fe Cal " " ")	" " "
$\bar{A} \cdot \bar{F} \cdot B \cdot C \cdot T$	(Quiet " " ")	" " "

where H_2V_2 requires at least 2 cells in the crossed H and V counters to be hit, F is the logical or of F1 - F3 counters and Eliq and Efe require energy deposition in the calorimeters above a threshold.

Spill splitting was done only for the neutrino running. During the antineutrino running, due to the lower event rate, all events were accepted (Spill 2 was the entire spill). An A·B·C through-going muon trigger was used 10% of the time as a monitor of the calorimeter and counter response. Details concerning the logic and triggers can

be found in Appendix VIII.

8. Data Logging

Details concerning the time sequence of events and the information recorded can be found in Appendix VIII. The time sequence is started by the accelerator and ends when the computer finishes reading data from the acquisition electronics. During this time the spark chambers fire and are recorded on film along with fiducial marks and frame numbers. Information written on tape includes hodoscope hits, trigger counter hits, time-of-flight (TOF) of counters and triggers with respect to the trigger, spill time and intensity, counter and trigger scalers, and the pulse height (ADC) information from the calorimeters.

In addition to data recording, the computer system provided diagnostic displays of single events and histograms of accumulated TOF's, hit patterns, and Landau distributions for the calorimeters.

9. Recapitulation

The salient features of the apparatus can be briefly summarized:

- A) large muon angular acceptance averaging about 600 milliradians
- B) muon momentum resolution of $15\% \Delta p/p$
- C) hadron energy resolution of $10\% - 20\% \Delta E/E$

- D) angle and position information in 1 spark chamber of ± 10 milliradians, ± 1 mm.
- E) repeated sampling of muon track position and dE/dx .
- F) redundancy from counters, calorimeters, and film for event selection and background rejection
- G) time resolutions of 100 nsec triggers, 200 nsec calorimeters, 2 μ sec spark chambers
- H) 3 target densities
- I) 275 tons fiducial mass
- J) wide band high intensity beams

LIST OF FIGURES

Chapter 2

- 2.1 Schematic of the target detector.
- 2.2 Schematic of the counter positions in the target detector.
- 2.3 Schematic of the N-0 beamline at the Fermi National Accelerator Laboratory near Batavia, Illinois, U.S.A.

WGSC -----

Veto Counter

24'

100'

SUPER
MODULE

IRON
TARGET

LIQUID
CALORIMETER

IRON
CALORIMETER

24'
MAGNET

12'
MAGNET

50

LOCATION OF TRIGGER COUNTERS

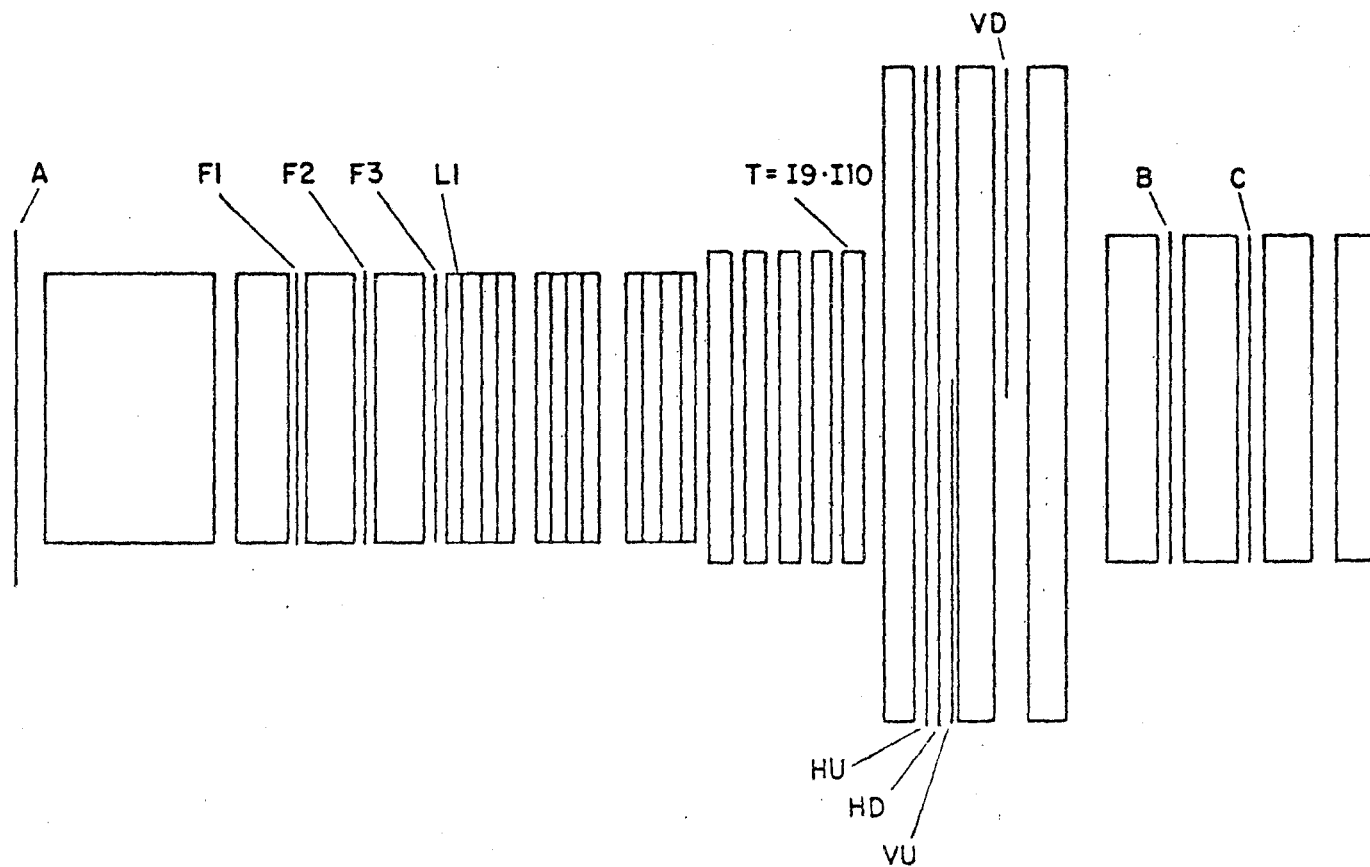


Figure 2.2 Schematic of the counter positions in the target detector

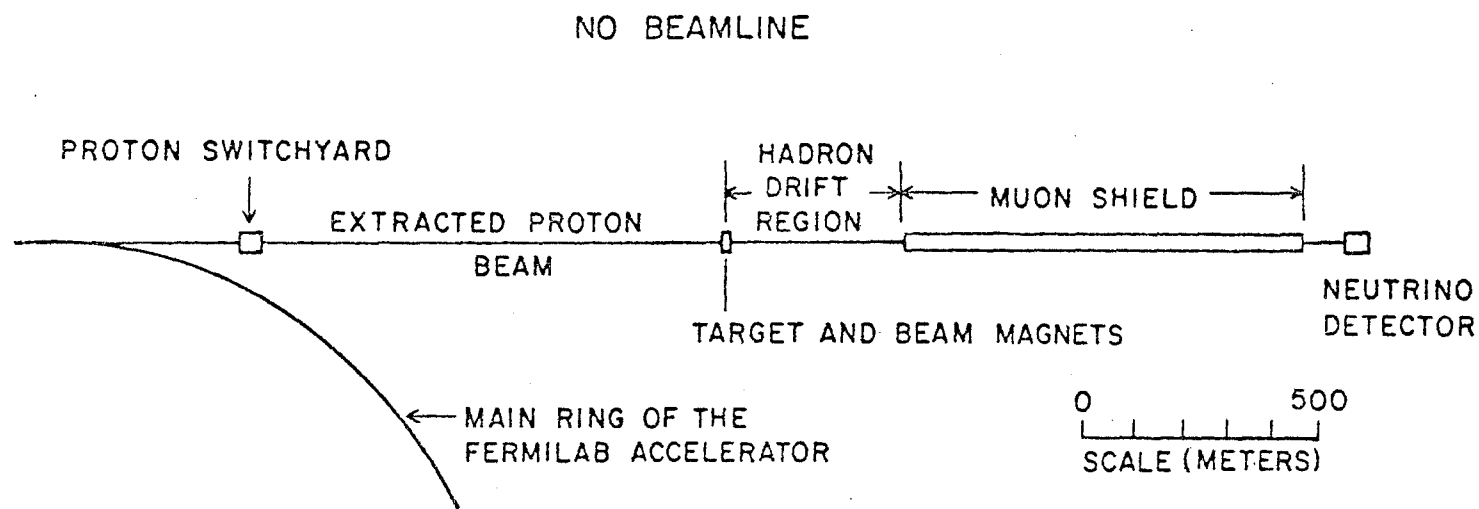


Figure 2.3 Schematic of the N-0 beamline at the Fermi National Accelerator Laboratory near Batavia, Illinois, U.S.A.

CHAPTER III

DIMUON ANALYSIS

3.1 Introduction

This chapter describes the analysis of the dimuon sample. Section 2 summarizes running conditions; section 3 discusses trigger rates and counter efficiency; section 4 describes the dimuon scan; section 5 describes event processing and cuts; section 6 describes corrections to the data sample and displays the corrected data; section 7 discusses backgrounds to dimuon events.

3.2 Summary of Data and Running

The data in this experiment was taken between August 1976 and July 1977. Table 3.2.1 is a summary of this data. During the Quad Triplet (Q.T.) and Bare target sign selected (BTSS) neutrino running the spill was split as described in Appendix 8 and Chapter 2. During the BTSS antineutrino running, spill 2 only ("unbiased" trigger) was used due to the smaller event rate in the targets. For all running, the average trigger rate was at most about 1 event/2 spills, implying a dead time of less than 30%. A run was normally defined as 1 roll of film, 1300 frames.

The magnet current in the toroids was set to focus the single muon events in 80% of the QT data, 50% of the BTSS antineutrino data and 0% of the BTSS neutrino data. Periodically, magnet-off runs were performed for alignment purposes.

Running conditions were checked as described in Chapter and Appendix 8, as well as by visual checks of the spark chambers. Changes made during data taking conditions were relatively minor as the apparatus was tuned during early running; run numbers for dimuons were from 111 through 148 QT, 214-274 BTSS antineutrino, 275-292 BTSS neutrino, with some runs removed for magnet-off, tests or minor errors. One troublesome aspect was spark chamber noise which reset or caused spurious signals in the acquisition electronics.

A change was made in the timing of the T counter after run 230, discussed in the next section. Since the trigger rates in spill 1 and spill 2 were not measured separately after run 230 as described in the following subsections, the overall rate of neutrino dimuon events relative to single muon events will use only QT data. Appendix XI summarizes the single muon events.

3.3 Triggers and Counter Efficiency

During the tune up runs, the stray magnetic fields in the 24' magnet were discovered to have a large effect on the horizontal and vertical (HV) counter tube operation, especially on V. Extra shielding measures were initiated (Appendix 8) and the voltage on the vertical counters was increased to raise the pulse height. After this the efficiency was checked using BCT cosmic ray triggers with the magnet on/off and the AND/OR circuits which combine tube signals from opposing hodoscope tubes either set to AND or OR (Appendix 8). The results

are shown in Table 3.3.1. To maximize the efficiency of triggers, the tubes were left on OR; however, this gave a singles (noise) rate in V of about 1 mHz. Thus a dimuon (Dimu) trigger ($H_2V_1 + H_1V_2$) (subscripts are hit multiplicity) was abandoned in favor of H_2V_2 to reduce spurious noise triggers. This also reduced the trigger acceptance for dimuon events for those triggers requiring Dimu since dimuon tracks opening close to the horizontal or vertical directions might hit only 1 horizontal or vertical counter cell. For good dimuon events in running not requiring the dimuon triggers (spill 2 calorimeter events), $76 \pm 14\%$ of the events had H_2V_2 latched, while $16 \pm 4\%$ had $(H_2V_1 + H_1V_2)$ - only latched. This variation is consistent with geometric efficiency studies of the acceptance using real events and taking into account counter efficiency. The efficiency for dimuon events in the apparatus is discussed later in this chapter. After run 230, the dimuon requirement added $H_2 - VU_1 - VD_1$, 2 horizontal hits and 1 in each of the 2 vertical counter banks to form H_2V_2 . The efficiency of H, V for the data set was determined from good BCT triggered events to be 96% each. The efficiency of B, C and T counters was determined by events which had good muon tracks in B, C, and T to be 95%, 87% and 96%, respectively, after run 230. Before that time, the bottom half of the T counter was out of time. By taking a large sample of single muon events distributed throughout the cross section of the apparatus, the efficiency of T was determined to be as shown in Figure 3.3.1.

The smooth curve is drawn to guide the eye; in monte carlo studies a simple interpolation is made between points to correct the data.

The energy trigger efficiencies were measured by using a sample of events with the HV counters set and determining whether or not the energy triggers appeared as a function of measured energy. These turn-on curves are shown in Figure 3.3.2; again a simple interpolation was made between points in the monte carlo of the triggers.

In the QT and BTSS neutrino running the spill split was adjusted so that roughly an equal number of triggers were taken in each spill. Experimentally, by turning off spill 1 or spill 2 it was determined that the number of triggers in spill 1 was $0.25/10^{13}$ pot (protons on target) and $0.97/10^{13}$ pot in spill 2. The subsequent splitting varied somewhat over the running of the experiment (see Appendix 11), yielding an average of 38% spill 1, 62% spill 2 triggers.

The overall trigger fractions for the split spill are shown by the QT data given in Table 3.3.2 for each trigger. These varied by about 10% from run to run, depending somewhat on conditions of entering muons from other beam lines. The total average trigger rate was $0.48/10^{13}$ pot, consistent with the spill 1-spill 2 splitting. Note that in spill 1, the raw triggers follow roughly ratios of the target masses, which is to be expected as all triggers require 2 muons in the hodoscope (except for acceptance and energy thresholds), whereas in spill 2 the liquid and iron calorimeter (Liq & FeC) events nearly follow the ratio of target masses and the Dimu trigger

from the iron target (FeT) should be related to the overall dimuon rate to single muon events. In this crude approximation the dimuon rate would be $\approx 2\%$, close to the eventual answer.

In the single spill 2 BTSS $\bar{\nu}$ running, the trigger fractions changed somewhat when the bottom of T was retimed after run 230. The trigger rates before and after T was fixed are summarized in Table 3.3.2 together with the trigger fractions for the BTSS ν . The overall trigger rate for the BTSS $\bar{\nu}$ was $0.17/10^{13}$ pot and for the BTSS ν , $0.4/10^{13}$ pot. About 10% of the BCT triggers were attributable to through going muons which missed vetos; these "events" do not have a large effect on the triggers requiring energy and are attributable to cosmic rays and remnant muons from other beam lines. Of measured good single muon events, 25% were BCT only, with the remaining being calorimeter events.

For good dimuon events after cuts the trigger percentages are shown in Table 3.3.3 for QT and BTSS neutrino spill 1 and spill 2, and BTSS antineutrino (spill 2). The differences in 2 between neutrino and antineutrino are consistent with the error in T before run 230, as QT is the bulk of neutrino running. Latched counter data is summarized in Table 3.3.4 for good dimuon events after all cuts and is basically consistent with the trigger information in Table 3.3.3. Note that T is efficient in the latched data, but is partly out of time in the formation of the BCT trigger in the early running.

3.4 Dimuon Scan

Raw dimuon candidates were selected by visually scanning the spark chamber film. All film was scanned twice, once by physicists, and a second time by professional scanners at University of Wisconsin or Fermilab.

The general criteria were for 2 or more muon-like tracks penetrating many interaction lengths past the hadron shower with no obvious scattering. The first scan had no specific rules; for the second scan, after the hadron shower, each muon track was required to pass through at least 5 calorimeter chambers (4-5 interaction lengths), or 1 calorimeter and 1 magnet chamber. The requirements were kept deliberately very loose in order not to reject rare events early in the analysis. For dimuon events, there was no requirement that the tracks come from a common vertex but comments were required for all doubtful events. Table 3.4.1 lists the scanning efficiencies for all raw candidates and for dimuon events after all cuts. The cuts will be described in the next section; however, the momentum of each track must be more than 4.5 GeV.

A search was made for scanning inefficiency as a function of kinematic quantities, and there is only a small effect. For events with one of the muons with a momentum between 4.5 and 10 GeV, the overall scanning efficiency is $97 \pm 2\%$ for neutrino data and $99 \pm 1\%$ for antineutrino data. Table 3.4.2 lists the average values of the minimum momentum and E_{vis} for all events and events in scan 2. Within errors there are no differences.

3.5 Event Processing

After scanning, the sparks on film were measured and reconstructed in space as outlined in Appendix 6. The efficiency for reconstructing measured sparks is above 99%.

All events were then examined by physicists in order to match sparks between the stereo views and to reject spurious events. An interactive program⁵¹ fitted simple polynomials to tracks and allowed several cuts and information to be imposed before final fitting for momentum. These were:

1. rejection of sparks not associated with a muon track
2. matching corresponding sparks in different views and different chambers and labeling them as a track
3. rejection of portions of a muon track after an inelastic scatter
4. rejection of "events" which could not verticize in any portion of the apparatus--for example, entering muons from other sources
5. assignment of momentum by range to tracks which range out (stop in apparatus) and which fail the momentum fitting program calculated by curvature.
6. rejection of events for which the sign of the muon charge is undertermined.

Examples of points 3, 4, 5 above are shown in Figure 3.5.1 in reduced versions of the interactive display. In general, rejection of candidates was due to events where the muon(s) range out before

entering the magnets, events which had uncontained hadron showers close to the edges of the targets or were far outside the fiducial region, events which had a scattering track (not a muon) in the calorimeters, and false dimuon events due to multiple reflections of a single track in the chamber windows, stray tracks from chamber breakdown, or entering muons accompanying a single muon event. At this point $55 \pm 6\%$ of the QT, $43 \pm 6\%$ of the BTSS neutrino and $27 \pm 3\%$ of the BTSS antineutrino raw candidates survived scrutiny and were matched.

Events were then fitted for momentum as outlined in Appendix VII. Those events failing to fit were re-paired-and-re-fit, and/or massaged. The later procedure was a visual inspection of the event. Sparks which contributed a large amount to the chi-squared per degree-of-freedom (DOF) of the attempted fit were either removed from the fit or were used in the fit including only position information, and not angles. In addition, the initial guess of momentum and charge could be changed. Those events which had a chi-squared DOF - chi-squared DOF track 1 = chi-squared / DOF track 2 larger than 12 were rejected (see Appendix VII, X) unless they would be accepted by range with their sign determined by the magnet chambers. This introduces a small error with respect to the single muon events which are cut at chi-squared DOF; presumably a dimuon event has twice the probability to be rejected on a chi-squared / DOF of 6 cut. On the other hand, since each dimuon is inspected and paired, it may have a larger probability to fit. In any case, this is a small effect as can be seen from the chi-squared

distributions shown in Figures 3.5.2a and 3.5.2b. Only 1% of the tracks have a chi-squared / DOF greater than 6, and only 5% of the events have a total chi-squared / DOF between 6 and 12.

After the above procedures the σ/p calculated by the fitting program was $16 \pm 16\%$ for all events and $12 \pm 12\%$ for events with p_{\min} larger than 20 GeV, consistent with the single muon sample.

The fitting efficiencies are shown in Table 3.5.1 as a function of the number of magnet chambers included in the track. Also shown are the percentages of events as a function of magnet chambers included on a track which would be measurable (recovered) by range as indicated by the trajectories computed by the pairing program; i.e., the pairing output indicated that the track would stop inside the magnet toroids, assuming that the chambers were fully efficient. A comparison is also shown for the single muon fitting efficiency; this data has a lower efficiency because each event is not measured, examined or spark matched by hand. About 3-4% of the inefficiency for 3 or more magnet bends is due to events in the hole. The effect of the range measurement is small. For a momentum cut of 4.5 GeV, only 34% of the events with a 1 chamber track which fit pass this cut and only 6% of all the events with a 1 chamber track are recovered by range above this cut of which over 60% were of the wrong muon sign. For all events above all cuts, $3 \pm 1\%$ of the neutrino events and $2 \pm 2\%$ of the antineutrino events were recovered by range. About 2% of the events were judged in need of remeasurement and were remeasured.

At this point, each dimuon event was then combined with the on-line data for that event. The hadron energy E_H was calculated from the ADC information as discussed in Appendix 9. The energy information counter settings and relative T.O.F. of trigger and counters were combined with the 2 muon momentum vectors p_1 and p_2 to form a data summary set, to be used in the following analysis.

A vertex was calculated by extrapolating the tracks to the transverse plane of the start of the event as indicated by the counters, weighting each extrapolated point by $1/(\delta p/p)$ calculated by the momentum fitting program and averaging the 2 projected points to form a vertex. Energy loss (dE/dx) was added to each muon momentum from the vertex to the start of the fit.

The events were then cut on 4 quantities:

1. P minimum >4.5 GeV. This cut was chosen somewhat arbitrarily to ensure good acceptance and positive muon identification while retaining a large fraction of the charm dimuon phase space. It also matches cuts used in other experiments, to facilitate comparison of data.
2. vertex fiducial region transverse to the beam direction of $\pm 1.5m$ (iron calorimeter, iron target) or $\pm 1.3m$ (liquid calorimeter) about beam center to ensure containment of the hadron shower.
3. opposite sign on the muon charges.
4. time of flight of counters relative to the trigger within accepted ranges, to remove possible single muon events with an accidental.

A summary of the total fitted events and cuts applied is shown in Table 3.5.2 for the combined neutrino sample and the antineutrino sample. Except where specifically noted, this sample will be used in the remaining analysis.

The vertex distribution transverse to the beam is shown in Figure 3.5.3 for neutrino and antineutrino events. The target module of the vertex indicating the origin of the event along the beam direction in the apparatus and the transverse vertex distance D between the extrapolated points in the target module are shown in Figures 3.5.4 respectively for both neutrino and antineutrino. Of the events with vertex distance D greater than 40 cm, 85% are iron target events, not unexpected with the longer extrapolation distance. Of the 6 calorimeter events with D greater than 40 cm, 4 were liquid calorimeter events and all had one track with $\delta p/p$ larger than 17%, averaging 31%. Events with a projected vertex distance D greater than 40 cm were checked in the pairing information for the fitted vertex using the spark positions.

3.6 Efficiency

3.6.1 Geometric efficiency. The events were corrected for geometric acceptance by randomly rotating the momentum vectors of the events about the neutrino direction (z axis), translating the events randomly throughout the apparatus, transporting them through the apparatus including energy loss and then deciding whether the events would be accepted as dimuon events. For two muons entering the magnet, table 3.6.1 lists the average purely geometric

efficiency for all events translated to the 3 targets and requiring 1 or 2 magnet chambers. Also listed are the efficiencies requiring the tracks to pass through the last calorimeter chamber C9 before the 24' magnet. This is done for a 4.5 and 10 GeV minimum cut on muon momentum. The efficiency for each event is equal to the number of times an event is translated-rotated divided into the number of times it then passes the criteria for acceptance. In Table 3.6.1 the events were translated-rotated 300 times in each target. The low efficiencies in the iron target are mainly due to range losses from calorimeter events just above the momentum cut translated into the iron target.

The efficiency of each event was determined by introducing the trigger efficiency, the spark chamber efficiency and the relative fitting efficiency by chamber per track into the geometric translation-rotation. This was necessary as the fitting efficiency depends on the number of chambers on a track and hence also on the kinematics of the events. The overall spark chamber efficiency was 95% for dimuon events, including obscured tracks. This was measured by counting chambers inside the endpoints of a track and the chambers which had a useful spark. For events in the iron target, when translating to the calorimeters to compute an efficiency, no energy requirements were included in the acceptance. Assuming that iron target events are similar to calorimeter events, this is a small effect for dimuon events as can be seen from the EH distributions shown later in this chapter.

After each event was translated and rotated, it was transported through the apparatus including energy losses and bending. Each chamber and counter were set according to their efficiencies. It was then decided whether the event would trigger the apparatus and would be measurable. Figures 3.6.1a, b, c show the efficiency in a particular target for all events translated into that target. Figures 3.6.2 and 3.6.3 show the efficiencies for events originating in each target translated in that target for neutrino and anti-neutrino. In the above Figures 3.6.1-3.6.3, where appropriate, the calorimeter spill 2-spill 1 events are approximately indicated by the wavy line shown on the graphs. (The events in spill 2 have high efficiency since they only require 1 muon in the hodoscope.) The average efficiencies are stated on the graphs.

An overall efficiency of an event can thus be defined by weighting the efficiency of the event in each target by the fraction of total fiducial mass in that target and summing the efficiencies of all targets. For variables not requiring EH, this is done including all targets. For variables requiring EH, only the 2 calorimeters are used for the total fiducial mass. Events are then weighted by the reciprocal of the appropriate overall efficiency.

This overall efficiency is rigorously correct only if all dimuon events are independent of target density, which is not true due to pion and kaon decay background (Appendix XII and section 3.7).

On the other hand, for prompt dimuons (object of the experiment), which are independent of the target density, this is a more correct procedure to obtain a true efficiency for these events, since the true rate of production of these events in a target is proportional to the target mass, while the acceptance is different for each target. If the statistics were "infinite", the acceptance would not matter, but this is an experiment with small statistics, especially for calorimeter events. This is most troublesome in the calculation of the true dimuon rate relative to single muon events as a function of energy, since this rate involves a subtraction of background from pion and kaon decay. However, the difference in using overall efficiency or individual target efficiency is small in the calorimeters. This is because the efficiency of events in a given calorimeter target is within at most 7% of the efficiency of those events translated into the other calorimeter as shown in Table 3.6.2. Thus, whatever the error in using overall efficiency for the rate calculation, it will be small compared to the uncertainties involved in the background calculation, the statistics, and the input data to the efficiency program. The overall efficiencies for all targets (no EH variables) and for calorimeter events is shown in Figure 3.6.4 and 3.6.5.

The effect of the weight can be seen in Figures 3.6.6-3.6.15 where the distribution in p_1 , p_2 , EH and E_{vis} are displayed, as well as a scatter plot of p_1 vs. p_2 . All are shown weighted 1 with the

unweighted data plotted on the same scale (except p_1 vs p_2 no weight). The effect of the weight on the shapes of these distributions is gentle and grow less important with larger values of each variable. The curves shown on the figures are for a charm monte carlo, discussed in Chapter 4.

No large effect was found between events in spill 1 and spill2. Table 3.6.3 lists the average values for p_1 , p_2 , E_{vis} and E_H for (anti) neutrino, and spills 1 and 2 weighted and unweighted.

The overall efficiency correction is model independent only if there are no dimuon events which never meet the acceptance criteria independent of their position in the apparatus; i.e., that there are no "blind" regions in the dimuon phase space. For the models which are being considered, particularly the charm model, a large fraction of the total rate (50-60%) are above the cuts imposed on the data by the apparatus ($4-5 \text{ GeV } p_{min}$, $\theta < 400 \text{ mrad}$). Events above these cuts have good acceptance, and there are no blind regions for these models. On the other hand, it is possible that there are mechanisms which produce a majority of events outside the cuts, and this experiment is "blind" for these processes.

3.7 Dimuon Backgrounds

The two most important backgrounds for dimuon events are pion and kaon decay, and accidentals from 2 superimposed events or from entering muons. Appendix XII discusses the calculation of both of

these backgrounds.

Pions and kaons produced in the hadron shower can decay before they are absorbed, yielding dimuon events. The rate per single muon event varies approximately inversely with the absorption length of material traversed by the shower. This rate corresponds to $24 \pm 6\%$ and $16 \pm 9\%$ of the neutrino and antineutrino dimuon events in the calorimeters respectively, and falls to about 8% and 5.5% respectively in the iron target. The overall rate per single muon event is 5×10^{-4} and 3×10^{-4} per single muon event for the QT neutrino and BTSS antineutrino in pure iron for a 4.5 GeV p_{\min} cut. There are 25% uncertainties in the calculation, as discussed in Appendix XII. In the calculation of the dimuon rate, this background will be subtracted.

For comparisons with the shapes of distributions with charm, this background will have a small effect due to: a) the overall statistical power of the experiment and the uncertainties inherent in the charm model, and b) this background in many respect resembles charm as it is hadronically produced and occurs from a meson decay. Figures 3.7.1-3.7.3 show the distributions in E_{vis} , E_H and p_1 and p_2 for pion, kaon decay superimposed with a charm monte carlo, normalized to give the proper relative number of events from charm, and pion and kaon decay. Distributions that require E_H have a larger pion and kaon contribution due to the longer absorption length in the calorimeters. The effect in antineutrino is similar.

Basically, the shapes of these distributions are only marginally affected. The effects on other distributions will be discussed where appropriate in the next chapter.

Accidental dimuons are superimposed single muon events: two single muon events which occur at similar positions within the time resolution of the apparatus, or a single muon event with an entering muon which appears to form a vertex and enters within the time resolution of the apparatus. As discussed in Appendix XII, this rate is estimated to be less than 1% of the observed dimuon sample.

LIST OF TABLES

Chapter 3

- 3.2.1 Summary of data
- 3.3.1 HV counter efficiencies
- 3.3.2 Inclusive trigger rates
- 3.3.3 Triggers from T.O.F. tags for cut +- events
- 3.3.4 Latched counter data for cut +-events
- 3.4.1 Scanning efficiency for Dimuon candidates and events
- 3.4.2 Average values of E_{vis} and p_{min} , and efficiencies for
4.5 p_{min} 10 GeV, for neutrino and antineutrino
- 3.5.1 Fitting efficiency
- 3.5.2 Fitted events: % of cuts
- 3.6.1 Average geometric efficiency for all events translated
to each target with requirements as shown in table
- 3.6.2 Average efficiencies for calorimeter events translated
into various targets
- 3.6.3 Averages of measured quantities weighted and unweighted
by spill

LIST OF FIGURES

Chapter 3

- 3.3.1 Efficiency of the T counter before run 230 as a function of verticle position.
- 3.3.2 Calorimeter energy trigger efficiencies
- 3.5.1 Interactive track matching outputs for 3 candidates: no vertex, 1 and 2 chamber tracks recoverable, and an inelastic scatter. The solid lines show polynomial fits to the sparks, which are shown as thickened regions on the horizontal lines indicating the spark chambers.
- 3.5.2a,b Chi-squared per DOF for each track(s) and the sum of the chi-squared per DOF(fig a).
- 3.5.3 Vertex distributions transverse to the beam direction in the target module.
- 3.5.4 Target module of origin and the transverse distance between the 2 tracks in the target module; for both neutrino and anti-neutrino.
- 3.6.1a-c Efficiencies of all dimuon events translated into each target.
- 3.6.2 Efficiencies of events originating in each target translated in that target (neutrino) .
- 3.6.3 Same as 3.6.2 (anti-neutrino).

- 3.6.4 Overall efficiency for neutrino.
- 3.6.5 Overall efficiency for antineutrino.
- 3.6.6(7) Unweighted and weighted P_1 for (anti)neutrino.
- 3.6.8(9) " " " P_2 " " .
- 3.6.10(11) " " " EH " " .
- 3.6.12(13) " " " Evis " " .
- 3.6.14(15) Unweighted P_1 vs P_2 for (anti)neutrino.
- 3.7.1-3.7.4 Evis, EH, P_1 , and P_2 for pion and kaon decay
superimposed with a charm monte carlo.

Table 3.2.1. Summary of Data

Run Type	Number of Protons ($\times 10^{18}$)	Events in Calorimeters
Quad Triplet	0.8	21,000
BTSS Antineutrino	2.4	7,000
BTSS Neutrino	0.5	8,000

Table 3.3.1. HV Counter Efficiencies

Counter	Magnet ON/OFF	AND/OR	Efficiency
H*V	OFF	AND	$0.72 \pm .01$
H*V	OFF	OR	$0.91 \pm .02$
H*V	ON	AND	$0.63 \pm .03$
H*V	ON	OR	$0.90 \pm .02$
H	OFF	AND	$0.86 \pm .02$
V	OFF	AND	$0.82 \pm .02$
H	ON	OR	$0.97 \pm .02$
V	ON	OR	$0.94 \pm .02$

Table 3.3.2. Inclusive Trigger Rates (% of all triggered events)

Trigger	QT		BTSS Antineutrino		BTSS Neutrino	
	Spill 1	Spill 2	R 230	R 230	Spill 1	Spill 2
E liq Cal	25%	30%	14%	25%	27%	26%
E Fe Cal	40%	39%	20%	33%	43%	31%
BCT	n.a.	50%	58%	62%	n.a.	55%
DIMU	45%	8%	13%	5%	36%	5%

Table 3.3.3. Triggers from T.O.F. tags for cut +- dimuon events

		Triggers							
Neutrino QT+BTSS									
Spill 1 (62%) 111 events	Dimu	EFeC	ELiqC	FeC*LiQC	LiQC*Dimu	Dimu only	FeC only	LiQ only	
	43%	35%	33%	8%	2%	40%	23%	25%	
Spill 2 (38%) 69 events	Dimu	EFe	ELiq	BCT	Dimu only	FeC only	LiQ only	BCT only	Fe*LiQ
	32%	52%	23%	35%	30%	23%	7%	6%	12%
Antineutrino BTSS									
Spill 2 (100%) 51 events	Dimu	EFe	ELiq	BCT	Dimu only	FeC only	LiQ only	BCT only	Fe*LiQ
	29%	41%	27%	76%	4%	4%	6%	20%	10%

Table 3.3.4. Latched Counter Data for Cut +- Events

% of events with counter set	B	C	T	H ₂	V ₂
anti neutrino	95%	82%	100%	92%	92%
neutrino	95%	93%	97%	86%	93%

Table 3.4.1. Scanning Efficiency Dimuon Candidates and Events

Total Raw Candidates		ϵ_1	ϵ_2	ϵ	Fitted After Cuts	Events Scan 2 only	ϵ_1	ϵ_2	ϵ
482	QT	$76 \pm 2\%$	$73 \pm 2\%$	$94 \pm 1\%$	122	13	90%	79%	98%
442	BTSS $\bar{\nu}$	$81 \pm 3\%$	$66 \pm 3\%$	$9 \pm 1\%$	51	6	89%	80%	98%
294	BTSS ν	$90 \pm 1\%$	$76 \pm 3\%$	$99 \pm 1\%$	58	6	90%	77%	98%

Table 3.4.2

<u>$4.5 < p_{\text{min}} < 10\text{GeV}$</u>			<u>Average Values</u>			
ϵ_1	ϵ_2	ϵ			ν	$\bar{\nu}$
ν $88 \pm 6\%$	$76 \pm 7\%$	$97 \pm 2\%$	Evis	all	123 ± 61	98 ± 39
			(GeV)	Scan 2	134 ± 92	104 ± 39
$\bar{\nu}$ $89 \pm 7\%$	$89 \pm 7\%$	$99 \pm 1\%$	p_{min}	all	19 ± 20	20 ± 20
			(GeV)	Scan 2	19 ± 17	23 ± 20

Table 3.5.1. Fitting Efficiency

Events with bending:	Dimuon Fitting Efficiency	Recoverable by range in pairing prog.	Single muon fitting efficiency
1 toroid	$61 \pm 10\%$	92%	50%
2 toroids	$86 \pm 5\%$	60%	72%
3 or more toroids	$95 \pm 2\%$	n.a.	93%

Table 3.5.2. Fitted Events

CUTS:
 S=same sign dimuon cut
 P= $p_{\min} = 4.5$ GeV
 F=fiducial volume cut
 T=time of flight cut

	total fitted	S	P	S*P	F	F*S	F*P	T	T*S	T*P	T*F
Neutrino	357	19%	12%	7%	1%	0%	1%	5%	2%	1%	1%
Anti - Neutrino	103	15%	16%	6%	1%	0%	1%	5%	2%	4%	1%

Neutrino after above cuts: 180 total , 111 in calorimeters

Antineutrino after above cuts: 51 total , 35 in calorimeters

Table 3.6.1. Average Geometric Efficiency (%)
all events translated to each target

Requirements: M1=track traverses 1st toroid 24'
M2=track traverses 2nd toroid 24'
C9=track traverses last FeCal chamber

Targets	4.5 GeV P min				10 GeV P min			
	M1	M2	M1*C9	M2*C9	M1	M2	M1*C9	M2*C9
FeTgt	87 ± 20	80 ± 28	60 ± 28	55 ± 32	99 ± 4	99 ± 5	76 ± 20	76 ± 20
Liq Cal	99 ± 10	99 ± 4	94 ± 10	93 ± 11	99 ± 1	99 ± 2	97 ± 7	96 ± 8
Fe Cal	100	99 ± 2	99 ± 3	99 ± 2	100	100	99 ± 2	99 ± 2

Table 3.6.2. Average Efficiencies

		Calorimeter events translated in:		
		FeCal	Liq Cal	
FeCal Events	88%		82%	Neutrino
LiqC Events	79%		74%	
FeCal Events	97%		96%	Antineutrino
LiqC Events	98%		94%	

Table 3.6.3. Averages of Measured Quantities
Weighted and Unweighted by Spill

S1=Spill 1
S2=Spill 2

	Neutrino				Antineutrino	
	S1 no wt	S2 no wt	S1 wt	S2 wt	S2 no wt	S2 wt
P1 (GeV)	49.9 ± 37	57.9 ± 53	48.9 ± 38	55.0 ± 52	39.3 ± 26	37.1 ± 26
P2 (GeV)	22.8 ± 22	19.1 ± 19	20.1 ± 21	17.2 ± 17	20.2 ± 19	20.3 ± 20
EH (GeV)	55.4 ± 39	51.7 ± 46	55.3 ± 40	51.8 ± 46	38.1 ± 31	38.1 ± 32
Evis(GeV)	125.0 ± 55	123.5 ± 71	123.1 ± 55	120.3 ± 71	96.4 ± 39	96.2 ± 39

T counter efficiency bottom -
top before Run 230

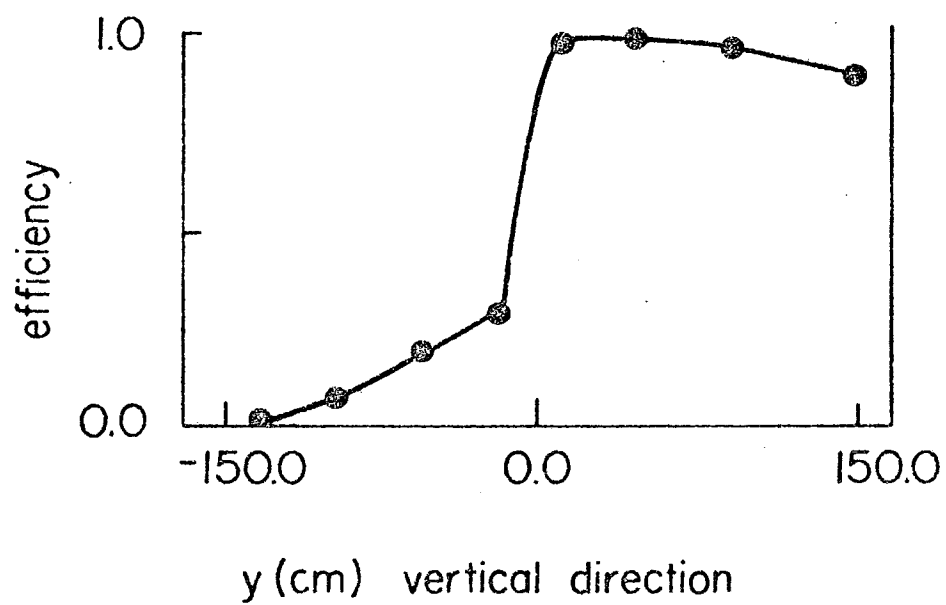


Figure 3.3.1

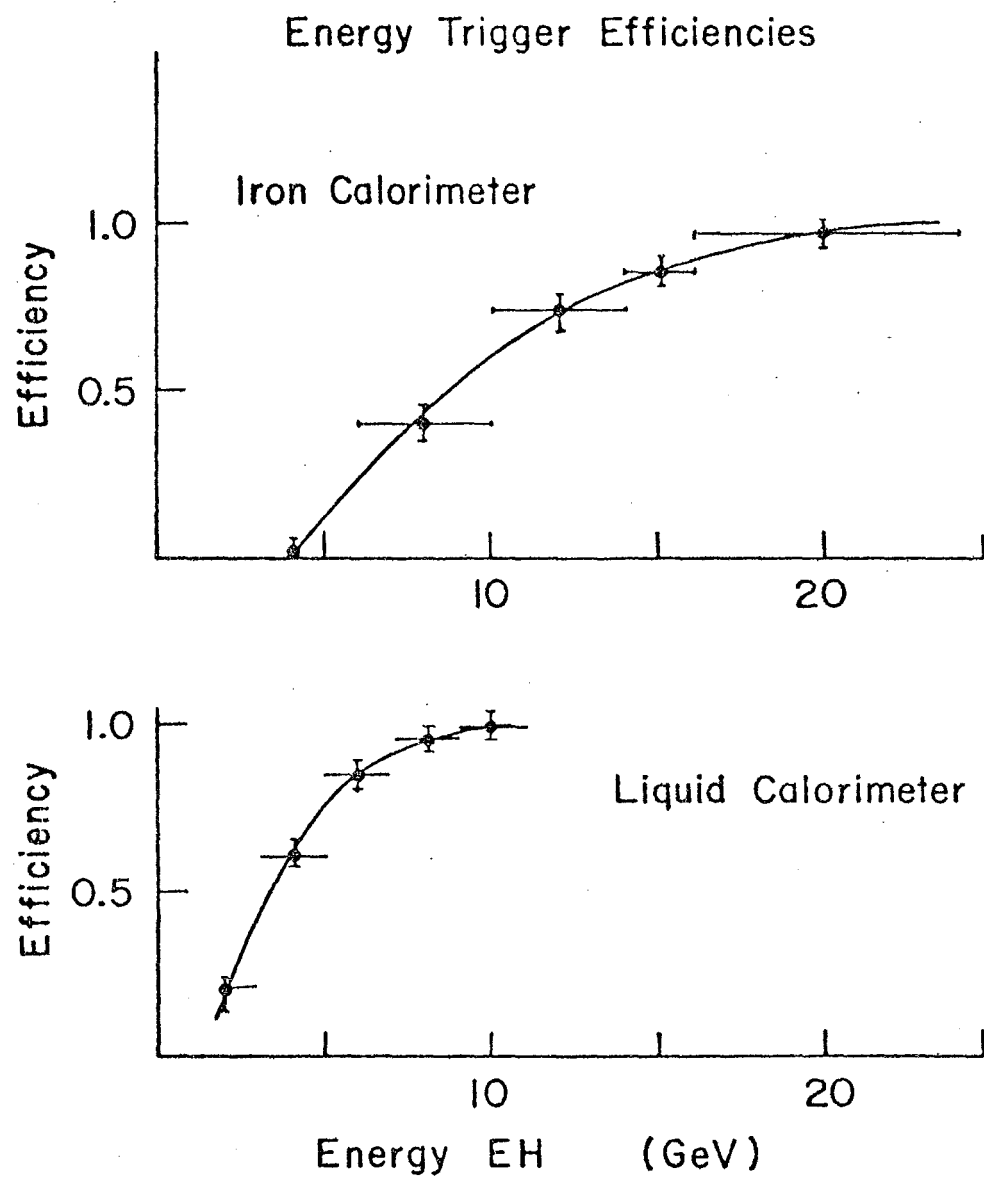
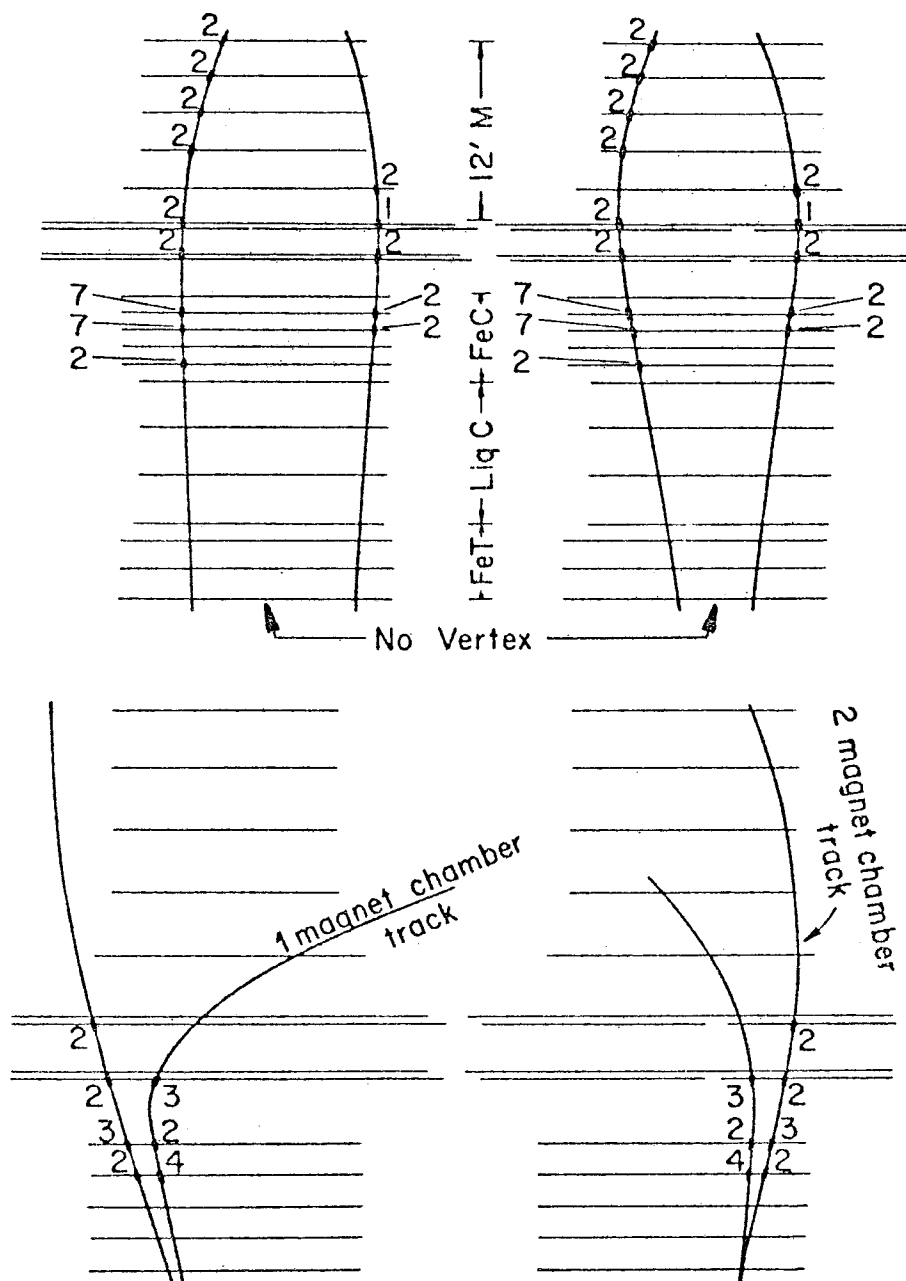


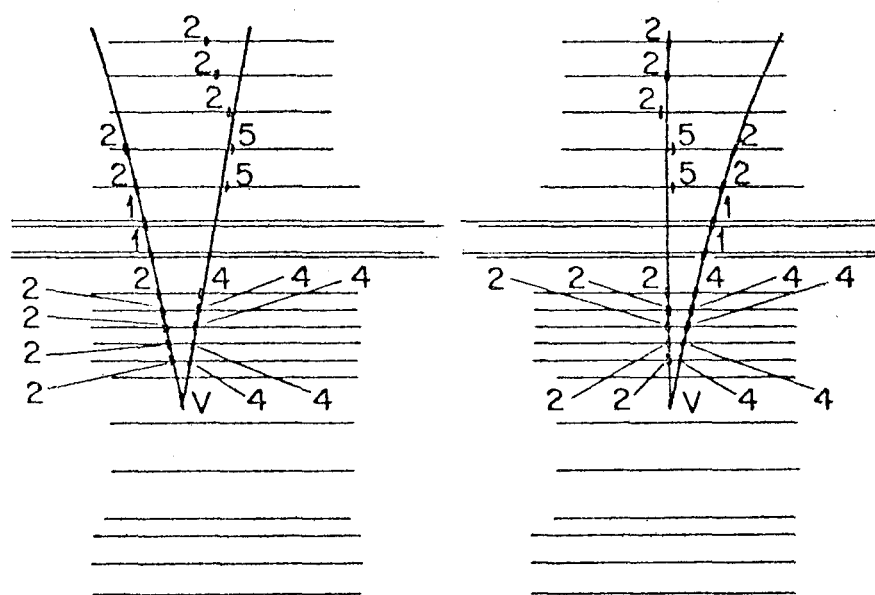
Figure 3.3.2

Pairing Program Displays



1 chamber track recoverable by Range, 2 chamber not

Figure 3.5.1



Inelastic scatter
12' spectrometer

Figure 3.5.1 (continued)

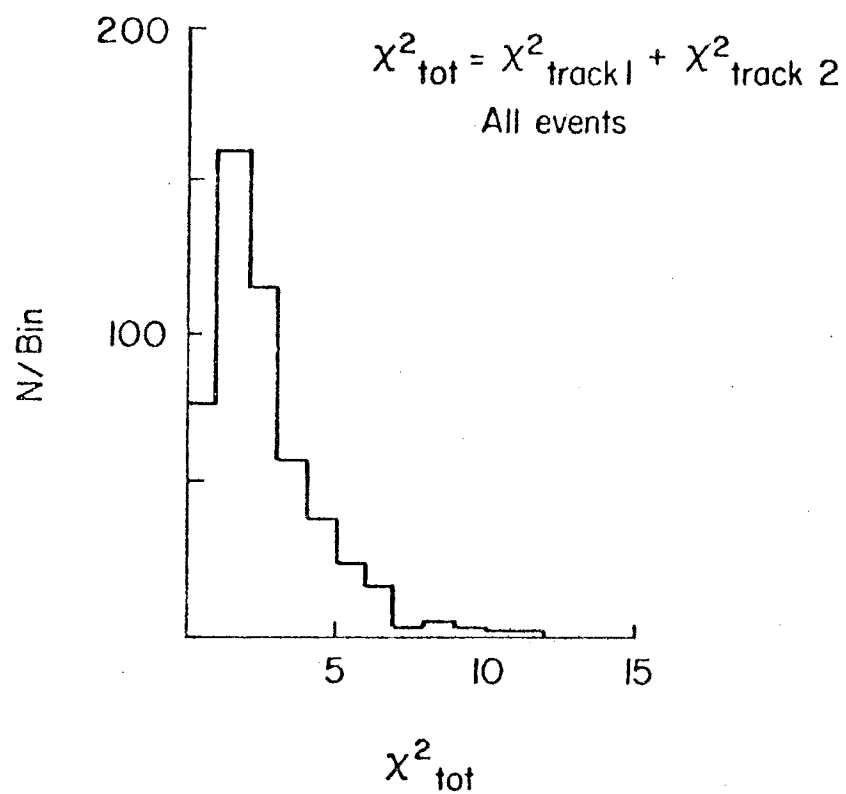


Figure 3.5.2 a

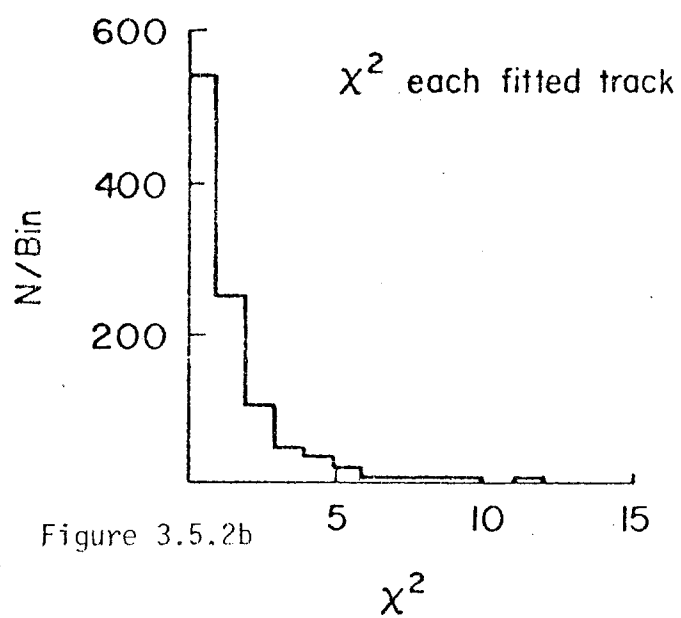


Figure 3.5.2b

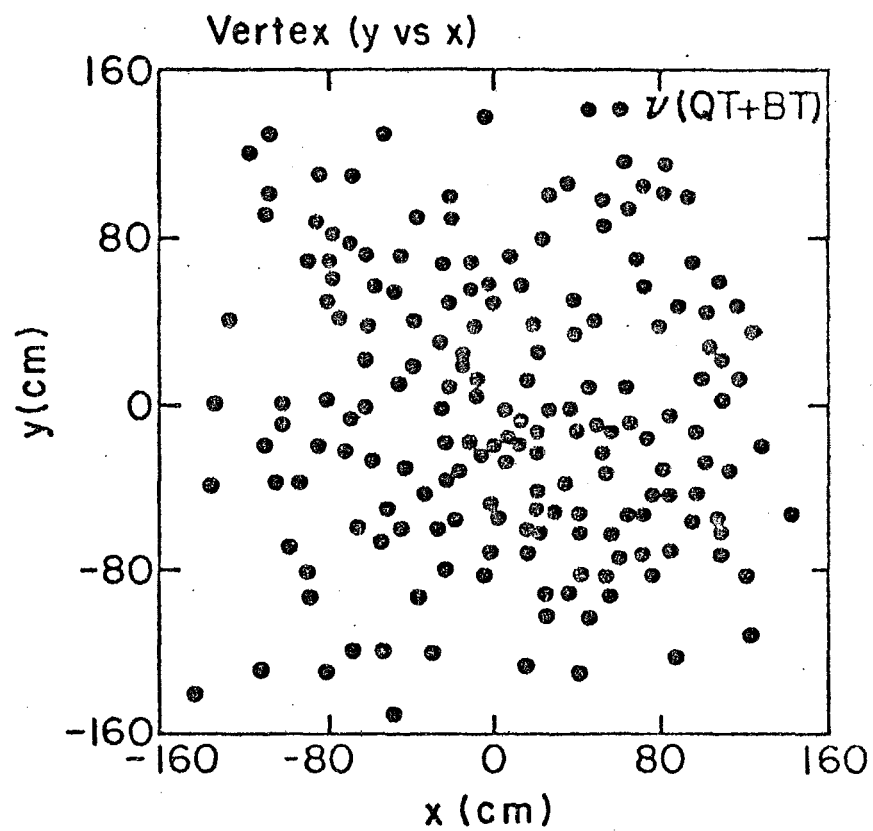
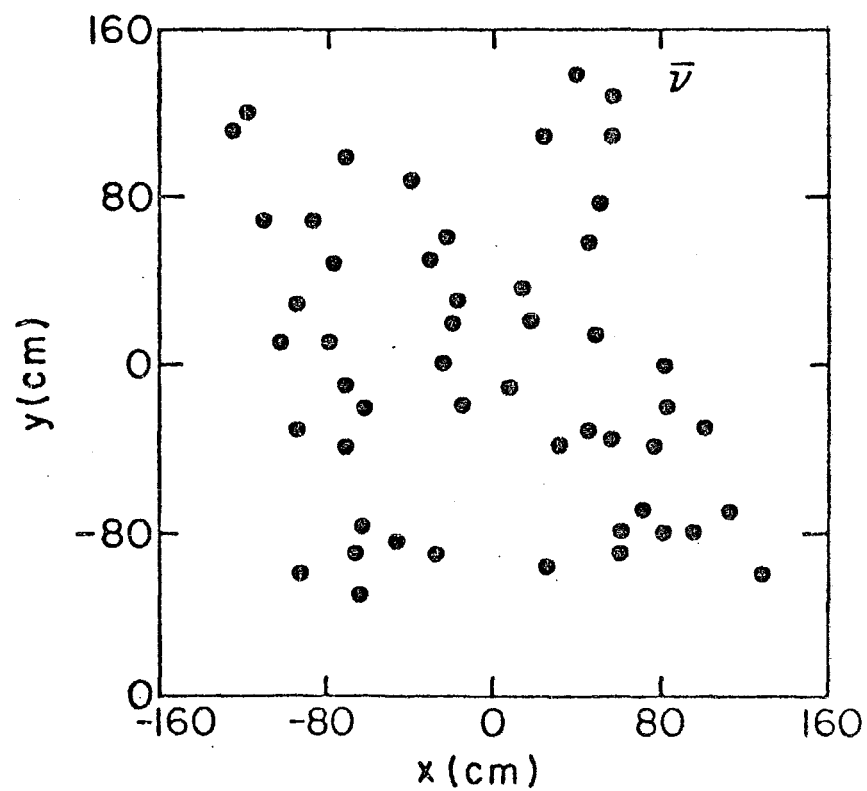


Figure 3.5.3



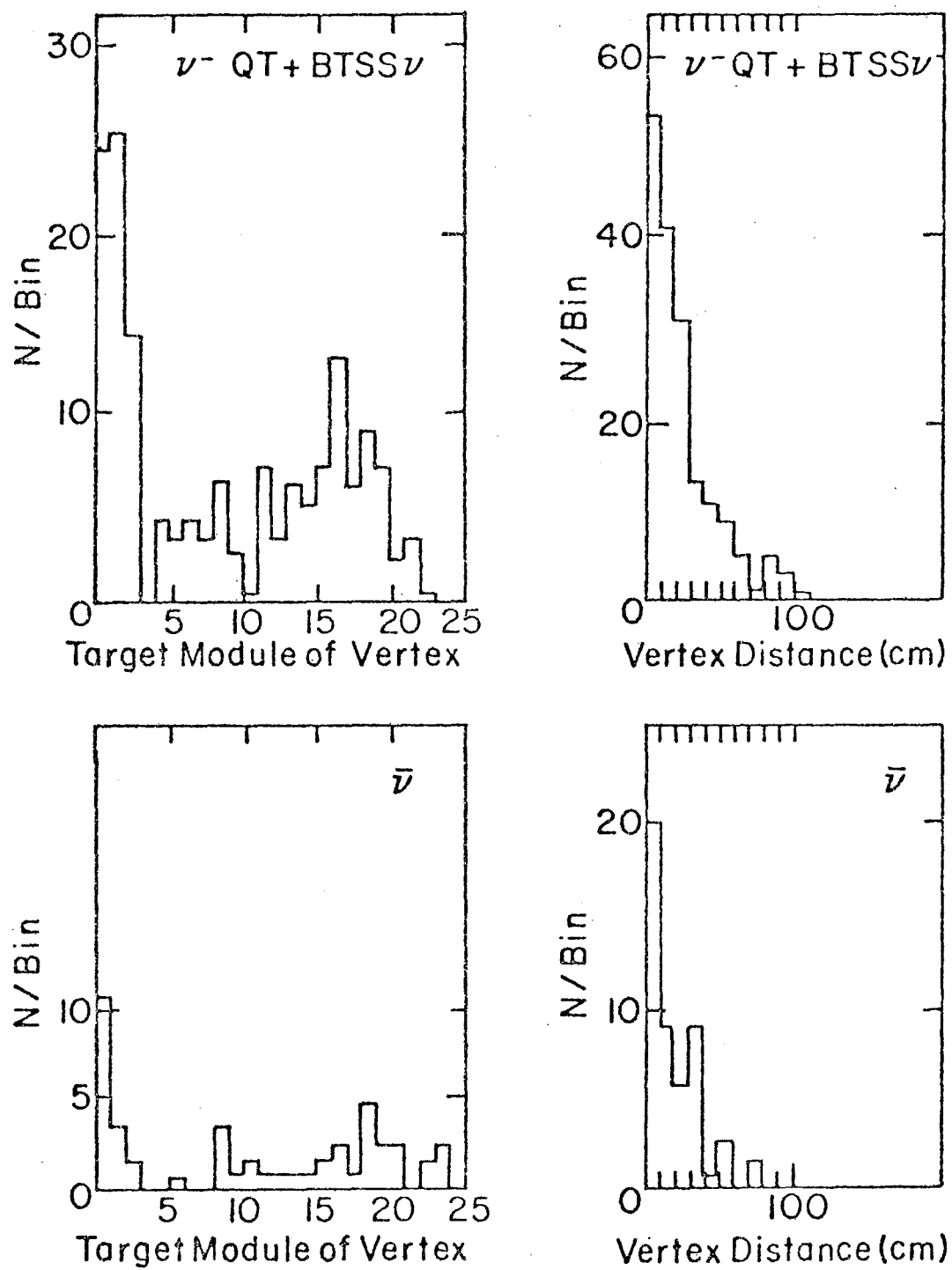


Figure 3.5.4

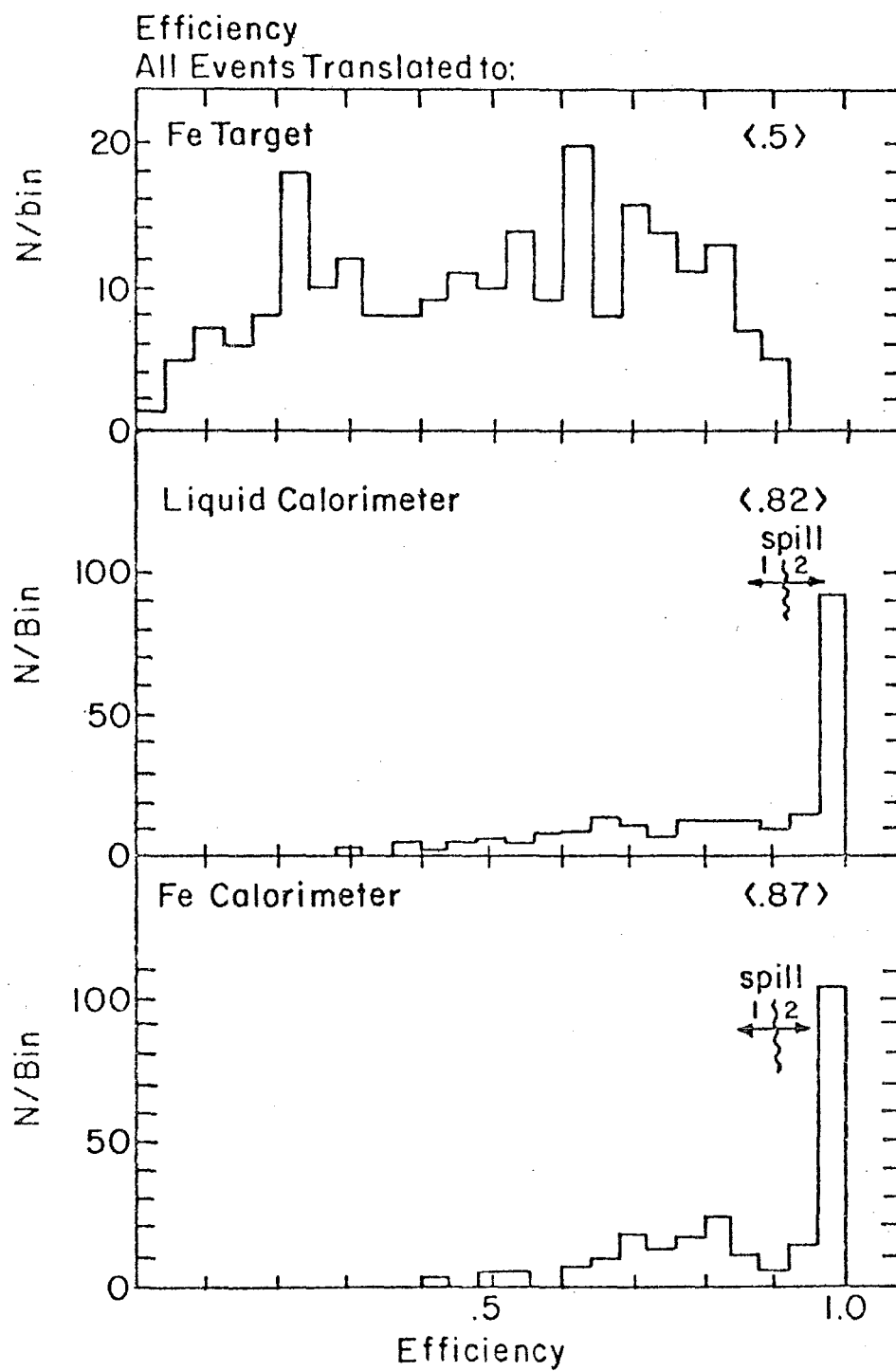


Figure 3.6.1 a-c

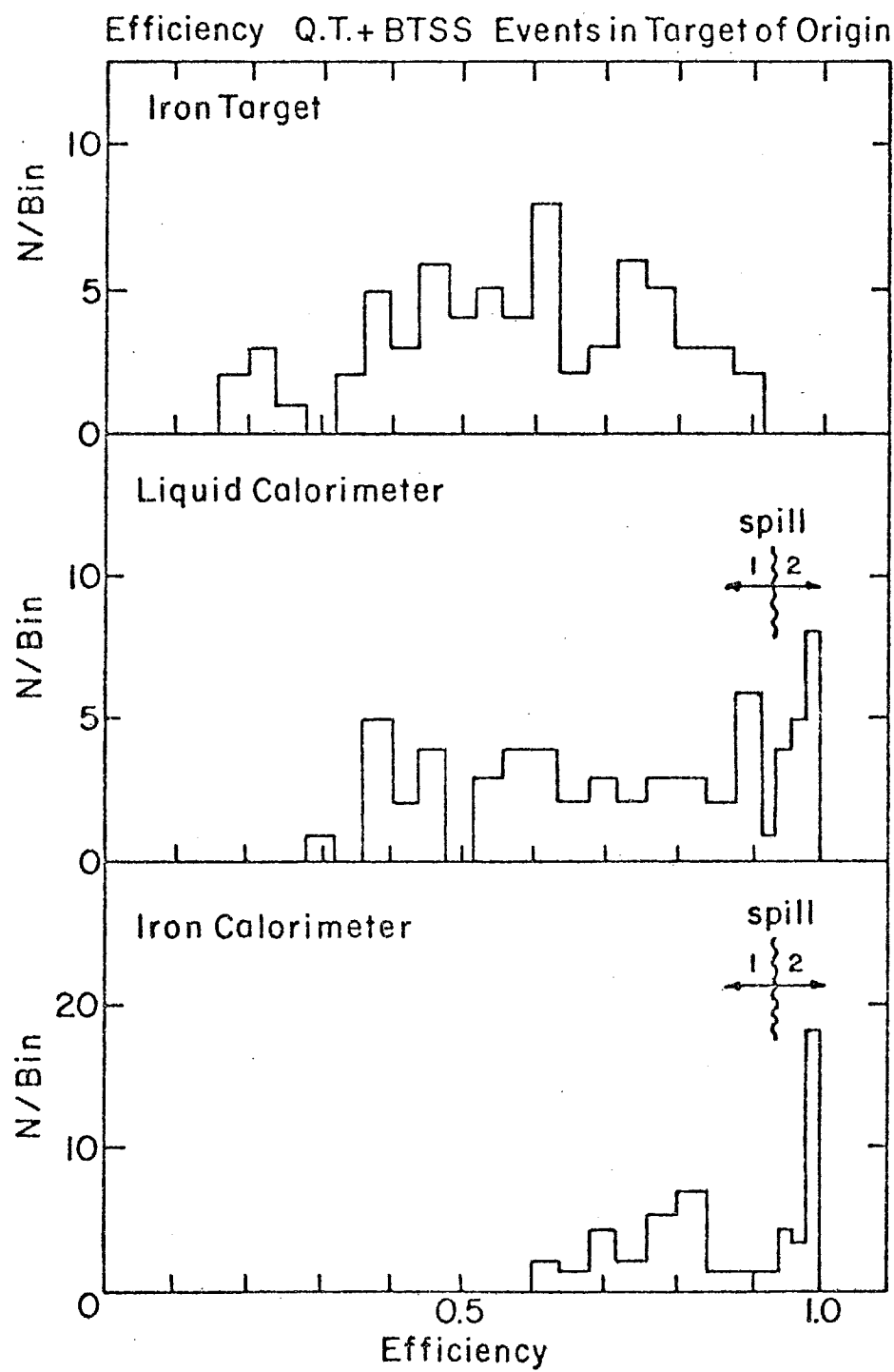
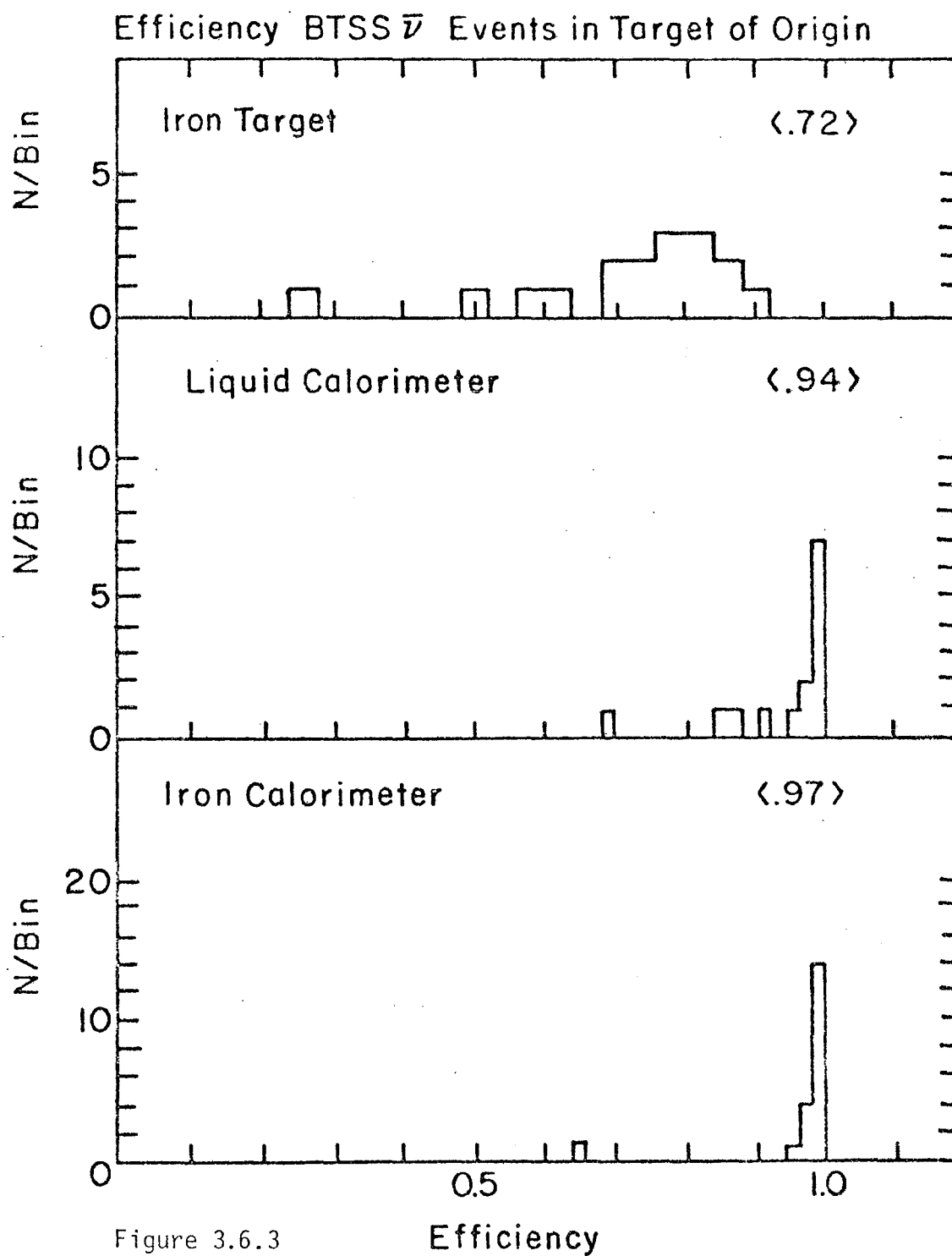


Figure 3.6.2



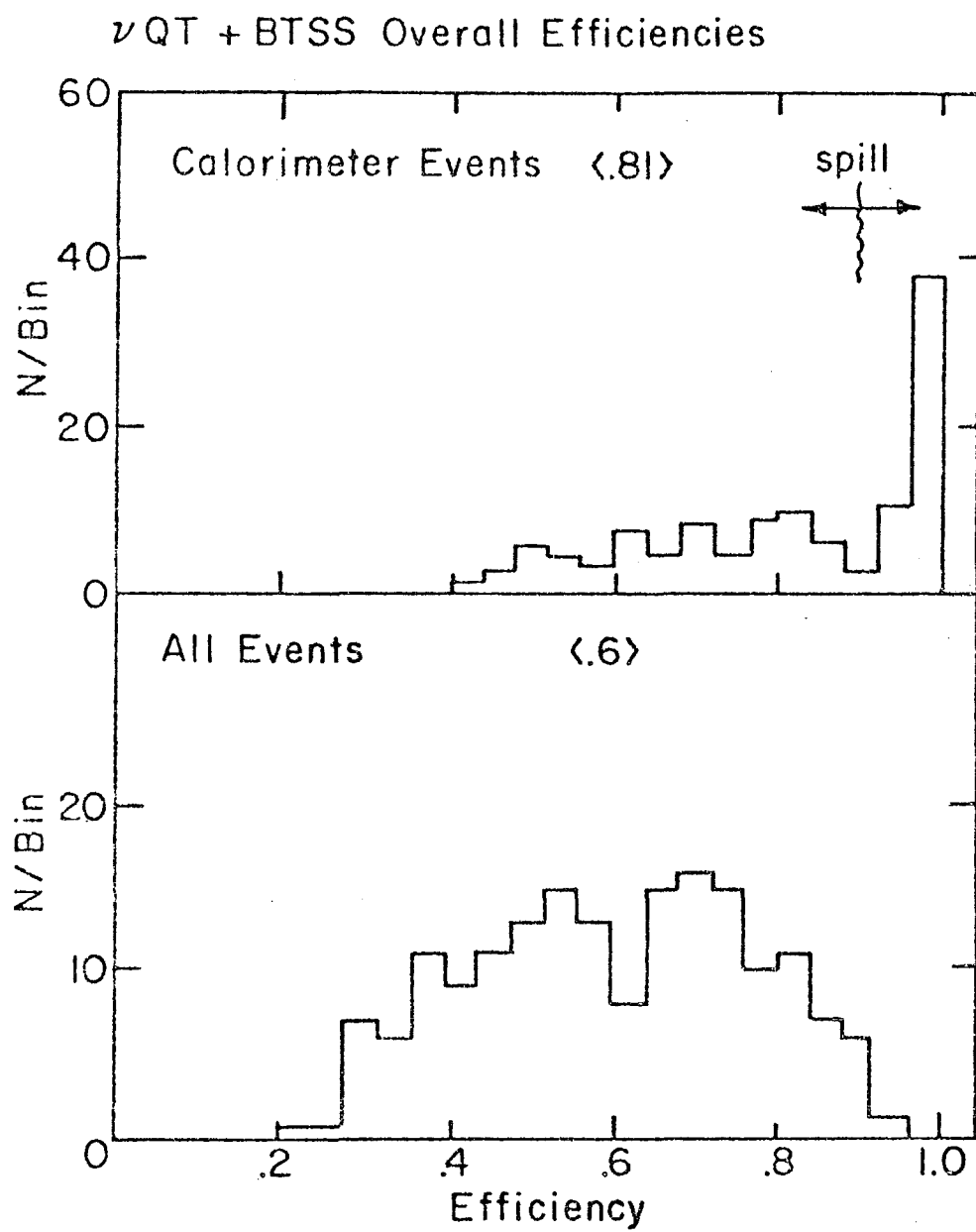


Figure 3.6.4

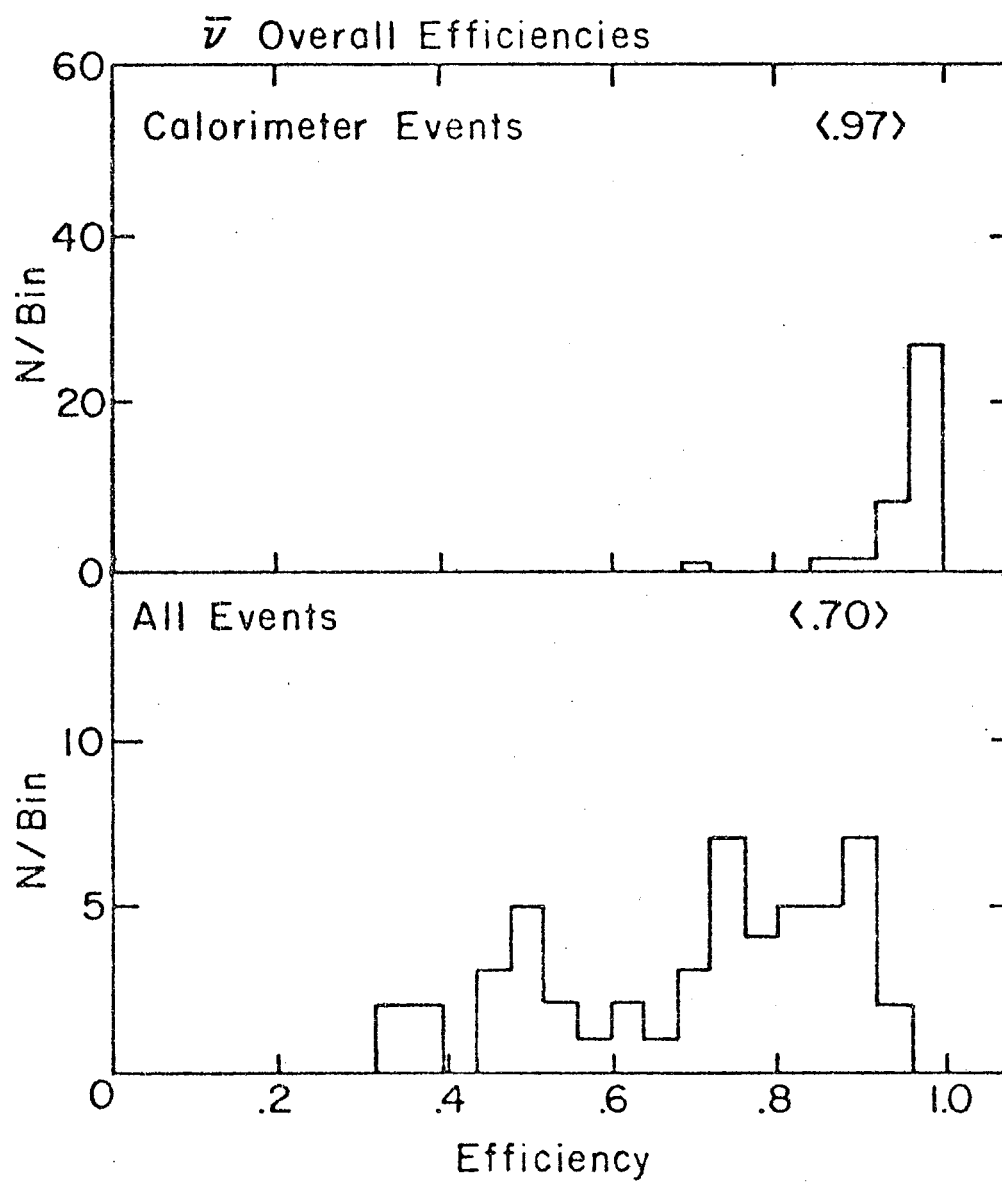


Figure 3.6.5

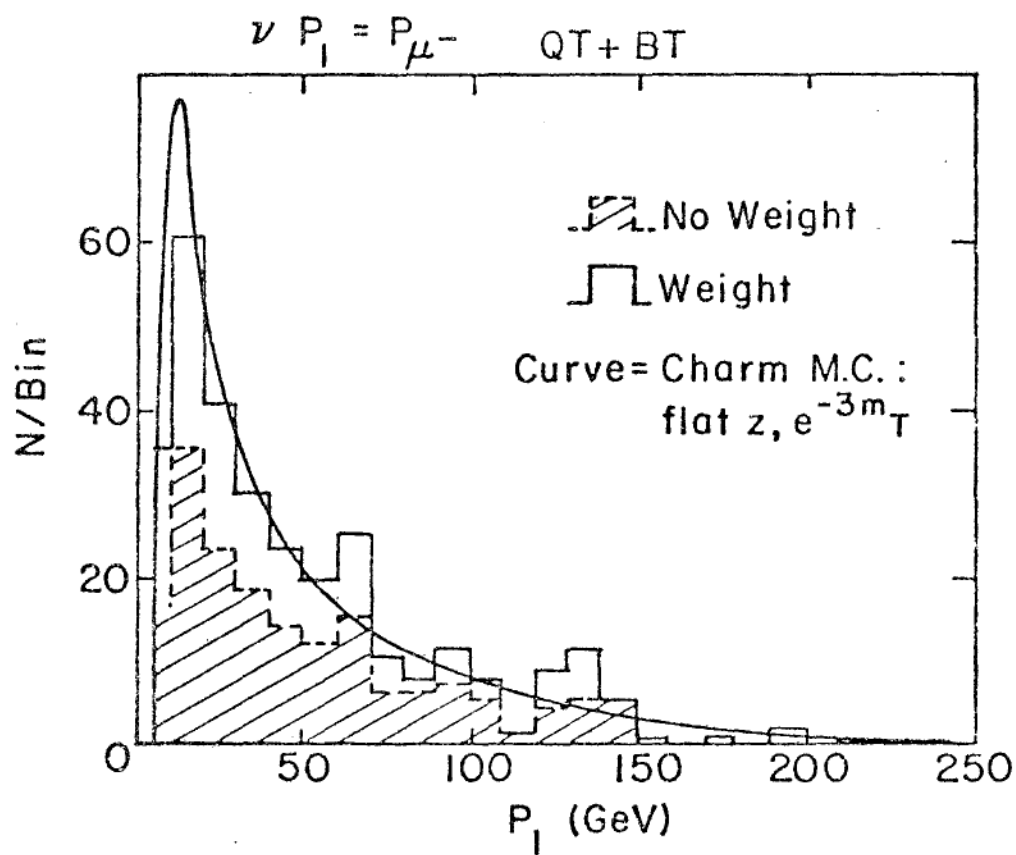


Figure 3.6.6

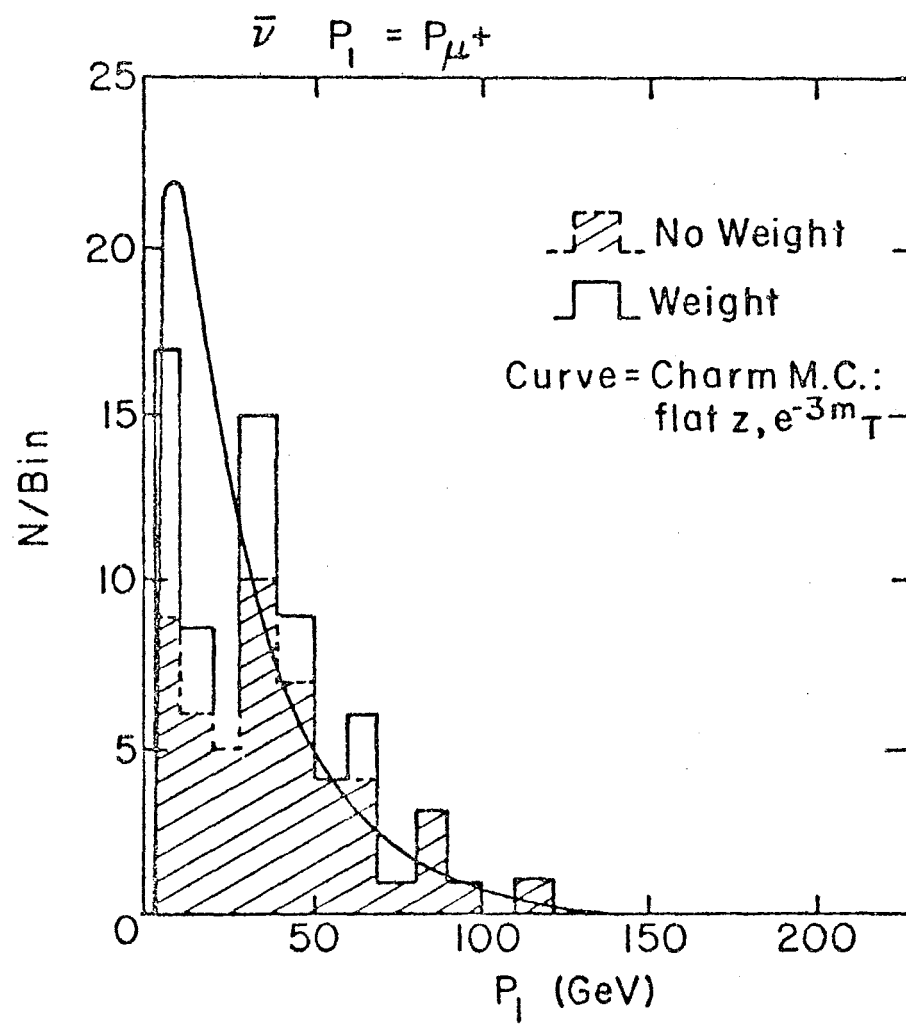


Figure 3.6.7

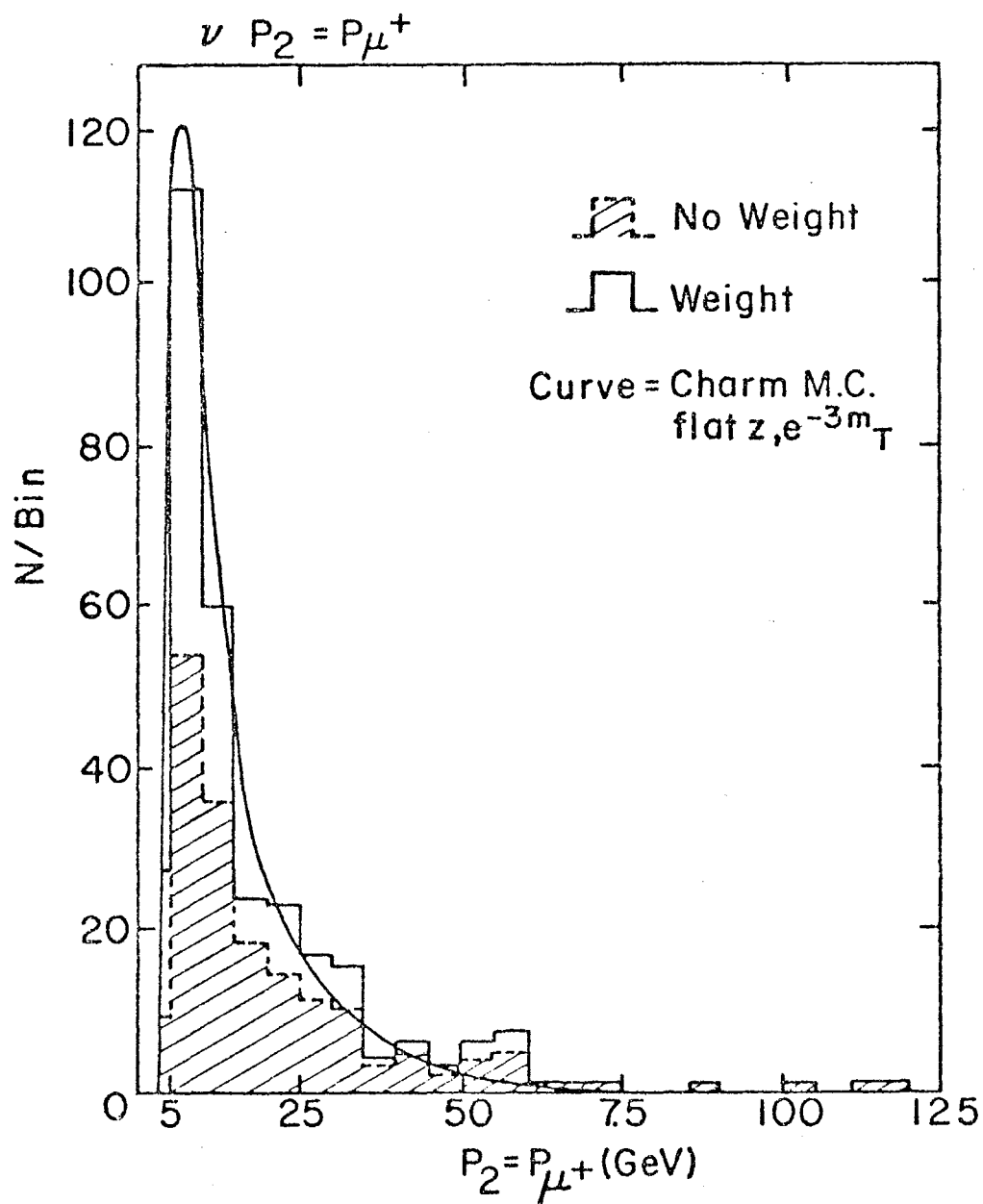


Figure 3.6.8

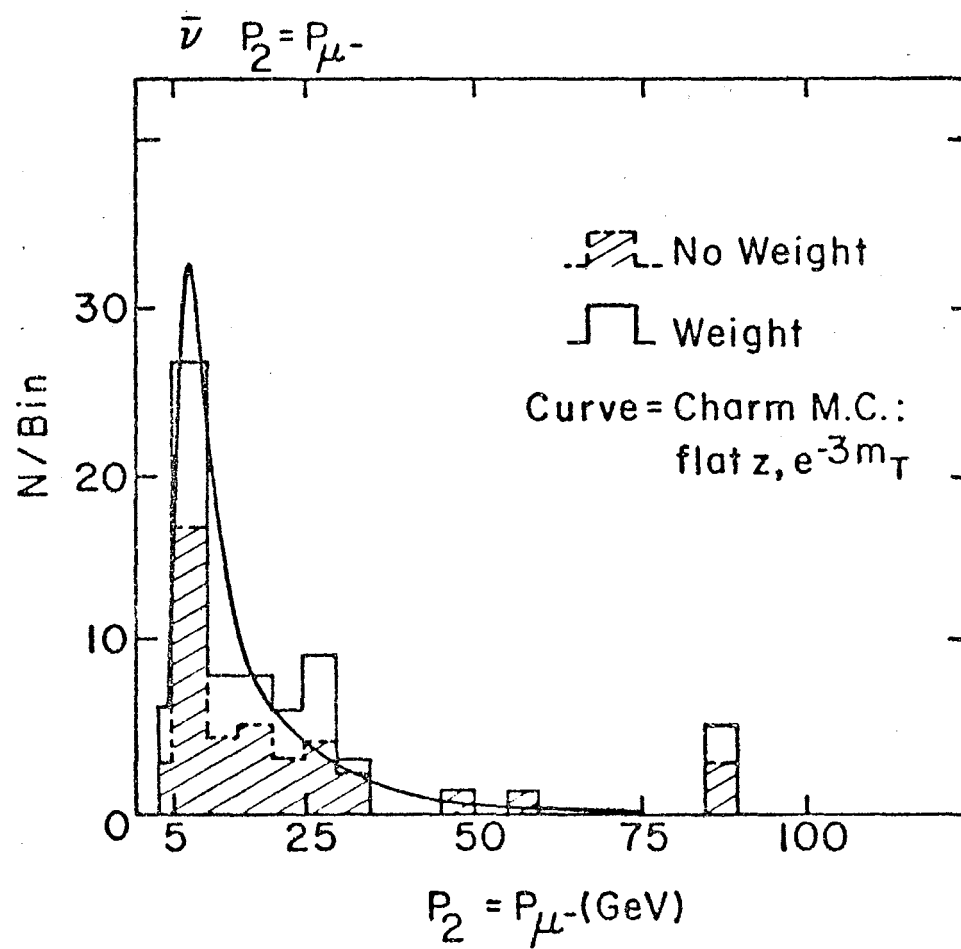


Figure 3.6.9

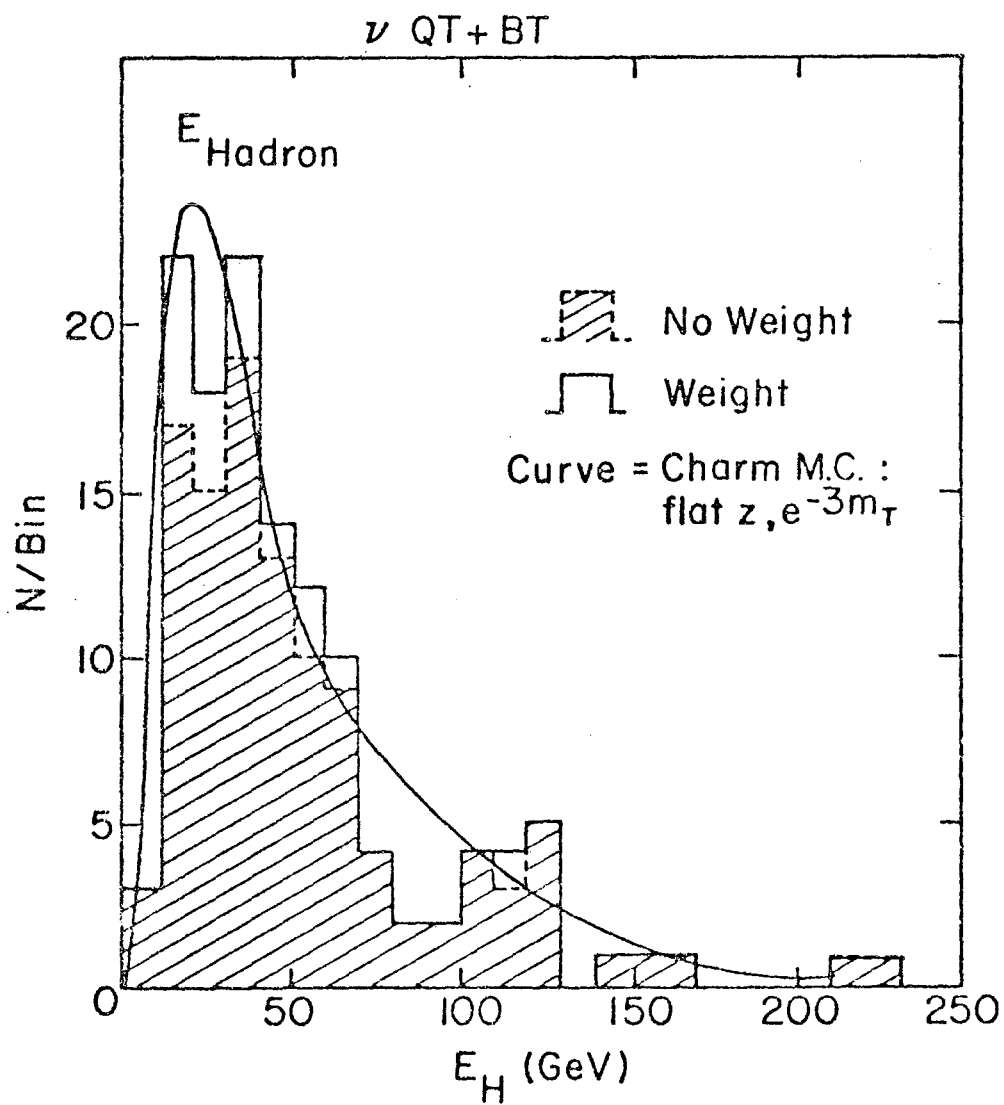


Figure 3.6.10

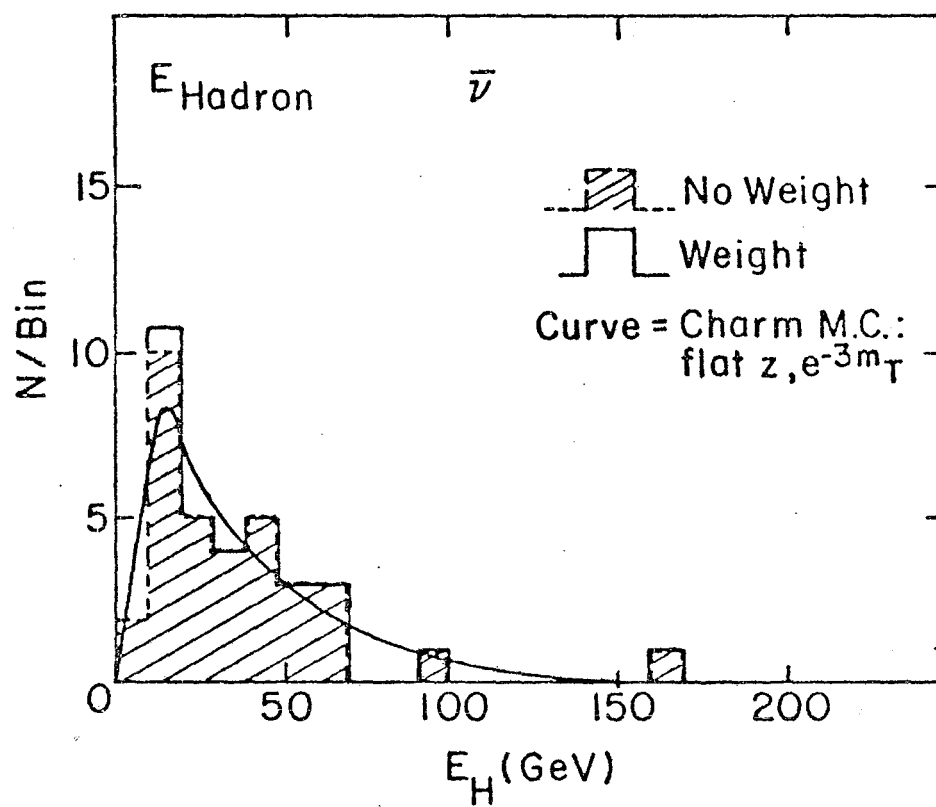


Figure 3.6.11

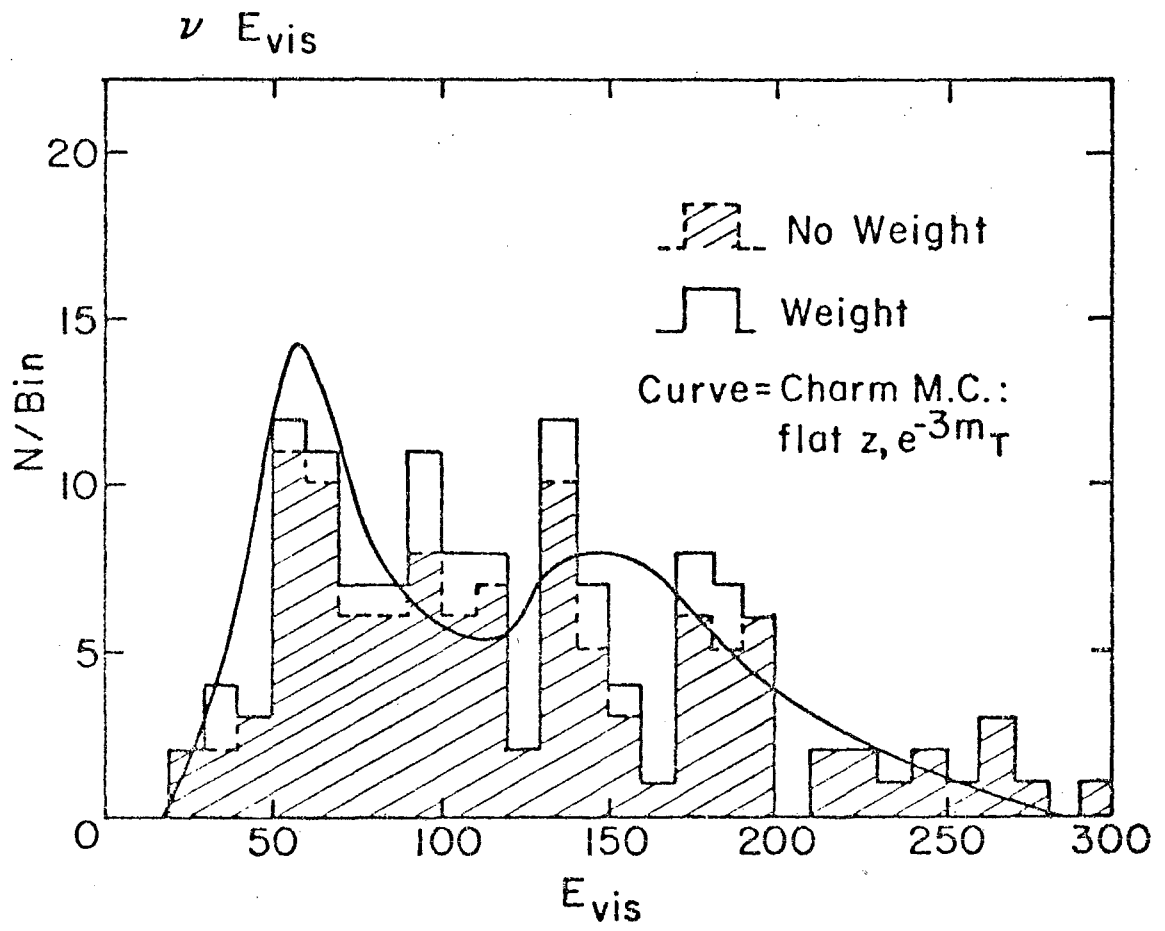


Figure 3.6.12

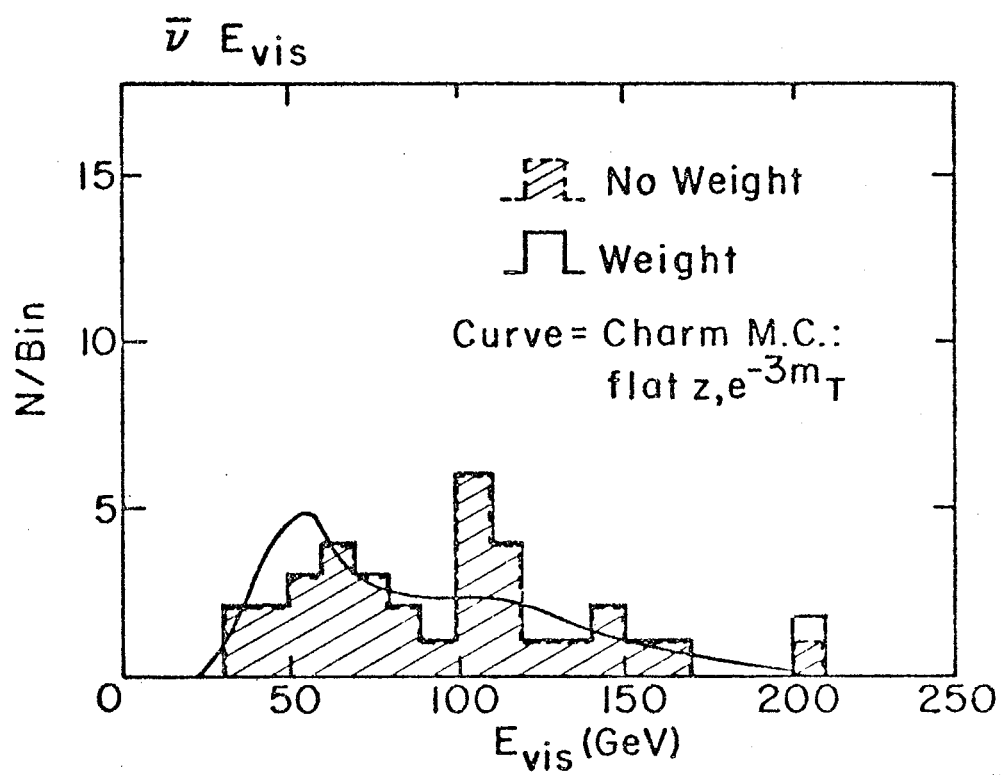


Figure 3.6.13

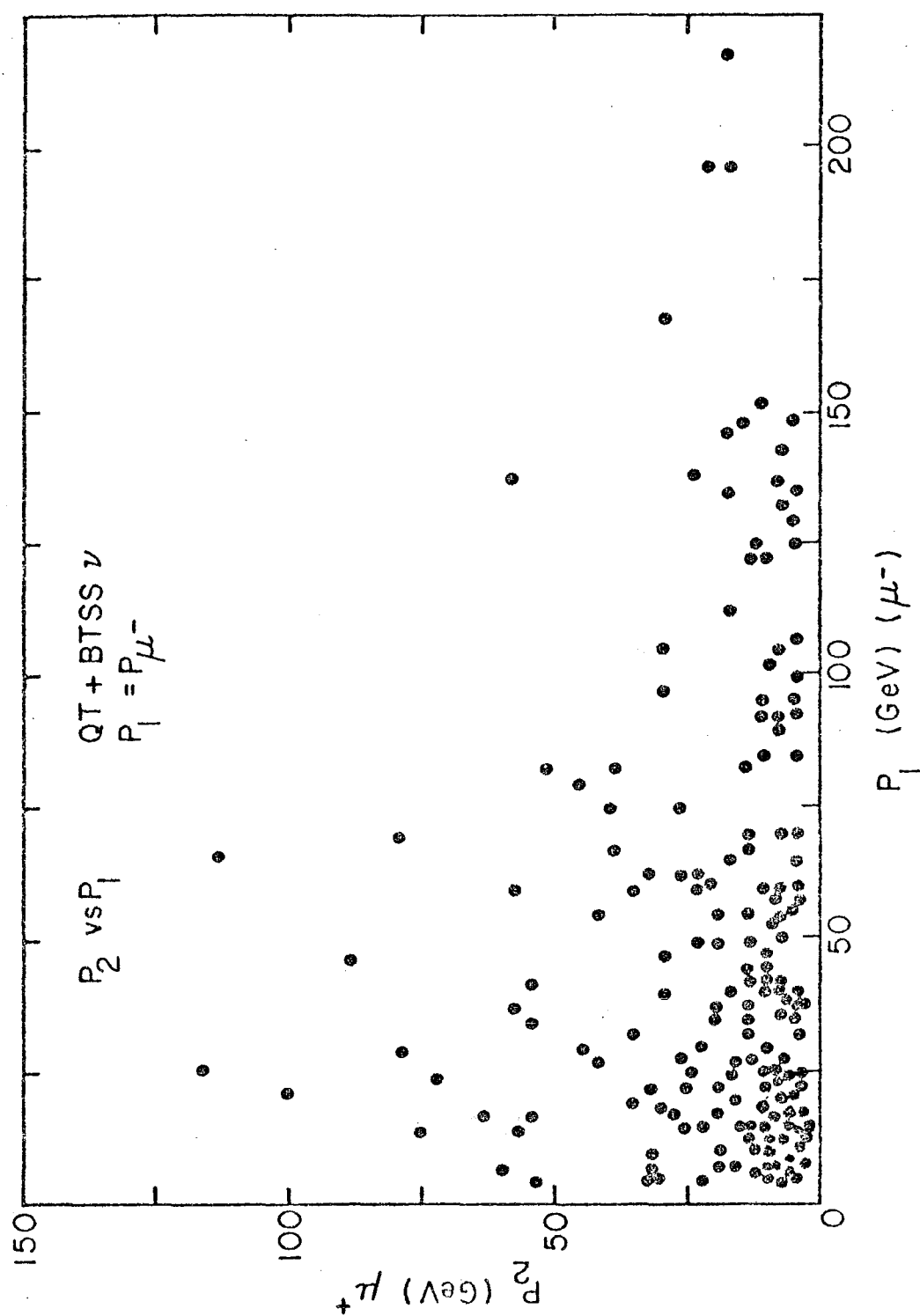


Figure 3.6.14

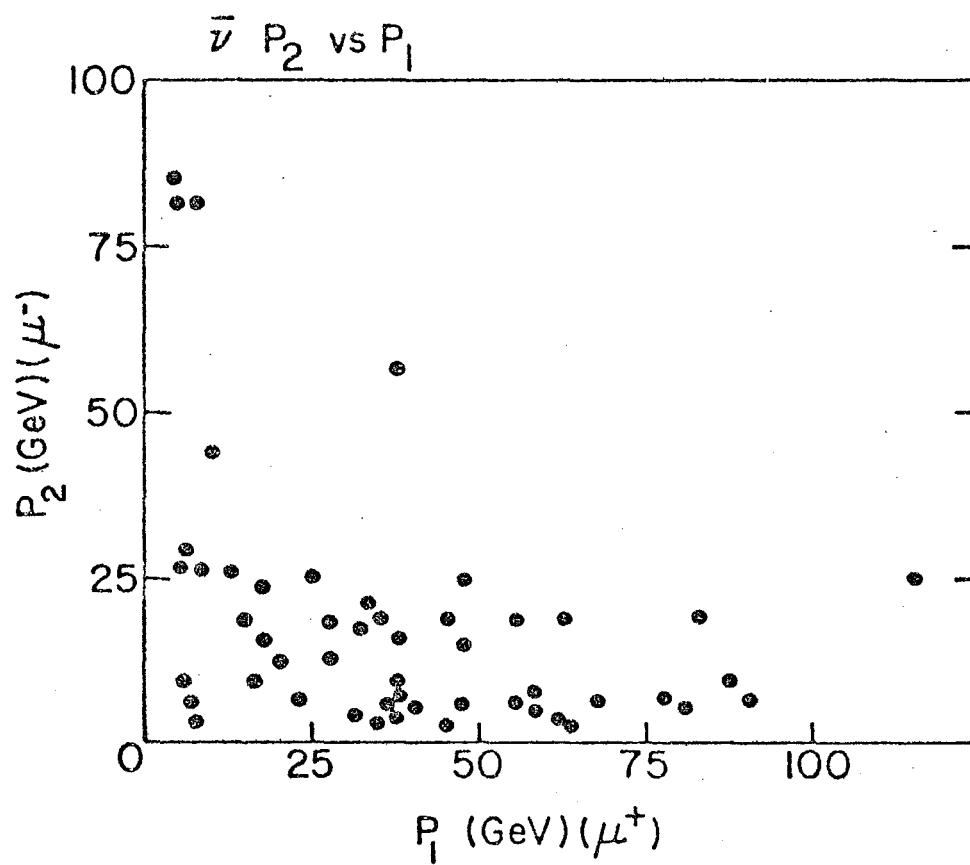


Figure 3.6.15

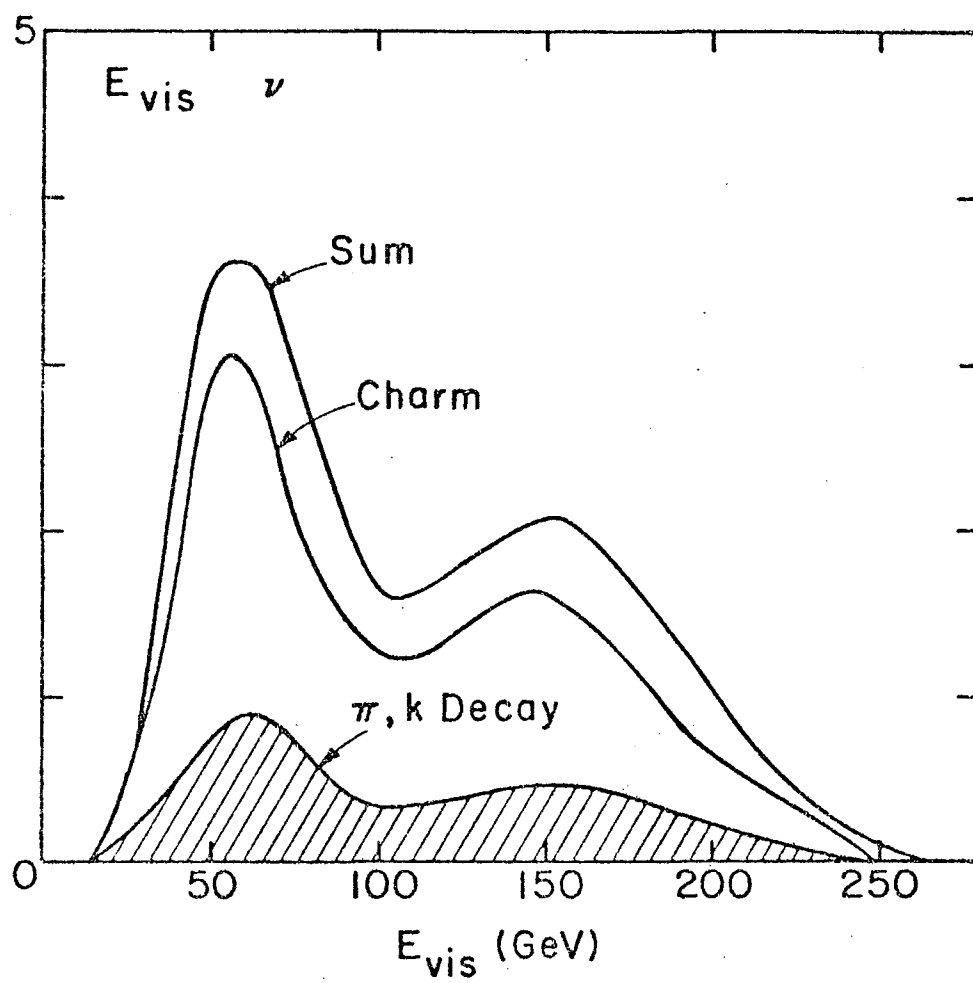


Figure 3.7.1

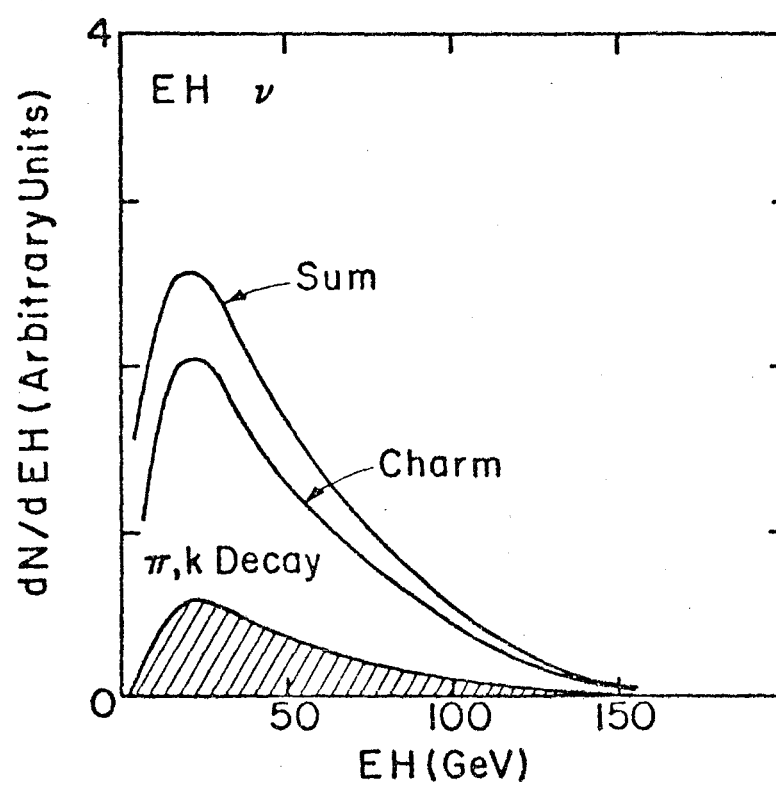


Figure 3.7.2

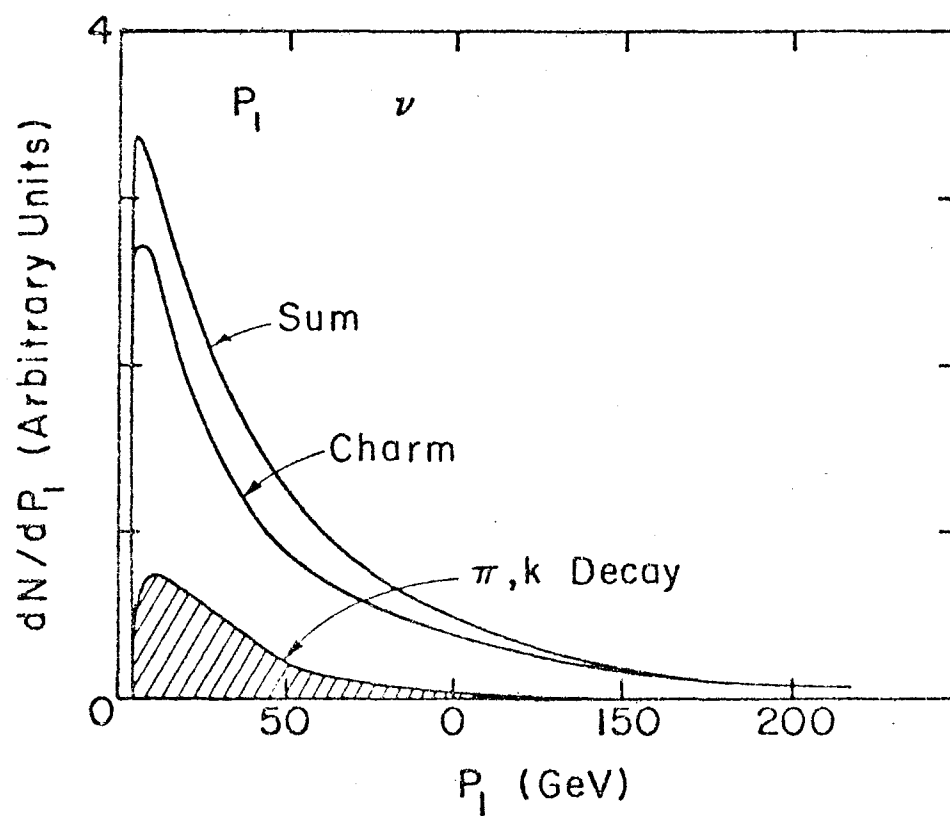


Figure 3.7.3

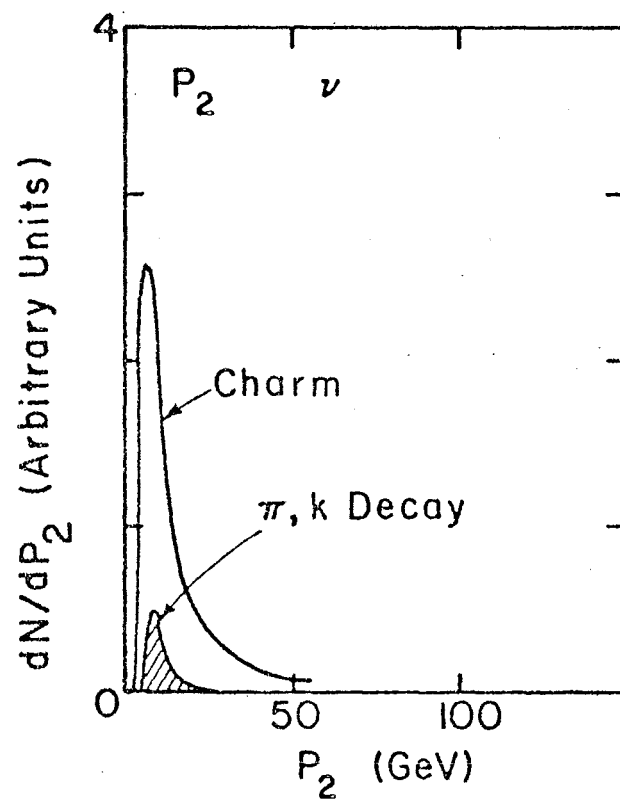


Figure 3.7.4

CHAPTER IV

DIMUON CHARACTERISTICS

4.1 Introduction

This chapter compares the opposite sign dimuon events with the theoretical framework set up in Chapter 1. Section 2 describes the charm monte carlo. Section 3 compares the charm monte carlo with data and discusses the dimuon rate with respect to single muons. Section 4 describes characteristics expected from other sources of dileptons and their signals in the data. Section 5 is a summary and concluding remarks.

4.2 Charm Monte Carlo

The charm monte carlo consists of 6 basic elements, which follow from the discussion in Chapter 1. These elements are:

1. (anti) neutrino energy generation
2. x and y generation
3. z generation
4. p_t generation
5. D decay
6. experimental resolution and cuts

The (anti) neutrino energy of an event was generated according to the flux distributions shown in Appendix I, assuming a linear energy dependence of the cross sections. The wrong sign backgrounds

were measured to be about 1 in 6, 1 in 6, and 1 in 20 for the QT, BTSS $\bar{\nu}$ and BTSS ν respectively. Since the QT and BTSS data are combined, the neutrino monte carlo uses the fluxes of the QT and BTSS running weighted by the integrated intensity for each beam. The shapes and relative normalization of the fluxes are important, but absolute normalization is not important for the purposes of this monte carlo.

The x and y distributions were generated by monte carlo integration of the differential cross section $d^2\sigma^{\nu,\bar{\nu}}/dx dy$ discussed in section 4 of Chapter 1, using slow rescaling and an SU(3) symmetric ocean.

The z and p_t distributions were taken from a variety of parametrizations, as discussed in Chapter 1:^{32,36, 37}

$$D(z) \approx e^{-3z}, \text{ flat, } z, \delta(z-.75)$$

$$F(p_t) \approx e^{-3m_T}, e^{-6m_T}, e^{-p_t/.5}$$

where $m_T = (m^2 + p_t^2)^{1/2}$. The direction of the D meson is emitted randomly around the w-direction; i.e., the distribution in the azimuth angle ϕ_w about the w direction of the D is flat.

The D decays were discussed in Chapter 1. To a good approximation, these decays can be generated by sequentially generating a 2 body phase space decay with an effective mass for the $(\mu\nu)$ system, $D \rightarrow k + (\mu\nu)$, followed by generating a second 2 body decay $(\mu\nu) \rightarrow \mu + \nu$ and then weighting the decay by the subsequently calculated matrix

element. The decay used $m_C = m_D - 1.87$ and 50% K, 50% K^* .³⁹

The observed hadron energy ($E_H = E_\nu - P_1 - P_2 - E_{\nu \text{ decay}}$) and the muon momenta angles and magnitudes are smeared by the momenta and energy resolutions, and the total energy $E_{\text{vis}} = E_H + E_1 + E_2$ recalculated. In comparing with data, the appropriate cuts $P_{\text{min}} < 4.5$ GeV and the polar angles < 400 mrad. Unless explicitly stated otherwise, muon 1 is the (positive) negative muon for (anti) neutrino, and muon 2 is the (negative) positive muon for (anti) neutrino. Since neutrino and antineutrino dimuon events cannot be reliably distinguished on an event by event basis, the "wrong-sign" events generated in the monte carlo (i.e., antineutrino in the neutrino sample) have muon 1 and muon 2 interchanged so that monte carlo events are treated like the data.

The curves overlaid on Figures 3.6.6-3.6.15 in the previous chapter show the first results of this monte carlo for E_{vis} , E_H , p_1 and p_2 normalized to the same area as the corrected data. The agreement is good; correction due to pion and kaon decay can be seen from the figures in section 3.7 and is small.

For the majority of characteristics, a flat z distribution, $F(p_t) \approx e^{-(3-6) m_T}$ describe the data quite well. The data is relatively insensitive to variations in z and p_t distributions due to the 3 body D decay which automatically pushes p_2 to low average values and causes p_t to reflect the mass of the D. Where appropriate in the following sections, monte carlo differences in various

characteristics due to varying z and p_t distributions will be indicated. Effects of pion and kaon decay will also be indicated.

4.3 Characteristics of Dimuon Events and Charm

General. The characteristics of the data which can be compared to charm basically follow from the observation that $P_{\mu 2}$ lies along the W-boson direction up to a p_t reflecting the 3 body decay of the D and heavy particle production.

As there are 3 "quantities" measured in this experiment, namely P_1 , P_2 and EH, there are a variety of variables that can be formed from these quantities to test theoretical predictions for dimuon production models. For variables defined using only components of muon momenta, all dimuon events can be used; for those requiring EH, only calorimeter events can be included. Chi-square tests comparing monte carlo and data and quantitative information are discussed in section 4.3.10 after the introduction to the various distributions. For reviews of the uses and interpretations of the characteristics discussed in the following sub-sections, see the articles in reference 32.

4.3.1. $\Delta\phi$ The 2 muons from a charm model tend to be emitted opposite to each other, projected into the plane perpendicular to the neutrino direction. The variable $\Delta\phi$, defined as the difference in the azimuthal angle of the 2 muons (i.e., the angle between

the components of the momenta perpendicular to the neutrino direction), is depicted in the perspective view of Figure 4.3.1. This variable is peaked toward 180° as shown in Figures 4.3.2 and 4.3.3 for neutrino and antineutrino. The contribution of pion, kaon decay is indicated along with the total monte carlo for charm. A softer z distribution causes $\Delta\phi$ to peak less strongly toward 180° as shown by the 2 monte carlo curves (including background). Qualitatively, since the charm quark is emitted along the W direction, and P_W and P_l "kick" transverse to each other ($\nu \rightarrow W + \mu$) this behavior is expected from charm. Changing the p_t distribution to $\exp(-3m_t)$ makes little difference in this variable.

4.3.2 α . The decay muon generally occurs at a much lower momentum than the primary (lepton vertex) muon. This is shown most easily by an asymmetry parameter

$$\alpha = \frac{P_1 - P_2}{P_1 + P_2}$$

where 1, 2 refer to the lepton, hadron vertex respectively. The distribution for this parameter is peaked toward $\alpha = 1$ as shown in Figures 4.3.4 and 4.3.5 for ν , $\bar{\nu}$. The effect of the wrong sign background is shown in Figure 4.3.4. The monte carlo indicates that a cut of $\alpha < -.3$ removes between 90% and 95% of the wrong sign background in the dimuon sample. This cut will be used later in calculating the charm dimuon rate relative to single muons. The effect of pion, kaon decay is shown on Figure 4.3.5. It is mainly

restricted to positive values of α . Note that the curves are labeled with the z and p_t distributions used in the charm contribution.

4.3.3. P_{out} . The production plane is defined as the plane containing the incident lepton, the outgoing lepton, and the W-boson momentum vectors. P_{out} is defined as the component of momentum of the second (decay) muon perpendicular to the plane:

$$P_{out} = \left| \frac{\vec{P}_2 \cdot (\vec{P}_1 \times \vec{P}_v)}{|\vec{P}_1 \times \vec{P}_v|} \right|$$

This is shown schematically in Figure 4.3.6. Note that \vec{P}_W is defined by $\vec{P}_v = \vec{P}_1 + \vec{P}_W$, and $\vec{P}_W = (-P_{x1}, -P_{y1}, E_{vis} - P_{z1})$ for $\vec{P}_v = E_v \hat{z}$.

In the case of dimuons, this is an "effective" definition, since there is a missing neutrino, lowering E_{vis} . The comparison between P_{out} and the charm monte carlo are shown in Figures 4.3.7 and 4.3.8 for ν, ν corrected data. As would be expected, the momentum out of the production plane is bounded by about 2 GeV, reflecting the charm mass and hadronic P_t production. The figure for neutrino shows the difference between $\exp[(-3, -6) m_t]$, which is quite small.

There are a small number of events with P_{out} larger than 2 GeV. For neutrino this corresponds to $2 \pm 1\%$ (weighted) of the events, and $4 \pm 2\%$ of the events with E_{vis} greater than 100 GeV. For antineutrino, this corresponds to $4 \pm 2\%$ of the events and $7 \pm 5\%$ of the events with E_{vis} greater than 100 GeV. However, if one requires $\alpha > 0$, then only 1% of neutrino and 0% of antineutrino events have

P out above 2 GeV (including wrong sign background), so this slight excess is not significant.

4.3.4. P_{tW} . Using the definition of P_W given in the previous section, P_{tW} is defined as the component of momentum of the second muon transverse to the W-direction:

$$P_{tW} = \left[P_2^2 - (P_W \cdot P_2 / |P_W|)^2 \right]^{1/2},$$

shown schematically in Figure 4.3.9. In a charm model, this is also bounded by charm mass and P_t production like P out. Data for neutrino and antineutrino are shown with monte carlo curves in Figures 4.3.10 and 4.3.11. Since the second muon can lie close to the production plane, P_{tW} is a somewhat more sensitive test of production models than P out. On the other hand, P out requires only muon momenta, while P_{tW} requires EH in order to find P_W . Thus P out distributions include iron target events, while P_{tW} distributions cannot.

It is interesting to remark that $F(P_t) \approx \exp(-3, -6)m_t$ changes the P_{tW} distribution slightly as indicated in the $\exp(-3m_t)$ may be slightly preferred.

As in the P out distribution, there are a small number of events with P_{tW} greater than 3 GeV, corresponding to about the same fractional excess. Again, this is only a very slight excess over the charm predictions, at the 1% level, and not significant.

4.3.5 $\Delta\phi_W$. The variable $\Delta\phi_W$ is shown schematically in Figure 4.3.9. It is the difference in the (azimuthal) angle between the 2 muons projected into a plane perpendicular to the W direction. For charm, this should be a flat distribution; i.e., the charm particle should be emitted isotropically in ϕ about the W. Figures 4.3.12 and 4.3.13 show the distribution in $\Delta\phi_W$ for $\nu, \bar{\nu}$. In the monte carlo, there is a slight rise toward 0° due to the wrong sign background and smearing, which is basically consistent with the data. This distribution requires hadron energy, and is restricted to calorimeter events.

4.3.6. m_{12} . Another variable which is useful to test models is the invariant mass of the muon pair.

$$m_{12}^2 = 2 m_\mu^2 + 2 (E_1 E_2 - P_1 \cdot P_2).$$

In general, this will be large, having average values of 2.9 GeV for ν and 2.4 GeV for $\bar{\nu}$ since the muons are emitted from different vertices (lepton, hadron) in a charm model. The distributions with the monte carlo curves are shown in Figures 4.3.14 and 4.3.15 for neutrino and antineutrino, with good agreement.

4.3.7. $z_{\mu 2}$. The variable $z_{\mu 2}$ is an effective z defined as $P_2 / (P_2 + E_H)$, since this is a quantity similar to $z = P_D / (y E_\nu)$ but measurable by this experiment. The $z_{\mu 2}$ distributions for ν and $\bar{\nu}$ are shown in Figures 4.3.16 and 4.3.17 with a flat z monte carlo. In

both cases there may be some excess in the data at higher values of $z_{\mu 2}$, perhaps indicating a "harder" z distribution. Figure 4.3.18 shows four different z distributions superposed, normalized to the same area. The 2 harder distributions $D(z) \approx z$, $D(z) \approx \delta(z-.75)$ are not substantial improvements. A theory for $D(z)$ would be useful, however, $D(z)$ has only mild influence on charm as a source of dimuons for the bulk of the events. For example average $z_{\mu 2}$ for $D(z) \approx \exp(-3z)$ is .2, $D(z) \approx \text{flat}$ is .25, and $D(z) \approx \delta(z-.75)$ is .31.

4.3.8. $x_{\text{vis}}, y_{\text{vis}}, Q_{\text{vis}}^2, W_{\text{vis}}^2$. The effective scaling variables $x_{\text{vis}}, y_{\text{vis}}$, and $Q_{\text{vis}}^2, W_{\text{vis}}^2$ are defined as

$$x_{\text{vis}} = \frac{Q_{\text{vis}}^2}{2mp(EH + P_2)}$$

$$y_{\text{vis}} = (EH + P_2)/E_{\text{vis}} = v_{\text{vis}}/E_{\text{vis}}$$

$$Q_{\text{vis}}^2 = 4p_1 E_{\text{vis}} \sin^2 \theta_1 / 2$$

$$W_{\text{vis}}^2 = 2mp E_{\text{vis}} y_{\text{vis}} (1 - x_{\text{vis}})$$

Distributions with the monte carlo overlaid are shown in Figures 4.3.19-4.3.26 for v, \bar{v} in x, y, Q^2, W^2 respectively. The agreement between theory and experiment is generally quite good for all of these. The monte carlo predicts x_{vis} for \bar{v} to have peaked somewhat

more strongly towards $x = 0$, since $\bar{\nu}$ charm production proceeds only from ocean quarks, perhaps indicating $xS(x) \sim (1-x)^7$ rather than $(1-x)^9$.³³ However, the overall $\bar{\nu}$ shape is peaked more strongly at low x than the ν sample as shown in the figures. A "harder" z distribution (rather than flat) would not have agreed as well with the y distributions.³² The pion, kaon background contribution for the y distributions is shown for ν , $\bar{\nu}$, having a quite different shape for ν versus $\bar{\nu}$.

4.3.9 Dimuon Rates. The dimuon rate relative to single muon events is found by using the corrected single muon data discussed in Appendix XI. For the rate calculation, only events from the calorimeters were used, with fiducial volume cuts chosen equally to those used for the single muon sample. Background dimuon events from pion, kaon decay were subtracted, as discussed in Appendix XII and Chapter 3. In addition, the sample was cut by restricting α to be greater than -0.3 to obtain a purer sample of ν or $\bar{\nu}$. Assuming charm is a correct description, this causes a loss of no more than 5% of ν or $\bar{\nu}$ depending somewhat on the parameters of the model.

$$\text{The corrected rates } R^\nu = \frac{\sigma(\mu \bar{\mu})}{\sigma(\mu)} , \quad R^{\bar{\nu}} = \frac{\sigma(\bar{\mu} \mu)}{\sigma(\bar{\mu})}$$

for ν and $\bar{\nu}$ as a function of energy are shown in Figures 4.3.27, 4.3.28. The monte carlo curves shown are for 2 branching ratios for $D \rightarrow uK\nu$, 10% and 15%.³² Note that the errors quoted are statis-

tical only, and do not take into account systematic errors in the π, K decay calculation (est. 25%) or the acceptance corrections for dimuon and single muon events (est. 10%).

The rates are somewhat high for ν , since the preferred value of the D branching ratio is $10 \pm 2\%$, however, both $\nu, \bar{\nu}$ are both compatible with charm predictions. The rise in the rate with E_{vis} is mainly an artifact of the experimental requirements, in particular $P_{min} > 4.5$ GeV. The rates with no cut and without slow rescaling are 1.5-2% for ν and 1-1.5% for $\bar{\nu}$ (depending on the branching ratio) well above charm threshold. Including slow rescaling and cuts implies an experimental loss of 40-50% of the events above 100 GeV due to events below the momentum cut. As discussed in reference 32 of Chapter 1, it is possible to increase the effective rate of dimuons somewhat by using a z distribution more strongly peaked toward $z = 1$, since the second muon will then have a higher average momentum. This would allow the neutrino sample to be more consistent with a lower muonic branching ratio.. The slow rescaling monte carlo predicts

$$R_2 = R^{\bar{\nu}} / R^{\nu} = 1.1$$

for E_{vis} between 110 and 200 GeV. This experiment measures $R_2 = 1.1 \pm .52$, in excellent agreement. However, lower energy points are larger than the predicted values, as shown in Figure 4.3.29, but agree within errors.

While this data is compatible with the SU(3) symmetric ocean

and slow rescaling in the monte carlo, using the formulae discussed in Chapter 1:

$$\bar{S}/D \approx \tan^2 \theta_c R_1 (R_2^{-1} - R_1)^{-1}$$

$$R_1 = \frac{\sigma^{\bar{\nu}}}{\sigma^{\nu}}$$

$$Q = \int x q(x) dx$$

imply that $\bar{S}/D = .06 \pm .04$, above 110 GeV. This formula is expected to be low by as much as 50% as it does not take the threshold effects into account; however, it is consistent with the assumed quark density parametrization.

Although this data is consistent with an SU(3) symmetric ocean, it is interesting to speculate on the possibility of an SU(4) symmetric ocean. As discussed in Chapter 1, the dimuon data is not very sensitive to charm quarks in the ocean due to the $(1-y)^2$ cross section dependence, and the probably weak energy transfer mechanism to the charm quark which is left to decay (Figure 1.4.1c). In a crude approximation, assuming "left-over" charm particle production like $(1-x_F)^5$, where x_F is Feynman x, these considerations would lead to an average z relative to the other charm mechanisms for the leftover quark of about 0.07 versus 0.5 for a flat z. Hence an SU(4) symmetric ocean would not affect the dimuon rate significantly for this experiment, above the experimental cuts. This possibility will have interesting consequences

for b-quark production. It is suspected that the ocean is broken in the same way that "quark masses" are for constituent quarks. However, the notion of quark masses, especially in a dynamical (current) situation are ill defined.^{25,34}

4.3.10 Summary of Charm Dimuon Distributions. Slow rescaling charm production from an SU(3) symmetric ocean explains the shapes of the distributions of many experimental quantities measured in dimuon events from neutrino and antineutrino. A consistent z distribution is $D(z)$ constant, although for some distributions a harder distribution may be preferable.

Chi-square tests are shown in Table 4.3.1 comparing dimuon events and the area normalized charm predictions for several of the preceding sections of this chapter. The bin sizes were chosen from the distributions for the Chi-square rule of thumb criteria:

- 1) equal probability/bin
- 2) at least 5 points/bin
- 3) size consistent with resolution

and

$$\chi^2 = \sum_i \frac{[\text{Data}(\text{bin}_i) - \text{Theory}(\text{bin}_i)]^2}{[\text{Data}(\text{bin}_i)]}$$

the agreement is good, although fine details of shapes are masked by low statistics, especially in antineutrino.

Table 4.3.2 lists the average values of a variety of quantities, both for all E_{vis} and selected quantities for E_{vis} larger than 100 GeV. The Charm predictions are listed in brackets. The \pm errors are simply the standard deviations of the averages. Note that quantities like P_{out} and P_{tW} change little with energy (all E , $E > 100$ GeV) as expected from charm decay, while others like $\Delta\phi$, m_{12} and α move to higher values as expected from neutrino-nucleon scattering kinematics with charm production. The gross features of the shapes remain similar above 100 GeV. Most values are in reasonable agreement with the charm predictions.

4.4 Dimuons from Other Sources and Charm

4.4.1. Introduction. This section discusses the ways the experimental distributions of the previous section would change when additional sources are added to the charm contribution. Only 2 sources will be considered, b-quark production and an L^0 of mass ≈ 2 GeV, as was discussed in Chapter 1. A simple attempt is made to show that charm is consistent up to statistical accuracy with essentially the entire data sample.

4.4.2. b-quark and L^0 monte carlo. The b-quark and L^0 monte carlo used the same calculation apparatus set up for the charm monte carlo. For the b-quark production, simple approximations were used: 50% ocean, 50% valence for $\bar{\nu}$, 100% ocean for ν ,

$(1-y)^2$ y distributions, and b-decays to 50% u, 50% c quarks.

For the L^0 , the decay was generated like charm 3-body decays weighting the decay by the $V \pm A$ matrix element from the references in section 1.5.5. As the L^0 mass used was only 1.8 GeV, no attempt was made to recalculate the double differential cross section; a simple energy threshold of 30 GeV was used. For this monte carlo, $V \pm A$ have only small differences. Table 4.4.1 lists averages of selected variables for b-quark and L^0 production.

4.4.3. Comparisons with charm. Six of the experimental quantities discussed in section 4.3 are shown in Figures 4.4.1-4.4.6 for all 3 monte carlo normalized to the same area for neutrinos. These variables are α , $\Delta\phi$, P_{out} , P_{tW} , $\Delta\phi_W$ and m_{12} . For the purposes and assumptions of this work, neutrino and antineutrino shapes are very similar to each other for b-quark and L^0 production reflecting more the masses and properties of the particles produced. For L^0 production by antineutrinos, the muon spectra can be harder than for neutrino L^0 production if the assumption of $(1-y)^2$ is used for antineutrino. The rates for b-quark production, of course, depend on the quark content of the nucleon, and can be quite different for ν , $\bar{\nu}$.

Figure 4.4.1 shows that the α distribution is basically not a sensitive test for either b or L^0 , while $\Delta\phi$, $\Delta\phi_W$, and m_{12} (Figures 4.4.2-4) are sensitive to L^0 production. Similarly P_{out}

P_{tW} (Figures 4.4.5-6) have sensitivity to b-quark production.

A chi-square test can be made of the goodness of fit of charm together with varying amount of b-quark or L^0 to the ν data shown in section 4.3:

$$\chi^2 = \sum_i \frac{(D_i - A c_i - B t_i)^2}{(D_i)}$$

where D_i is the number of events in bin i
 c_i is the fraction of charm generated events in bin i
 t_i is the fraction of L^0 or b-quark generated events in bin i

and $A + B = \sum_i D_i$, the total number of events. Thus the percentage of charm dimuons to all dimuon events is

$$F_c = (A / \sum_i D_i) \times 100.$$

Figures 4.4.7 through 4.4.10 show the unnormalized chi-square as a function of F_c , the percentage of charm dimuons with either L^0 or b-quark contributing $(100 - F_c)$ percent to the total events, for 4 of the most sensitive distributions. Only charm with L^0 favors any L^0 contribution, being 98% charm, 2% L^0 . All the others (P_{out} , P_{tW} , m_{12}) favor 100% charm, 0% other. However, it is important to note the following:

- 1) The statistics of the experiment basically limit the usefulness of this test to the 10%-20% level as there are only at most 180 total events in these plots. This is partially reflected by the change of slope of these chi-square distributions between 80%-90% charm. For ν data, the statistical power is a factor 2 worse, and not useful.
- 2) In both P_{out} and P_{tW} tests, events with values of these variables larger than 2.5 GeV and 3 GeV respectively were left out of the fits as there were too few events per bin. These events will be used to put limits on b-quark production and mixing angles.

To further search for any extra contributions to dimuon events, events with E_{vis} greater than 100 GeV were used in 3 scatter plots: P_{out} against $\Delta\phi$ (Figure 4.4.11), M_{12} against P_{out} (Figure 4.4.12), and P_1 against P_2 (Figures 4.4.13 and 4.4.14).⁵¹ For the first 2 plots, the fraction of events from each source (Data, charm, b-quark, L^0) out of all events of that source are shown in each bin. There are 82 ν and 17 $\bar{\nu}$ events with $E_{vis} > 100$ GeV, yielding a marginal statistical power for $\bar{\nu}$ which are shown as number of events in brackets, not as fractional total events. For example, if b-quark production were to contribute 10% to the total rate, 0.1 times the percentage of

b-quark in each bin ± 0.9 times the percentage of charm in each bin should equal the percentage of data in each bin. There is no evidence in Figures 4.4.11 and 4.4.12 within the statistical power of the experiment (10%-20%) for any b-quark or L^0 production.

In figures 4.4.13 and 4.4.14 (P_1 vs P_2) an excess of events between the lines $P_2 = 2P_1$ and $P_2 = (\frac{1}{2})P_1$ would indicate L^0 production.⁵⁵

The approximate charm boundaries for 500 events in $\bar{\nu}$ and 1000 events in ν are also indicated by a line on each plot. In each case only 1 event could be considered outside this boundary, and is not significant considering the statistical fluctuations of the monte carlos.

In summary, no compelling evidence exists for a source of dimuon events other than charm generated by $\nu, \bar{\nu} + N$ collisions in this data. However, it is interesting to attempt to place an upper limit on the mixing angles of b-quarks. If one assumes that all events with P_{out} larger than 2 GeV and P_{TW} larger than 3 GeV are due to b-quark production, it is then possible to contrive a limit on the b-quark mixing angles subject to further assumptions about the nucleon quark context.

If events with $E_{\text{vis}} > 100$ GeV and with $P_{\text{out}} > 2$ GeV, $P_{\text{tw}} > 3$ GeV in ν , $\bar{\nu}$ are ascribed to b-quark production and decay, these events constitute about 1% of the ν and 2% of the $\bar{\nu}$ events, removing a residual 1-2% charm contribution. In b-quark production, at most 10% of the resulting 2μ signal is above these limits in P_t , implying a b-quark dimuon signal of 10% in ν and 20% in $\bar{\nu}$, above 100 GeV under the assumption given above. This is unlikely, but compatible with the shapes of distributions shown previously. If this b-quark signal were true, it implies that

$$\frac{\sigma(\bar{\nu}u \rightarrow b\bar{\mu}) + \sigma(\bar{\nu}c \rightarrow b\bar{\mu})}{\sigma(\bar{\nu}N \rightarrow \bar{\mu})} B(b \rightarrow \mu + x) \frac{1}{\epsilon} \lesssim$$

$$(6.6 \times 10^{-3}) \times 20\%,$$

with $\epsilon \approx 3$ for b relative to c production $B \approx 0.1$, the muonic branching ratio of b. If $c\bar{c}$ is negligible in the ocean, then the above implies that

$$g_{\mu b}^2 < 0.04$$

$$g_{\mu b} < 0.2$$

where g_{ub} is the u-b coupling strength relative to G_F . This is a factor of 2 larger than known limits on g_{ub} , ruling this possibility out.

If the ocean contains $c\bar{c}$ pairs, then

$$\frac{\sigma(\nu\bar{c} \rightarrow b\mu)}{\sigma(\nu N \rightarrow \mu)} \cdot B(\bar{b} \rightarrow \mu + x) \frac{1}{\epsilon} \lesssim (6 \times 10^{-3}) \times 10\%$$

implying that

$$g_{cb}^2 \lesssim 0.02/(C/D)$$

where g_{cb} is the c-b coupling strength and \bar{c} , D the integrated c,d densities. Since $g_{cb}^2 \lesssim 0.5$ from known limits, then setting $g_{cb}^2 = 0.5$ gives $C/D \lesssim 0.04$. If $g_{cb}^2 < 0.5$, C/D can grow proportionally. The effect in $\bar{\nu}$ is similar.

To check this possibility, charm ocean quarks give rise to like-sign dimuons via $\nu c \rightarrow \mu^- b \rightarrow c \rightarrow \mu^-$ cascades. With $B(b \rightarrow c) = 0.5$, $B(c \rightarrow \mu) = 0.1$ then $\sigma(\mu^- \mu^-)/\sigma(\mu^-) \approx (1-3) \times 10^{-4}$ depending on acceptance corrections for the cascade, and using $g_{cb}^2 = 0.5$, $C/D = 0.04$. This is barely compatible with the like-sign rates quoted by this experiment (4×10^{-4}), especially considering the possibility of $c\bar{c}$ production. However, it is interesting to note that C/D is not inconsistent with being as large as 4-5% at high energy. Note also that threshold suppression will be higher for c-b transitions than for u-b transitions since the remaining c quark must be from a charm particle.

As discussed in the first chapter, both the rate of $c\bar{c}$ production in hadronic (and presumably neutrino) collisions, and a large charm ocean are unexpected in the most simple QCD calculations, even above thresholds. However, $c\bar{c}$ production does indeed seem to occur at the 10^{-3} level in hadronic collisions, and it would be interesting if there is a relationship between $c\bar{c}$ production and a charm ocean. Finally, comparison with muon induced multimuon events⁵⁸ may shed light on this problem, since muons couple as the square of the quark charges via a neutral current (i.e. photon) while neutrino reactions treat quarks equally (up to threshold effects), and in charged currents, change their flavor.

4.5 Discussions and Conclusions

This experiment measured properties and relative rates of opposite sign dimuon production by neutrinos and antineutrinos. No conclusive evidence for any prompt source for these events other than weak charm production and decay (with background) was found. However it is still possible that b-quark production or other phenomena occur at the 10-20% level of the dimuon signal.

The data and its interpretation raise many questions:

1. What is the proper explanation for the charm fragmentation function, if it is flat as appears in the data, and can it be calculated? Does it have bearing on the properties of hadronic $c\bar{c}$ production?
2. What are the effects of including more sophisticated quark density parametrizations, with Q^2 and energy dependencies as would be expected in QCD calculations?
3. What is the charm sea, if any, and how does it relate to other phenomena? What is the symmetry breaking in the sea, and how is it related to quark masses?
4. Can $c\bar{c}$ production or neutral current direct muon production be distinguished from charm in opposite sign dimuon events? Are there better ways to extract b-quark production?

(and so on.) Perhaps some of these questions can be answered with higher statistics experiments; certainly the other multilepton topologies and other experimental techniques (eg. bubble chambers) are important to these questions; different reactions (eg. μN)⁵⁸ also bear on these questions. Finally, at higher energies, we may look forward to interesting dimuon data with neutrino beams and nucleon targets of many flavors.

LIST OF TABLES

Chapter 4

- 4.3.1. Unnormalized chi-squared: charm-data
- 4.3.2 Average values of variables with data, and charm predictions
- 4.4.1. Average values of quantities from b-quark and L^0 monte carlos

LIST OF FIGURES

Chapter 4

- 4.3.1 Schematic definition of $\Delta\phi$.
- 4.3.2,3 $\Delta\phi$ distribution for $\nu, \bar{\nu}$ showing π, K decay and the effect of 2 z-distributions.
- 4.3.4,5 α distributions for neutrino and anti-neutrino.
- 4.3.6 Schematic definition of P out.
- 4.3.7,8 P out distributions for neutrino and anti-neutrino.
- 4.3.9 Schematic definition of $P_{tW}, \Delta\phi_W$.
- 4.3.10,11 P_{tW} distributions for neutrino and anti-neutrino.
- 4.3.12,13 $\Delta\phi_W$ distributions for $\nu, \bar{\nu}$.
- 4.3.14,15 m_{12} distributions for $\nu, \bar{\nu}$.
- 4.3.16,17 z_{μ_2} distributions for $\nu, \bar{\nu}$.
- 4.3.18 z distributions for several parametrizations of z .
- 4.3.19-26 $x_{vis}, y_{vis}, Q_{vis}^2, W_{vis}^2$ distributions for neutrino and antineutrino (by pairs).
- 4.3.27,28 R^ν, \bar{R}^ν ; the dimuon to single muon rates for $\nu, \bar{\nu}$ as functions of energy.
- 4.3.29 R_2 , the ratio of ratios \bar{R}^ν / R^ν as a function of E_{vis} .
- 4.4.1-6 Monte carlo distributions for $\alpha, \Delta\phi, P$ out, $P_{tW}, m_{12}, \Delta\phi_W$, for charm, b-quark and L^0 produced dimuons.

- 4.4.7-10 Chi-squared distributions for joint monte carlos of charm with L^0 contributions (m_{12} , $\Delta\phi$) and charm with b-quark (P_{out} , P_{tw}) as functions of the % charm in the monte carlo.
- 4.4.11 Scatter plot of m_{12} vs P_{out} , showing the % of data, charm, L^0 , and b-quark expected in each bin clockwise from the upper left in each bin, assuming that each monte carlo explains the whole of each bin (refer to text). The anti-neutrino data is shown in () as events, not %.(E_{vis} 100 GeV)
- 4.4.12 Similar to 4.4.11, except P_{out} vs $\Delta\phi$. Note that the 2 events at large P_{out} have errors in P_{out} larger than the bin size shown (for convenience); the errors on P_{out} for these 2 events are about 50%. (E_{vis} 100 GeV)
- 4.4.13,14 Scatter plots P_1 vs P_2 for E_{vis} larger than 100 GeV for $\nu, \bar{\nu}$. The charm line is only approximate, having some upward concavity for a curve of equal probability. However the monte carlo indicates events fluctuate outside even this line to the 0.1% level. These low level fluctuations in the monte carlo and the data make definitive statements impossible at the 5% level.

Table 4.3.1. Unnormalized χ^2 : charm - data

variable	χ^2	ν DOF	χ^2	ν DOF
α	1.0	7	4.1	3
$\Delta\Phi$	0.8	5	1.92	3
$\Delta\Phi_w$	1.3	4	1.74	3
P_{tw}	0.4	4	0.48	3
P_{out}	1.8	6	0.9	3
m_{12}	1.6	5	4.0	5

Table 4.3.2.

Average Values of Variables Data
Charm

		ALL E		E > 100	
		ν	ν	ν	ν
$\Delta\Phi$	data	124.0 ± 47.3	120.0 ± 44.5	132.7 ± 43.5	128.8 ± 30.1
	charm	124 ± 47	116 ± 49	127 ± 47	123 ± 49
α	data	0.37 ± 0.45	0.26 ± 0.53	0.47 ± 0.48	0.26 ± 0.59
	charm	0.37 ± 0.42	0.27 ± 0.42	0.47 ± 0.43	0.4 ± 0.4
m_{12} (GeV)	data	2.9 ± 1.9	2.45 ± 1.32	3.6 ± 2.1	3.0 ± 1.2
	charm	3.2 ± 5.0	2.4 ± 2.7	4.0 ± 7.6	3.1 ± 4.9
P_{tw} (GeV)	data	0.81 ± 0.83	1.55 ± 2.7	0.89 ± 0.95	1.24 ± 1.0
	charm	0.75 ± 0.68	1.0 ± 0.84	0.76 ± 0.74	0.9 ± 1.0
P_{out} (GeV)	data	0.52 ± 0.75	0.65 ± 0.65	0.6 ± 0.9	0.86 ± 0.68
	charm	0.43 ± 0.39	0.60 ± 0.58	0.43 ± 0.43	0.60 ± 0.59
$\Delta\Phi_w$ (deg)	data	80.6 ± 55.3	78.6 ± 51.3	90.9 ± 55.9	96.9 ± 47.8
	charm	84 ± 53	88 ± 53	85 ± 54	91 ± 54
Z_μ	data	0.29 ± 0.18	0.35 ± 0.21	0.26 ± 0.20	0.30 ± 0.24
	charm	0.26 ± 0.17	0.29 ± 0.17	0.22 ± 0.16	0.22 ± 0.16
X_{vis}	data	0.22 ± 0.23	0.19 ± 0.20	0.20 ± 0.21	0.19 ± 0.21
	charm	0.22 ± 0.2	0.11 ± 0.11	0.23 ± 0.24	0.14 ± 0.17
Y_{vis}	data	0.59 ± 0.22	0.59 ± 0.22	0.58 ± 0.24	0.63 ± 0.22
	charm	0.60 ± 0.20	0.64 ± 0.22	0.58 ± 0.24	0.62 ± 0.23

		ALL E		E > 100	
		ν	ν	ν	ν
Q^2 (GeV ²)	data	28.7 \pm 41.0	20.3 \pm 58.2	37.6 \pm 49.0	30.6 \pm 39.6
	charm	27 \pm 36	11 \pm 13	37 \pm 14	21 \pm 20
W^2 (GeV ²)	data	104.9 \pm 95.9	77.8 \pm 78.3	136.0 \pm 113.1	122.0 \pm 51.9
	charm	101 \pm 72	93 \pm 66	137 \pm 80	146 \pm 73
E_{vis} (GeV)	data	122.9 \pm 61	96.2 \pm 39.3		
	charm	114 \pm 60	90 \pm 50		
EH (GeV)	data	53.8 \pm 41.8	38.9 \pm 31.5		
	charm	53 \pm 41	41 \pm 33		
P1 (GeV)	data	51.2 \pm 45.2	37.1 \pm 25.6		
	charm	46 \pm 40	34 \pm 29		
P2 (GeV)	data	19.2 \pm 19.8	20.3 \pm 20.3		
	charm	15 \pm 12	15 \pm 14		
Θ_1 (mrad)	data	73.6 \pm 49.2	88.6 \pm 69.7		
Θ_2 (mrad)	data	67 \pm 48.5	80.9 \pm 62.4		
PT ₁ beam	data	2.8 \pm 2.4	2.5 \pm 2.4		
PT ₂ beam	data	0.96 \pm 0.93	1.35 \pm 1.5		

Table 4.4.1. b-quark, L^0 Average Monte Carlo Values $E > 100$ GeV

	b-quark	L^0
M_{12} (GeV)	3.3 ± 2.0	1.3 ± 0.8
Φ (deg)	105 ± 51	48 ± 44
α	0.38 ± 0.45	0.0 ± 0.4
P_{out} (GeV)	0.89 ± 0.7	0.89 ± 0.85
Φ_w (deg)	87 ± 52	36 ± 37
P_{tw} (GeV)	1.4 ± 0.8	2.8 ± 6
Z_{μ^2}	0.21 ± 0.16	N.A.

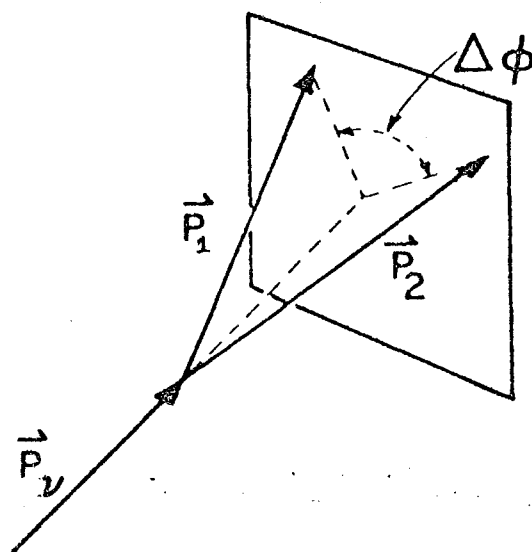


Figure 4.3.1

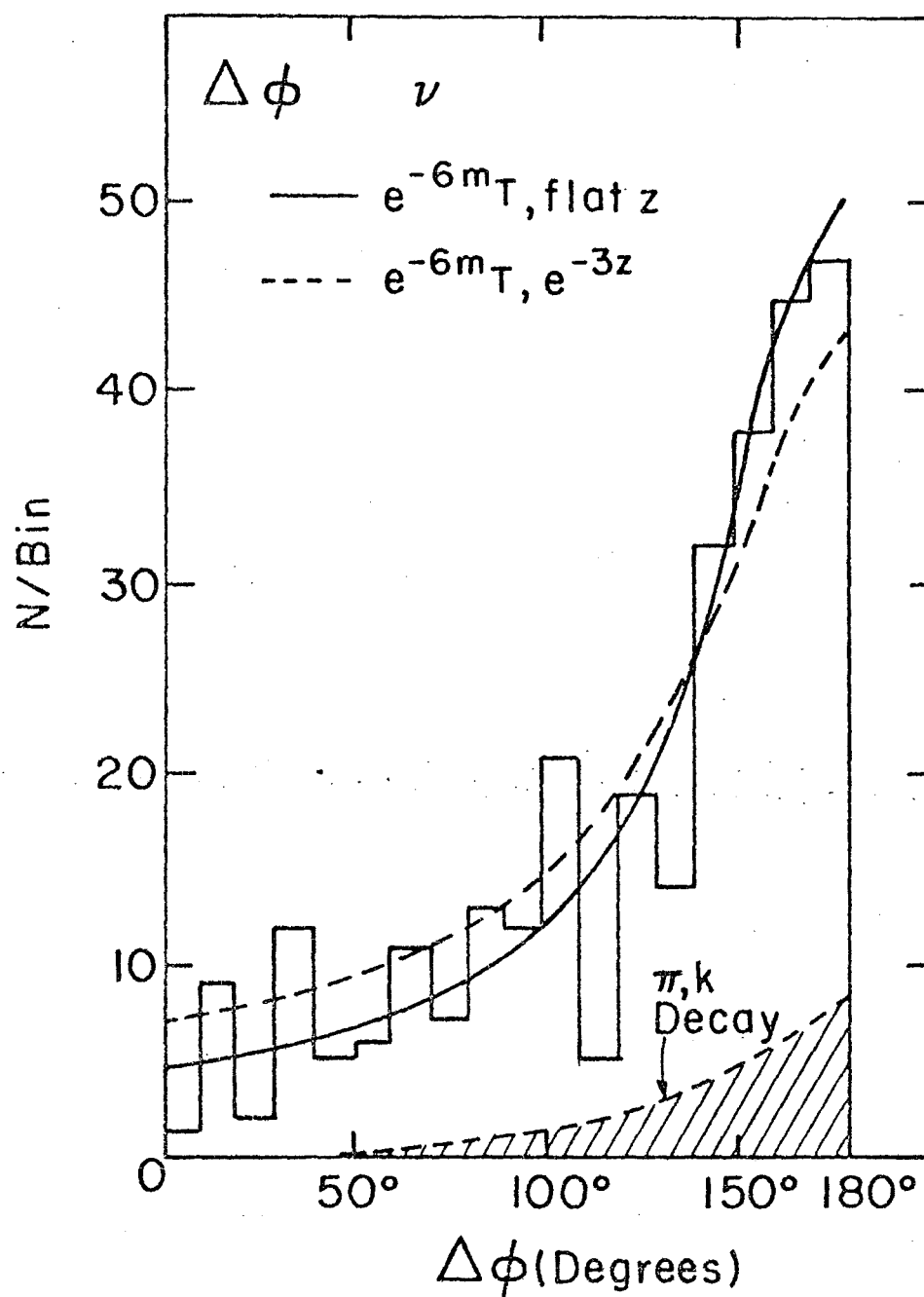


Figure 4.3.2

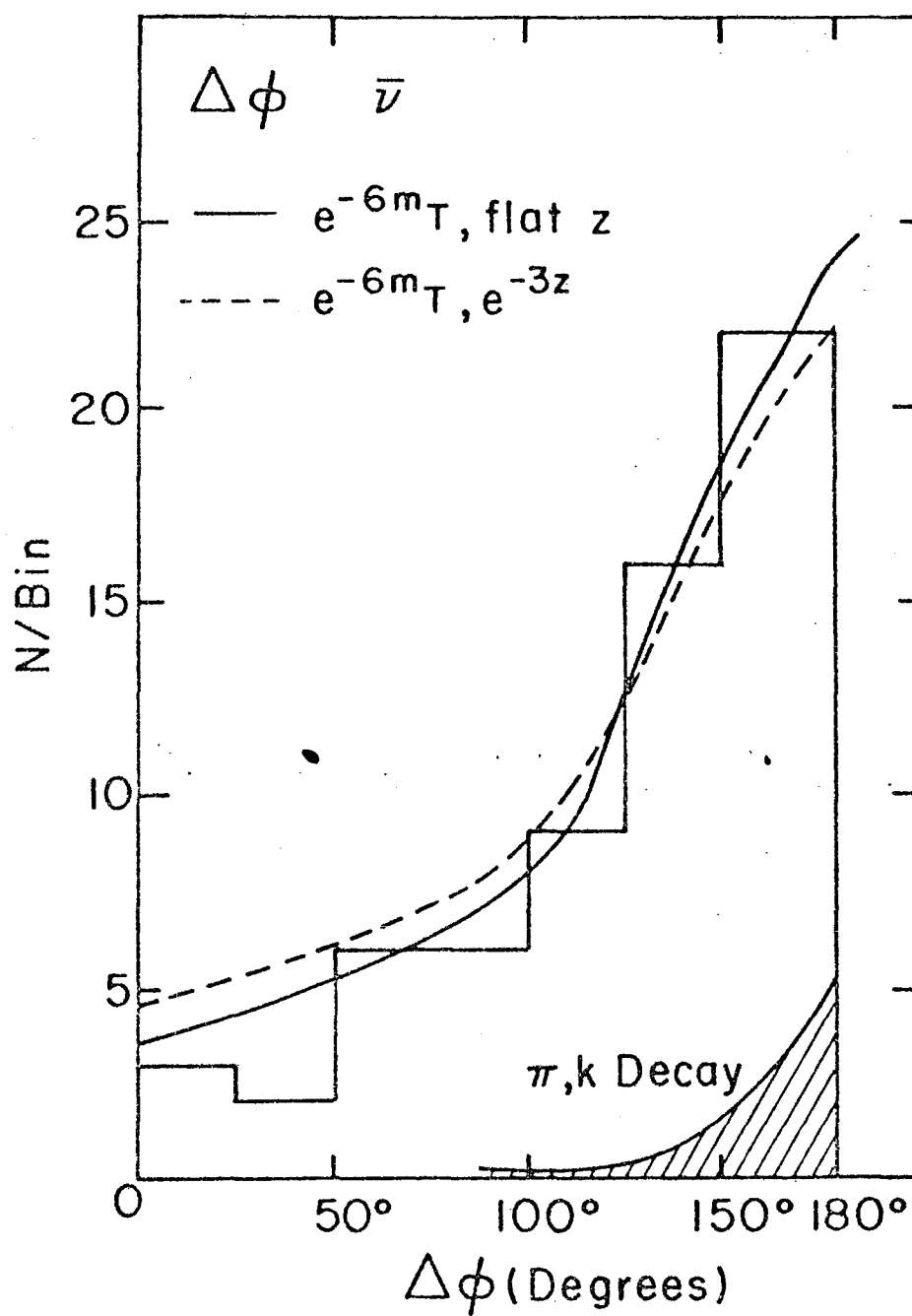


Figure 4.3.3

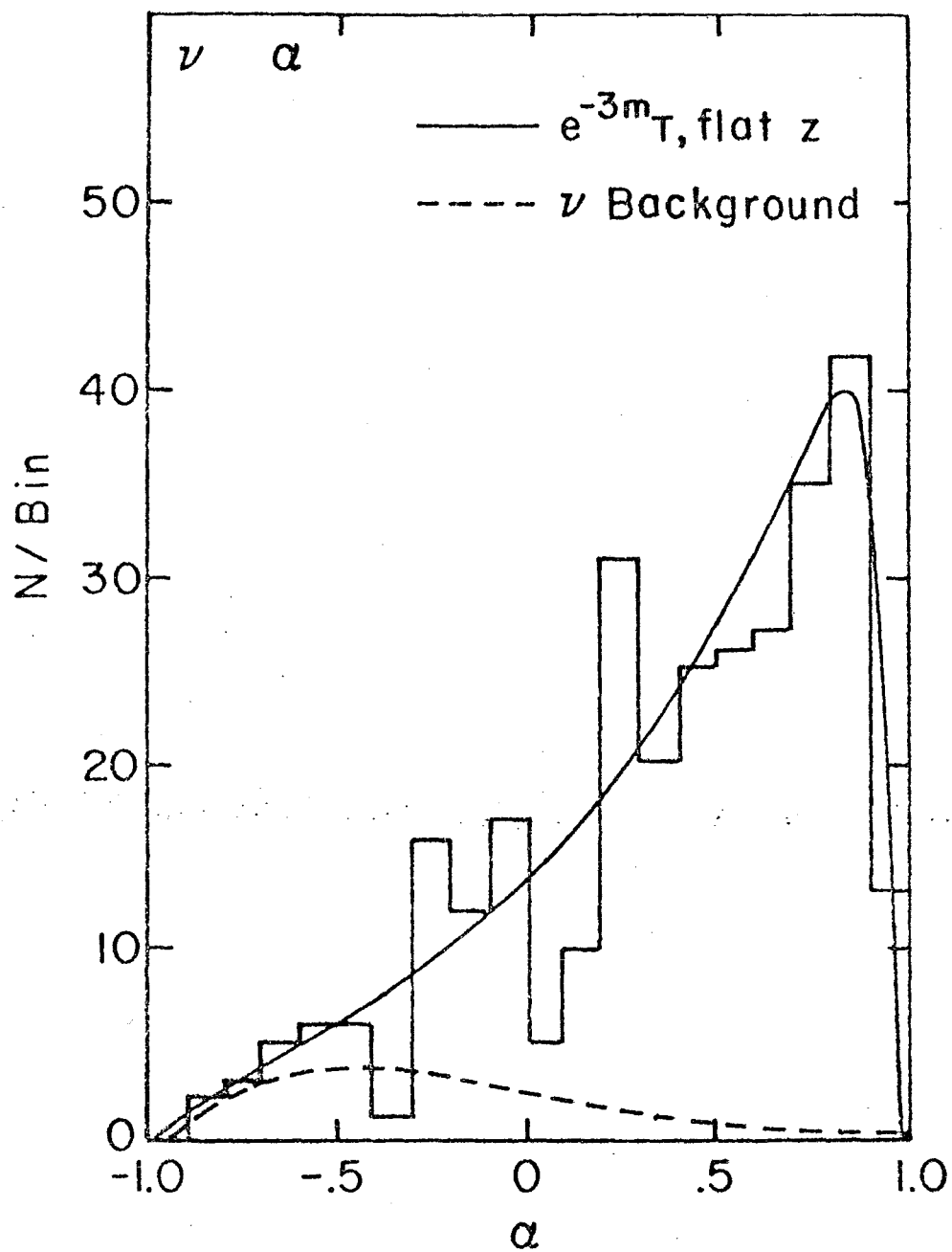


Figure 4.3.4

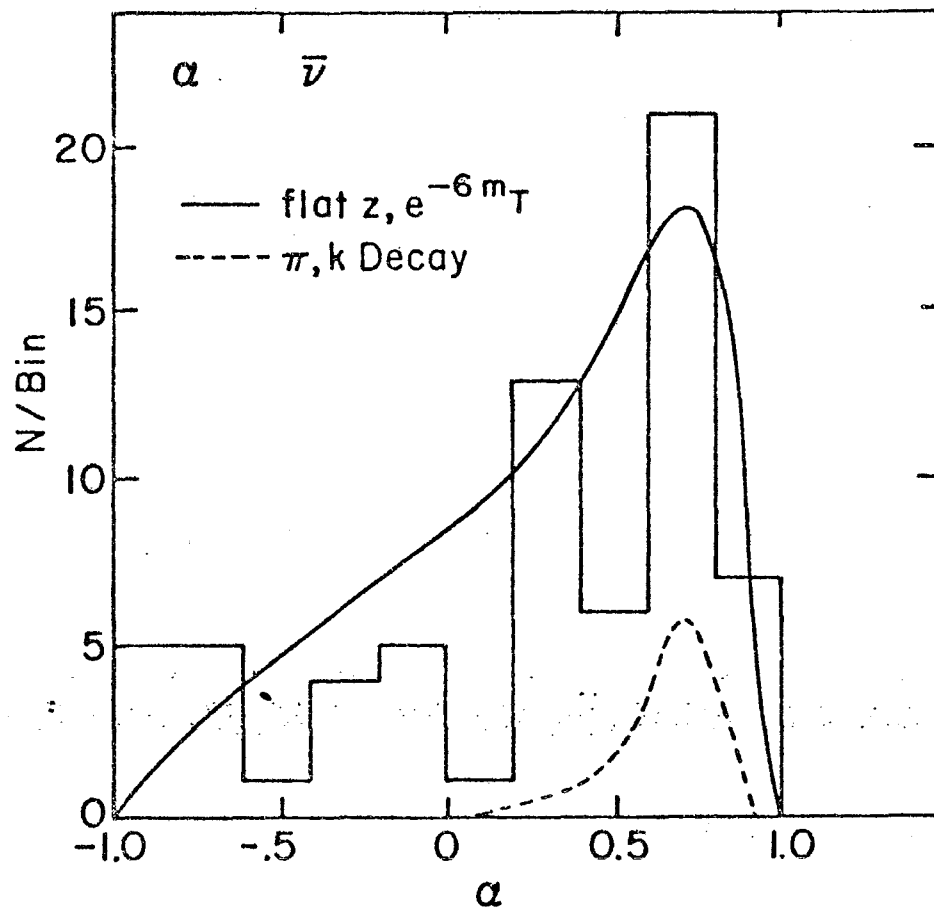


Figure 4.3.5

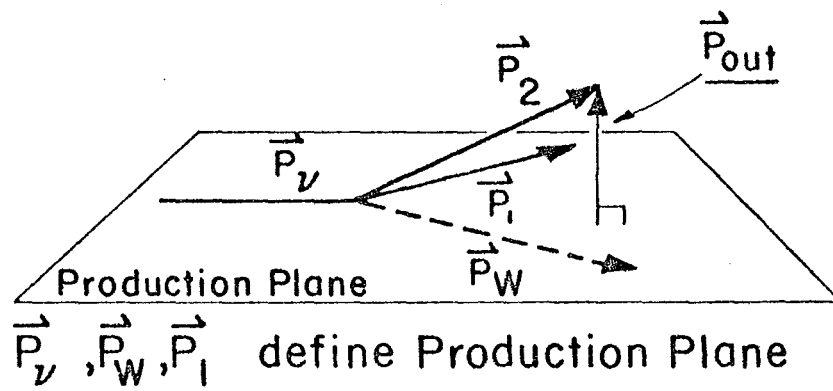


Figure 4.3.6

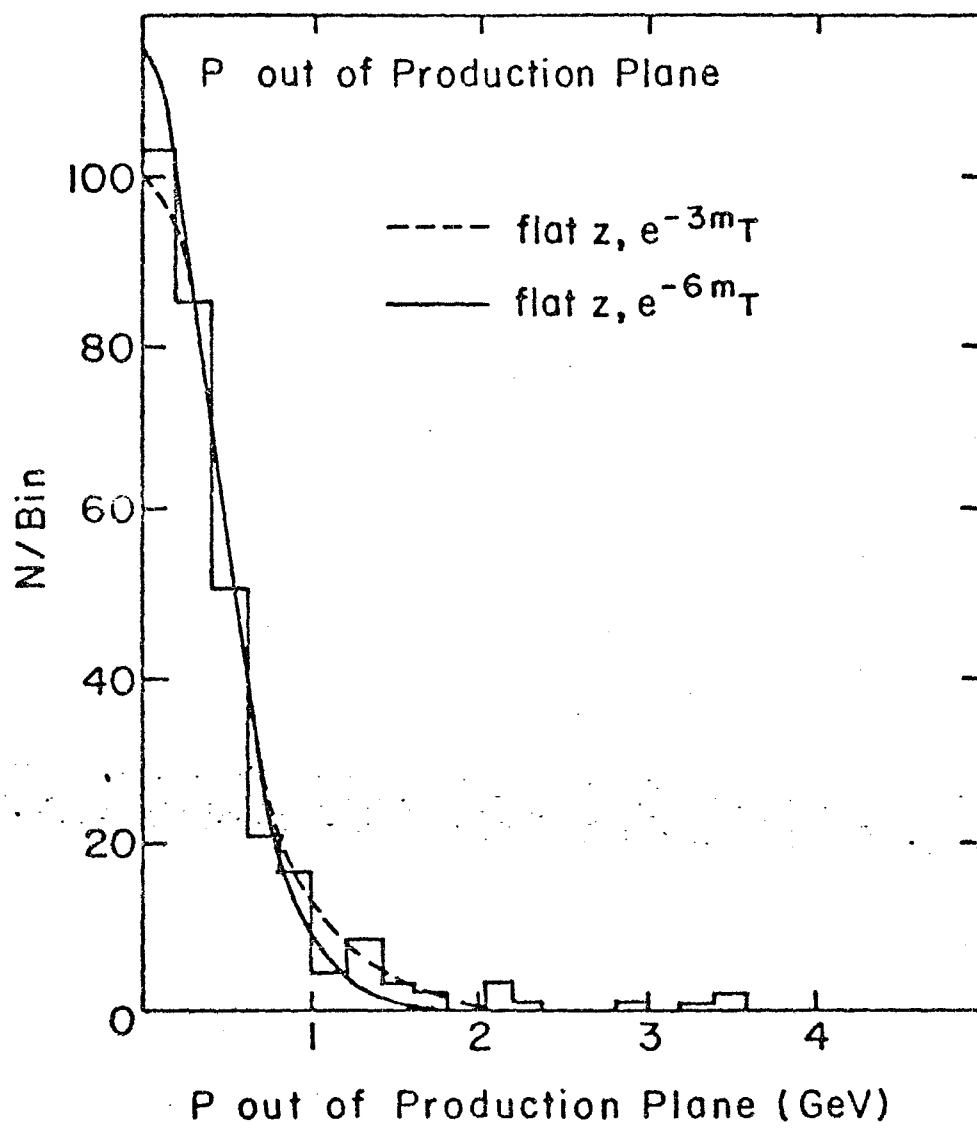


Figure 4.3.7

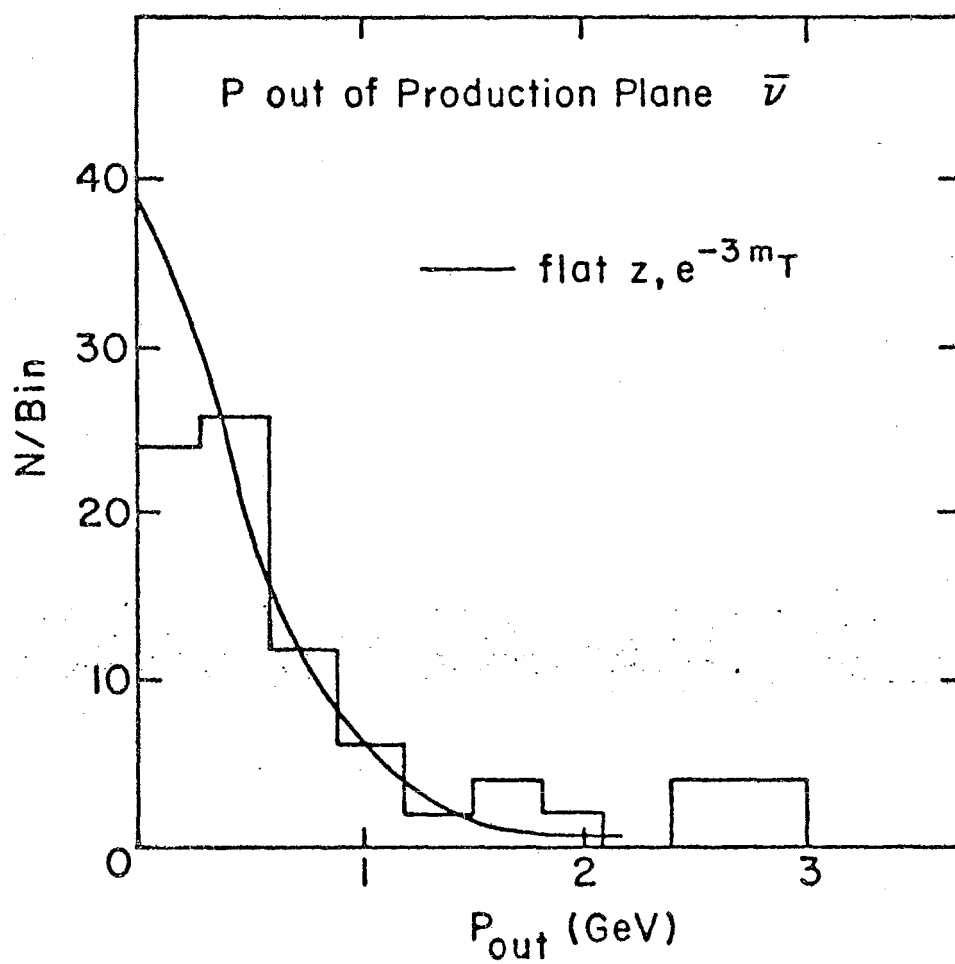


Figure 4.3.8

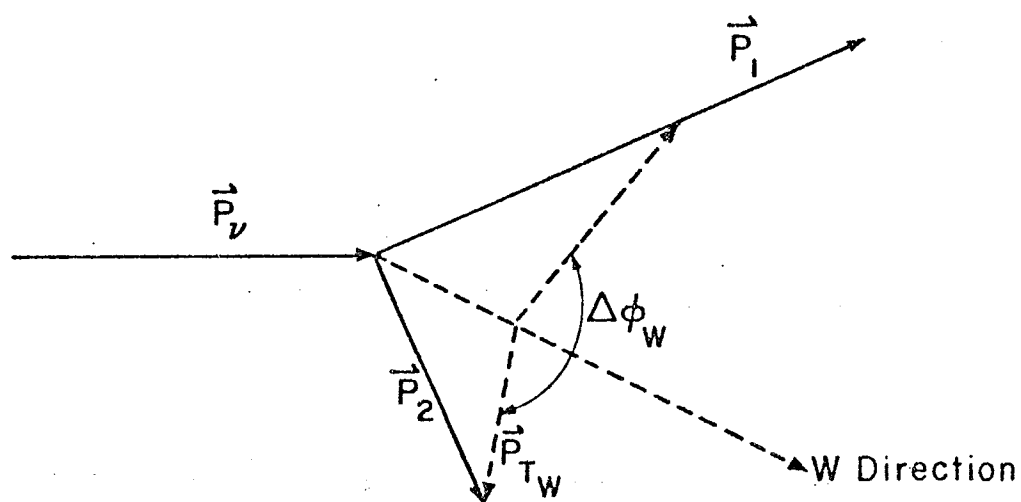


Figure 4.3.9

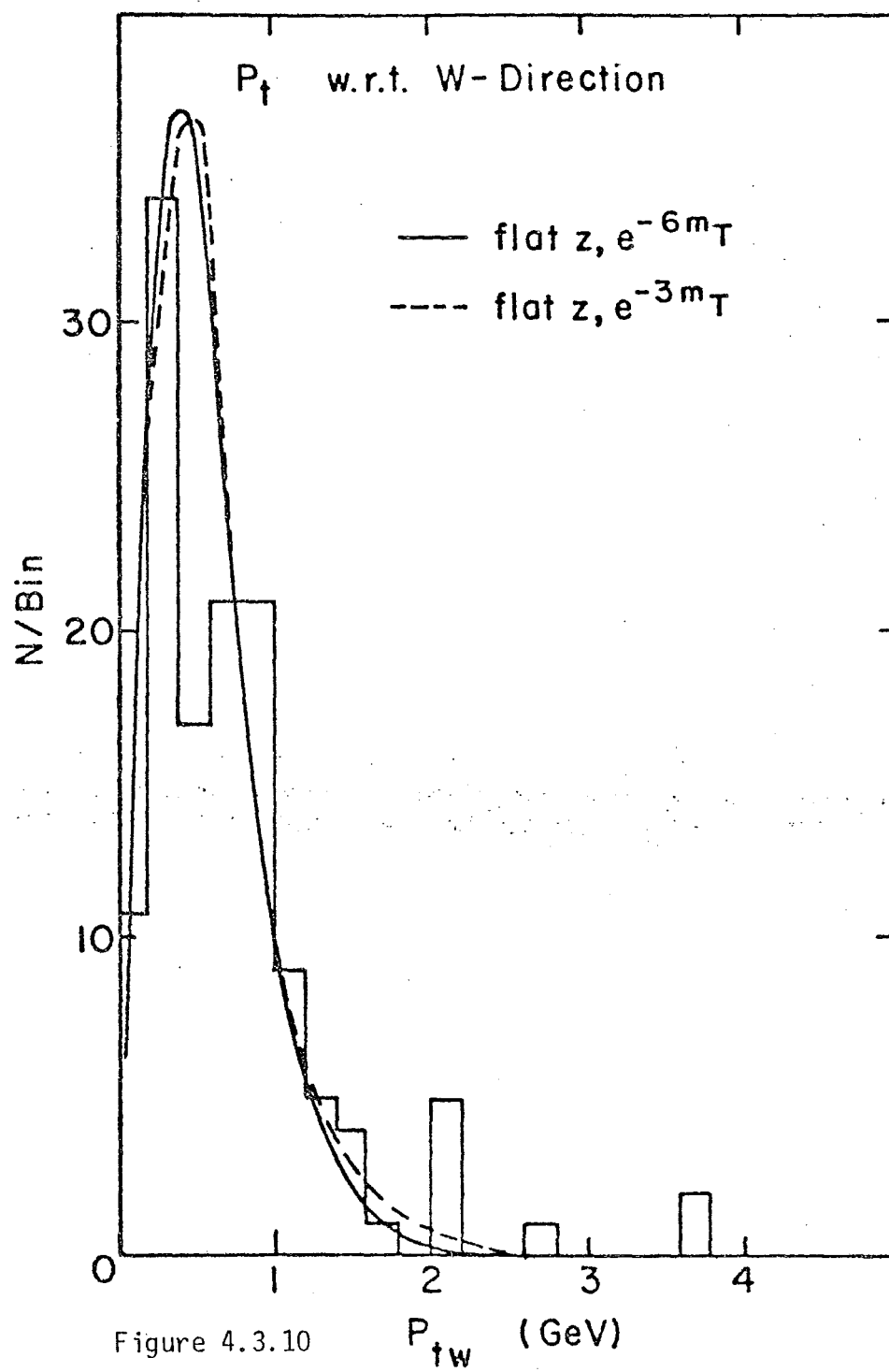


Figure 4.3.10

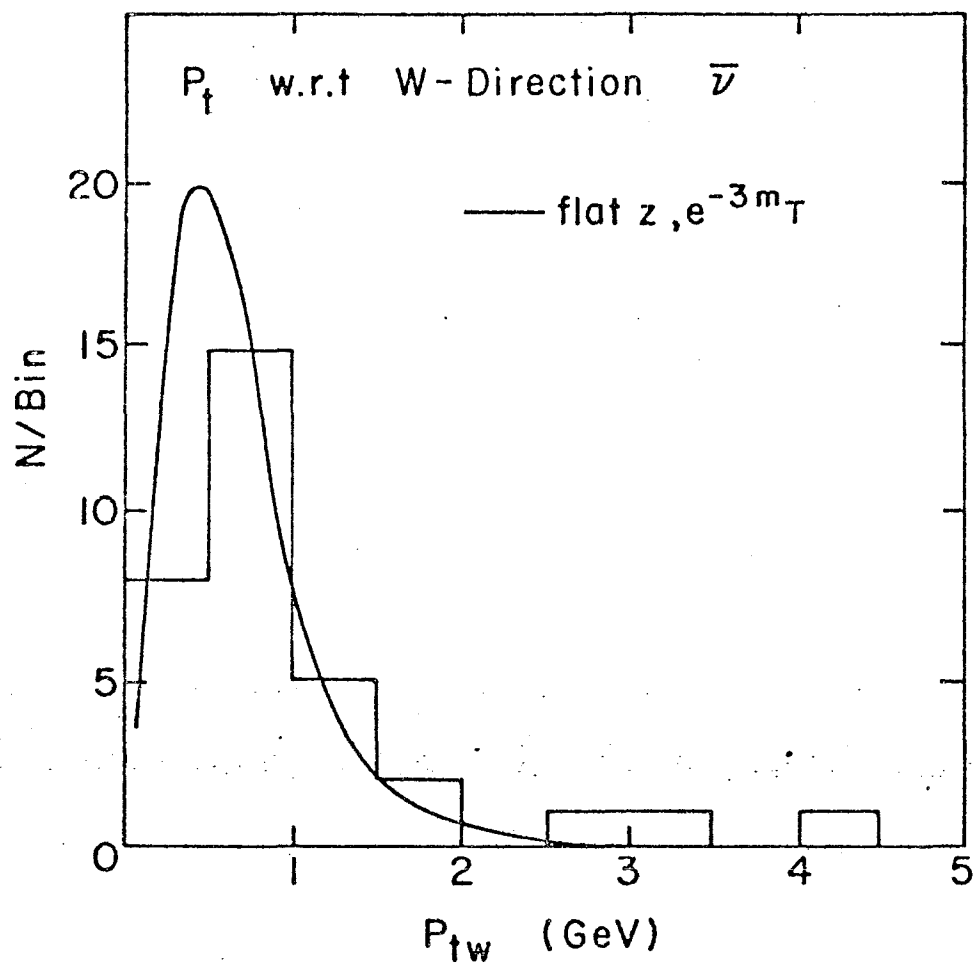


Figure 4.3.11

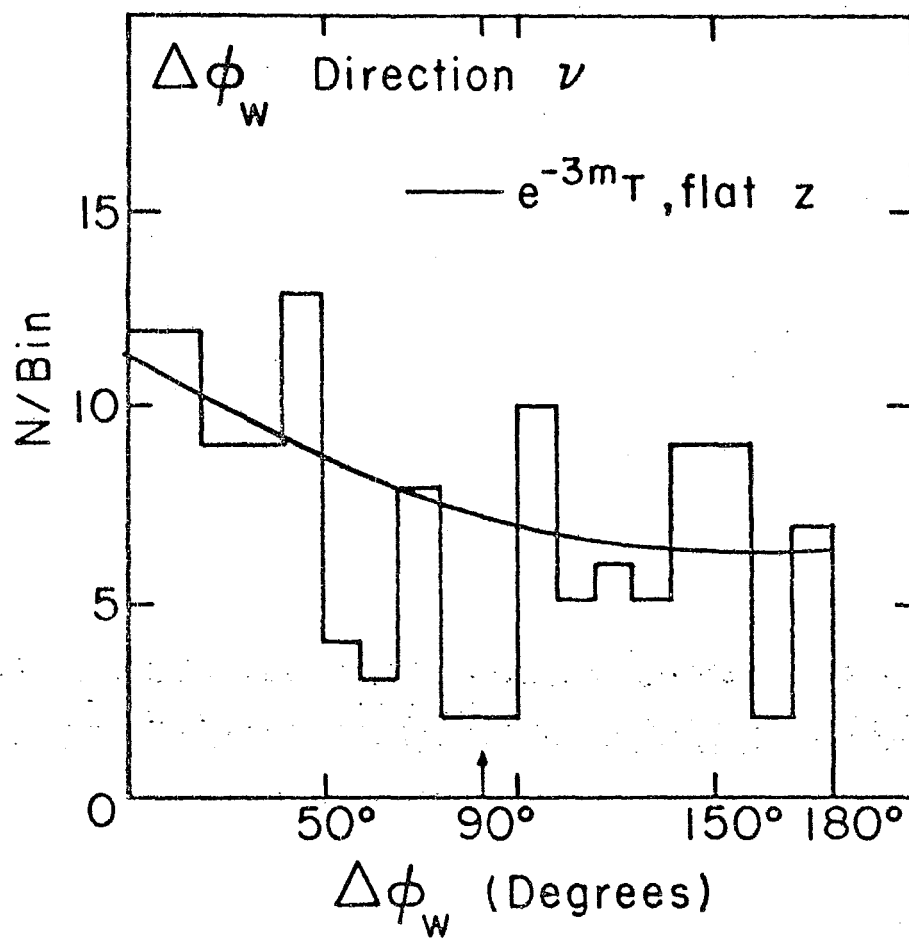


Figure 4.3.12

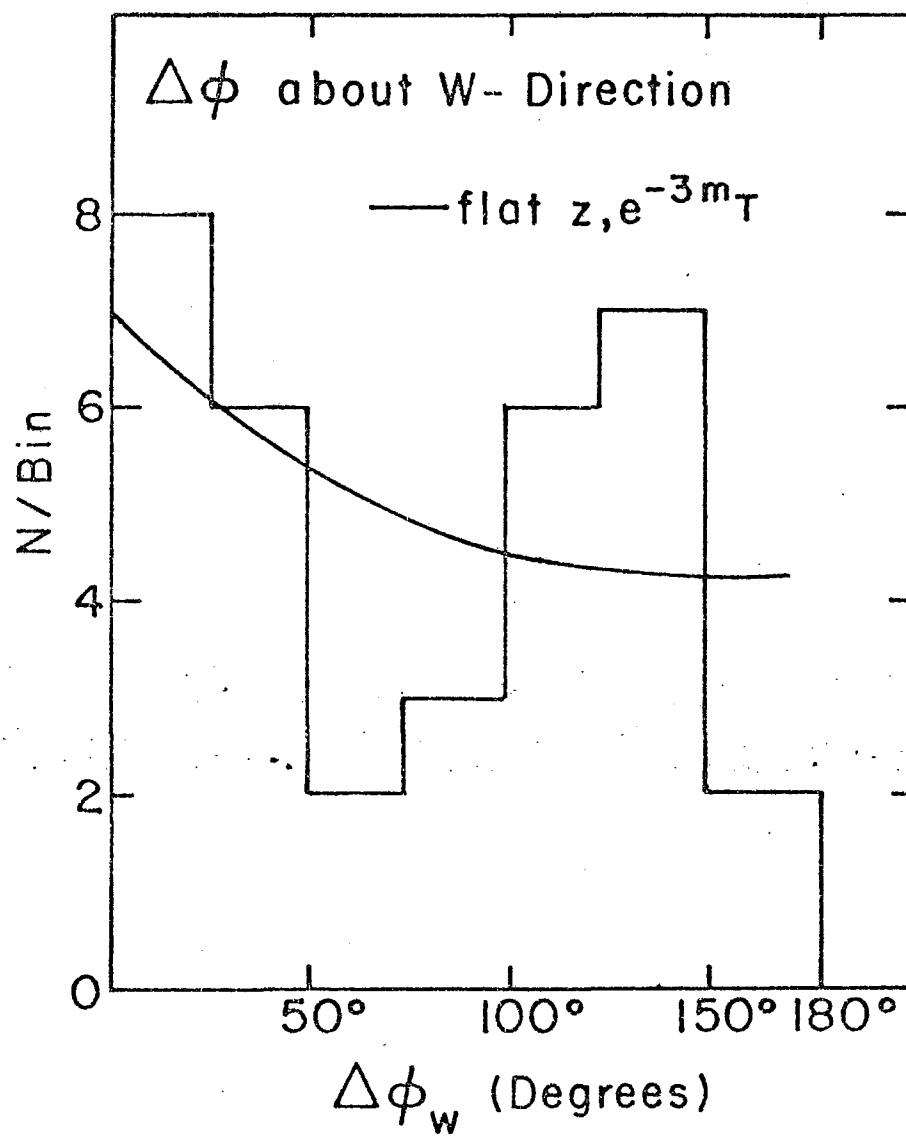


Figure 4.3.13

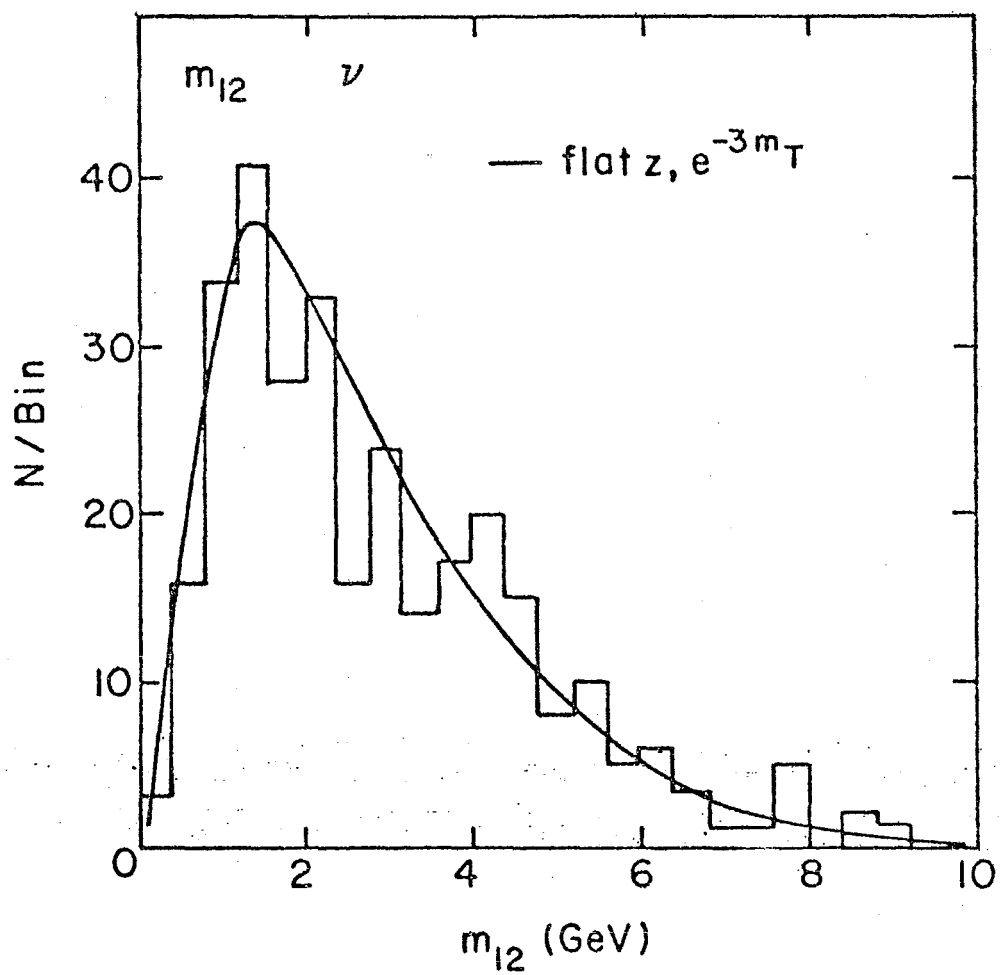


Figure 4.3.14

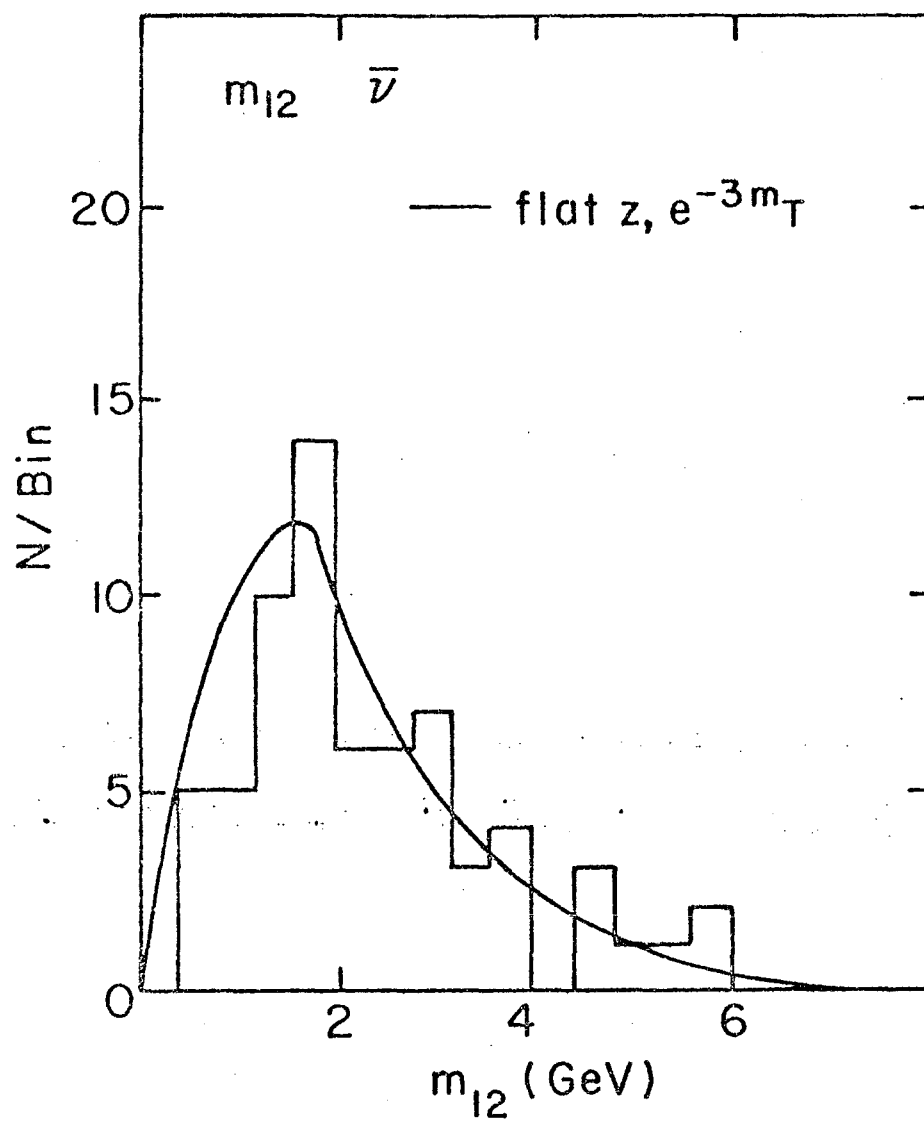


Figure 4.3.15

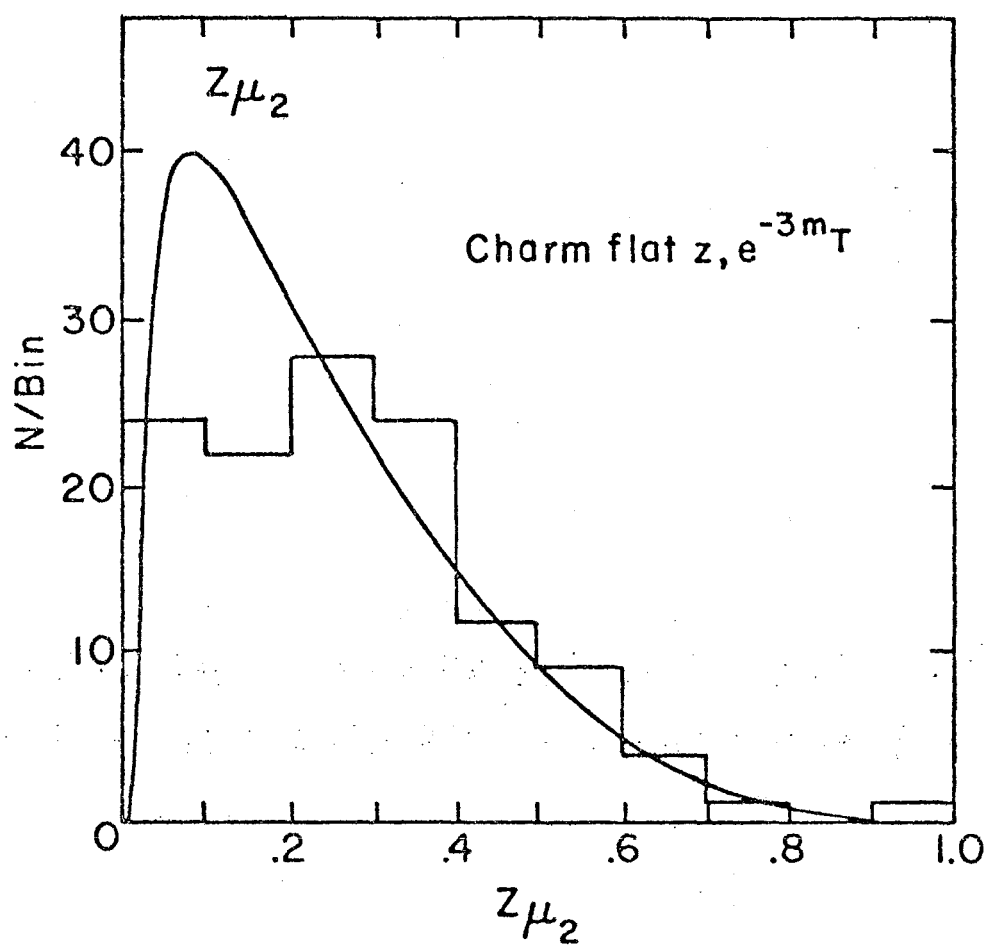


Figure 4.3.16

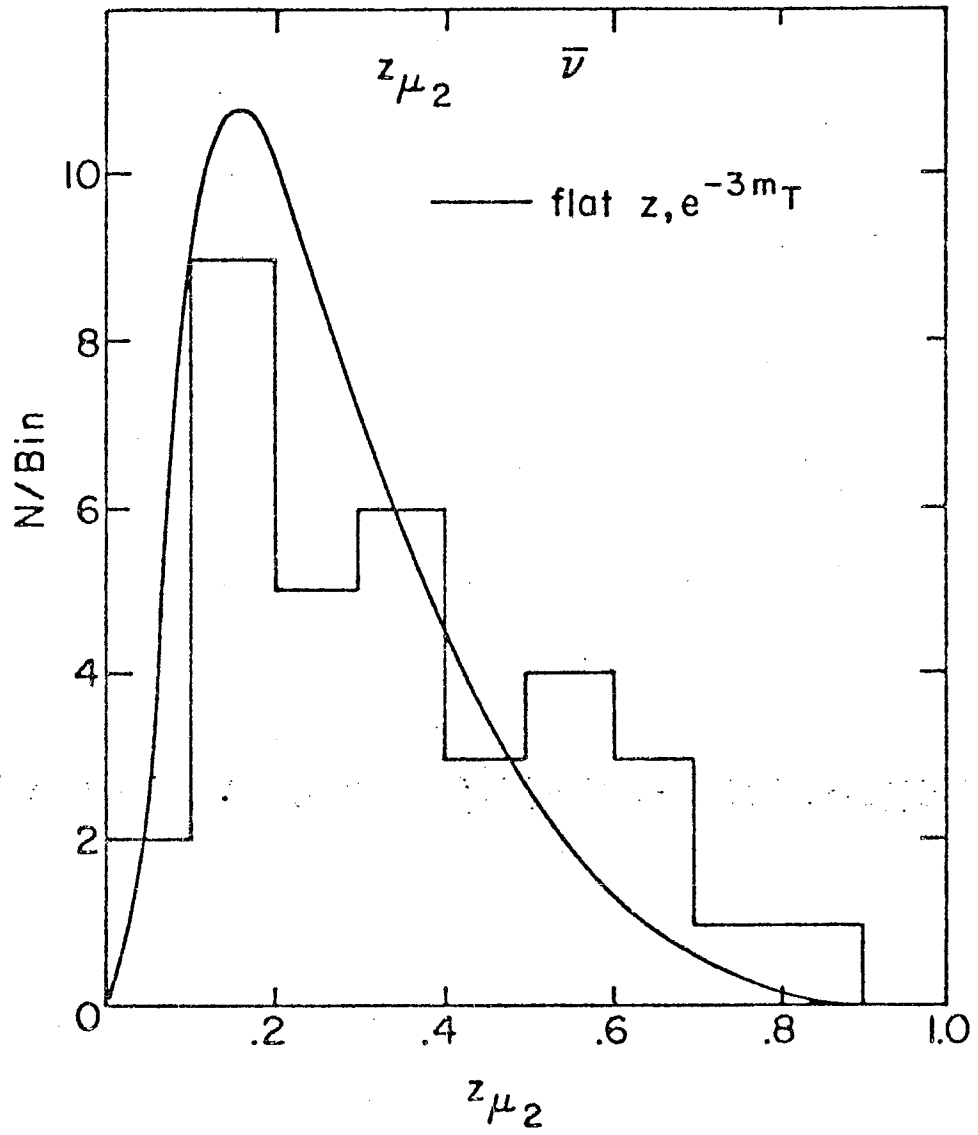


Figure 4.3.17

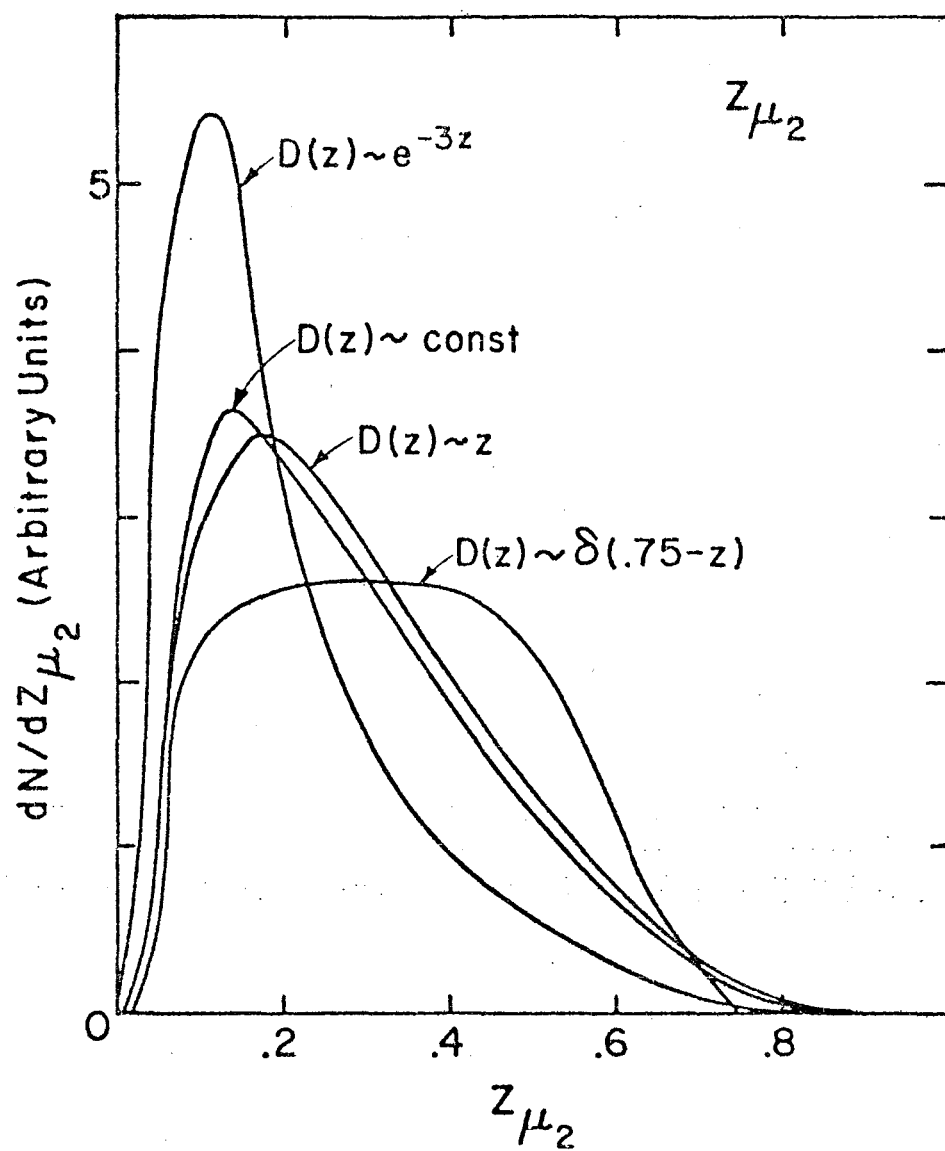


Figure 4.3.18

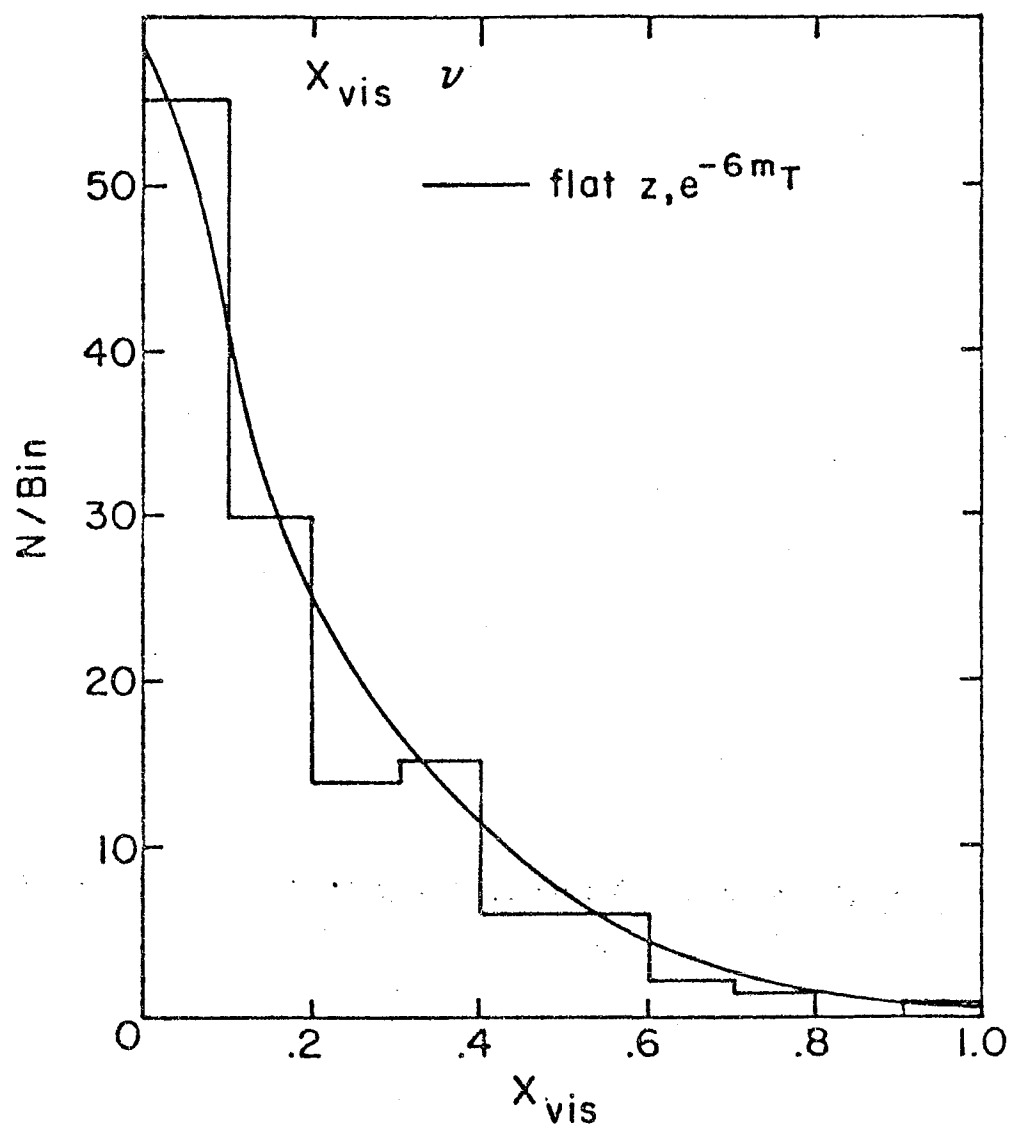


Figure 4.3.19

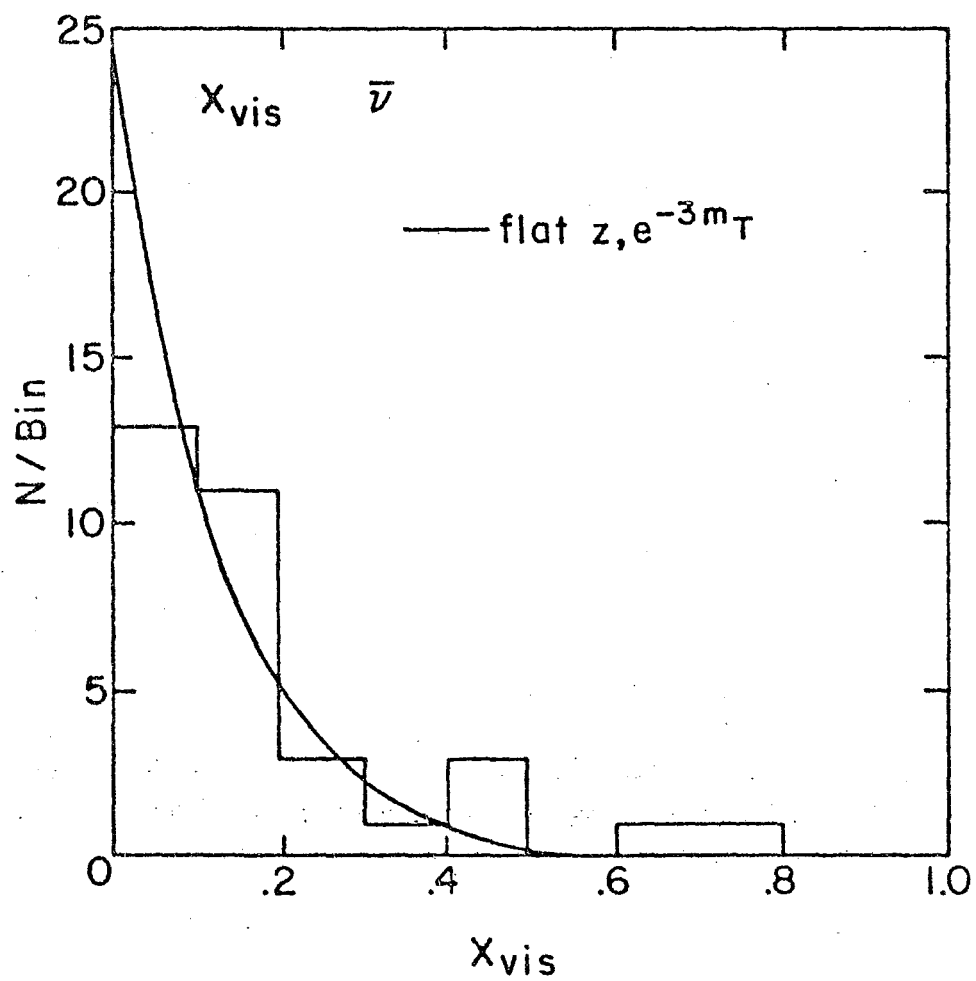


Figure 4.3.20

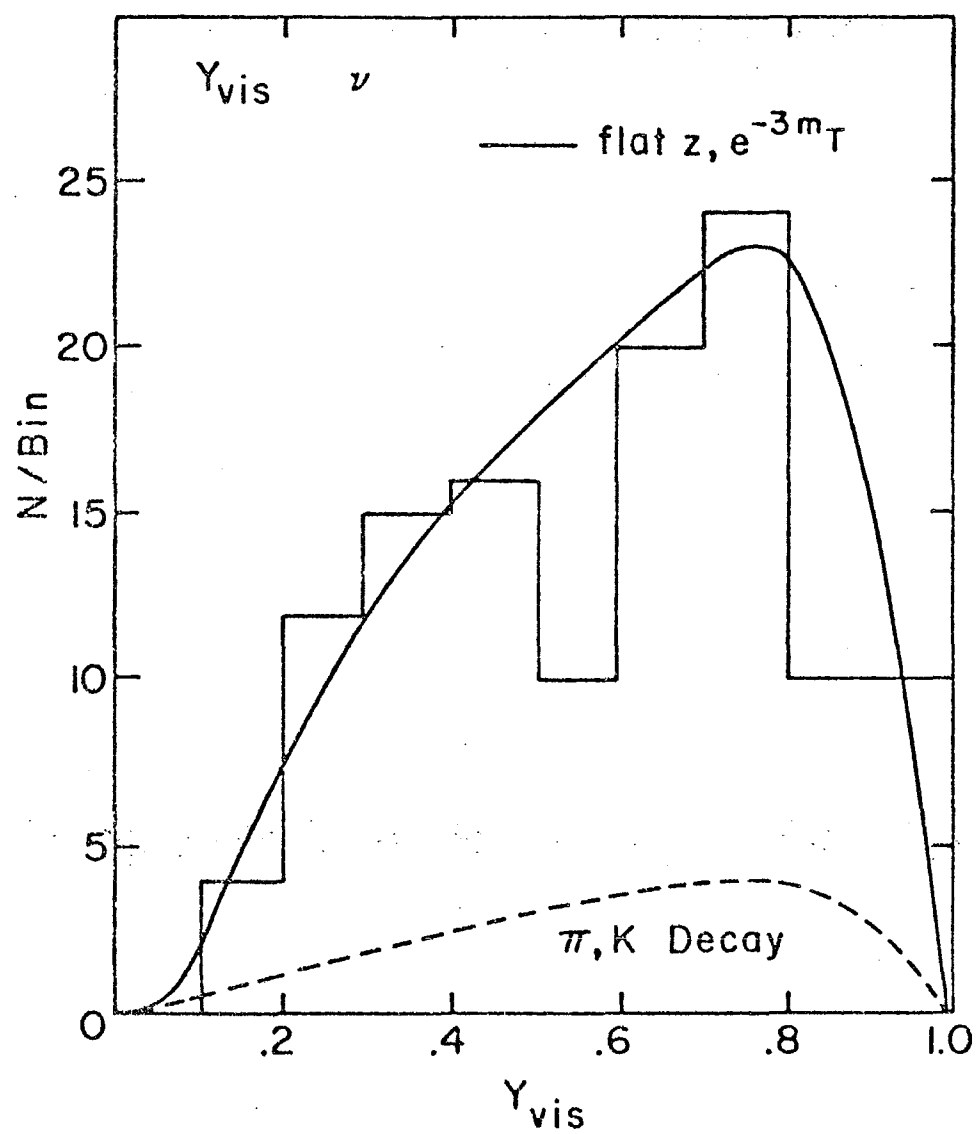


Figure 4.3.21

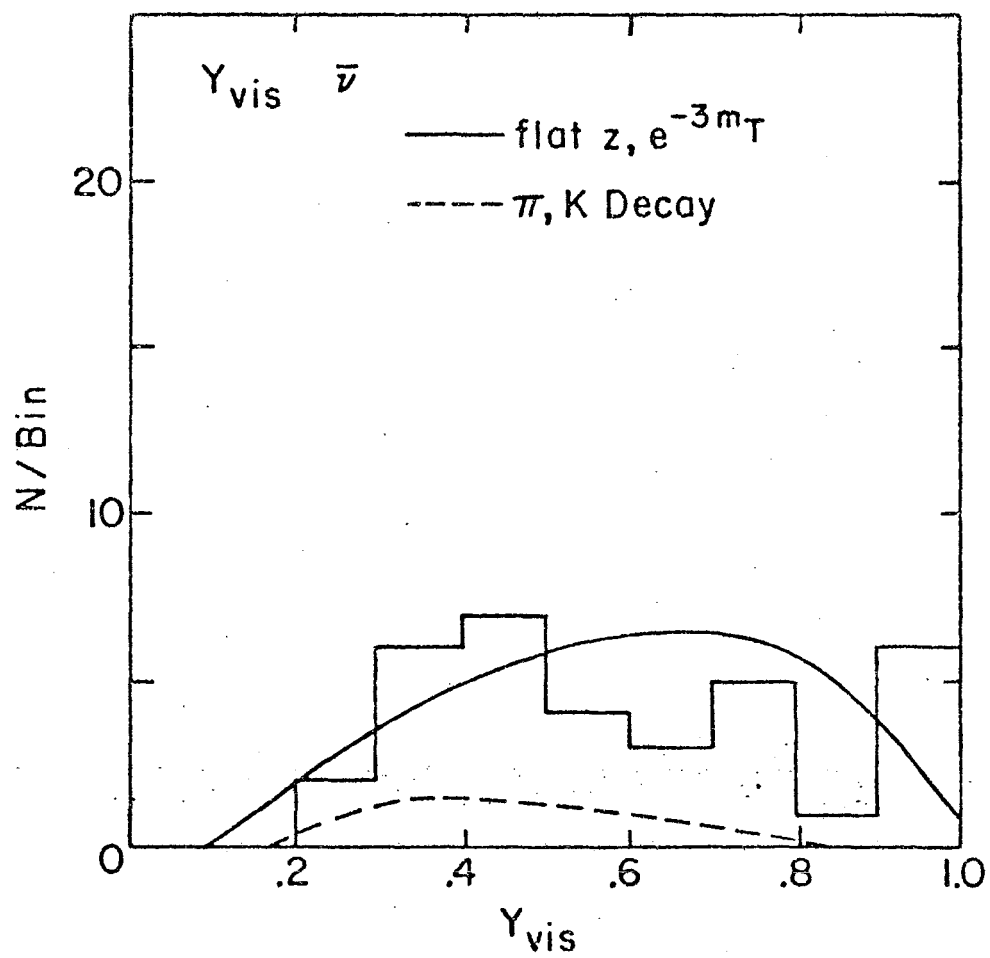


Figure 4.3.22

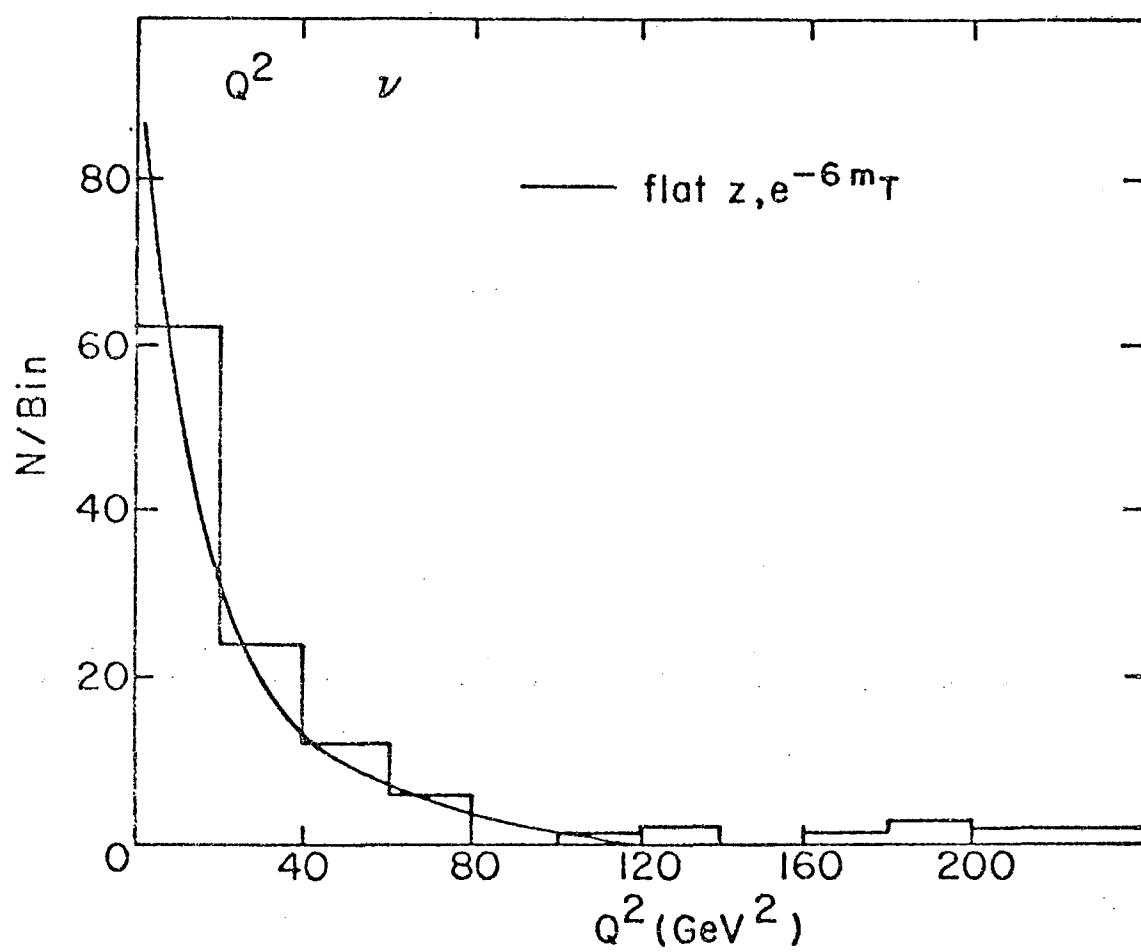


Figure 4.3.23

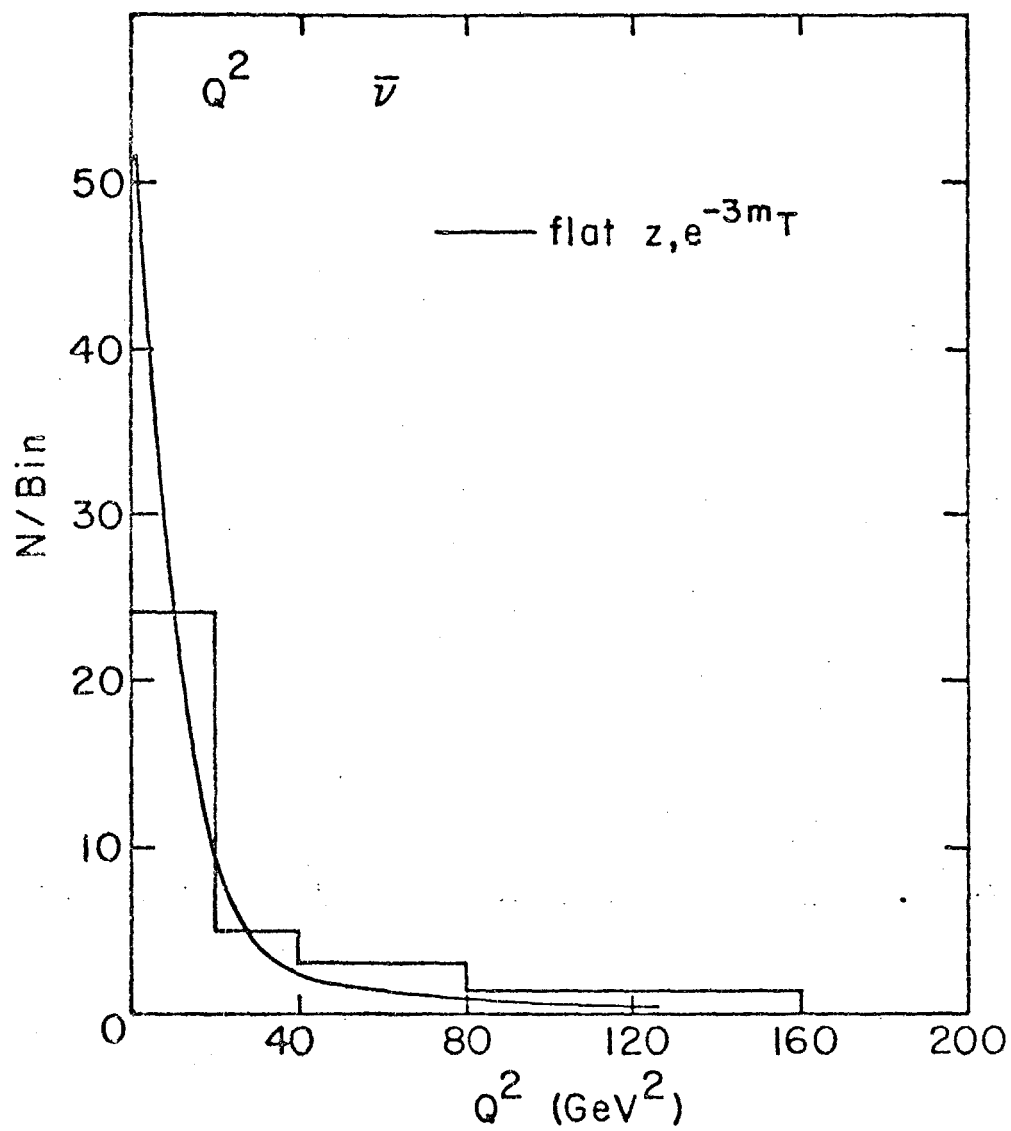


Figure 4.3.24

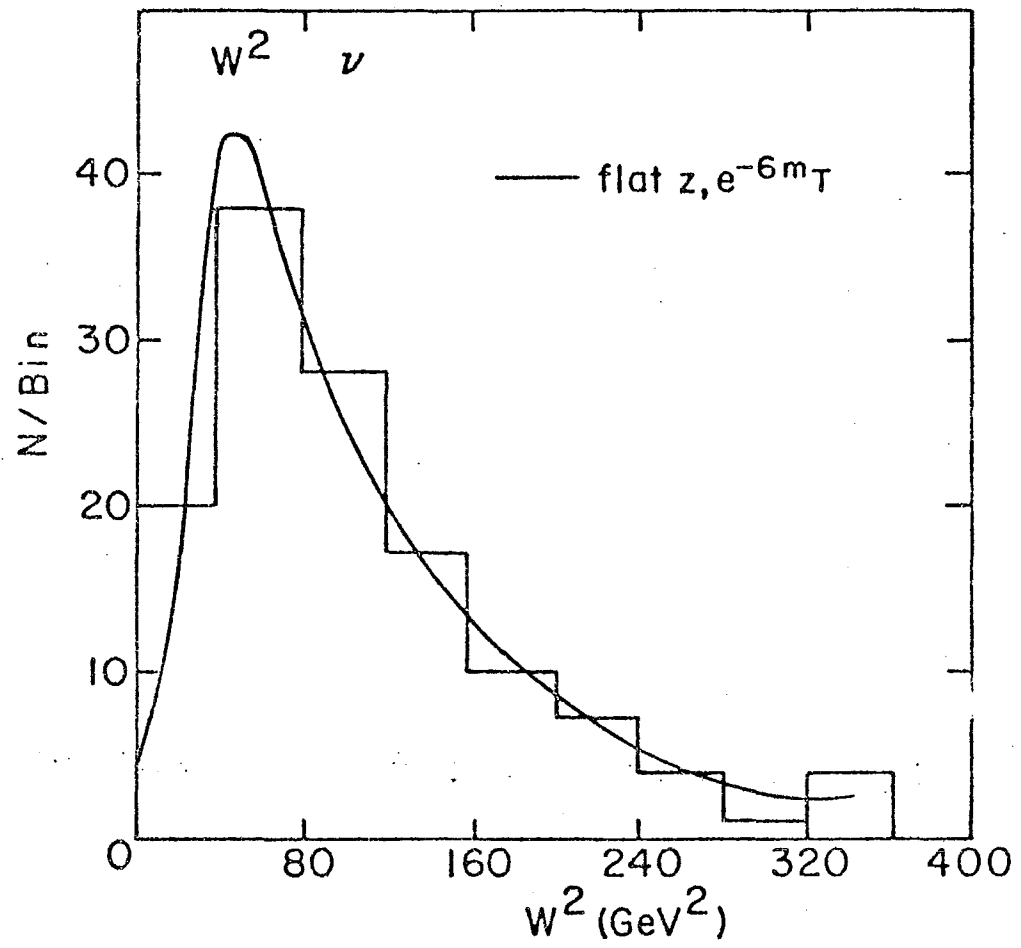


Figure 4.3.25

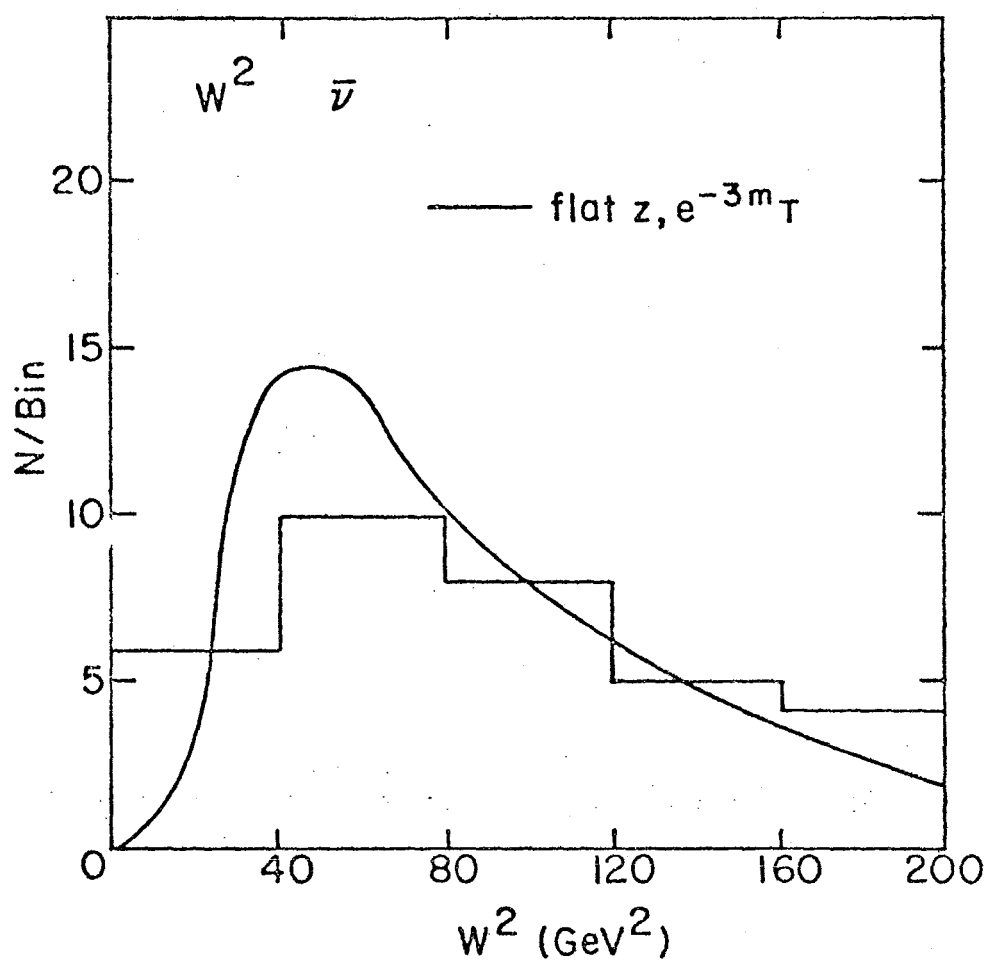


Figure 4.3.26

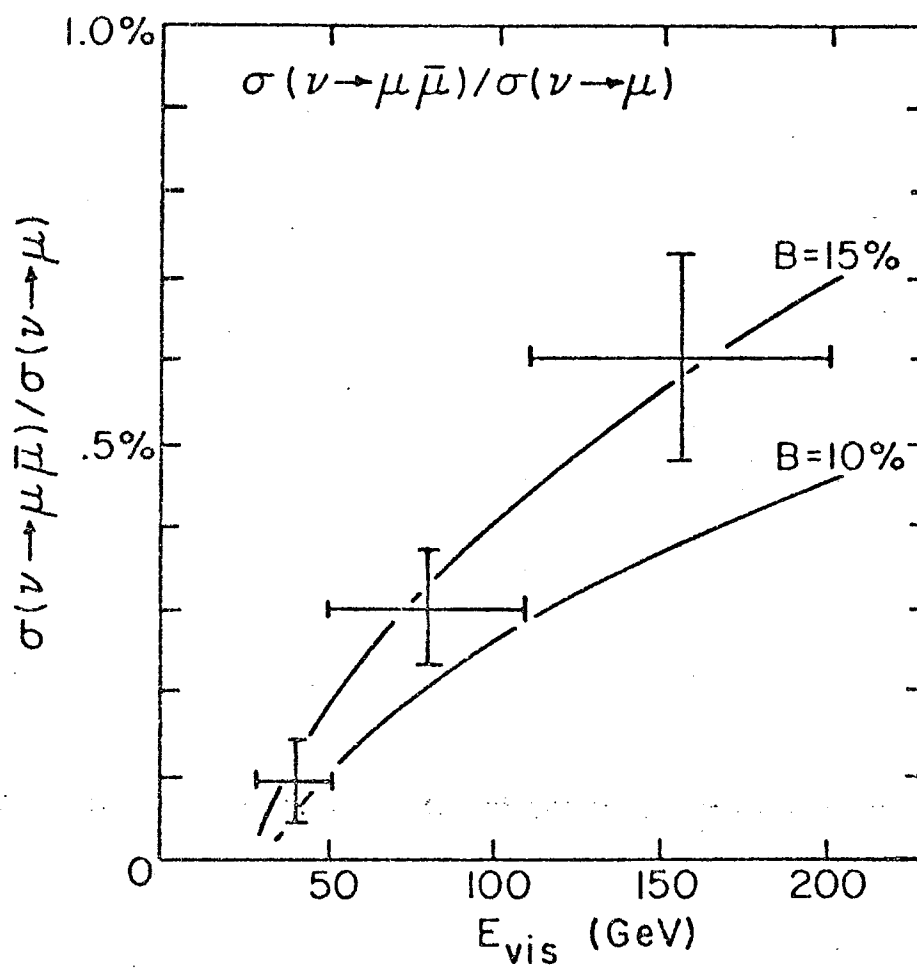


Figure 4.3:27

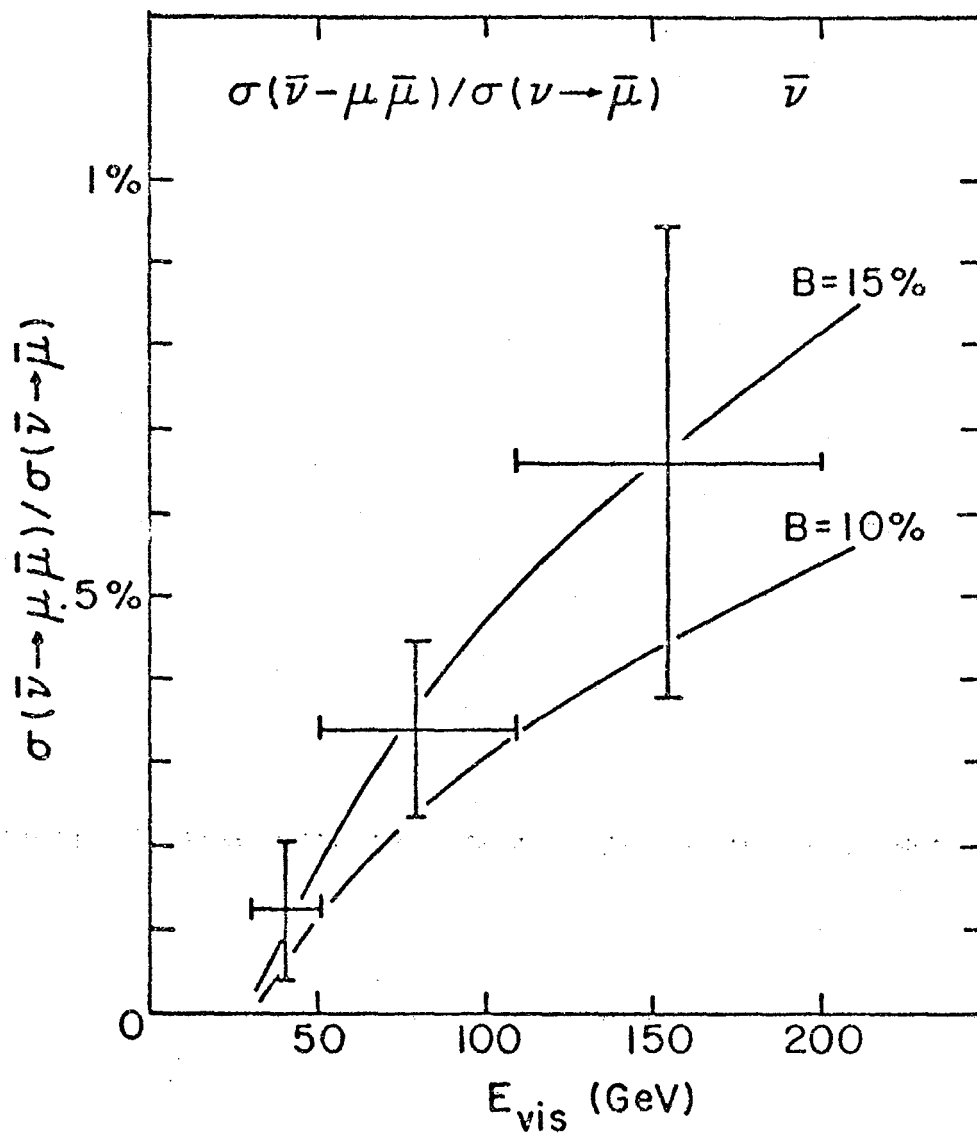


Figure 4.3.28

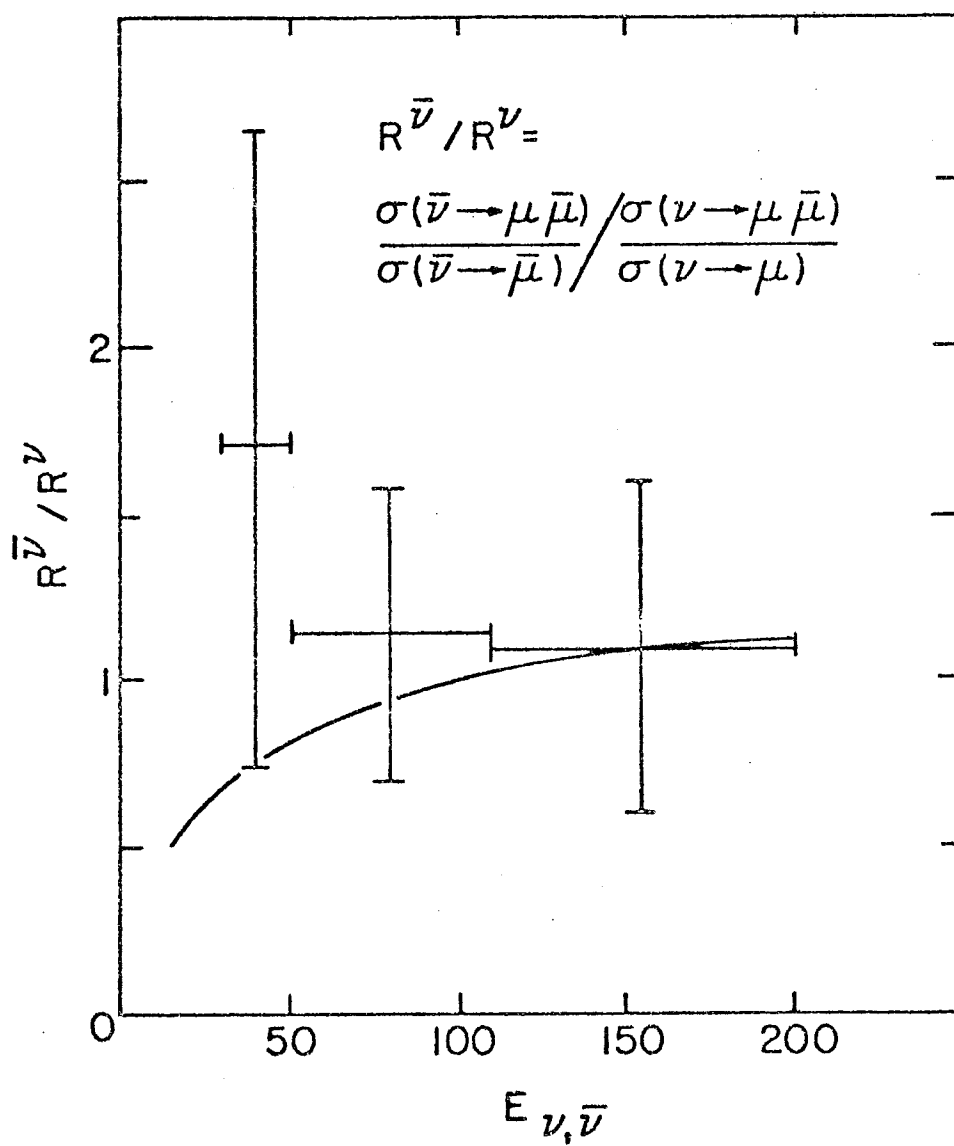


Figure 4.3.29

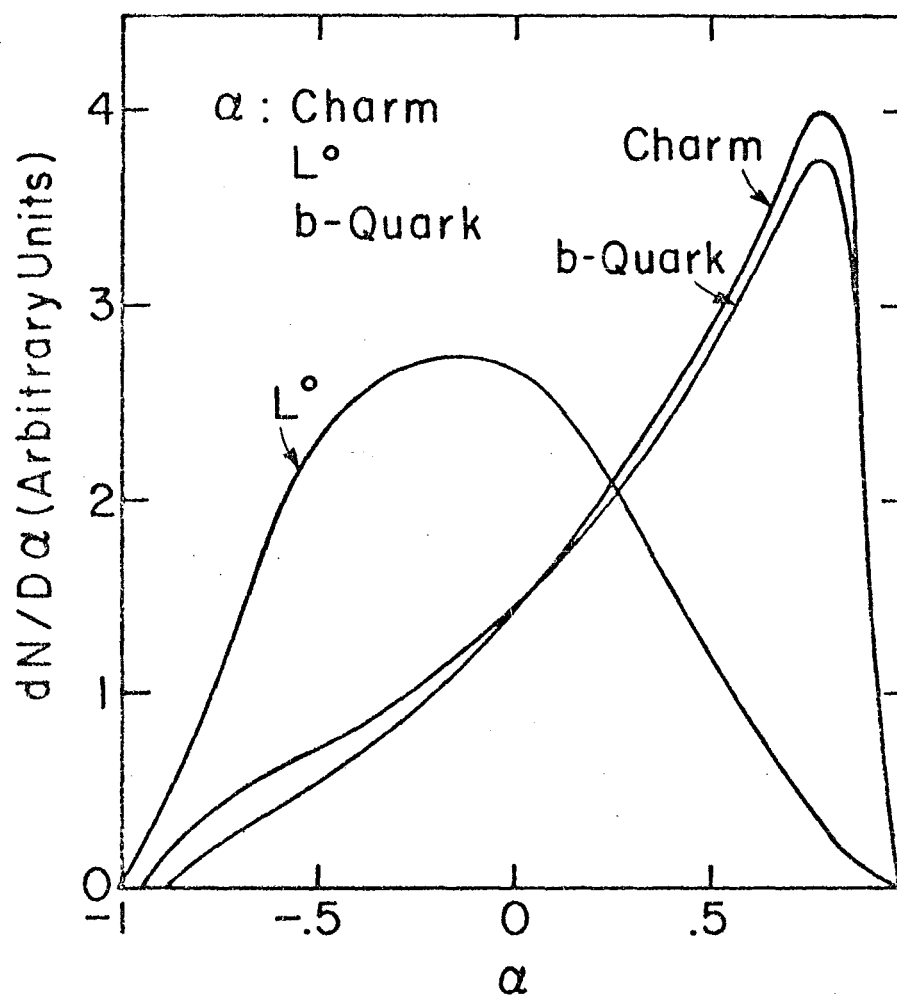


Figure 4.4.1

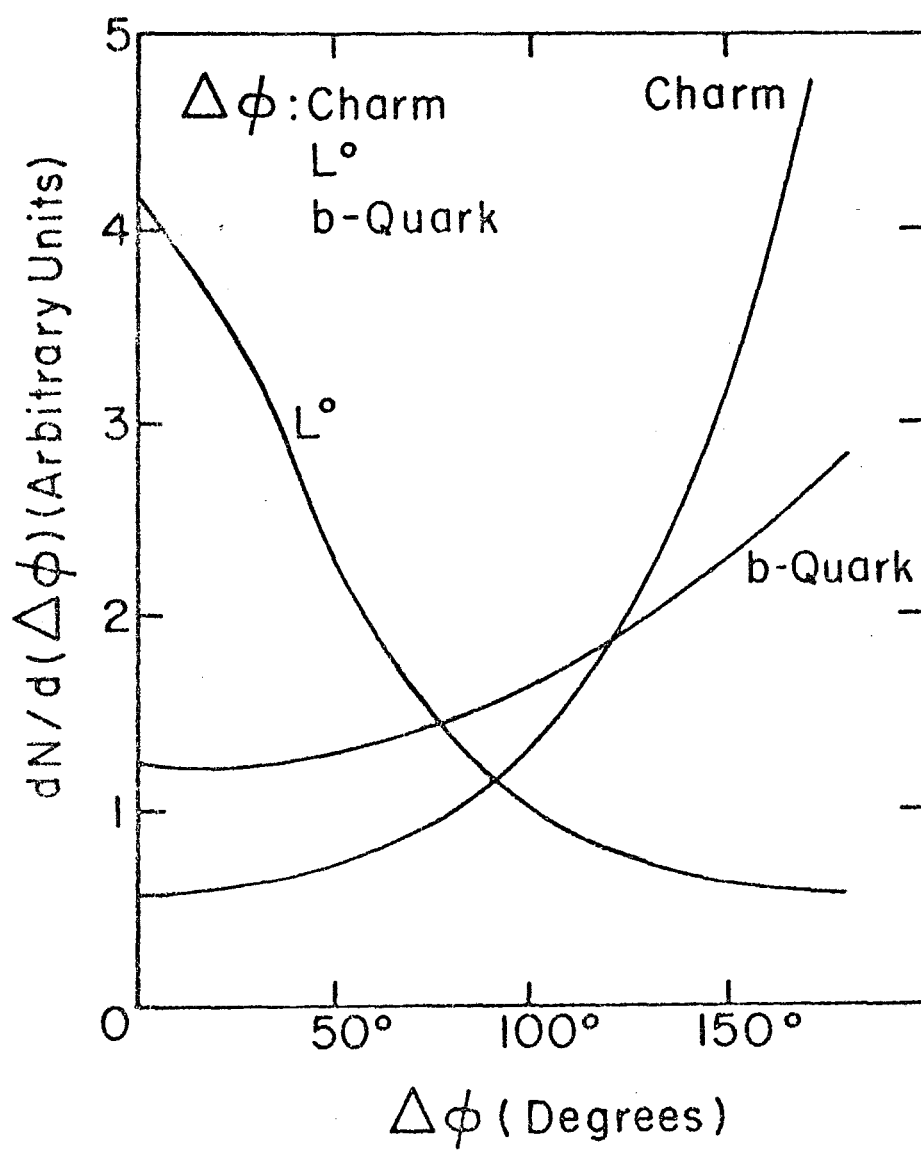


Figure 4.4.2

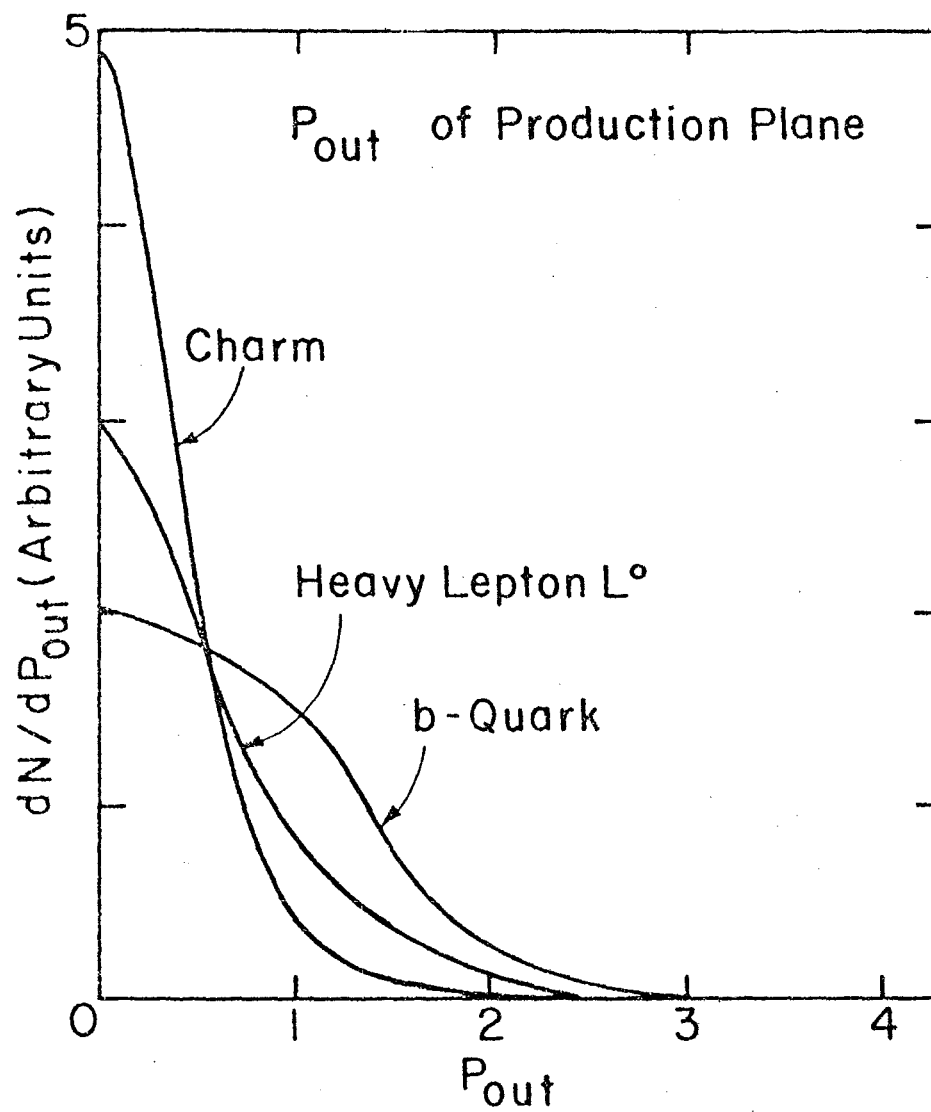


Figure 4.4.3

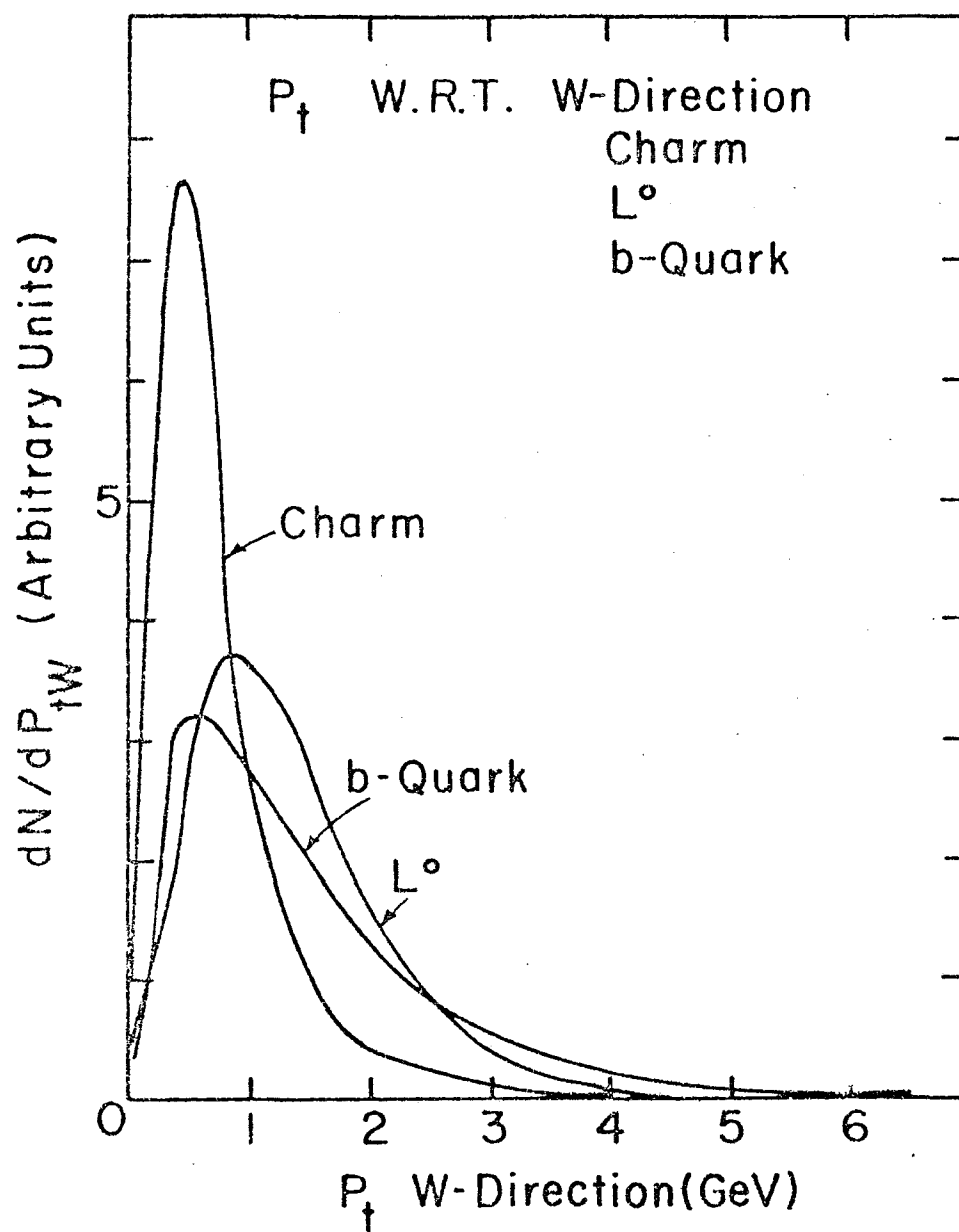


Figure 4.4.4

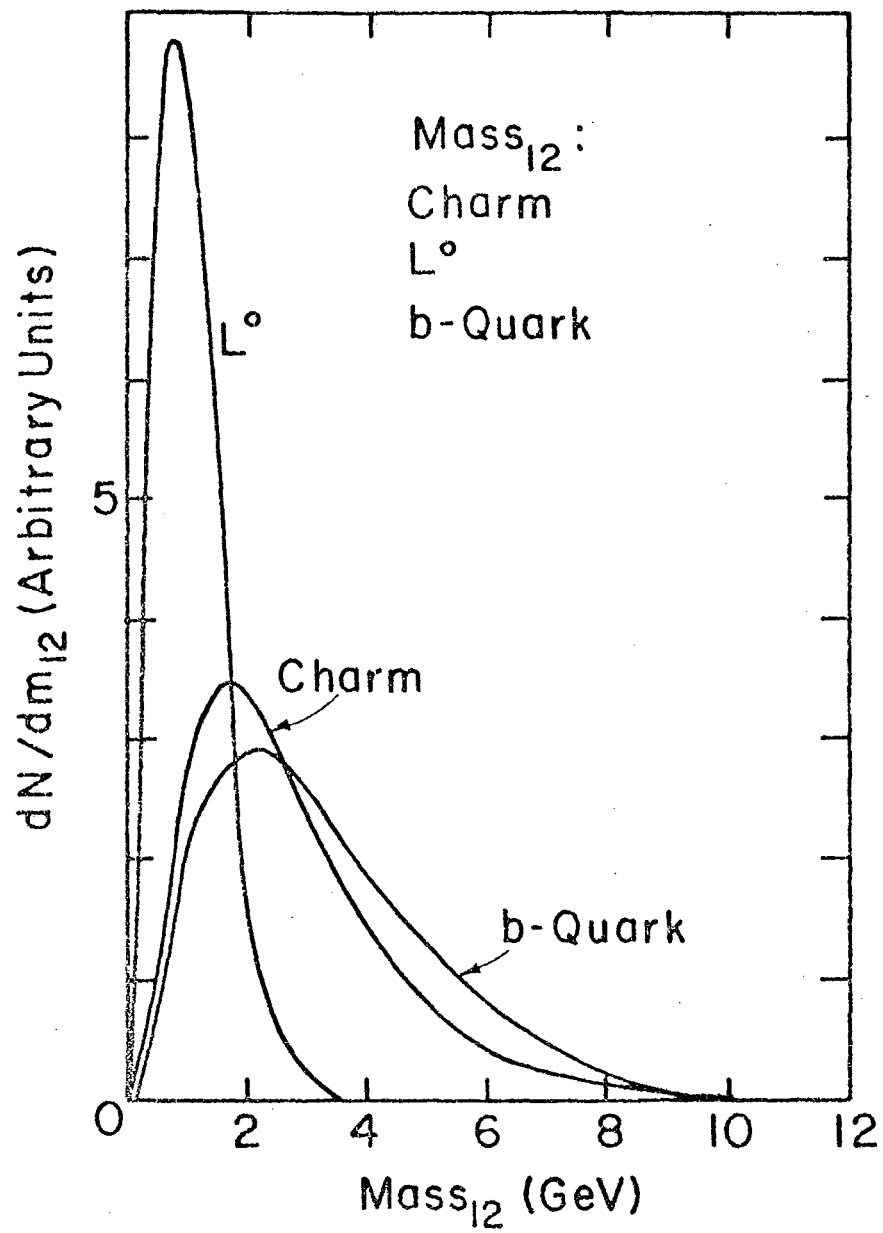


Figure 4.4.5.

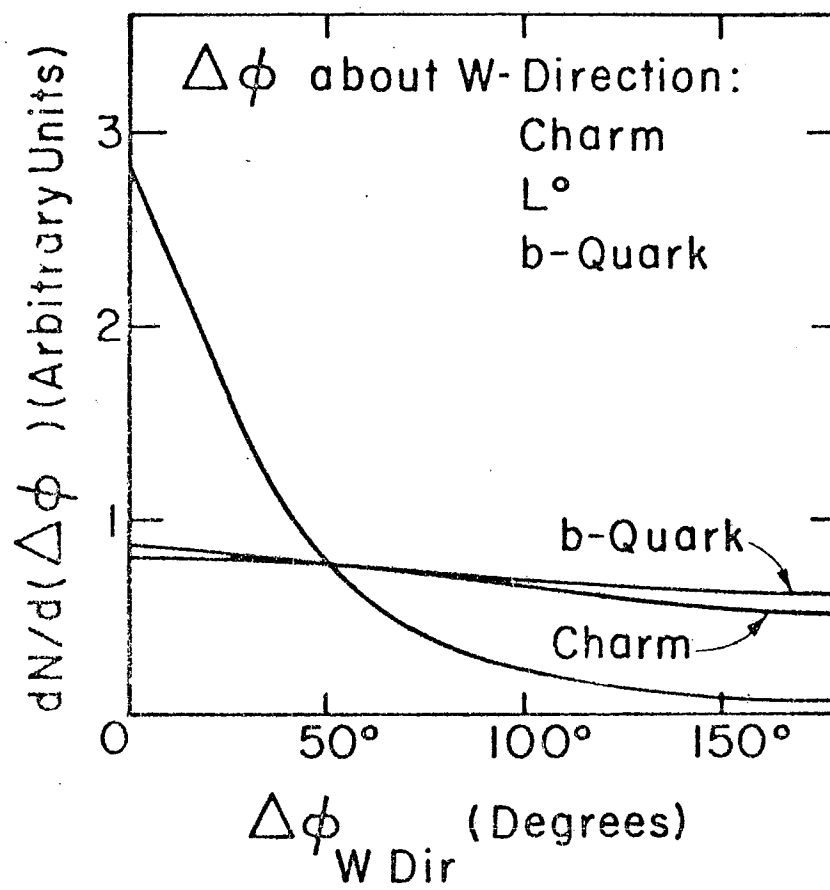


Figure 4.4.6

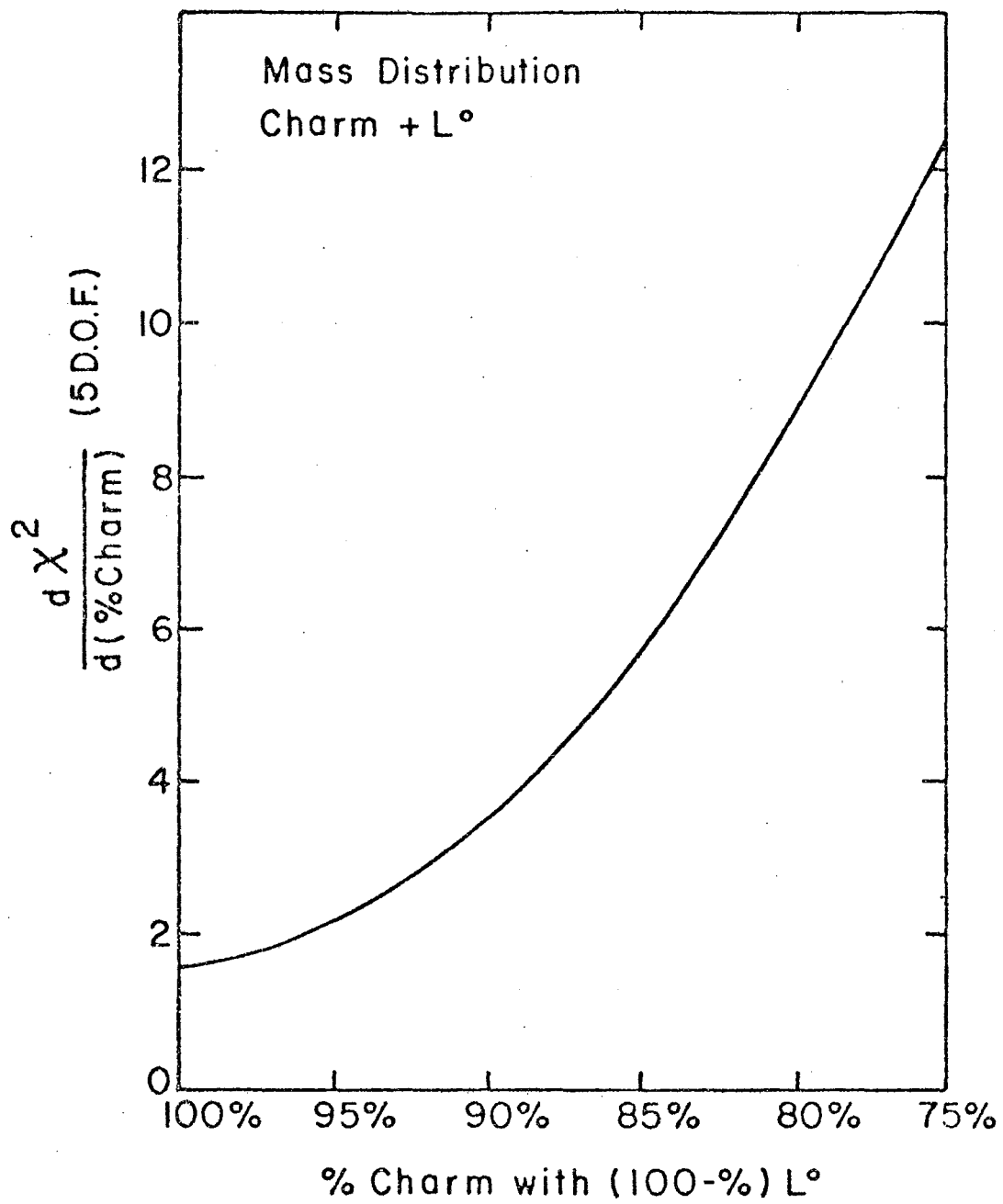


Figure 4.4.7

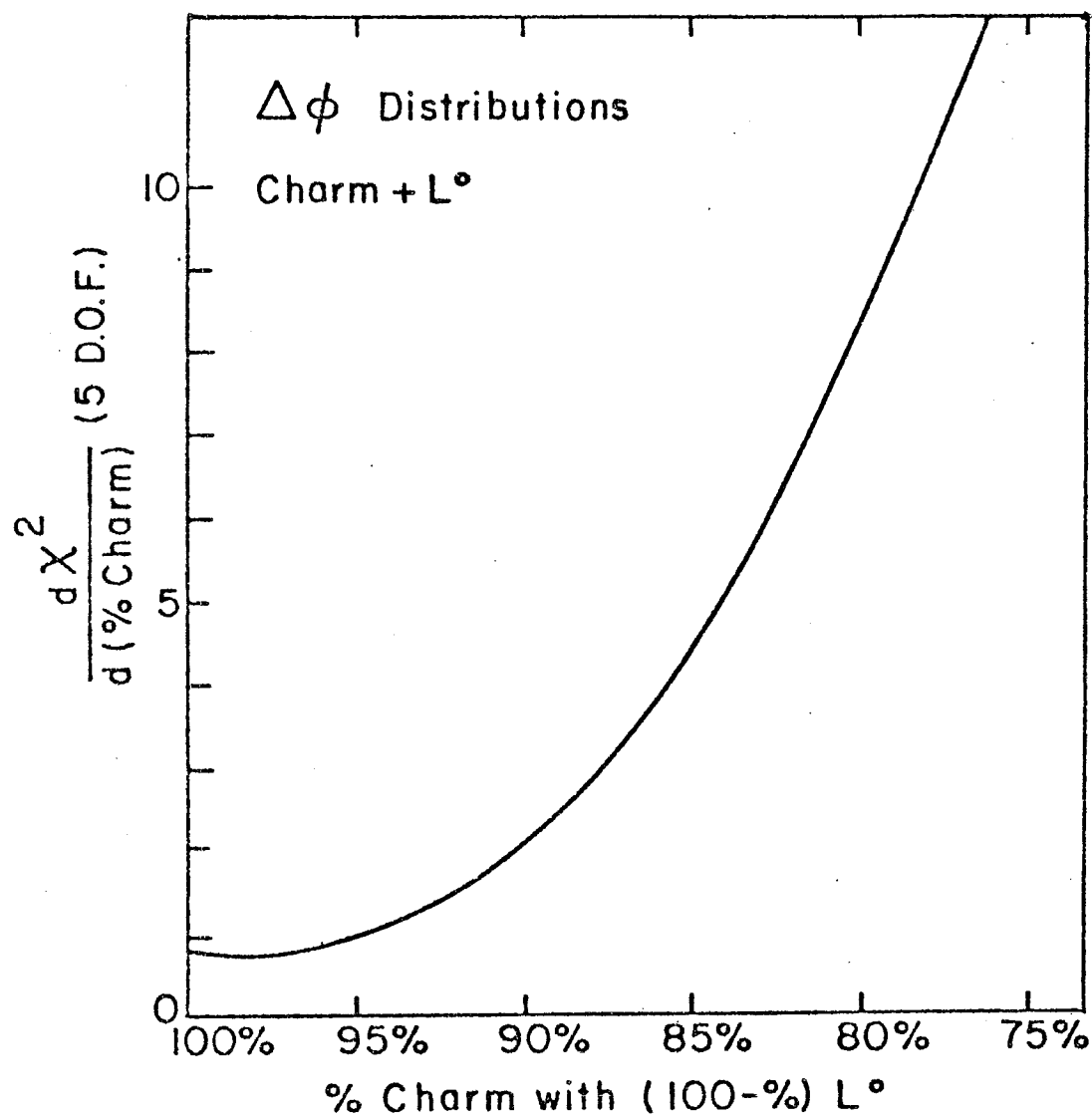


Figure 4.4.8

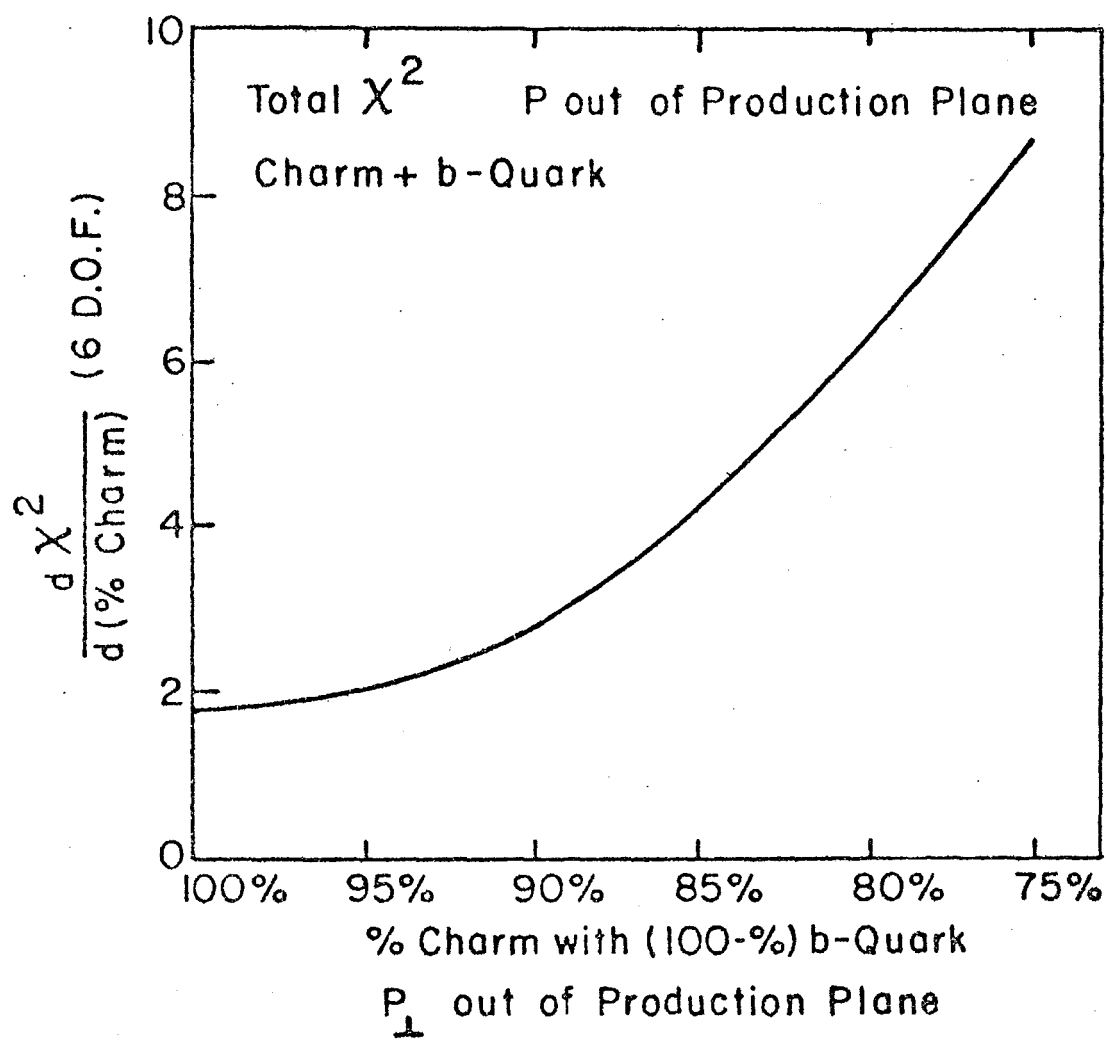


Figure 4.4.9

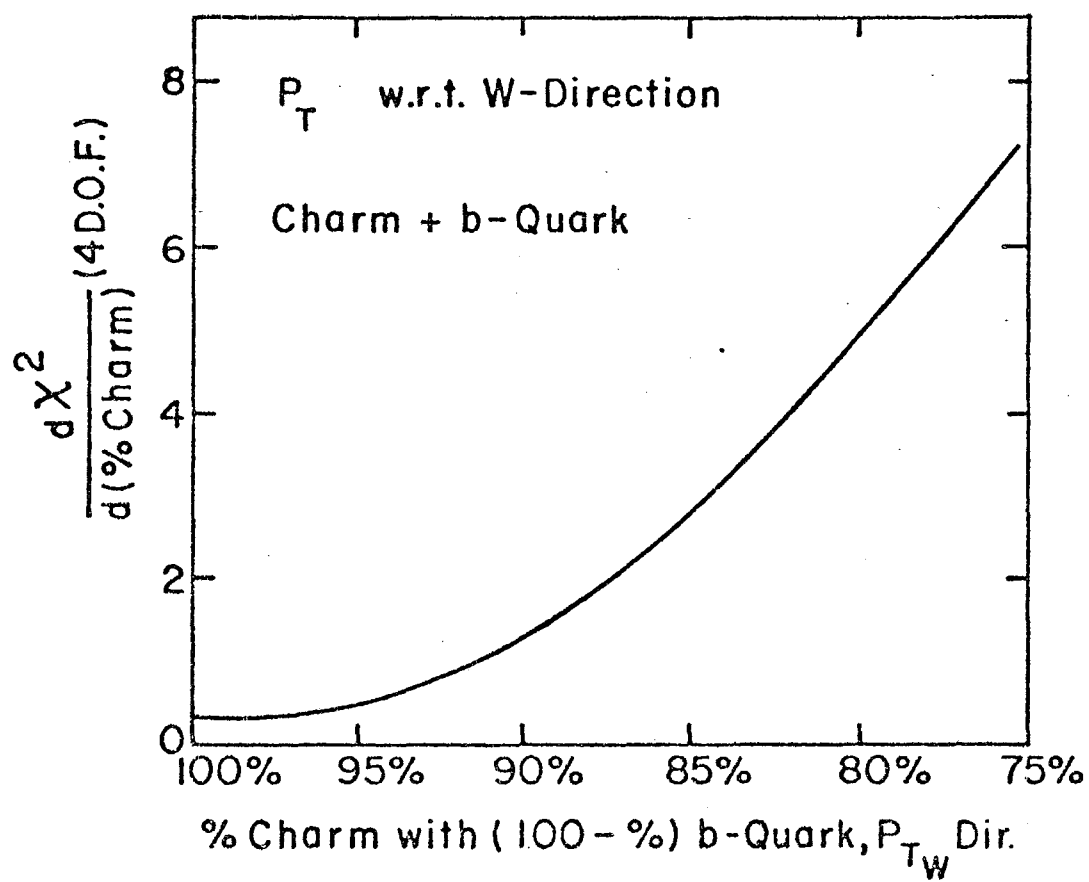


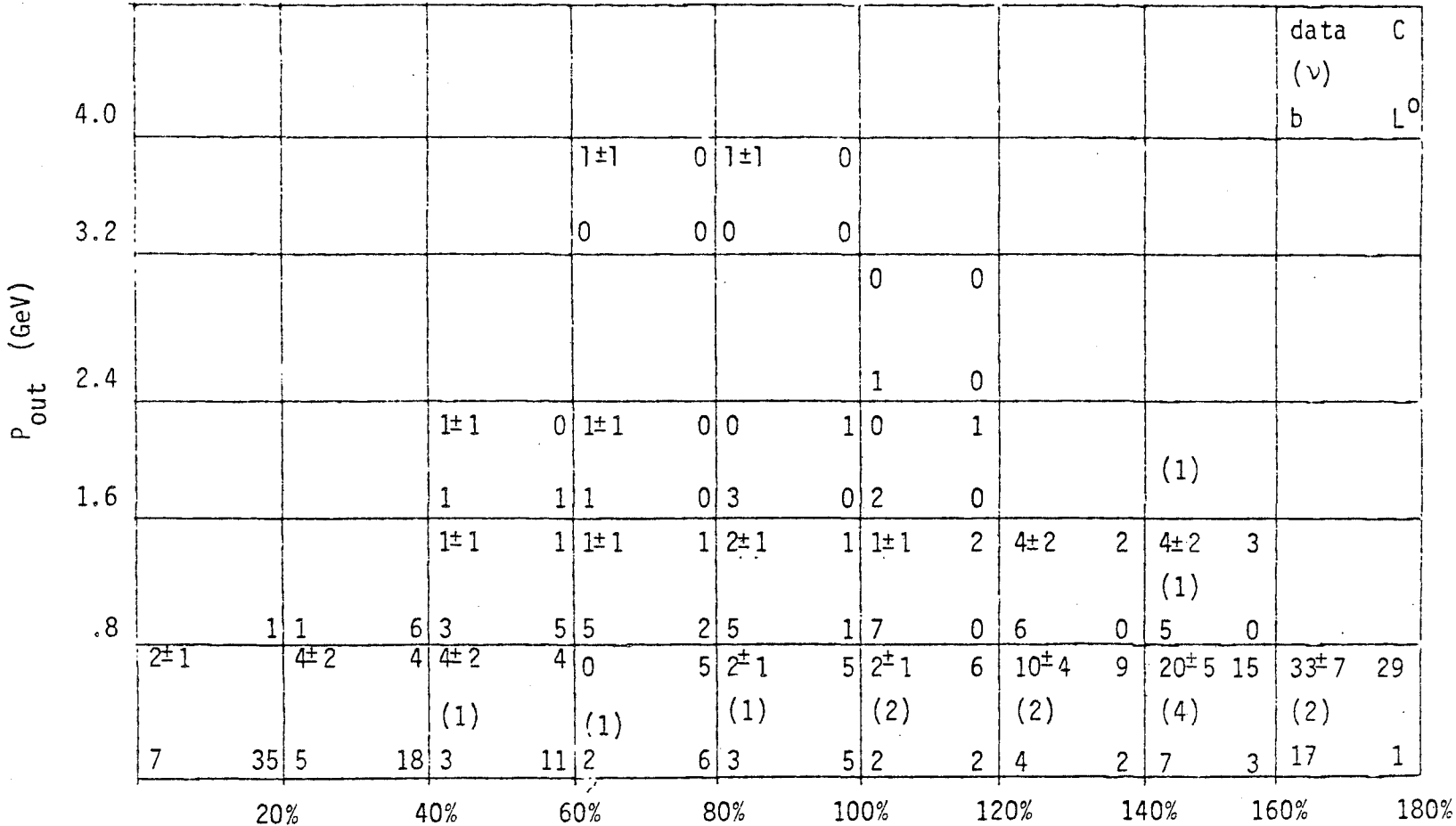
Figure 4.4.10

ν % of events Data, charm, b-quark, L^0

6	4 \pm 2	3	0	2	1 \pm 1	1	0	0	0	0			data C	
	1	0	1	0	1	0	1	0	1	0			($\bar{\nu}$) b	L^0
5	9 \pm 3 (1)	6	7 \pm 3	2	0	1	2 \pm 2	0	(1)					
4	1	0	2	0	2	0	2	0						
4	7 \pm 3 (1)	8	2 \pm 2 (2)	4	2 \pm 2	2	1 \pm 1 (1)	1	0	0	0	0		1 \pm 1 0
	2	0	3	0	4	0	3	0	1	0	1	0		0 0
3	13 \pm 4 (2)	12	4 \pm 2 (2)	6	4 \pm 2	4	0	3	1 \pm 1	0	1 \pm 1	0	0	0
2	7	1	5	1	5	1	5	1	1	1	0	1	0	1
2	12 \pm 4	14	0 (3)	5	0	2	0	0	0	0	0	0	0	0
	8	20	8	15	5	10	1	3	0	3	0	2	0	1
1	6 \pm 3	10	2 \pm 2	2	0	1	0	1	0	0	1 \pm 1	0		
0	7	25	5	13	5	4	5	4	0	3	0	0		

Pout GeV
Figure 4.4.11

✓ % of events Data, Charm, b-quark, L^0



$\Delta\phi$ (deg)
Figure 4.4.12

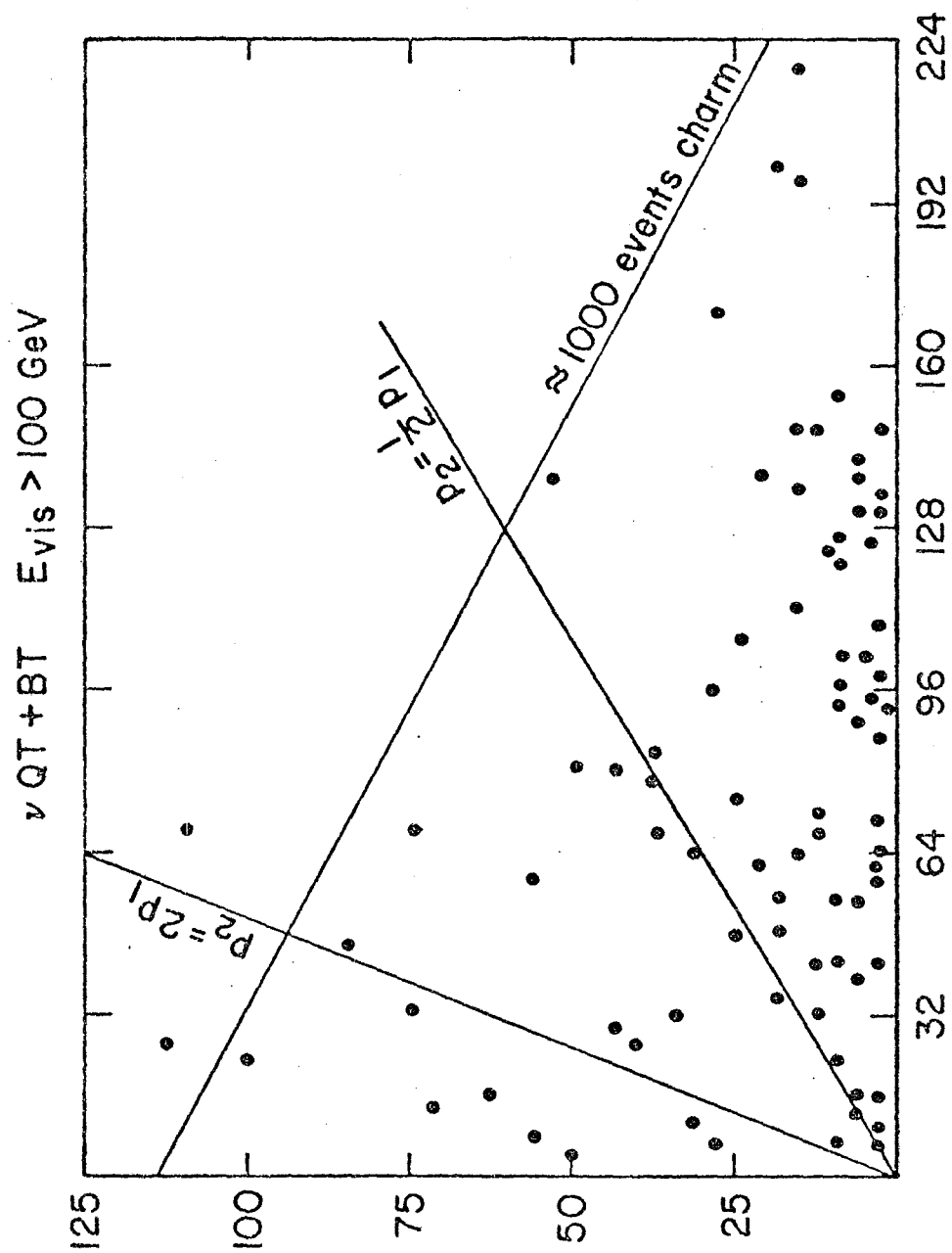


Figure 4.4.13

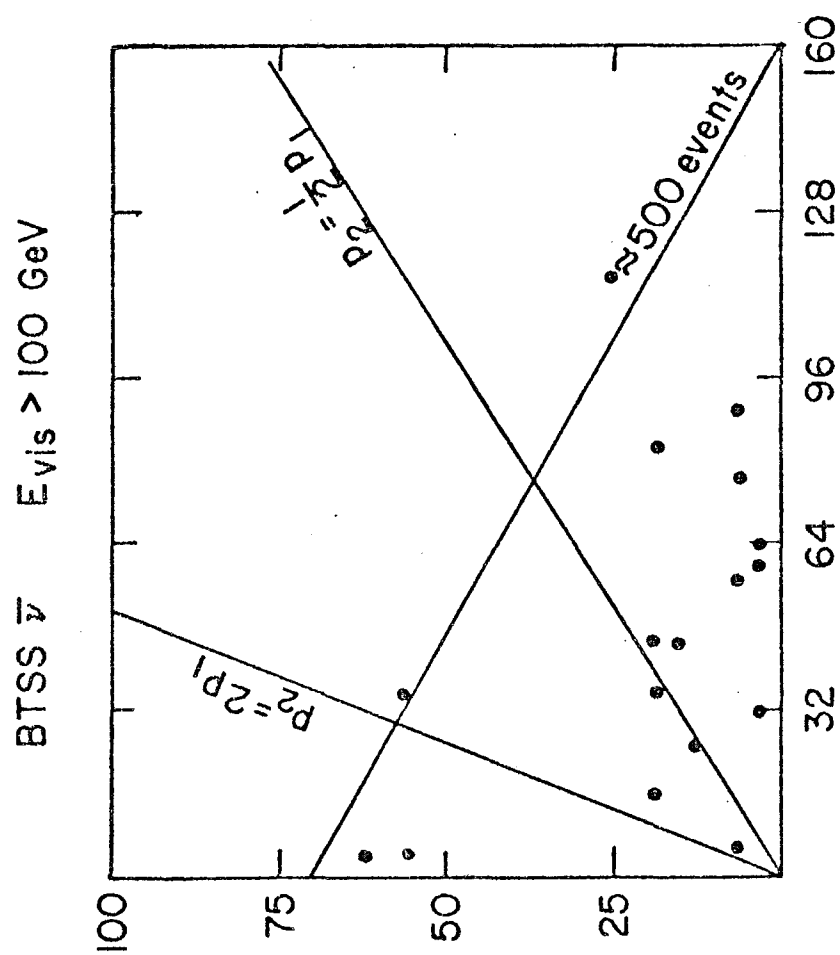


Figure 4.4.14

REFERENCES

Chapters 1-4

1. W. Pauli, Proc. of Solvay Congress, 324 (1933).
2. F. Reines and C. Cowan, Science 124, 103 (1956).
3. G. Danby et al., Phys. Rev. Lett. 9, 529 (1962).
4. See for example,
 - D. Perkins, Argonne Preprint, ANL-HEP-PR-76-54 (1976);
 - G. Friedman and H. Kendall, Ann. Rev. Nucl. Sci. 22, 203 (1972);
 - C. Llewellyn-Smith, Phys. Rep. 3C, 261 (1975);
 - B. Gordon et al., Phys. Rev. Lett. 41, 615 (1978);
 - General review articles can be found in ref. 17 and
 - J. Steinberger, Proc. 1976 CERN summer school;
 - K. Kleinknecht, Proc. 1977 CERN summer school.
5. M. Gell-Mann, Phys. Lett. 8, 214 (1964)
6. R.P. Feynman, Photon-Hadron Interactions, W. A. Benjamin, (1972)
7. H. D. Politzer, Phys. Reports 14C, 131 (1974);
 - D. Gross and F. Wilczek, Phys. Rev. D8, 3633 (1973),
 - and references therein.
8. F. J. Hasert et al., Phys. Lett. 46B, 138 (1973)
 - A. Benvenuti et al., Phys. Rev. Lett 32, 800 (1974)

9. S. Weinberg, Phys. Rev. Lett. 34, 419 (1975);
A. Salam in Elementary Particle Physics (Nobel Symposium No. 8) ed. N. Svartholm (1975) .
10. A. Benvenuti et al., Phys. Rev. Lett. 34, 419 (1975);
M. Holder et al., Phys. Lett. 69B, 377 (1977);
A. Asratyn et al., ITEP (USSR) pub ITEP-108 (1977);
A. Benvenuti et al., Phys. Rev. Lett. 41, 1204 (1978).
11. J. Blietschau et al., CERN pub, CERN/D.Ph.II/PHYS 75-49 (1975);
J. Von Krogh et al., Proc. Madison Conf. on New Particle Production, ed. D. Cline (1976).
12. S. Glashow, J. Illiopoulos, and J. Maiani, Phys. Rev. D2, 1285 (1970);
M. Gaillard, B. Lee, and J. Rosner, Rev. Mod. Phys. 47, 277 (1975).
G. Goldhaber et al., Phys. Rev. Lett. 37, 255, (1976)
13. B. Barish et al., Phys. Rev. Lett. 38, 577 (1977);
A. Benvenuti et al., Phys. Rev. Lett. 38, 1110 (1977);
M. Holder et al., Phys. Lett. 70B, 393 (1977).
14. A. Benvenuti et al., Phys. Rev. Lett. 41, 725 (1978).
15. M. Holder et al., Phys. Lett. 73B, 105 (1978);
R.J. Loveless et al, UW Report C00-088-29 (1978);
F. Bobisut et al., Proc. Oxford Conf. Neutr. 1978,
presented by M.G.D. Gilchriese.

16. J.D. Bjorken and E. Paschos, Phys. Rev. D1, 3152 (1970)
and ref. therein.
17. See, for example, the reviews of ref. 4., and
F.E. Close, Daresbury N.P. Lab Lecture Note Series #12,
DNPL/R31 (1973);
B. Lee, FNAL pub, NAL-CONF-74/50-THY (1974);
S. Adler, FNAL pub, NAL-CONF-74/39-THY (1974);
P. Landshoff, CERN pub, Ref.TH.2157-CERN(1976);
D.Cline and W.F. Fry, Ann. Rev. Nucl. Sci. 27, 209 (1977);
M.K. Gaillard, ed. Weak Interactions, INPNPP pub, Paris,
France, (1977);
P. Landshoff, Proc. CERN Summer School, CERN-78-10(1978).
18. J. D. Bjorken, Phys. Rev. 179, 1547 (1969).
19. G. C. Fox, Nucl. Phys. B134, 269 (1978).
20. However, note the results of G.S. LaRue et al., Phys.
Rev. Lett. 38, 1011 (1977).
21. H. Lipkin, Phys. Rev. Lett. 24, 1629 (1978);
O.W. Greenberg, Phys. Rev. Lett. 13, 598 (1964).
22. A. Bodek et al., SLAC-Pub-1442(E) (1974);
F. Riorden et al., SLAC-Pub-1634 (1975);
A. Benvenuti et al., Phys. Rev. Lett. 42, 1317 (1979);
H. Anderson et al., FNAL pub-79/30-Exp (1979).

23. For a review of QCD, see ref. 7 and
 - A.J. Buras, FNAL-pub-79/17-THY (1979);
 - F. Halzen, Proc. XIX Int. Conf on H.E.P., Tokyo (1978);
 - R.D. Field, Caltech preprint, CALT-68-696 (1978);
 - E. Ma, U. Hawaii preprint, UH-511-329-79 (1979).
24. J. Kiskis, SLAC-Pub-1248 (t) (1973);
 - R. Barlow and S. Wolfram, Oxford. U. Preprint, OX-24-78(1978);
 - A. DeRujula et al., CERN Pub, Ref. TH.2593-CERN (1979).
25. A long list of authors have considered threshold and Q^2 effects with varying conclusions. Some references are:
 - E. Witten, Nucl. Phys. B104, 445 (1976);
 - H. Georgi and H.D. Politzer, Phys. Rev. Lett. 36, 1281(1976);
 - F. Close et al., Nucl. Phys. B117, 134 (1976);
 - D. Gross et al., Phys. Rev. D15, 2486 (1977);
 - F. Halzen and D. Scott, Phys. Lett. 69B, 773 (1977);
 - F. Halzen and D. Scott, UW Preprint C)) -881-8 (1977);
 - I. Karlinger and J.D. Sullivan, U. Illinois Prepr. (1977).
26. As an example, see C. Quigg, Lec. Notes on Weak Int., Fermilab pub (1976), and see following reference 27
27. A large number of reviews exist on this topic:
 - L. Maiani, Proc. CERN Summer School, CERN 76-20 (1976);
 - S. Weinberg, Physics Today, pg. 42 April 1977;
 - J. Illiopoulos, Proc. CERN Summer School 1977;
 - D. Baillin, Weak Interactions, Sussex U. Press, (1977);
 - N.P. Chang ed., Five Decades of Weak Int., Ann. N.Y. Phys.

- Soc., 294 (1977).
28. M. Kobayashi and T Maskawa, Progr. Theor. Phys. 49, 652, (1973).
 29. R.E. Shrock and L.L. Wang, Phys. Rev. Lett. 41,1692(1978);
V. Barger et al.,Phys. Rev. Lett. 42, 1585 (1979);
R. Phillips , Rutherford Preprint, RL-79 015 (1979).
 30. A. Pais, Rockefeller preprint C00-2332B-118 (1977).
 31. R. Carrigan, FNAL preprint 78/13 (1978) ; and also
ref. 10-12.
 32. T. Gottschalk, UW thesis unpublished (1978) ;
C-H. Lai, Fermilab pub-78/18-THY (1978);
V. Barger et al. , UW preprint C00-495 (1976);
V. Barger et al., UW preprint C00-504 (1976);
the first 2 refs. contain many important refs as well.
 33. V. Barger et al., Nucl. Phys. B102, 439 (1976);
S. Pakvasa et al., Phys. Rev. D10, 2124 (1974)
D. Duke et al.,FNAL-pub-77/95-THY (1977);
F. Dao et al., Phys. Rev. Lett. 39. 1388 (1977);
R. Field and R.P. Feynman, Phys. Rev. D15,2590 (1977);
D. Kaplan et al., Columbia-FNAL-Stony Brook prepr (1977);
J. de Groot et al.,Z.Phys.C.Part. Fields 1,143 (1979);
A. Benvenuti et al., Phys. Rev. Lett. 42, 1317(1979)

34. see references 25,32, and also
 A. Buras and K. Gaemers, Nucl. Phys. B132, 249 (1978).
35. H. Georgi and H. Politzer, Phys. Rev. Lett. 36, 1281 (1976);
 R.M. Barnett, Phys. Rev. Lett. 36, 1163 (1976).
36. V.Barger et al., Phys. Rev. D16,(1977);
 L.M. Sehgal and P.M. Zerwas, Nucl. Phys. B108,483 (1976).
37. Note the discussion of the limits on $D(z)$ in the first
 2 ref. in footnote 32 (ie., $z_{\min} = m_c/\nu$). References
 for large $D(z)$ as $z \rightarrow 1$ are :
 J.D. Bjorken, SLAC preprint Slac-PUB-1992 (1977);
 M. Suzuki, Phys. Lett. 71B, 139 (1977);
 J. Dias De Deus, Nucl. Phys. B138, 465 (1978);
 L.M. Sehgal, Proc. 1977 Int. Symp. on Lepton and Photon
 Int. at H.E., Hamburg (1977);
 V. Barger et al., Phys. Lett. 70B, 51 (1977).
38. J. D. Bjorken, SLAC report 191 (1975) and ref. therein.
39. References 32, and R. Imlay, J. Rich private communications
 E310 collaboration.
40. M. Perl, Summary Talk, Proc. XII Rencontre De Moriond (1978).
41. CDHS collaboration reports, CERN experiment WA-1, and
 M. Holder et al., Phys. Lett. 69B,377 (1977).
42. References 32, and CDHS collaboration report to Proc.
 XIV Rencontre De Moriond (1979).

43. A. Benvenuti et al., Phys. Rev. Lett. 41, 1204 (1978),
also ref 10.
44. For a review of multilepton final states, see
K. Tittle, Proc. XIX Int. Conf. on H.E.P., Tokyo (1978);
Multilepton section in Oxford Conf. on Neutrino Reactions,
U. Oxford, 1978;
A. K. Mann, Proc. XIX Int. Conf. on H.E.P., Tokyo (1978);
other refs in refs 10,11,13,14,17,5;
for like-sign dimuons, see reference 46.
45. T. Gottschalk, Ph.D. Thesis, UW, unpublished (1978);
J. Rich, Ph.D. Thesis, Harvard U., unpublished (1979);
V. Barger et al., UW preprint C00-881-13 (1978); this
last reference discusses Drell-Yan processes.
46. J. Smith and C. Albright, CERN pub., Ref.TH.2666-CERN(1979).
47. M.K. Gaillard et al., Nucl. Phys. B102, 326 (1976);
J. Bell et al, FNAL pub-78/24 (1978).
48. A. Benvenuti et al., HPWF collaboration proposal to FNAL
experiment E310 (1975)
49. For a review of beam-dump experiments see the section
"Contributions to Beam-Dump Experiments" in Proc. of
Oxford Neutrino Conf., Oxford U., 233 (1978);
Charm searches are reviewed by M. Boratav, CERN/EP
79/40(1979)

50. H. Goldberg, Phys. Rev. Lett. 39, 1598 (1977);
B. L. Young et al., Phys. Lett. 74B, 111 (1978);
G. L. Kane et al, Stony Brook Preprint, SUNY-ITP-SB-78-37 (1978);
P. Pandita et al., Phys. Lett. 77B, 193(1978);
F. Halzen, Proc. XIX Int. Conf. on H.E.P., Tokyo (1978);
M. Gluck and E. Reya, Phys. Lett. 83B, 98 (1979).
51. C. Albright and J. Smith, Phys. Lett. 77B, 94 (1978);
R.J.N. Philips, Rutherford preprint, RL-79-015 (1979);
also ref 46.
52. Mark J collaboration at PETRA, Hamburg, DESY preprint (1979), and private communication A Skuja.
53. See above reference 52 and also
C. Albright et al., Stony Brook Preprint, ITP-SB-77-32 (1977), and references cited therein.
54. P. Bosetti et al., Proc Oxford Conf. Neutrino Int., Oxford U., 83 (1978);
H. Faissner et al., Conf. Proc. Neutrino 78, Purdue U.(1978);
D. Baranov et al., Phys.Lett. 70B, 2669 (1977).
55. A.Pais and S. Treiman, Phys. Rev. D 14, 293 (1976);
V. Barger et al., Phys. Lett. 70B, 243 (1977); calculations for monte carlo use, esp. matrix elts., are found in:
V. Barger et al., UW preprint C00-604 (1977) and K.Bongardt, Inst. Theor. Kernphys., Karlsruhe, TKP 79-5 (1979).

56. J. Ellis et al., CERN pub., Ref. TH.2093-CERN (1975) (higgs);

Other general surveys can be found in:

PEP Summer Study, SLAC-pub (1974);

LEP Summer Study, CERN Pub., (1978)

57. Pairing, or Track Matching, Program written by P. Cooper.

58. M. Strovink, LBL preprint, LBL-9234 (1979).

APPENDIX I BEAMS

The experiment used the NØ beam lines at the Fermi National Accelerator Laboratory. The 400 GeV primary protons are resonantly extracted, split 3 ways and transported by a standard FODO line to a 12" BeO (or Alumina) target. Typically under good running conditions each burst (spill) contains 10^{13} protons and lasts between 2-10 msec with substructure in time resembling the 53 mhz main ring RF. The repetition rate for spills varied slightly, but typically was 10 sec.

The protons produce pions and kaons in the target and these secondaries together with the untargetted protons then enter 1 of 2 magnetic lines. The first is the Quadrapole Triplet (QT) consisting of 2 sets of quad doublets and a quad singlet. The currents are set to focus point to parallel, the target being the focus, for 225 GeV positive and negative hadrons. The second is the Bare Target Sign Selected (BTSS) beam, consisting of 2 dipoles and a beam dump. The first dipole bifurcates the beam by charge and the second is used to direct the secondaries of desired charge toward the apparatus, while the wrong sign secondaries are then dumped.

The secondaries from these two lines then enter a 1300 m drift tube where about 10% of the pions and kaons decay into $\mu\nu$. A 1 km earth shield (berm) absorbs the remaining hadrons and filters out the muons by range. The beam emerging from the berm consists of about 10^9 neutrinos and an "equilibrium" muon flux, normally less than 10 per spill from neutrino regeneration in the end of the berm.

Both the QT and BTSS beams are high intensity and broad band; no narrow momentum selection is made on the secondaries. The fluxes as a function of energy are shown in figure for neutrinos and antineutrinos in each beam. The utility of the QT is the enhancement of the high energy neutrino flux over a bare target. The BTSS beams, on the other hand, produce relatively pure beams of either ν or $\bar{\nu}$. The event rates for ν relative to $\bar{\nu}$ are 6:1 QT, 1:6 BTSS $\bar{\nu}$ and 20:1 BTSS ν .

A general feature of these beams is that the ν flux coming from the positive secondaries is higher in energy than the $\bar{\nu}$ flux from the negative secondaries due to diffractive production of positives. For example, in the QT, the average (anti) neutrino energy interacting is 60 (90) GeV. The event rates for QT neutrinos and BTSS antineutrinos are given in Appendix 12 on the single muon data.

The beams were monitored by a secondary emission monitor (SEM), a 90° monitor (90°M), and segmented wire ionization chambers (SWIC). The SEM measured the total protons delivered to the target integrated over a spill. The SWIC's and the 90°M monitored targetting. The 90°M was a counter placed at 90° to the target, measuring the flux of secondaries. If the target integrity and beam targetting remain stable, the 90° monitor should also remain stable. The SWIC's measured the beam profile and position in (x,y) before and after the target and allowed vernier steering of the incident protons.

Appendix I

References

1. J. Sanford, Ann. Rev. Nucl. Sci. 26, 151 (1976).
2. A. Skuja et al., FNAL tech. memo, TM-626A (1976).
3. R. Stefanski et al., FNAL tech. memo, TM-646 (1976).
4. C. Kerns, IEEE Trans. on Nucl. Sci., NS-23, 1104(1975)

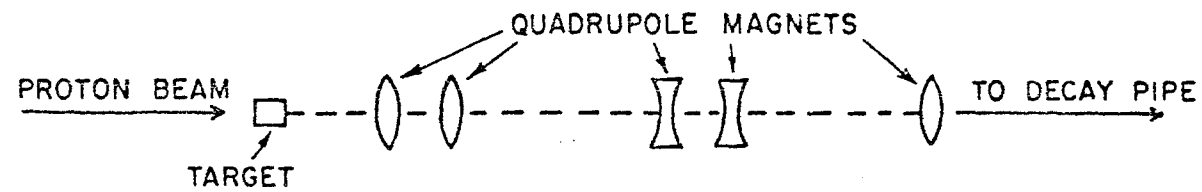
Figures

A1.1 Schematic of QT and BTSS beam lines.

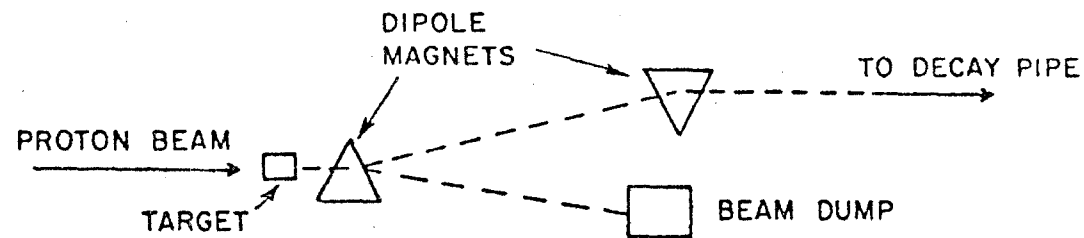
A1.2 Beam spectra for QT and BTSS $\nu, \bar{\nu}$ beams.

NEUTRINO BEAMLINES

A) QUADRUPOLE TRIPLET



B) BARE TARGET SIGN SELECTED



HORIZONTAL SCALE 0 25'

Figure A 1.7

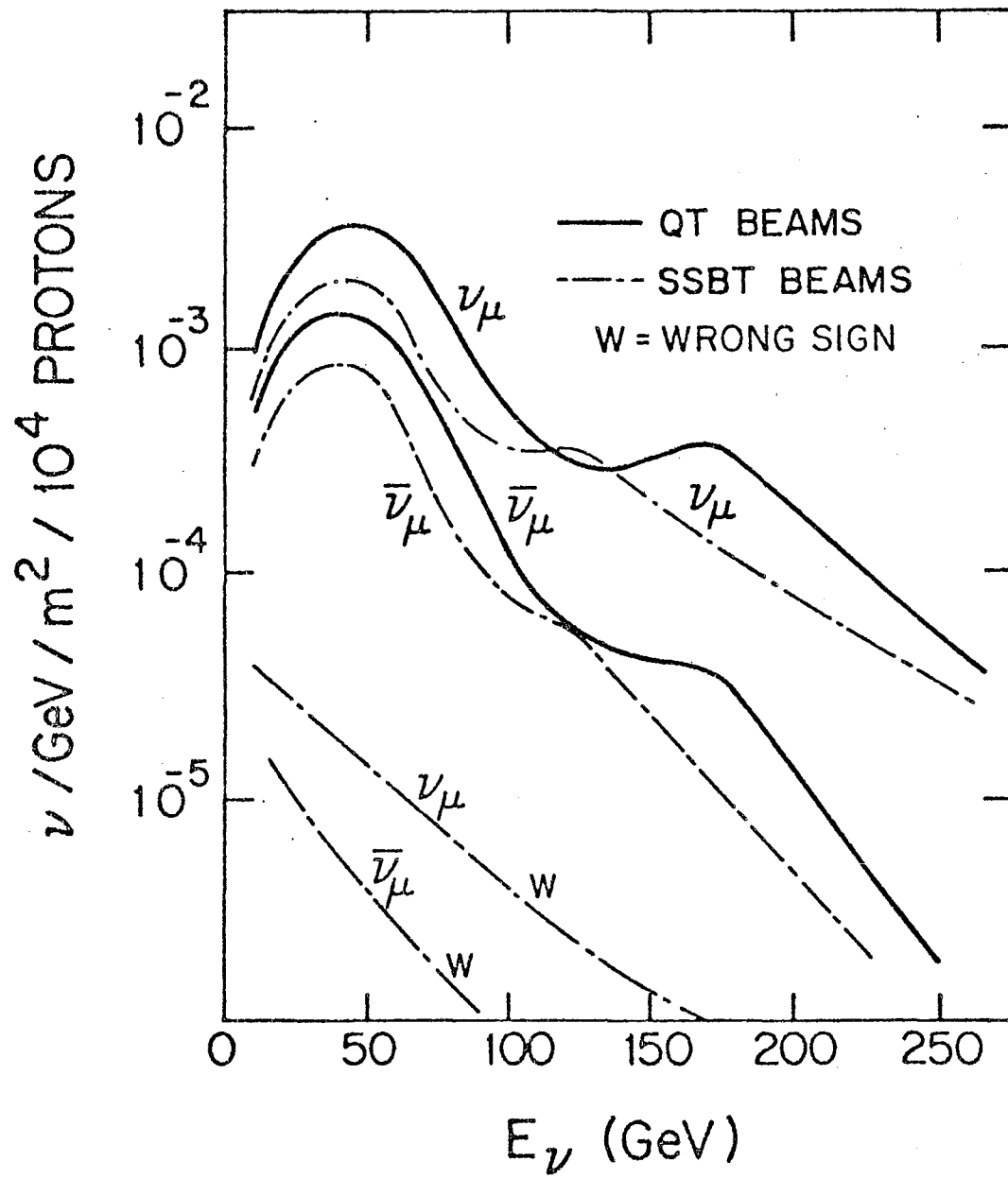


Figure A 1.2

APPENDIX II

Calorimeter Construction and Electronics

1. Liquid Calorimeter

The liquid calorimeter consists of 12 equal slabs of liquid scintillator (Table A2.1), each 18" thick, 11.5' x 9.5' transverse to the beam. The slabs are held in 6 tanks consisting of a square steel channel frame with 3/8" steel plates bolted to the frame transverse to the beam. The plates are coated with a teflon film ($n=1.35$) to utilize total internal reflection to pipe the light to photomultipliers. There are 12 5" photomultipliers¹, 6 on each of 2 opposing sides of the frame as shown in figure A3.1. They view the liquid through lucite windows and are optically coupled with a silicone fluid.

The H.V. is distributed to the tubes with booster supplies on 3 of the dynodes in addition to a resistor-divider chain to prevent the tubes from sagging under the large light levels attainable in a hadron shower. The tubes on each side to a module are daisy-chained using anode and last dynode signals on twinax² from tube-to-tube. The tube signals on opposing sides of a module are then passively added, amplified 5X, split, one signal attenuated 40X, and both digitized. The splitting was done to achieve a larger dynamic range in energy, from about 100 MeV minimum ionizing to 40 GeV per module deposited. The twinax provides common

mode noise rejection during signal travel to the electronics house. Figure A3.2 shows the schematic electronics for these calorimeters. An internal pulsed l.e.d. system was used to balance the tube H.V. on each module.

2. Iron Calorimeter

The iron calorimeter (Fe Cal) was constructed of alternating slabs of iron and liquid scintillator, interspersed with spark chambers. There were 10 slabs of flame cut iron, 4" thick, 12' square. Ten planes of 2 Trigger Counters per plane were installed between these plates to sample ionization.

Two Trigger Counter modules are shown in figure A2.3, used as an Fe Cal plane. Each module is a welded tank constructed of 1/8" sheet steel 6'x12'x4'. The inside walls were also coated with teflon film to facilitate light collection. The light was sampled in 5 strips formed by optical dividers running the long length of the tank as shown by the dotted lines in the figure. Each strip was viewed by a 2" photomultiplier³ on each end. Tetrahedral mirrors adiabatically collected the light from the strip to the tube face. Each tube was coupled to the lucite windows through a spring compressed gel "cookie" and a lucite cylinder which contained Am^{241} (alpha source) and scintillator for tube balancing and calibration. A standard resistor-divider base with a variable drop between dynodes 2 and 3 for balancing powered

these tubes. The signals were daisy-chained in twinax and handled virtually identically to the liquid calorimeter signals.

3. General

The total masses of these 2 calorimeters are 60 tons liquid calorimeter and 150 tons iron calorimeter. Their use as energy measurement devices is discussed in Appendix IX. Using liquid scintillator required special handling in the form of cleanliness and dry conditions. Water at the 100 ppm level will turn the mineral oil based scintillator milky. In addition, as light was collected over 12', filtering to remove dirt and dust was essential. A pump equipped with anhydrous seepage tanks and micron filters was used for the above purposes. Under good working conditions, light was attenuated by about a factor 7 from end to end and minimum ionizing particles corresponded to about 10 photoelectrons on a tube at the far end of the counter.

Appendix II:

References

1. RCA 8055
2. twinax is a shielded twisted pair cable.
3. RCA 6342a/v1.
4. Nuclear Enterprises NE235A

Figures

- A2.1 Liquid Calorimeter module.
- A2.2 Liquid Calorimeter electronics.
- A2.3 Iron Calorimeter module= 2 trigger counter modules.

Table A.2.1. Properties of Liquid Scintillator⁴

Hydrogen/Carbon Ratio	1.93 .05
Index of Refraction	1.47
Optical Absorption Coefficient	.58/Meter
Density	.858 g/cm ³
Absorption Length	84 cm
Radiation Length	53 cm
Mean DE/DX (minimum ionizing)	1.79 Mev/cm

LIQUID CALORIMETER TANK

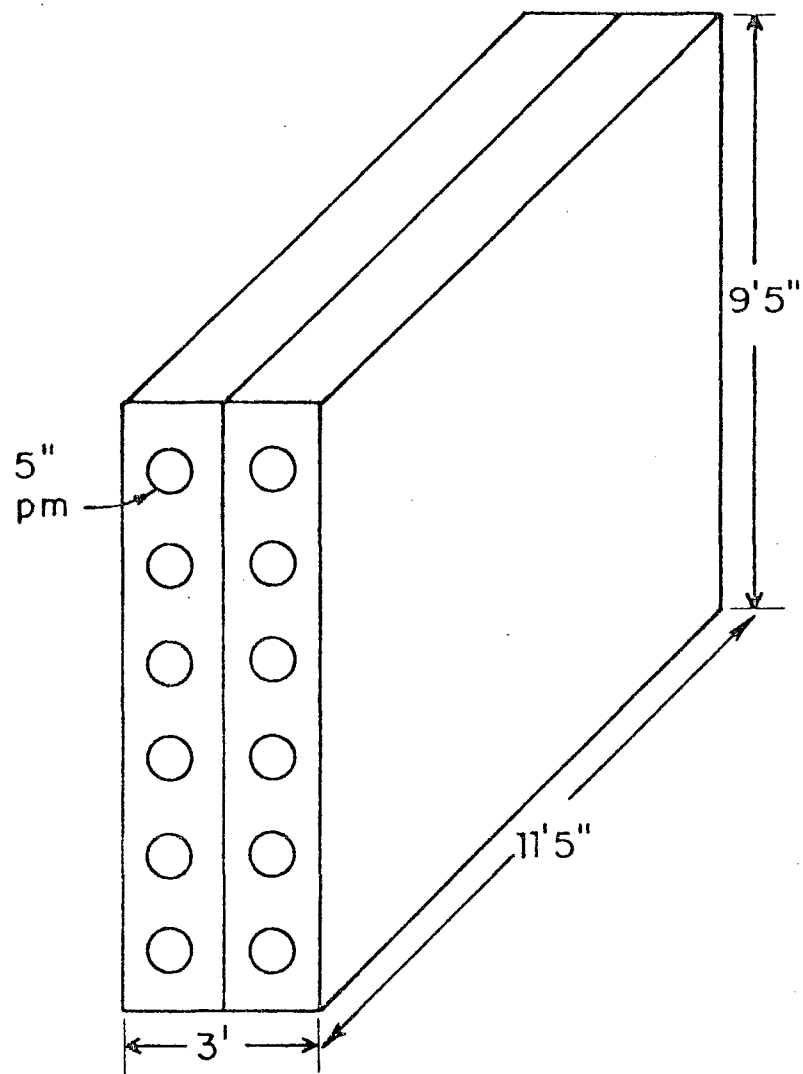


Figure A 2.1

LIQUID CALORIMETER ELECTRONICS

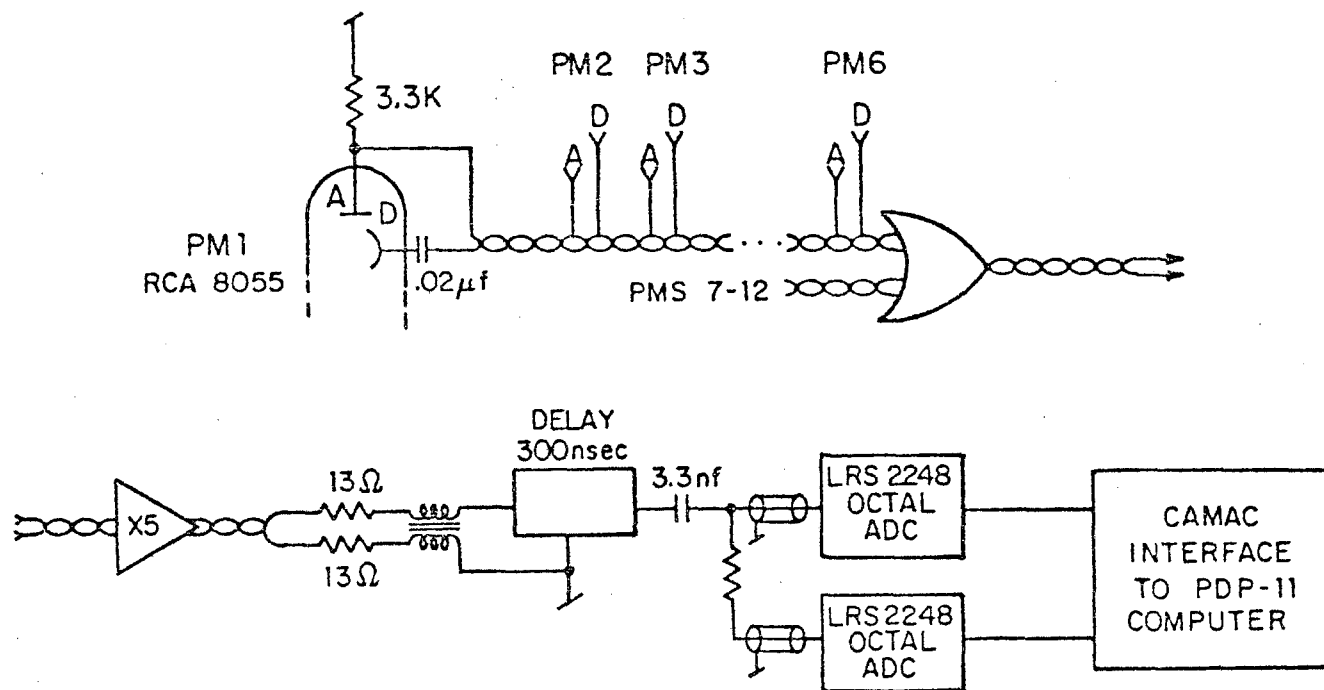


Figure A 2.2

IRON CALORIMETER MODULE

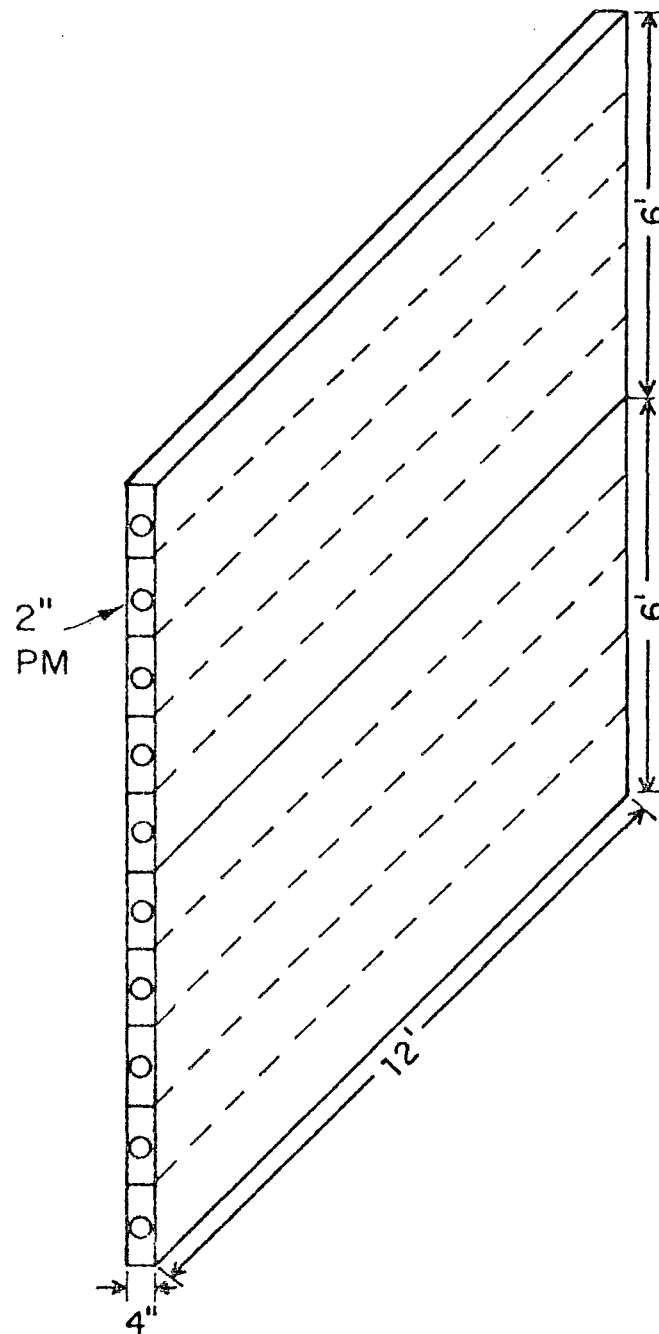


Figure A 2.3

APPENDIX III

Spark Chambers

The spark chambers were wide gap optical spark chambers (WGOSC). They were used to determine the muon track positions and, to a lesser degree, the origin of events by recording the hadron shower tracks. Their special utility was the ability to determine angles as well as positions from the wide gap sparks. The chamber positions in the apparatus are shown in figure 2 of chapter 2. There were 9 chambers interspersed through the calorimeters and planes of chambers were placed behind each magnet toroid.

Each chamber consisted of a central -HV electrode plane sandwiched by 2 ground electrode planes to make a 2 gap chamber. The 5 cm space between planes was covered by $\frac{1}{4}$ " lucite windows to view the interior. Each electrode plane was constructed of an Al skin over Al honeycomb 1.3 cm thick. The chambers in the 24' and last 4 chambers in the 12' spectrometers were 3.1 x 3.1 m in size; the remaining chambers were 3.7 x 3.7 m². In the 24' magnet, 4 3.1 m chambers were staggered together to cover the useful area of the toroids so that each chamber could be viewed directly from the side and top without looking through another chamber.

Each chamber had fiducials attached to it (figure A3.1). These consisted of a light box with a cross machined in an Al plate. They were attached to the chamber looking along the light path to the cameras in the 15° (front) and 90° (top) views. The back and bottom

fiducials were mounted so that the cross was viewed by the cameras looking through both windows of the chamber in a particular view. The front and top fiducials were flashed for 1-2 seconds for each event. The back fiducials were used for optical alignment.

The fiducial positions in space were known to first order by survey and ruler measurement. The fiducials on each chamber were measured relative to 2 fiducials; these 2 fiducials were then surveyed using theodolites and tapes from several floor positions to determine positions relative to the magnets, aided by a precision line surveyed on the floor by the Fermilab survey crew. Prior to final survey the chambers were plumbed and rotated slightly until they were aligned along the optical paths, then clamped into position. The (x,y) positions transverse to the beam were finally aligned chamber-to-chamber by straight-through muons taken with the magnets off. This procedure allowed a final alignment (shifts) and typically amounted to several millimeters. In addition this procedure helped to smooth out miscalculated optical distortions in the apparatus (Appendix VI). The final accuracy of the positions of the chambers is estimated to be about 2 mm, which in general is smaller than the multiple scattering error for momentum measurement.

The chambers were connected to a gas plenum which circulated fresh 80% Ne + 20% He at 2 cm³/sec. About 2-3 weeks from air conditions were required to sustain good sparks (with a higher flush rate).

An event trigger causes a NIM pulse to actuate a spark gap driver, which in turn fires a thyatron across a capacitor bank. The

resulting 7.5 kV pulse triggers a 3 stage Marx generator for each WGOSC. Each stage is charged in parallel to -11 kV and switched in series by 3 spark gaps fired by the 7.5 kV pulse. The resulting -33 kV pulse is connected to the center electrode of each chamber.

Sparks are then produced along the ionization trail by charged particles traversing the chamber. The maximum time between the passage of a particle and the appearance of the 33 kV pulse for the production of a good spark was about 10 μ sec (the ion recombination time). To improve this time resolution and reduce the number of extraneous tracks, a 200 V/cm ion clearing field was applied between the center and outer electrodes. The resulting live time was about 2 μ sec.

The chamber labels are C1-C9 for the upstream to downstream calorimeter chambers and M3-M9 for the upstream-downstream magnet chambers.

Appendix III:

References

1. Scientific Accesories Corp. 002A.
2. E G & G Model HY-62.
3. F. Messing, unpublished thesis ,U of Penn., 1975.

Figures

A3.1 Schematic of chamber and fiducial construction.

CHAMBER AND FIDUCIAL POSITIONS

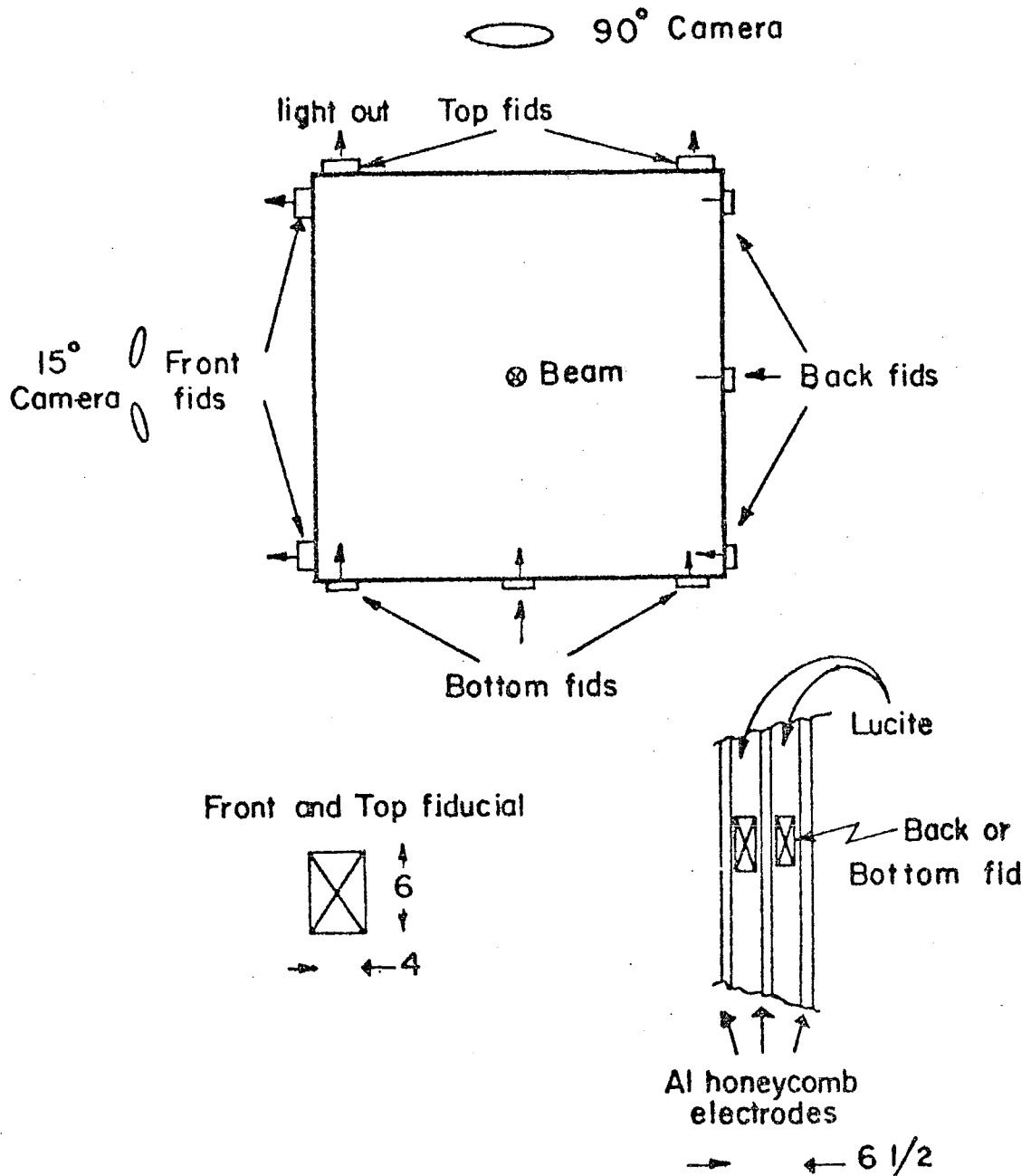


Figure A 3.1

APPENDIX IV

Muon Spectrometer Construction

The Muon Momentum Spectrometer consists of spark chambers and an allied optical system to record tracks and solid iron toroidal magnets to bend the muon tracks. The spark chambers and optics are described in Appendices III and V. The muon toroids were constructed in 2 types: 12' and 24' diameter magnets.

The 12' magnet consisted of 4 toroidal sections (figure A4.1). The sections were made by stacking together 6 flame-cut solid iron toroids (discs) each 20 cm thick, inner radius 15 cm, outer radius 183 cm (6'). The magnet sections were energized by 144 turns of hollow water cooled copper conductor, cross section about 2 cm² arranged in 12 coil bundles of 12 coils each. The magnets were driven into saturation at about 800 amps, the normal running current. Hall probes could be inserted into 3 mm radial gaps in each iron section to measure the magnetic field produced.

The 24' magnet was of similar construction, with 3 sections, each section consisting of 3 20 cm thick toroidal discs, inner radius 15 cm, outer radius 365 cm (12'). It also had 3 mm radial gaps for field measurement. Each section had 84 copper water cooled coils arranged in 7 bundles of 12 each, powered to 800 amps by standard beam line type power supplies². The total I^2R power dissipated by both magnets was about 400-500 kwatts. The low conductivity cooling water was circulated through cooling coils outside

the experimental hall at 90 psi, 120°F.

The magnetic field is given by

$$B = \mu(H)H.$$

Under the assumption that there are no air gaps and that the field lines are circles,

$$H = I/2\pi r$$

with r in meters, B in k Gauss, and μ , the permeability of iron is a function of H . With a small radial gap of width l , the magnetic field becomes

$$B = \mu I / (2\pi r + \mu l / \mu^0)$$

The fields were measured by commercially available Hall probes³ and calibrated with permanent magnets, the calibration being good to at least 0.1%. The calibrated fields are shown as solid lines in figures A4.2 and A4.3 for the 12' and 24' magnets respectively. The circular points are data points and the agreement is good to better than 5%. The relatively larger disagreement in the 24' magnet is probably attributable to worse radial gap tolerances and registration among iron pieces in construction, and also iron filings in the gap.

Appendix IV:

References

1. A. Benvenuti et al., N.I.M. 125, 457 (1975).
2. Transrex Corp, or LING Corp.
3. Bell, Inc.

Figures

- A4.1 12' magnet perspective view.
- A4.2 Magnetic field vs. radius 12' magnets; curve calculated.
- A4.3 Magnetic field vs. radius 24' magnets; curve calculated

12' MAGNET

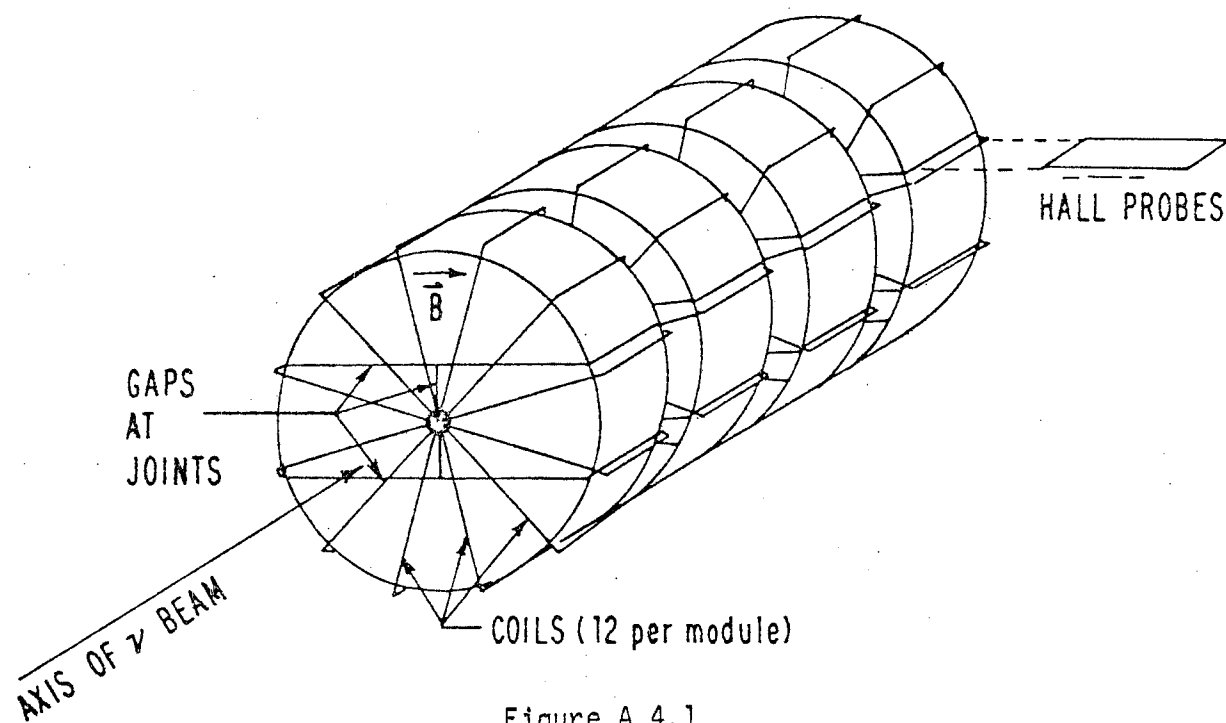


Figure A 4.1

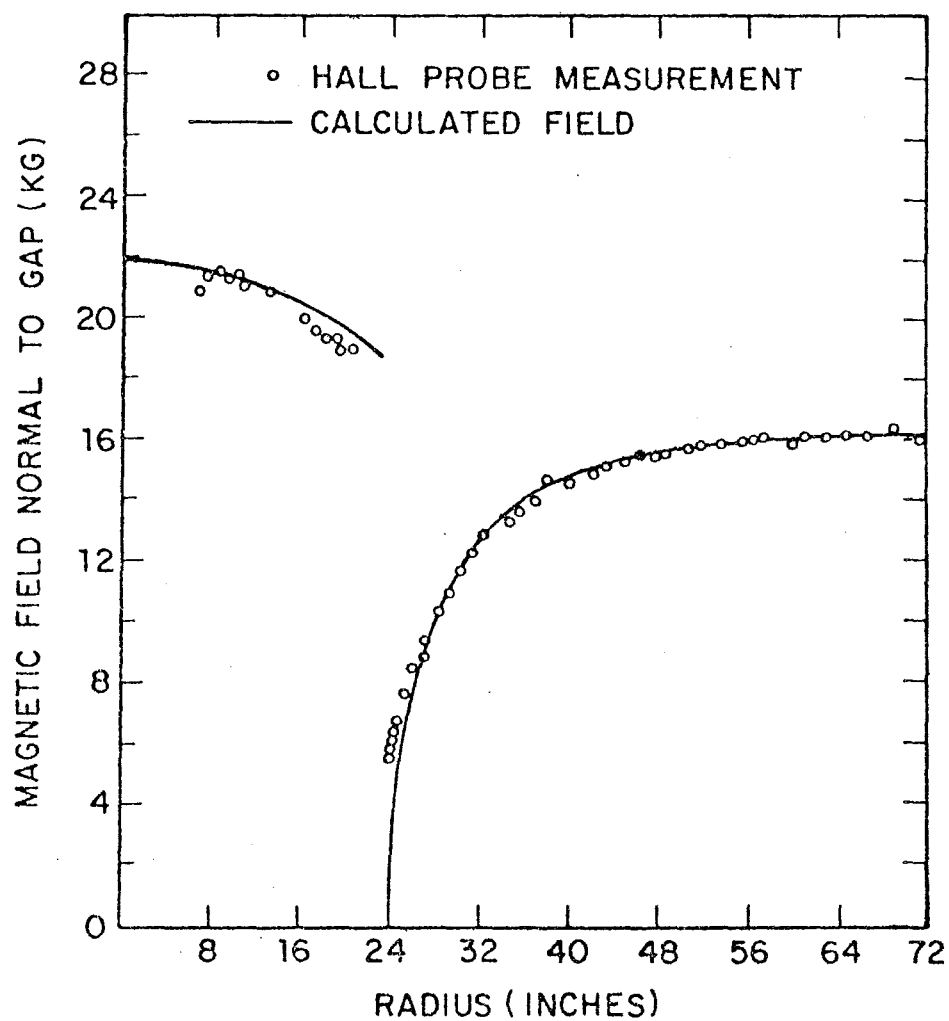
12¹ MAGNET FIELD

Figure A 4.2

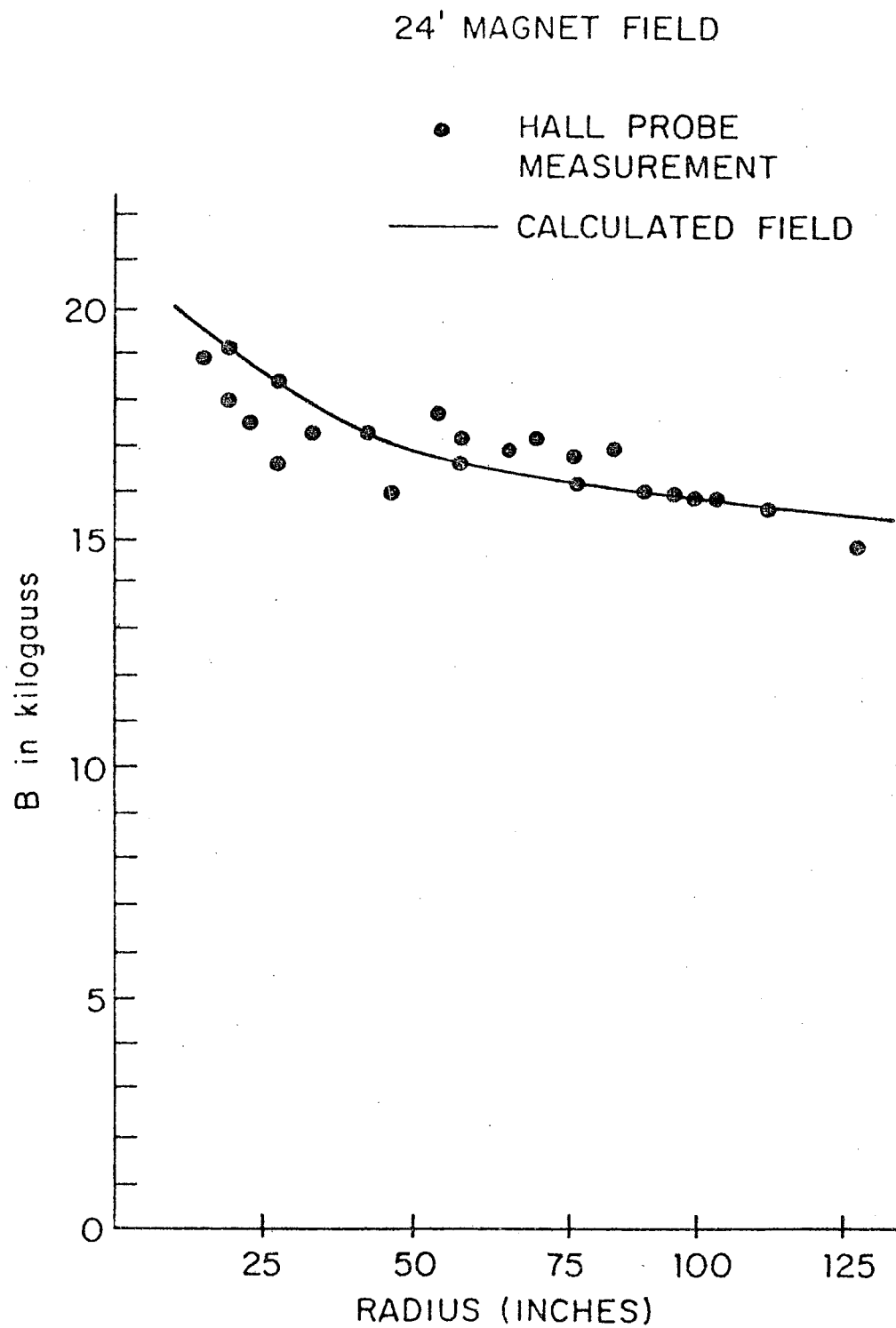


Figure A 4.3

APPENDIX V

Optics

The spark coordinates and directions were recorded on film using a folded mirror and camera system to view the chamber volume through the lucite windows ($\frac{1}{4}$ " on 12' chambers and $\frac{1}{2}$ " lucite on 10' chambers). In order to reconstruct tracks on space and remove ambiguities, each chamber was photographed in 3 views.

Two of the views were from the side of the apparatus with the optic axis located ± 7.5 degrees in the verticle direction (around z axis) from the horizontal (x axis). Positive x is toward the center of the camera lenses of these 2 views, called the 15° top and bottom views. The beam is the z axis, downstream being +z. Positive y is up. The third view, the 90° view "looks" along -y, down toward the floor of the apparatus from near the roof of the Hall. An equivalent system is shown in figure A5.1.

There were 2 mirror systems to image the 3 views onto cameras, the 15° optics and the 90° optics. The 15° optics imaged the 2 $\pm 7.5^\circ$ side views onto one film plane on 1 film transport (camera) through 4 lenses. The 15° mirror system, shown in figure A5.2, collected and folded the light paths from each chamber so that the chambers appeared to be adjacent to one another on the film without modules or toroids between them. This saved space on the film and made photographing such a large apparatus possible on one film plane. The collected light was reflected as shown into the sets of

stereo mirrors, schematically indicated as a box in figure A5.2, inclined at the proper angles to create the $\pm 7.5^\circ$ angles of view (figure A5.1). In the 24' magnet the $+7.5^\circ$ view is replaced by a 0° view due to space limitations in the verticle direction.

The 90° mirror system is shown in figure A5.3. It imaged the chambers onto 2 cameras, one for the calorimeters and one for the spectrometer.

Table A5.1 shows the path lengths and lenses for each system. The film transports were surplus aircraft cameras, modified to accept 500' reels of 70 mm sprocketed film, and were electrically driven, using pressurized air and vacuum to protect and clamp the film during the winding sequence.

In such a large optical system, optical distortions become a serious limitation to ultimate performance. These come from several sources. The most important is from non-planar mirror surfaces, followed by camera lense optics, measuring optics and chamber windows. To help remove these in the reconstruction precision grids were constructed, mounted on the chambers and photographed. Since the relative spacing between crossings on the grids is known, the relative optical error in spark position along the chamber is then corrected for in reconstruction. Corrections overall were typically about 1-2 cm, or 1% of the chamber size. The back and bottom fiducials were used to correct the optic axis positions as well as distortions. The lucite windows are also included in the optical paths during the determination of the spark positions. A discus-

sion of the reconstruction is in the following appendix.

Finally, a data box for each camera displayed run and frame numbers with an L.E.D. array, updated on each frame during the fiducial flash. Figures A5.4 and A5.5 show the film from the 90^0 view and a magnified portion showing the resolution between sparks for an unusual trimuon event.

Appendix V:

Figures

- A5.1 Equivalent optical system for 3 views.
- A5.2 Schematic of 15 optics.
- A5.3 Schematic of 90 optics.
- A5.4 90 view of an unusual 3 muon event;
- A5.5 Magnified portion of A5.4 showing separation of closely spaced tracks.

Table 5.1.

90° OPTICS

Chambers	Path Lengths	Lens Focal Length
M5-M9	24'	105 mm
M5'-M3	36'	80 mm
C6-C9	33'	135 mm
C1-C5	23'	105 mm

15° OPTICS

Calorimeter Top View	73'	300 mm
Calorimeter Bottom View	73'	150 mm
24' Magnet Direct View	44.9'	105 mm
24' Magnet Bottom View	47.9'	Same lens as 24' magnet (105 mm)
12' Magnet Bottom View	53'	Same lens as 24' magnet (105 mm)
12' Magnet Top View	55'	210 mm

There are five lenses in the 15° Stereo Camera. The fifth is for the data box.

All lenses are set to F16.

EQUIVALENT OPTICAL SYSTEM

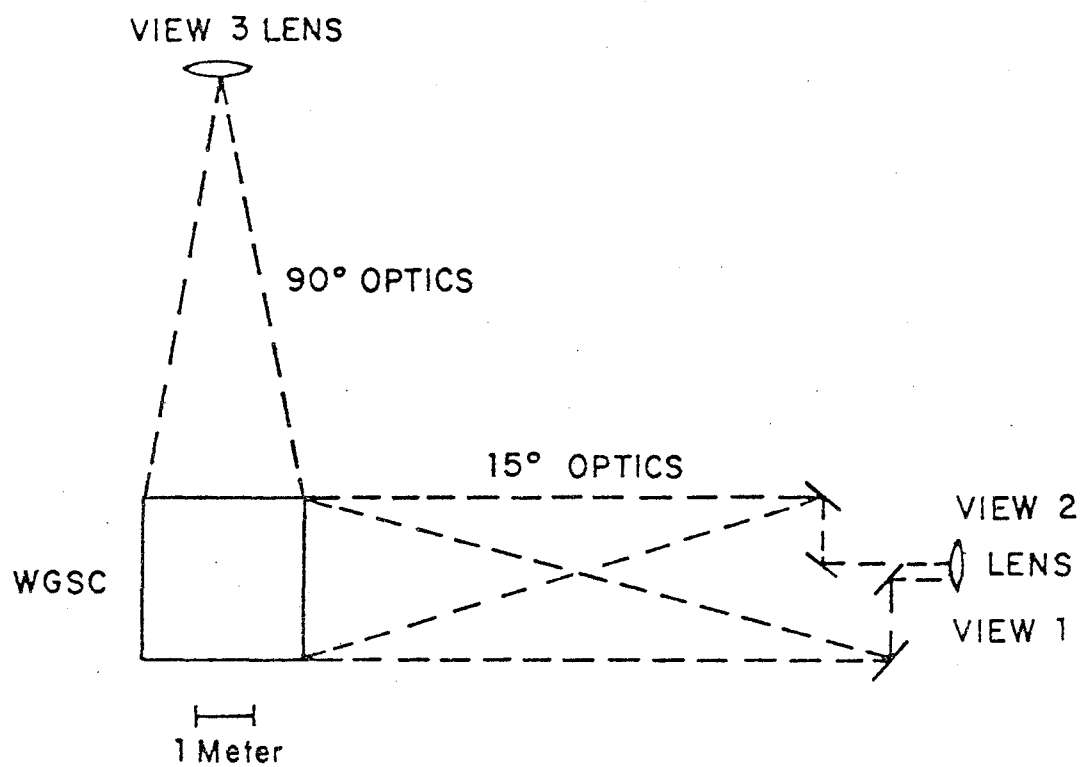


Figure A 5.1

15° OPTICS - TOP VIEW

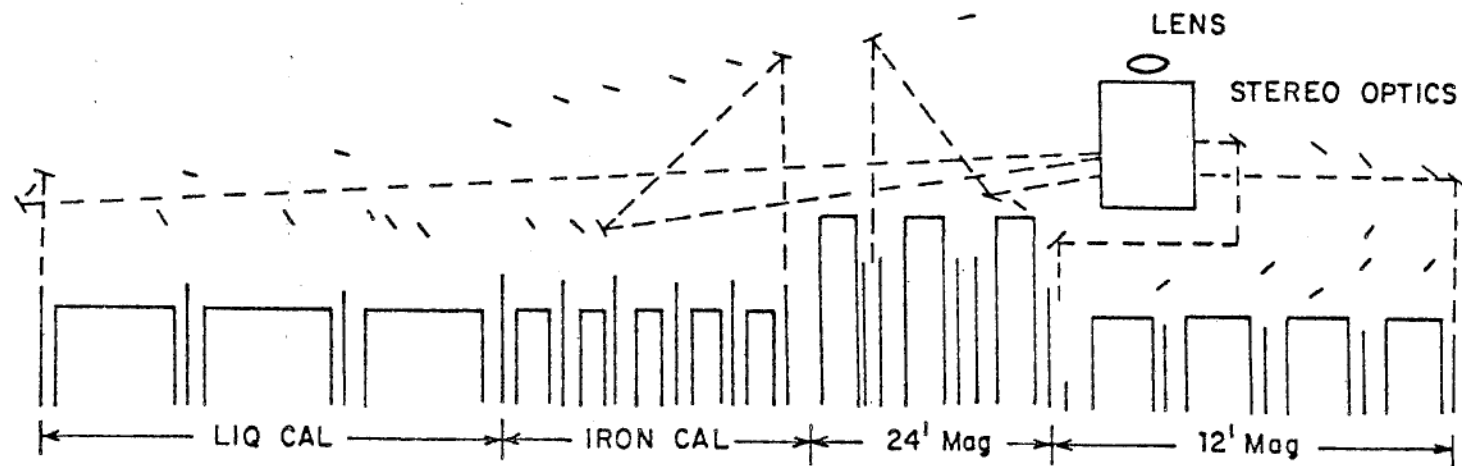
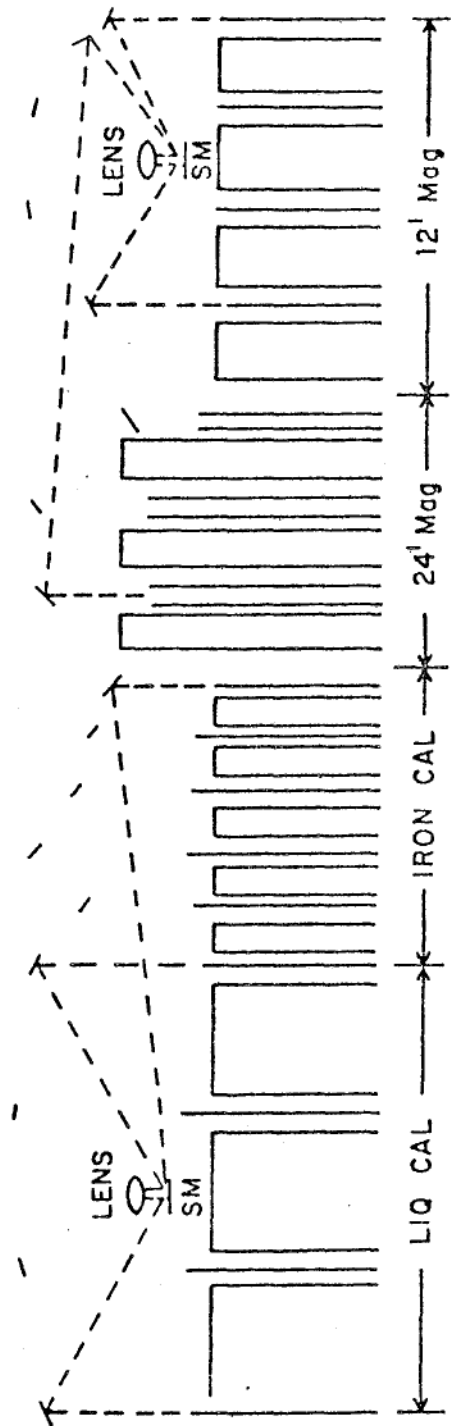


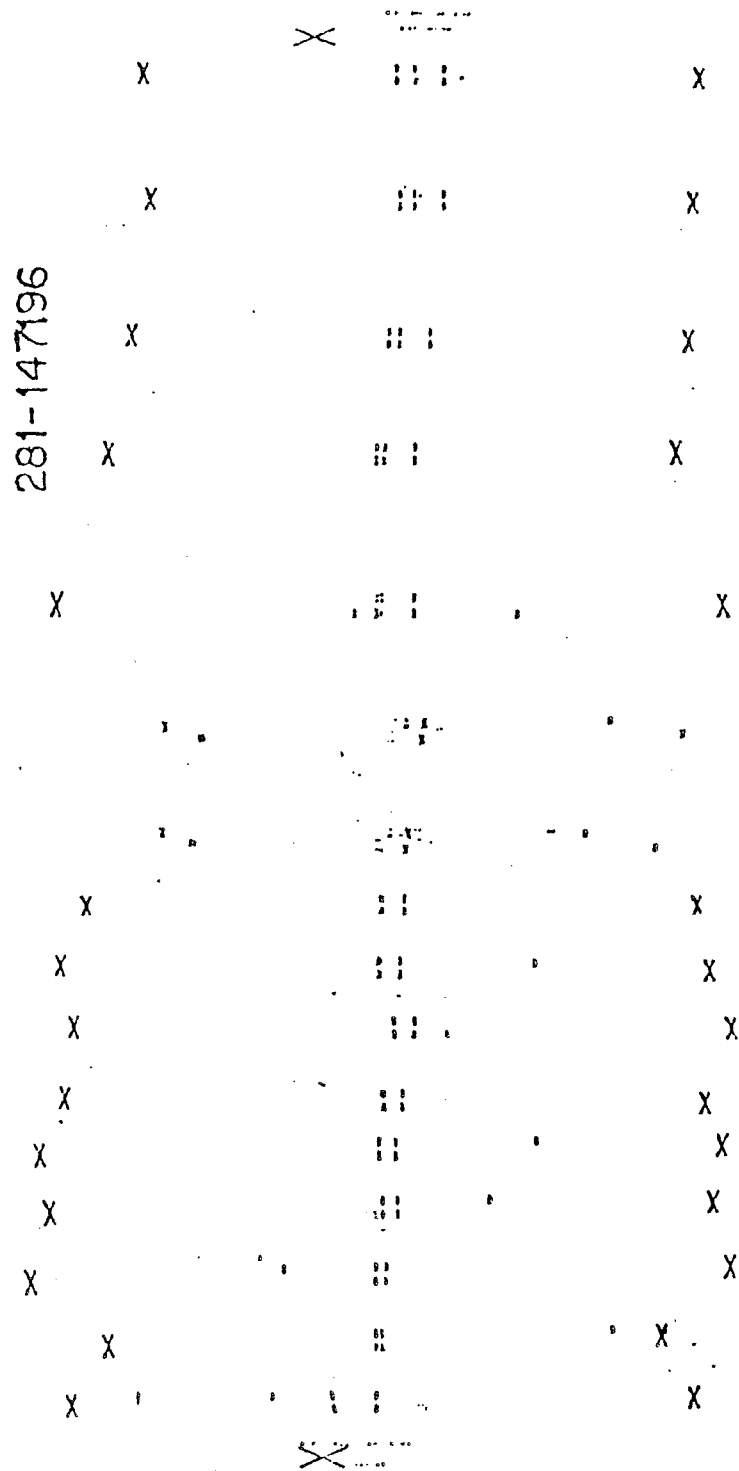
Figure 5.2

90° OPTICS - SIDE VIEW



SM = STRIP MIRRORS

Figure A 5.3



EVENT 281-196

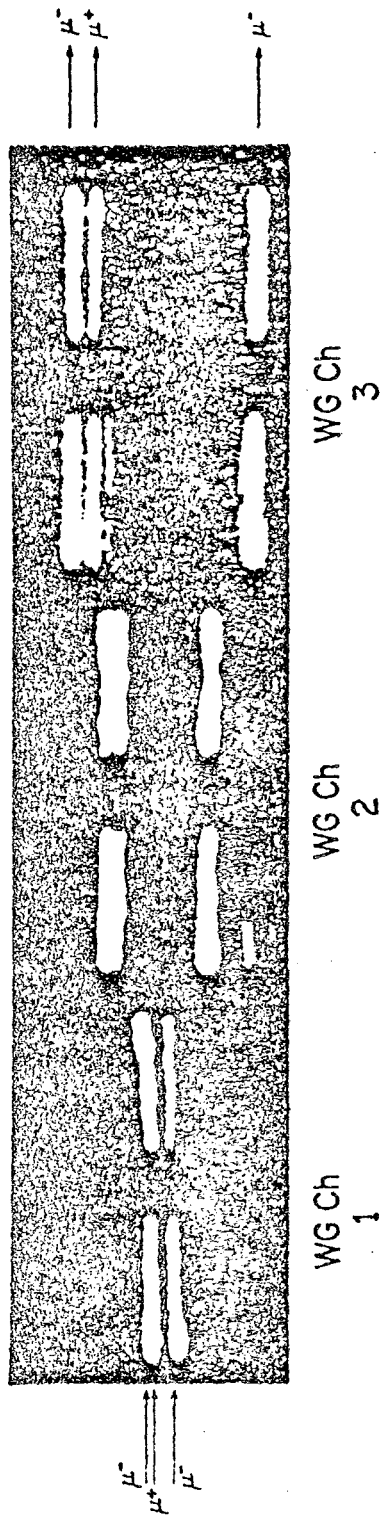


Figure A 5.5

APPENDIX VI

Reconstruction in Space

The spacial reconstruction of the spark coordinates relative to the apparatus, and ultimately relative to the magnetic fields, first required 2 factors to be known: the location in space of the fiducial marks on the chambers (Appendix III), and a measurement of optical distortions and the optical paths (Appendix V).

The reconstruction procedure is then the following. The film for an event was digitized by image plane machines at University of Wisconsin or by SAMM¹ at F.N.A.L., taking 6 (x,y) points on each spark in each view and 1 on each fiducial. The sparks in each view are labeled and, for dimuon events, matched from view-to-view and chamber-to-chamber into tracks by measures. The three stereo images of a spark are then converted to real space projections on the fiducial plane in each stereo view from knowledge of the fiducial positions, optical distortions and the optical axes. Projective rays are then traced from the camera position through the planar spark in each view. The distance of closest approach of these rays from each other is then calculated. The spark in space is then defined as the skew line segment which minimizes the distance of closest approach between it and all of the projected rays. This procedure is illustrated in figure A6.1. Except for calculated sparks outside of the chambers, all combinations of (x,y) coordinates and (α,β) direction cosines for the skew segments are then published on the reconstruc-

tion output for each calculated spark. A degree of optimization is attempted by trying to match planar sparks in the 15° views by similar projected ray slopes.

The resolution on individual sparks was about 1 mm for position and about 10 mrad for spark angle. Measurement error contributes typically less than 1 mrad.

A final step considered as part of reconstruction for multimoun events was to manually match reconstructed sparks into tracks from chamber to chamber. This was accomplished by a Pairing Program by displaying on a video terminal all the reconstructed sparks in the 90° (plan) and 15° (elevation) views. A physicist then picked out the proper total trajectory in each view. A spark associated with the trajectory in one view but not in the other because of ambiguities in the reconstruction could then be eliminated by noting the position of a given reconstructed spark relative to the trajectory in both views. In addition, the pairing program fitted preliminary trajectories through the selected sparks enabling further judgment for proper tracks. This was especially useful in the calorimeters, where the large number of sparks associated with hadron showers made the combinatorial problem for automatic track matching intractable.

Appendix VI:

References

1. D. Bogert et al., Proc. Oxford Conf Comp. Scanning, (1974).

Figures

A6.i Schematic of the reconstruction strategy.

RECONSTRUCTION of SPARKS

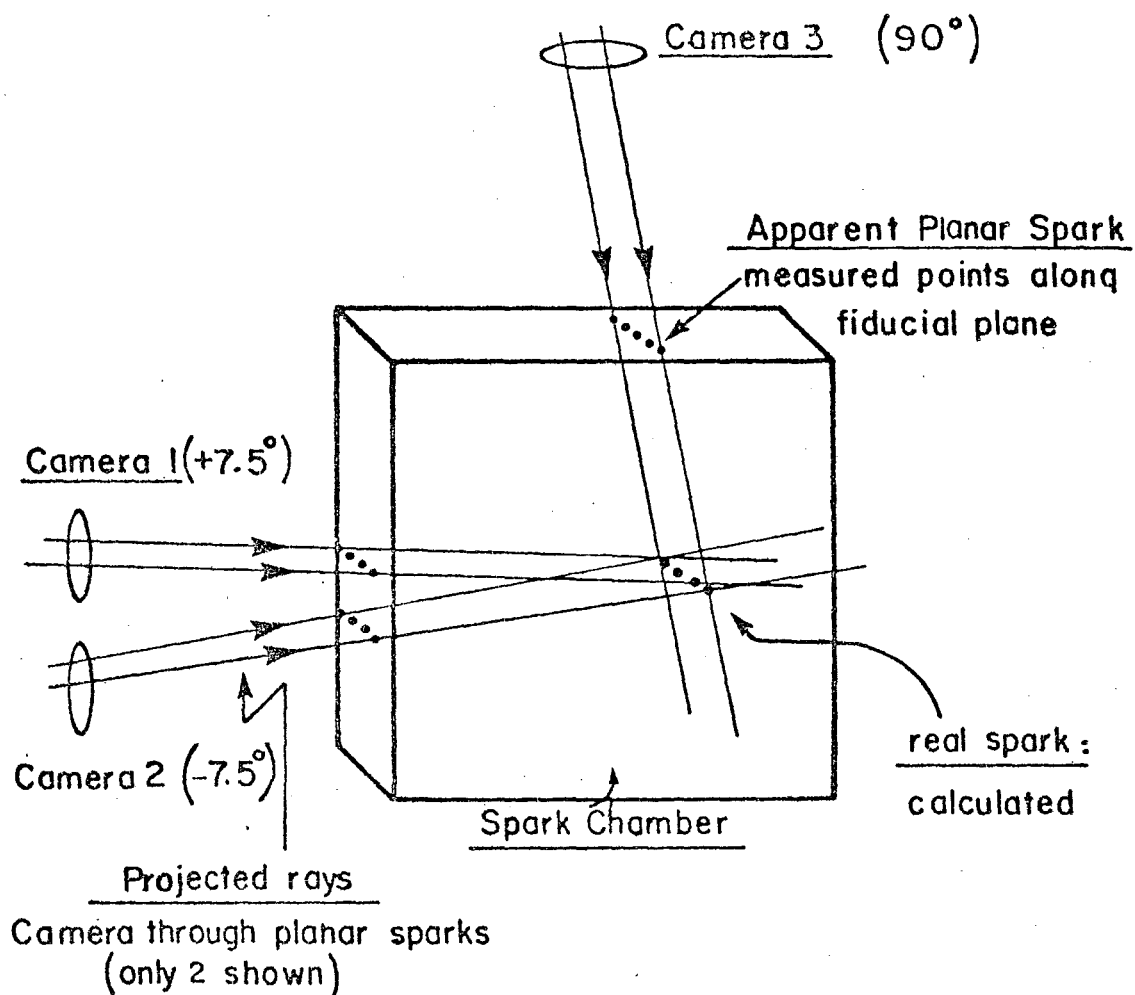


Figure A 6.1

APPENDIX VII

Momentum Fitting

The momentum fitting procedure requires 2 preliminary pieces of information. They are the values of the magnetic field B in space (Appendix IV), and the matched spark coordinates and direction cosines (Appendix VI).

A charged particle moving in vacuum through a constant magnetic field \vec{B} with momentum \vec{p} will traverse a circular helix which is obtained by solving the Lorentz force law

$$\frac{d\vec{p}}{dt} = q(\vec{\beta} \times \vec{B})$$

where $\vec{\beta}$ is the velocity and \vec{B} is the field. The helix is given parametrically by

$$\begin{aligned} x &= (-1/k) \sin(\phi_0 - ks \cos\lambda) - \sin\phi_0 + x_0 \\ y &= (1/k) \cos(\phi_0 - ks \cos\lambda) - \cos\phi_0 + y_0 \\ z &= s \sin\lambda + z_0 \end{aligned}$$

where \vec{B} is locally $(0,0,B)$, s is arc length, λ is the dip angle and ϕ_0 is the azimuth angle of \vec{p} at $s=0$. The projected curvature k is given by $k=1/\rho$ and $p=qB\rho/\cos\lambda$. An orbit is shown in figure

In the case of solid toroids, energy loss must be added to the analysis. The equation of motion becomes

$$\frac{d\vec{p}}{dt} = q(\vec{\beta} \times \vec{B}) + e\vec{p}$$

ϵ is a retarding force in the direction of p . By assuming a relation $(p/p_0) = (R/R_0)^\alpha$ where p_0, R_0 are the momentum and range at the beginning of the track, $\alpha = \frac{R}{p} \frac{dp}{dR}$, s is the distance along the track, and $s/R^0 = w$, the equation of motion then becomes:

$$p \frac{d^2 \vec{x}}{dw^2} + \frac{dp}{dw} \frac{d\vec{x}}{dw} = s_0 q B \left(\frac{d\vec{x}}{dw} \times \vec{B} \right) + R_0 \epsilon \vec{p}$$

The exact solution for a constant field is essentially a slowly expanding helix for momenta above about 3 GeV. Over small "boxes" in the magnet the field can be taken as uniform, the energy loss is small and the trajectory in a "box" is computed.

To fit for the momentum of a track, an iterative scheme was programmed to minimize the function:

$$\begin{aligned} X^2(p_x, p_y, p_z, x_0, y_0) = & \\ & \frac{(x_i^{sc} - x_i^c)^2}{\sigma_x^2} + \frac{(y_i^{sc} - y_i^c)^2}{\sigma_y^2} \\ & \frac{(\alpha_i^{sc} - \alpha_i^c)^2}{\sigma_\alpha^2} + \frac{(\beta_i^{sc} - \beta_i^c)^2}{\sigma_\beta^2} \end{aligned}$$

where $p = (p_x, p_y, p_z)$ is the initial momentum and x_0, y_0 are the transverse coordinate of the muon track at some arbitrary z point, usually at chamber 7. The sum over i is over all the spark chambers in the fit. The measured spark transverse coordinates and direction cosines for a spark in the i^{th} chamber $x_i^{sc}, y_i^{sc}, \alpha_i^{sc}, \beta_i^{sc}$ are

read in from the reconstruction program. The corresponding variables with superscript c are calculated variables at each chamber and are a function of p , x_0 and y_0 , where the value of B for the helix is locally calculated along with the energy loss in the iron. The values of p , x_0 and y_0 are fed in from the previous iterations. The initial guess for p is obtained from a circle fit to the first sparks of a track, the radius being roughly proportional to the momentum.

In obtaining the best fit, the program also attempts to minimize χ^2 by dropping altogether a spark with a large contribution to χ^2 , or by using just either spark position or direction.

The output of this program PFIT, written by Don Reeder, is \vec{p} and \vec{x} , the momentum at a point in the apparatus, normally at chambers C6-C9 at the end of the apparatus. The final value of the momentum is then given by adding the range between the event origin and x , normally being less than 5 GeV.

Appendix VII:

References

1. R.P. Shutt, ed., Bubble and Spark Chambers, vol. 2, pg 3, Academic Press, 1967.

Figures

- A7.1 Orbit of a negatively charged particle of constant energy in a uniform magnetic field.

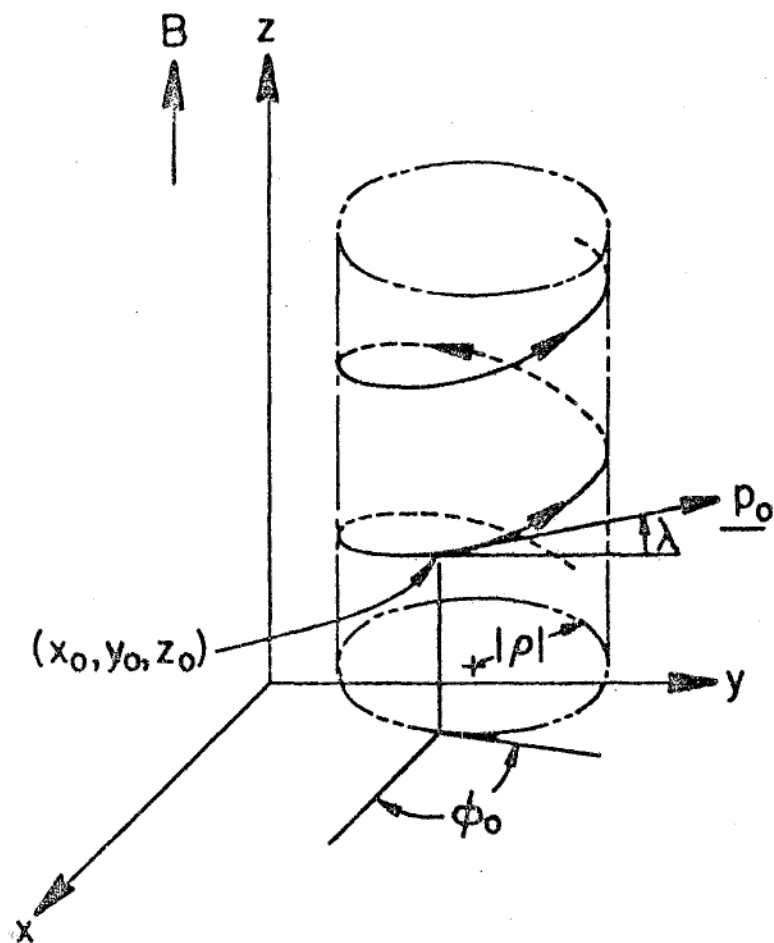


Figure A 7.1

APPENDIX VIII

Trigger Counters, Trigger Logic and Data Acquisition

1. Trigger Counters

The trigger counter modules for the F_1 , F_2 , F_3 , T, H and V counters are liquid scintillator counters constructed identically to the modules in the iron calorimeter. See Appendix 2 and figure A2.3 therein. The H and V counter phototubes have additional magnetic shielding in the form of iron cylinders and 2" long lucite spacers to move the tubes further into the iron shield. The HV counters also have X8 amplifiers directly mounted on the tube base with coaxial cable runs. The V (vertical) counters, mounted in the 24' magnet so that the tubes and strips are vertical, have conical lucite window inserts protruding into the liquid to increase optical coupling and to reduce the effects of oil films, dirt and air bubbles on the windows.

The vertical and horizontal (HV) counters form a crossed hodoscope with 1.2' resolution in space, placed in the 24' magnet. They are shown in figures A8.1 and A8.2 and are formed from 4 trigger counter modules each. There are 20 vertical and 20 horizontal strips each 23.5' long when overlapped. Due to space limitations the vertical counter was split into upstream (bottom) half, VU, and downstream (upper) half, VD, inserted into the 2 gaps of the 24' magnet respectively. The strips were read out by actively adding

the pulses from opposite tubes. The H counter was immediately logically combined into 20 strips while the vertical counter was read out as 40 VU and 40 VD strips. The hits in the strips were latched in CAMAC as well as being formed into the trigger logic. Figure A8.4 shows the hodoscope logic. The AND/OR circuits were used in OR for the vertical counters during the data analyzed in these runs.

The $F_1 - F_2$ counters installed after the 3 blocks of the iron target, were also identical to the Fe Cal slabs, but each were segmented by reading out as 2 sets of 4 horizontal strips in the bottom and middle and one set of 2 horizontal strips at the top. These were then combined logically to form an F counter signal. The top strip, F_{top} was also used as part of the veto in some of the triggers, as this portion of the iron target was higher than the liquid calorimeter.

The T counter was the logical OR of the last 2 iron calorimeter modules and has no segmentation.

The B,C counters were liquid scintillator counters constructed of 3 tanks as shown in figure A8.3, measuring $3.6 \times 1.2 \times 0.1$ m, viewed on each end by 4 phototubes (8/tank). These bottom, middle and top (B_B etc) sections were separately read out and latched, and fanned to the trigger logic as B and C signals. Counters A, the veto counter, was identical with B,C except for an extra tank (4 altogether), and the cracks were covered by strips of

plastic counters. Thus A had 5 signals latched, A_{bb} , A_b , A_m , A_t and A_{strip} .

2. Trigger Logic

The overall trigger system was described in the introduction to the apparatus (Chapter 2, section 5). Figure A8.4 explains the logic to derive subtriggers DIMU and HV. DIMU basically requires 2 or more muons in the hodoscope in order to enrich the multimMuon sample, while HV requires a 2-fold coincidence in the hodoscope. Figure A8.5 shows the analog and threshold logic for the 2 calorimeters. The Fe C used module Fe C (1-8) only to form a trigger, to minimize events which would cause hadron punch through into the spectrometer. Figure A8.6 shows various simple sub-logic parts for the trigger counters. Figure A8.7a shows the timing sequence of spill splitting: the targetted protons are divided logically into spill 1 and spill 2. Figure A8.7b shows how this was used to redefine HV as DIMU for spill 1 and HV + DIMU for spill 2, to enrich the multilepton sample in spill 1, and to obtain an unbiased sample of events in spill 2.

The event triggers are shown in figure A8.8. The ABC trigger was used every 10 spills to obtain Landau distribution muons through the calorimeter, where the "test" signal was generated via the acquisition program. A' BCT was used in spill 1 to obtain a sample of events with low hadron energy, basically low y events. (Also

called "quiet" muon events.) Since nearly all the neutrino energy is carried by the muon at low y , the muons will be at small angles and magnetically stiff, penetrating to the B and C counters. The next trigger, A T' DIMU, is a dimuon trigger from the iron target. Since single muons are basically not useful from the iron target, this is the only iron target trigger. In addition, this trigger is active in both spills thus providing a monitor for the spill splitting. The last 2 triggers, requiring energy, do not require deep muon penetration in the spectrometer (requiring only the hodoscope) and are thus sensitive to high y events. These triggers are A' Eliq HV and A' $E_{Fe\ 1-8}^{HVT}$. In addition, these 2 triggers enrich the dimuon sample in spill 1 since HV \rightarrow DIMU as described above. The last 2 logic cells shown are A' $E_F\ 1-5$ DIMU T and AT'DIMU F_{3-10} , which were latched in an attempt to monitor the behaviors of the dimuon triggers ($E_F\ 1-5$, F_{3-10} are shown in figure A8.5), however these were unreliable as they had no TOF's.

3. Data Acquisition

Figure A8.9 shows the acquisition logic, and figure A8.10 shows the time sequence of events. The Main Accelerator Control (MAC) system generated a beam gate about 2-5 msec before the neutrinos arrive at the target-detector lasting between 2-5 msec during which time events were accepted. If triggered, a veto locks out further triggers (Event Veto). CAMAC² gates were then generated, recording

the appropriate delayed ADC, TOF, Pattern Unit and Hodoscope information. Subsequently the spark chambers were fired and about 25 μ sec later (due to RF noise and ringing) a computer interrupt (A) was generated, causing the CAMAC information to be read into a buffer spare (about 1 msec). During this time a fiducial flash and camera advance sequence were initiated. At the end of each spill regardless of an event occurring a second interrupt (B) was generated, buffering apparatus scalars and the beam monitoring information (SEM, 90° M) from CAMAC to the computer. The computer system consisting of a D.E.C. PDP-11 interfaced with a BISON Box (interrupts) and an E.G.G. BDØ11 to an A-1 type crate controller (CAMAC) then wrote the buffer onto magnetic tape. The disc operated system allowed use of a FORTRAN program to perform diagnostics between spills. Landau Distributions, TOF histograms, and bit patterns helped in the checking of tubes and logic. After each run, a summary was generated. Table A8.1 is a complete list of TOF, P.U. and Scaler information recorded, and figure A8.11 shows a typical event display.

Appendix VIII:

References

1. RCA 8575.
2. CAMAC is a bus-oriented, modular digital data acquisition system supported by the NIM committee, and described in the IEEE tutorial issue on CAMAC (1970).

Figures

- A8.1 Schematic of the Verticle hodoscope.
- A8.2 Schematic of the Horizontal hodoscope.
- A8.3 B,C counters.
- A8.4 Hodoscope logic.
- A8.5 Calorimeter analog and threshold logic.
- A8.6 Sub-logic for counters and triggers (2 pages).
- A8.7a Time sequence for spill splitting.
- A8.7b Spill 1 HV, Spill 2 HV+Dimu definition.
- A8.8 Event triggers.
- A8.9 Acquisition logic schematic.
- A8.10 Time sequence of data taking.
- A8.11 Event displays, reduced from computer output.

Table A8.1. Pattern Unit, T.O.F., and Scaler Data

Bit	Pattern Unit #1	Pattern Unit #2	TOFS					
1	A bottom bottom	Vert.Hodo Upstrm 1	H					
2	A bottom	" " Dwnstr 1	ABC					
3	A middle	" " Upstrm 2	A'BCT					
4	A top	" " Dwnstr 2	A'EliqHV					
5	A strip	Horizontal Hodo 1	A					
6	B bottom	" " 2	B					
7	B middle	Fe Target #1	C					
8	B top	" " #2	V					
9	C bottom	" " #3	A Dimu T'					
10	C middle	" " Anti	HV					
11	C top		A'EFe HV T					
12	T (Fe9*Fe10)		F sum					
13	Eliq	FeCal 3-10 5/8.thrsh						
14	EFe	Dimu flag						
15	EFe 1-5 HV A' T	Spill 1						
16	Pix ON	Beam ON						
Scalers	V3 A EfA' Clock2 A T	V4 B E1A' E1HVA F1	H3 C EfE1A' EfHVTA' F2	H4 F DmuT'A BCTA' F3	V1 HV SEM clock1	V2 ABC 90° E1DmA'	H1 DimuAT' ASp1 EfDmTA' #spills	H2 ATF ASp2 BCDmTA'Sp1 #events

VERTICAL HODOSCOPE

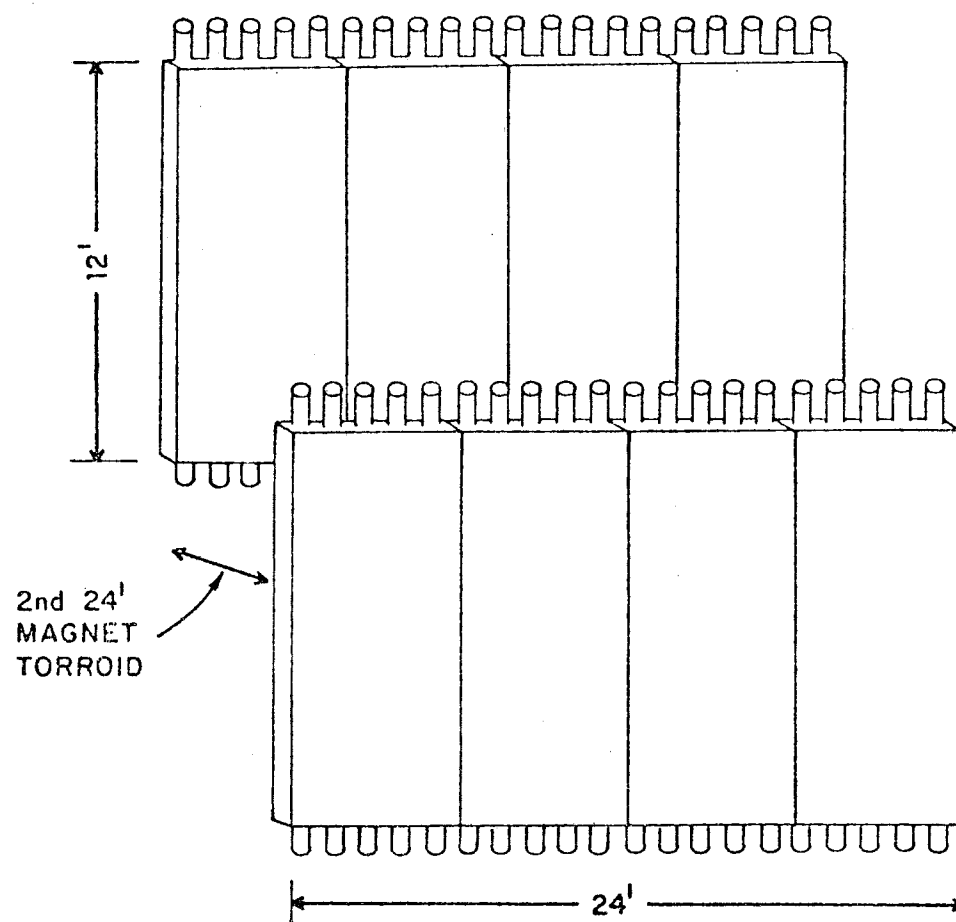


Figure A 8.1

HORIZONTAL HODOSCOPE

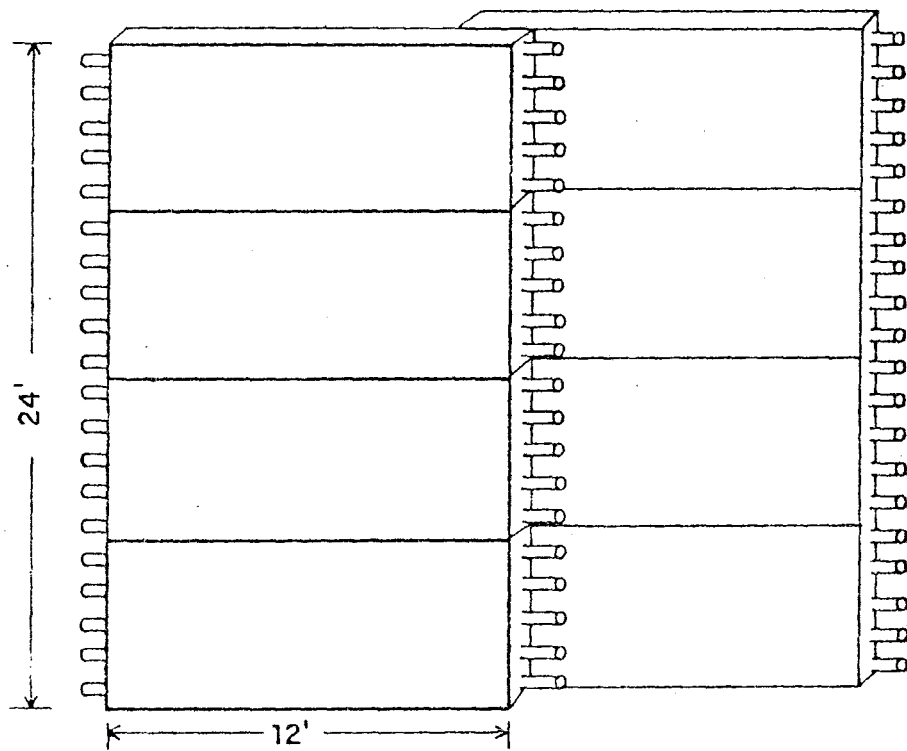


Figure A 8.2

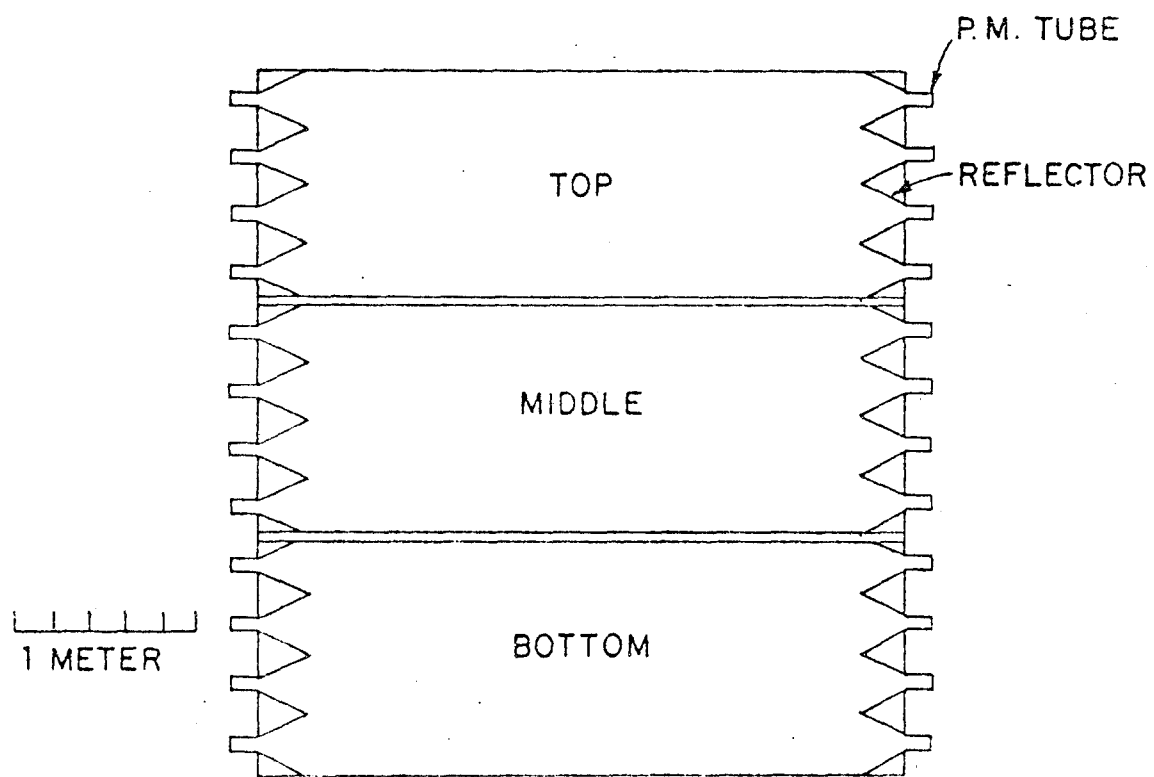


Figure A 8.3 LIQUID SCINTILLATOR TRIGGER COUNTERS B AND C

HODOSCOPE LOGIC

ML = MULTIPLICITY LOGIC UNIT

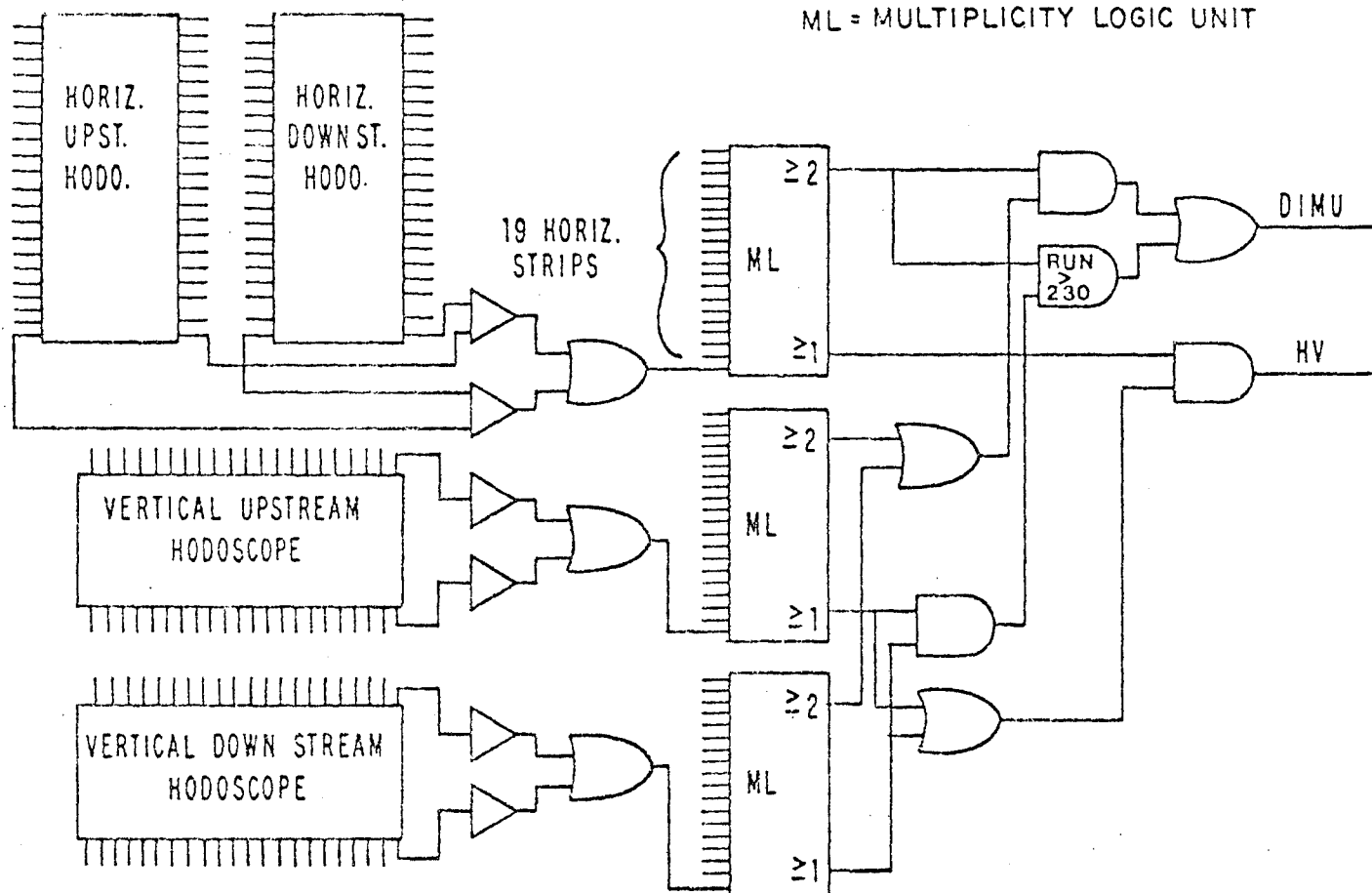
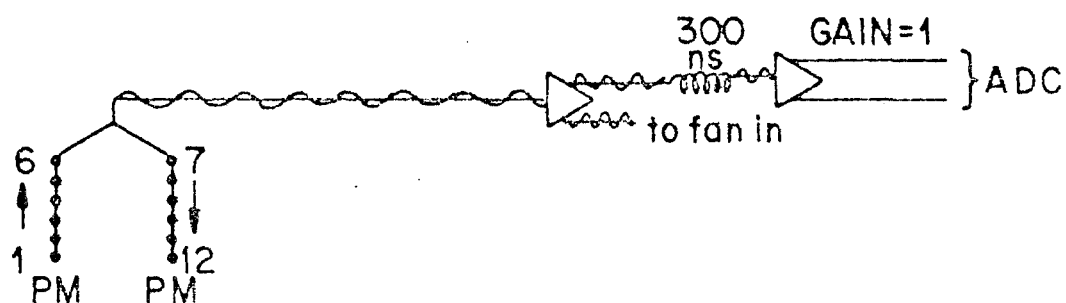


Figure A 8.4

Liquid Calorimeter Analog to Digital



Liquid Calorimeter Energy Trigger

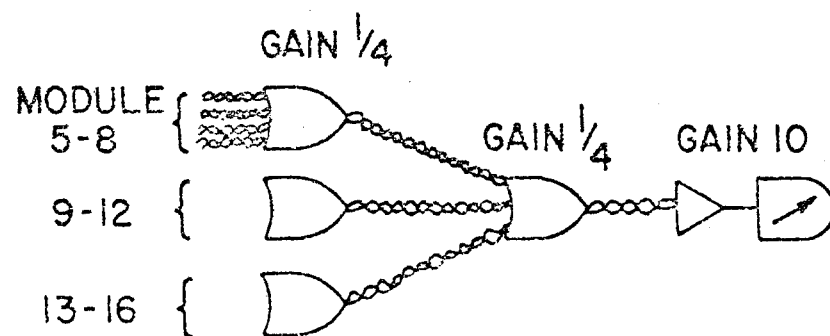
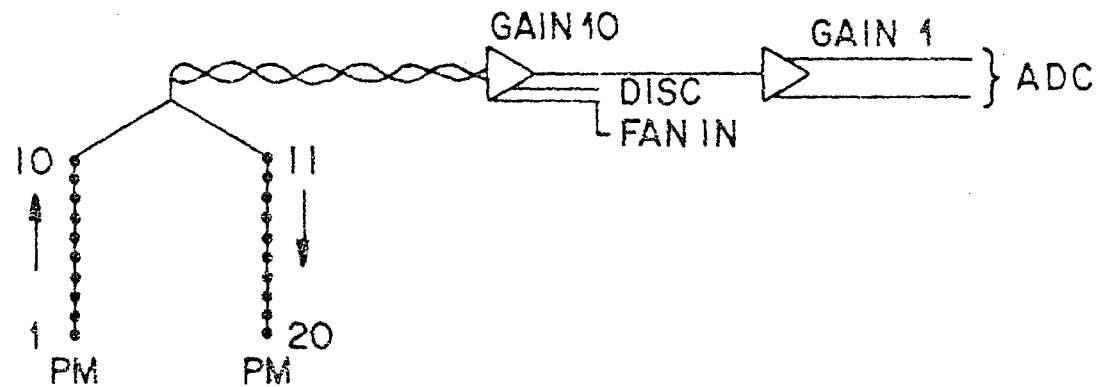


Figure A 8.5

Iron Calorimeter Analog to Digital



Iron Calorimeter Energy Trigger and Latches

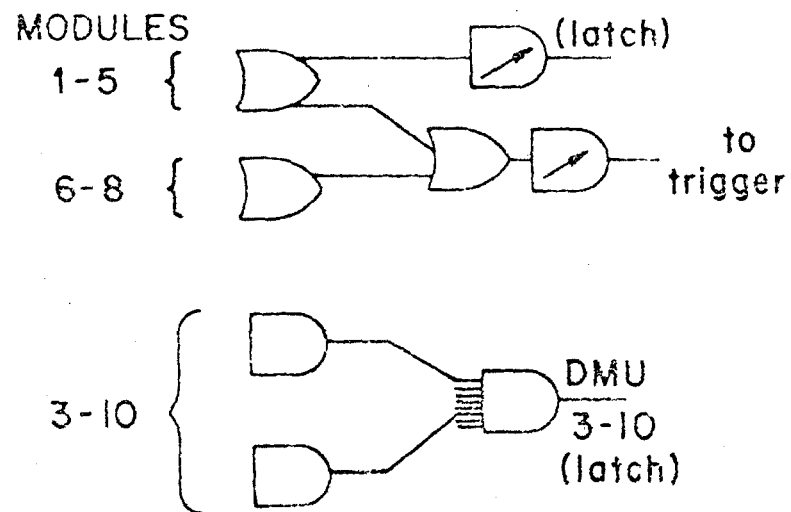
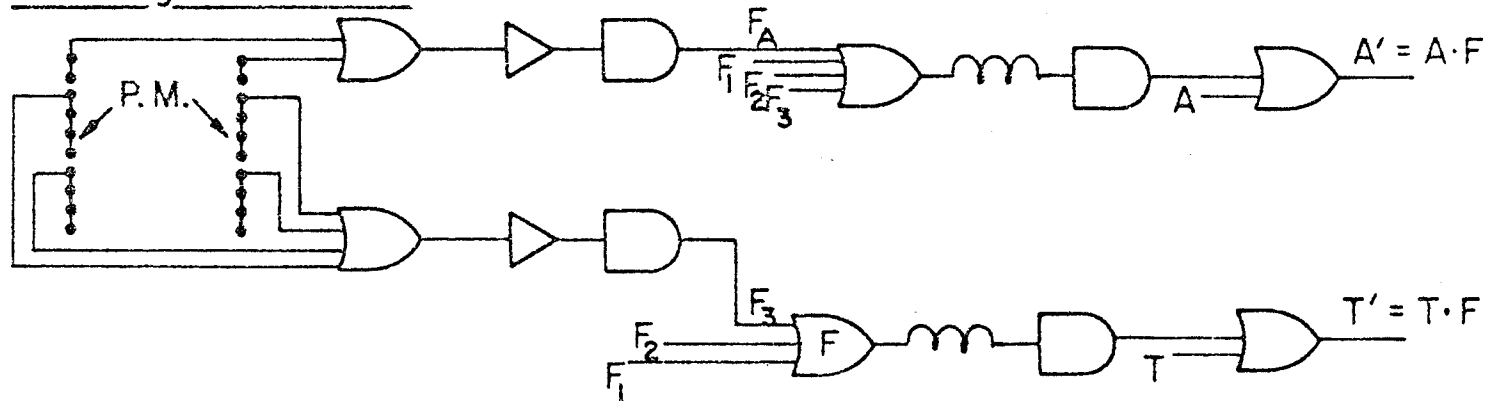


Figure A 8.5 (continued)

Fe Target Counters



A.B.C. Trigger Counters

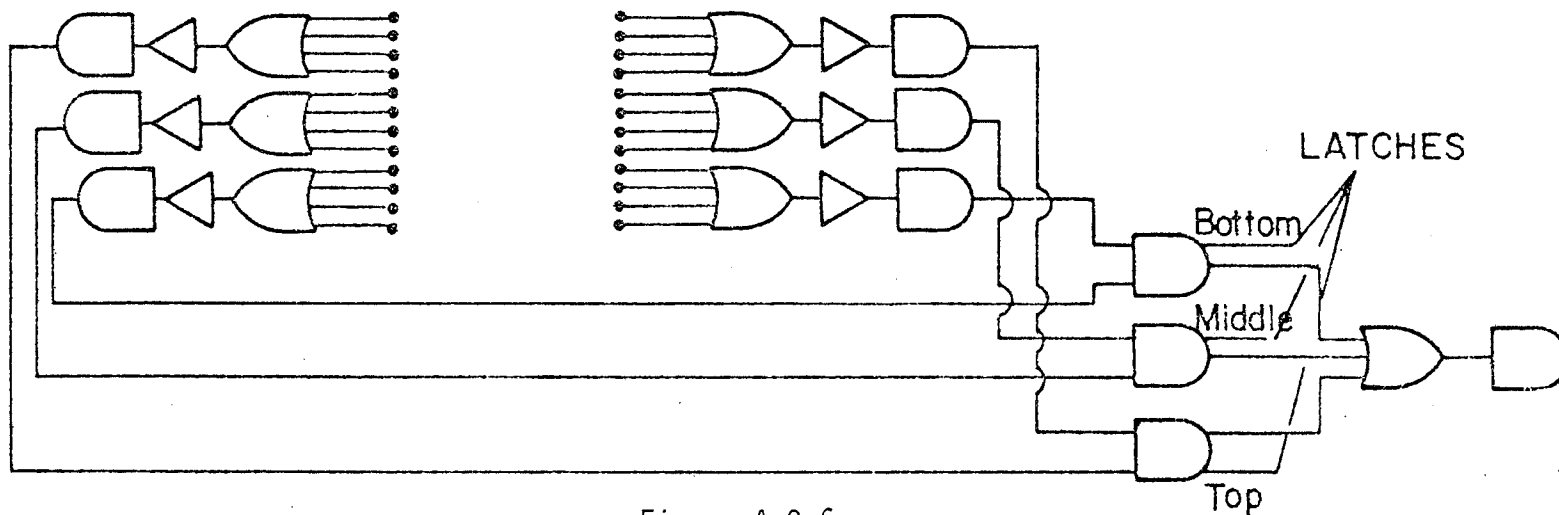
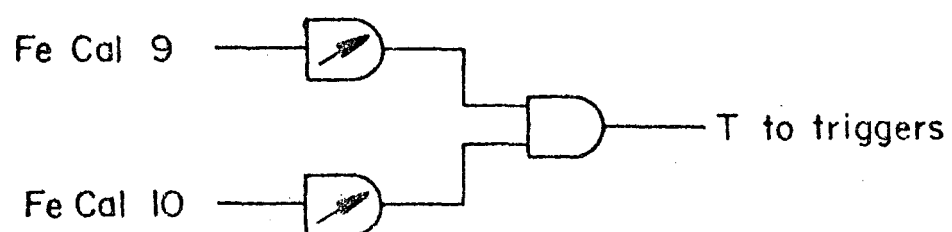
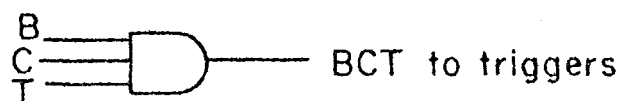


Figure A 8.6

T counter sub-logic



BCT sub-logic



ABC sub-logic

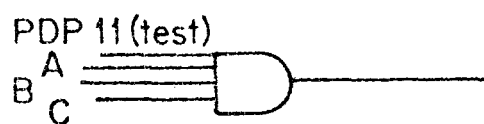


Figure A 8.6 (continued)

Spill 1 - Spill 2 Time and Logic

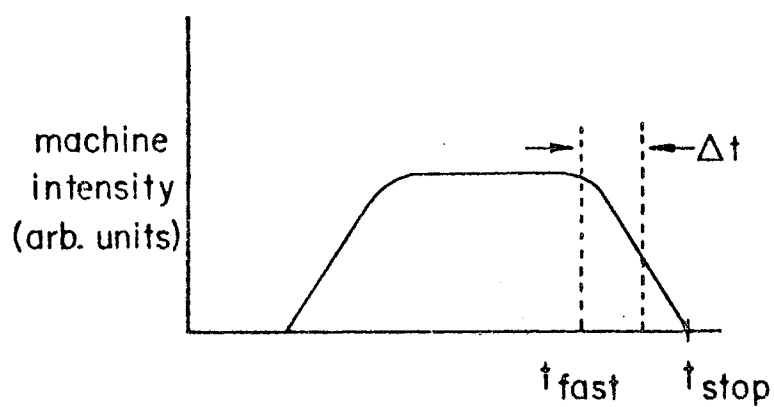
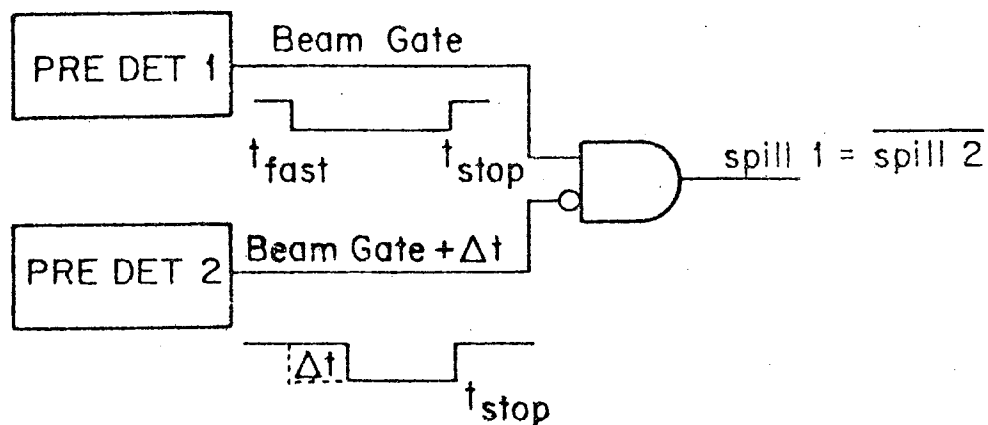


Figure A 8.7a

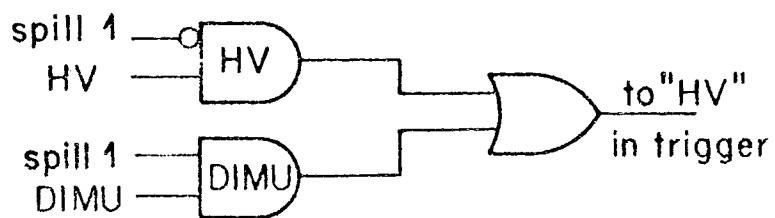


Figure A 8.7b

Event Triggers

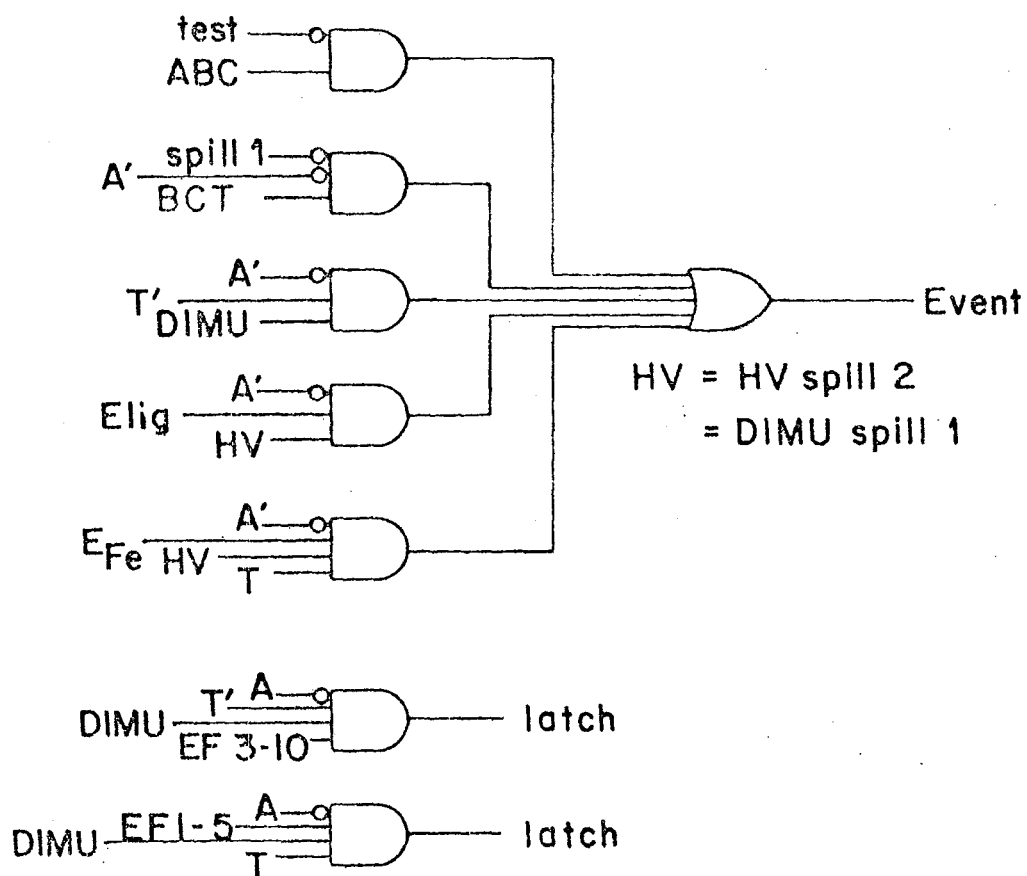


Figure A 8.3

Acquisition Logic

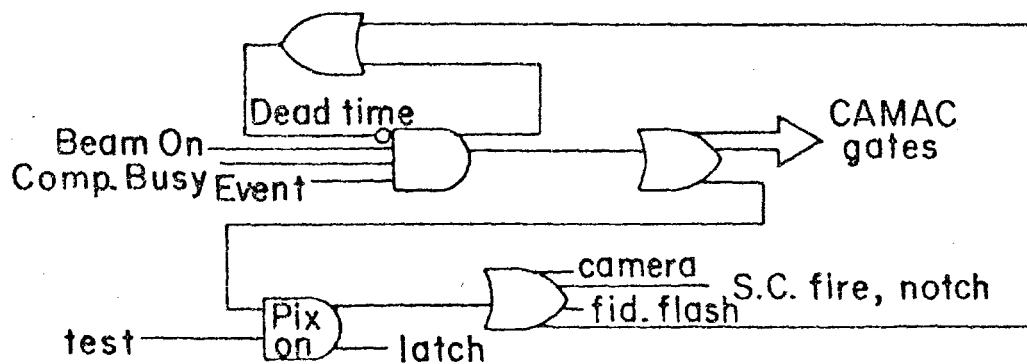


Figure A 8.9

SPILL SEQUENCE

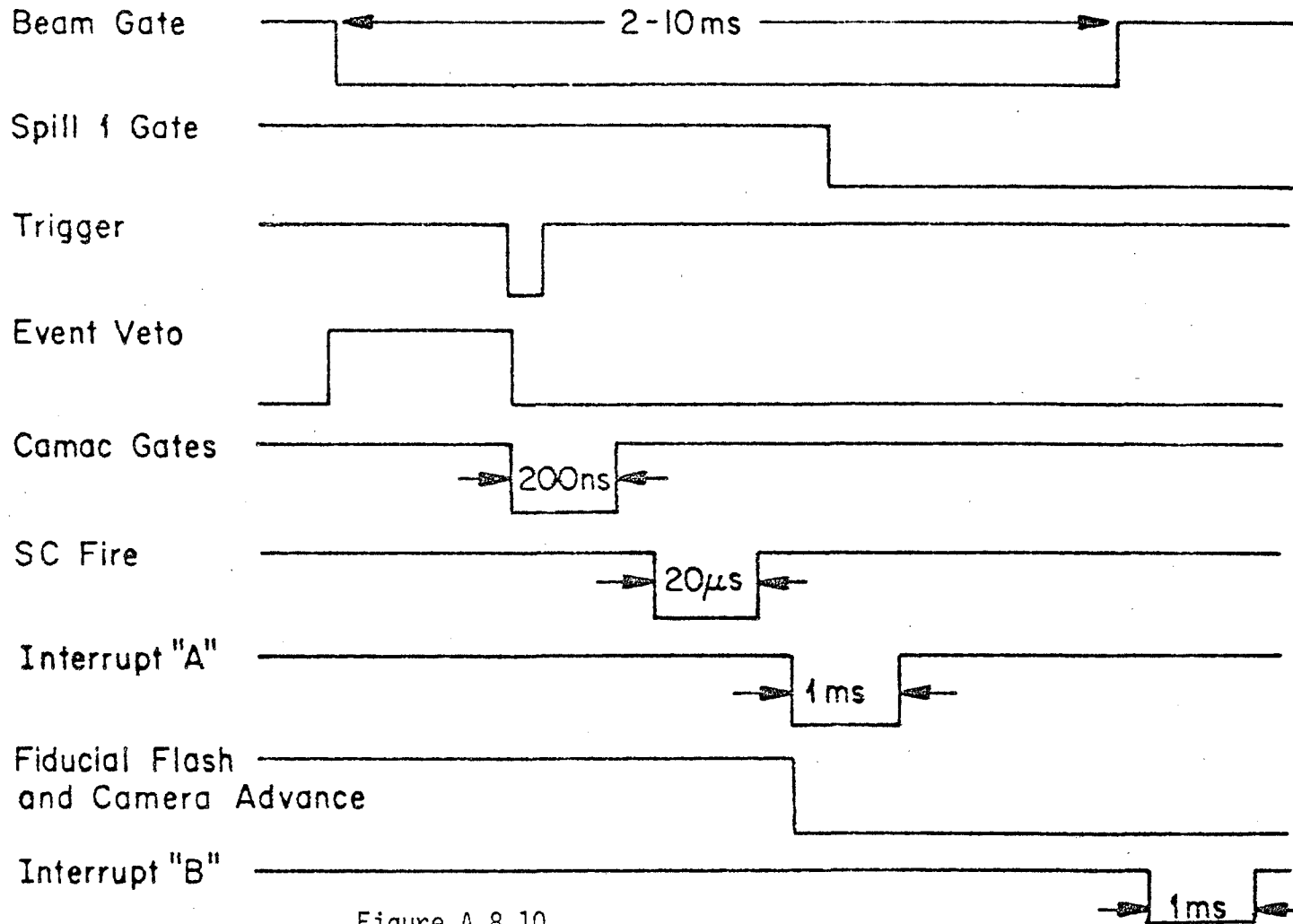


Figure A 8.10

Figure A 8.11 Reduced online computer display of electronic information in an event.

APPENDIX IX

Calorimeter Calibration and Energy Measurement

The calorimeters were calibrated in two ways. The first was a relative calibration using through-going muons, and the second was using mono-energetic hadrons.

The relative calibration was used during running conditions as a check of the operation of the apparatus and to keep the tubes balanced relative to each other. Typically one ABC trigger was taken every 10 spills to generate a sample of nearly minimum ionizing events from muons transversing the calorimeters. (dE/dx increases by 50% from minimum by 50 GeV, however this represents only about 50 MeV per module.) The pulse height distribution (Landau) was then used in the measurement of the hadron energy. The muon provides a light source corresponding to a known energy loss (minimum ionizing) which could be calculated from the known properties of materials and the dimensions of the apparatus. The ADC channel (integrated charge) corresponding to the peak of the Landau distribution thus corresponds approximately to an energy loss given by dE/dx for minimum ionizing. A pulse height could then be converted to the units of the Landau peak-pedestal separation giving energy in units of minimum ionizing. The peak was found by fitting the ADC channel distribution with a Landau convoluted with a Gaussian 2 bins wide.

An absolute calibration of the energy was achieved without

reference to calculated data on materials by using hadron beams of known momentum. The iron target was removed and a beam line set up as in figure A9.1.¹ (For the iron calorimeter calibration, the liquid calorimeter tanks were emptied.) Momentum in the beam ranged from about 10-100 GeV with a bite of 0.5%. Steering verniers allowed beam movement of ± 1 meter at the apparatus both horizontally and vertically, normally incident within 3-4 degrees.

Showers starting in liquid calorimeter modules 2 and 3 were used for the calibration. This maximized longitudinal containment. Figure A9.2 is a histogram of the integrated charge (pulse height) converted to minimum ionizing particles for a 50 GeV positive hadron beam.

The conversion to minimum ionizing particles was obtained by taking Landau data with muons from the beam, generated by placing a polyethylene hadron filter in the beam (figure A9.3). The peak was then extracted by subtracting the pedestal and fitting the ADC pulse height distribution convoluted with a Gaussian with $\sigma = 1$ bin.

The transition curve as a function of depth (in units of liquid modules) is shown in figure A9.4 for 50 GeV positives starting in module 2. As shown in the figure, the showers were not fully contained. The pulse height in the Fe Cal was added to the Liq Cal weighted by the ratio of ratios of (energy/pulse height). The ratio of the beam energy to integrated charge is shown for 7 energies in figure A9.5a taken with positive and negative hadrons. The

function which gives energy from pulse height is thus approximately linear with a small exponential piece below about 20 GeV:

$$E = 0.094M (1 + 0.477 \exp(-0.009M))$$

where M is the total pulse height in units of minimum ionizing and E is in GeV.

The energy resolution in the liquid calorimeter is shown in figure A9.5b as a function of the width of the pulse height spectra. As expected it is nearly constant over the energy range measured at about 10%. The transverse uniformity was studied by scanning across the face of the liquid calorimeter within the fiducial volume (± 120 m). This was uniform to 10%.

The iron calorimeter was studied in a similar fashion. A typical pulse height spectrum and transition curve are shown in figures A9.6 and A9.7, with a Landau distribution from the calibration beam shown in figure A9.8. Note that the showers are essentially fully contained. The ratio of energy to pulse height and resolution vs. energy are shown in figures A9.8a and b. Since the iron calorimeter was optically segmented, there is some variation in the vertical direction which explains the 15% difference between positive and negative hadrons which were inadvertently steered into adjacent strips. The energy (GeV) from pulse height (minimum ionizing) function is

$$E = 0.175M (1 + 0.345 \exp(-0.0113M))$$

The resolution reflects the error in adjacent strips by adding in quadrature the standard deviations of the pulse height spectra with the 20% variation between adjacent strips.

Appendix IX:

References

1. A. Malensek, FNAL tech. memo, TM-717 (1977).

Figures

- A9.1 Schematic of the calibration beam line.
- A9.2 Liquid calorimeter pulse height spectrum for 50 GeV positives.
- A9.3 Liquid calorimeter Landau.
- A9.4 Liquid calorimeter transition curve.
- A9.5a,b Liquid calorimeter energy per charge, and resolution as functions of energy.
- A9.6 Iron Calorimeter pulse height for 50 GeV neg. hadrons.
- A9.7 Iron calorimeter Landaus.
- A9.8 Iron Calorimeter transition curve.
- A9.9a,b Iron calorimeter energy per charge, and resolution as functions of energy.
- A9.10 linearity for iron and liquid calorimeters as functions of energy.

CALIBRATION BEAM LINE

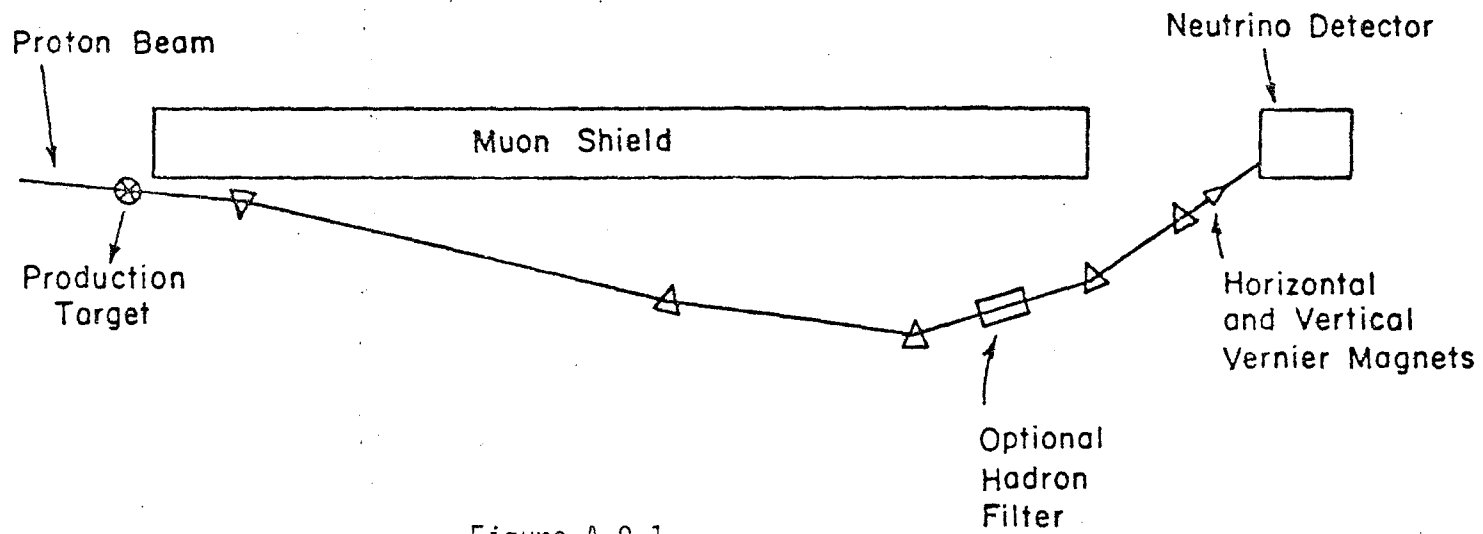


Figure A 9.1

RESPONSE OF THE LIQUID CALORIMETER
TO 50 GEV NEGATIVE HADRONS

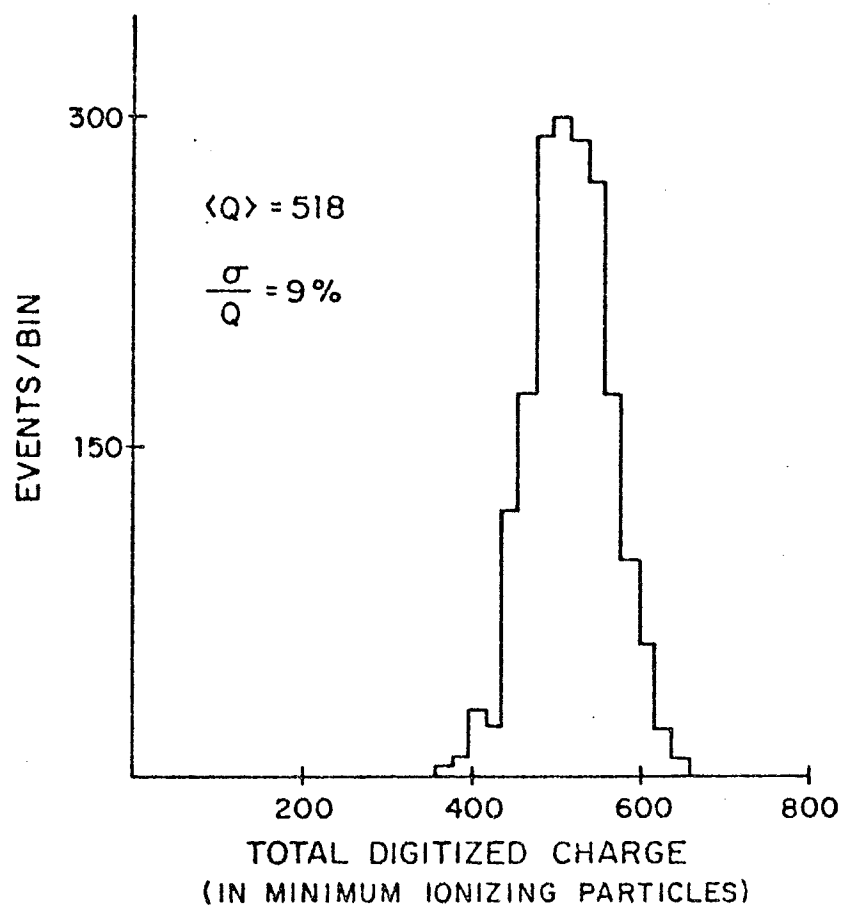


Figure A 9.2

LIQUID CALORIMETER LANDAU
(ONE MODULE)

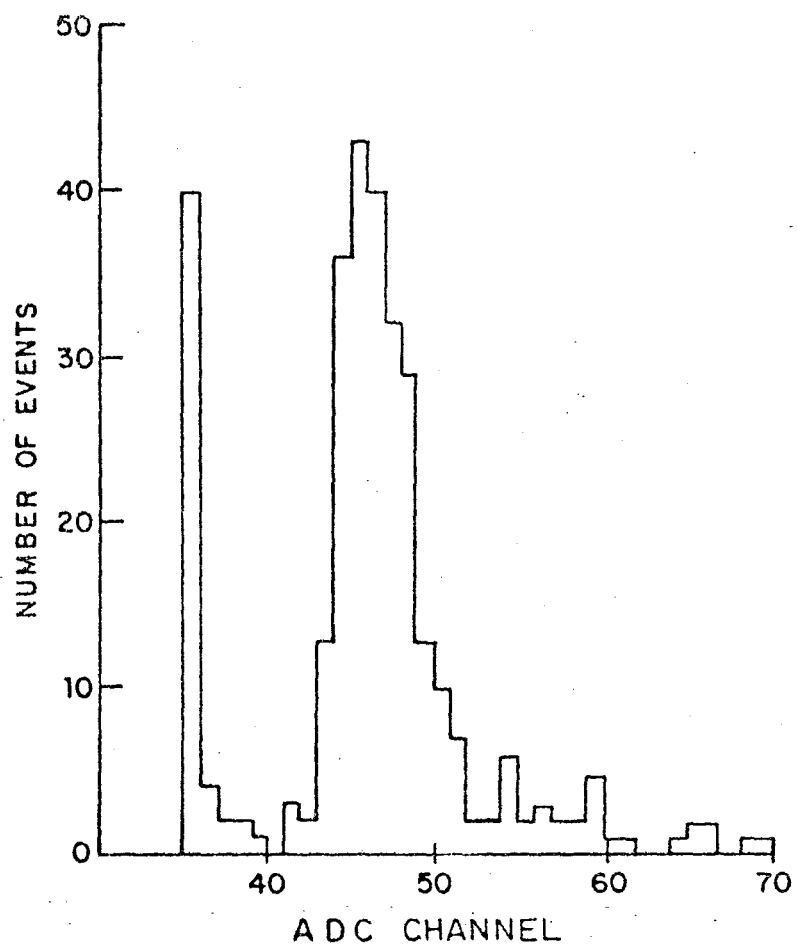


Figure A 9.3

AVERAGE TRANSITION CURVE FOR
THE LIQUID CALORIMETER
(50 GEV NEGATIVE HADRONS)

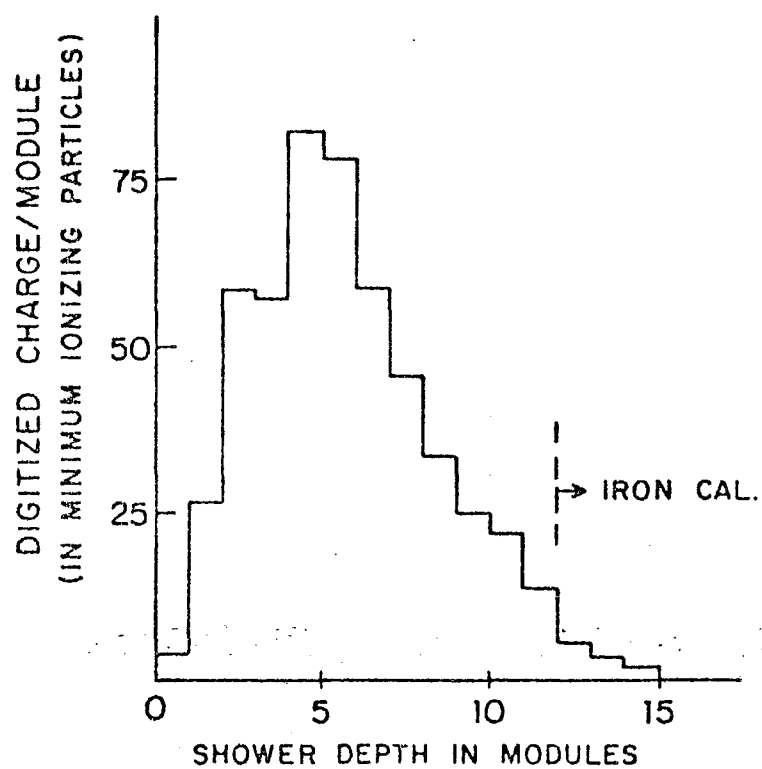


Figure A 9.4

LIQUID COLORIMETER

A) ENERGY/CHARGE COLLECTED VS. ENERGY

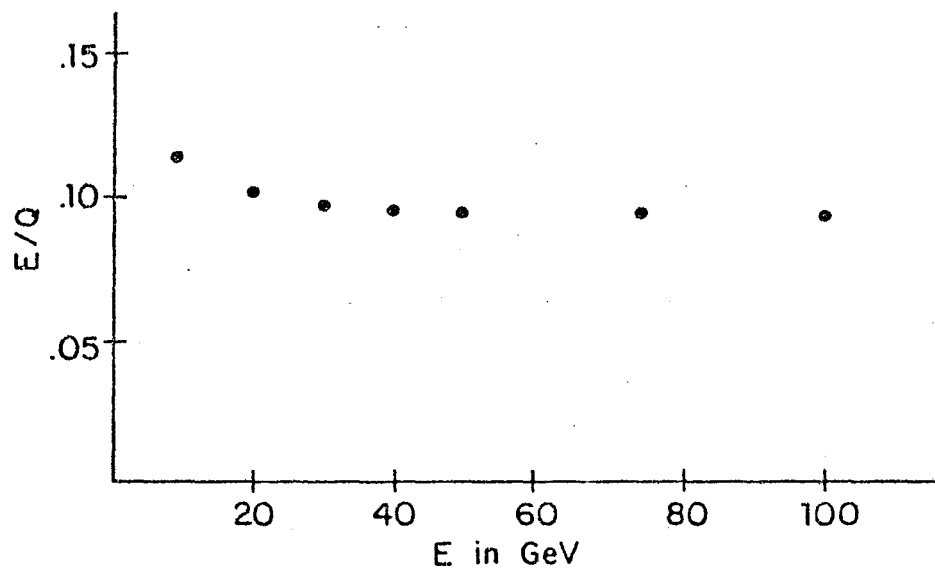


Figure A 9.5a

B) RESOLUTION VS. ENERGY

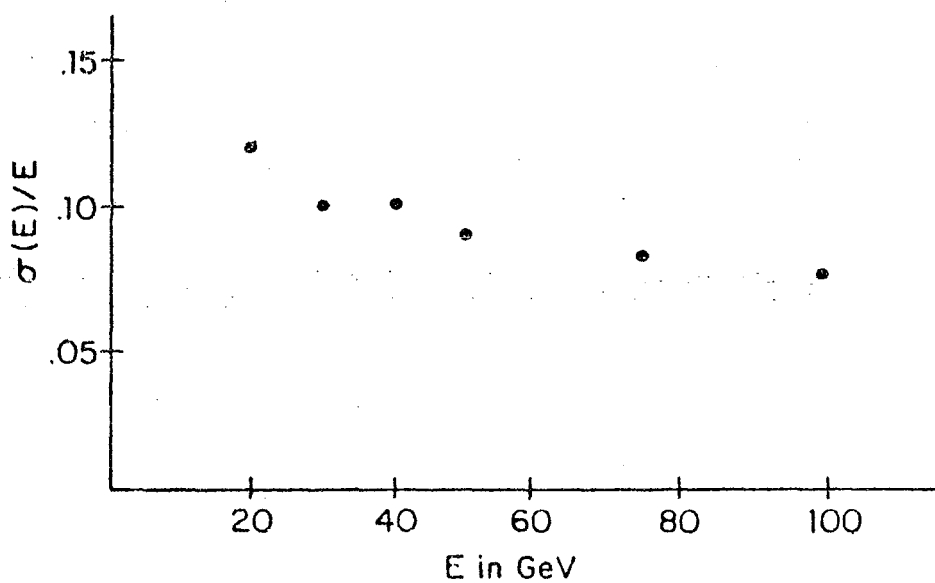


Figure A 9.5b

RESPONSE OF THE IRON CALORIMETER
TO 50 GeV NEGATIVE HADRONS

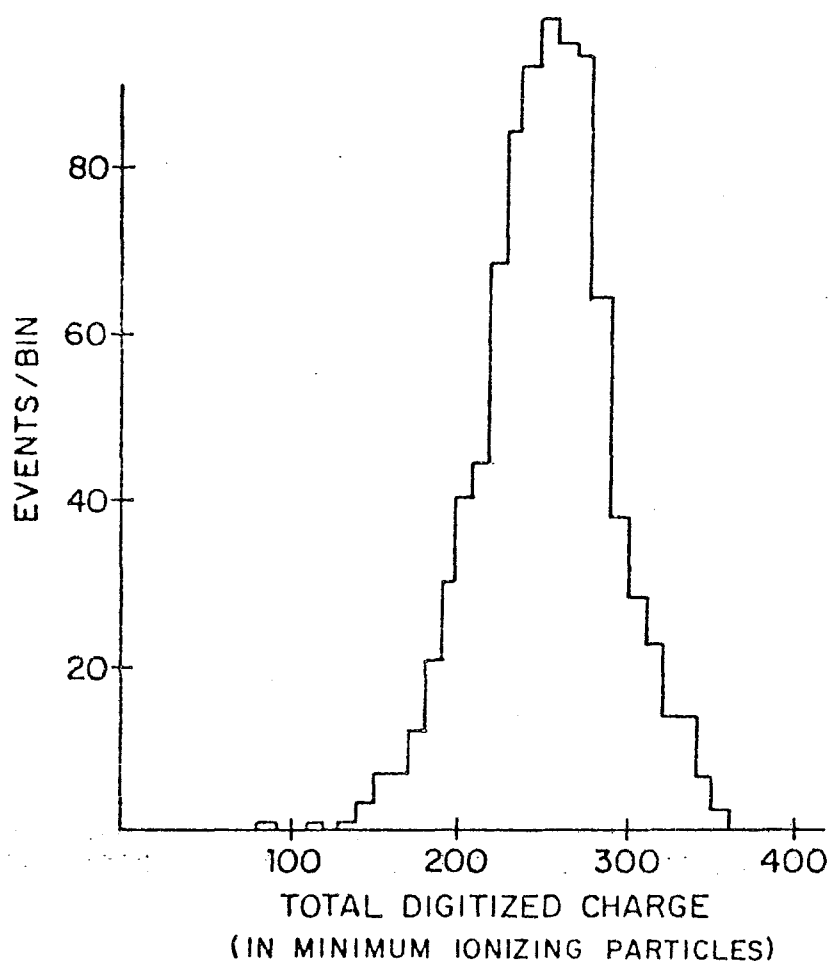


Figure A 9.6

IRON CALORIMETER LANDAU
(ONE MODULE)

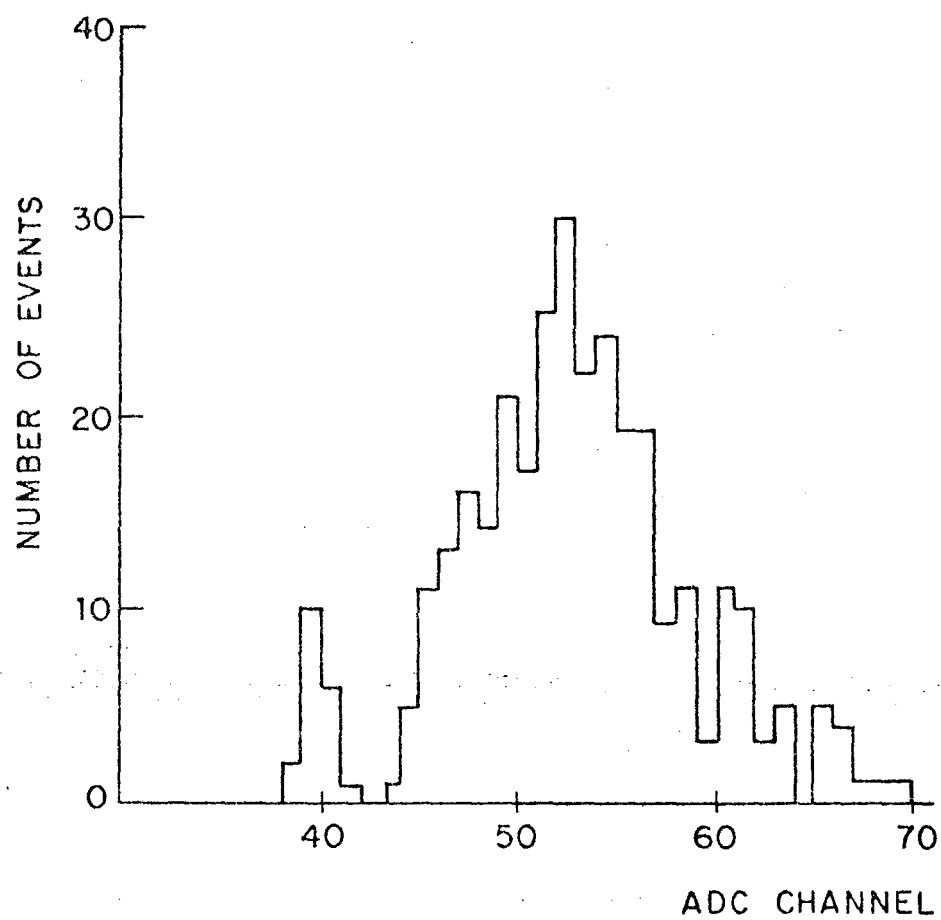


Figure A 9.7

AVERAGE TRANSITION CURVE FOR
THE IRON CALORIMETER
(50 GEV NEGATIVE HADRONS)

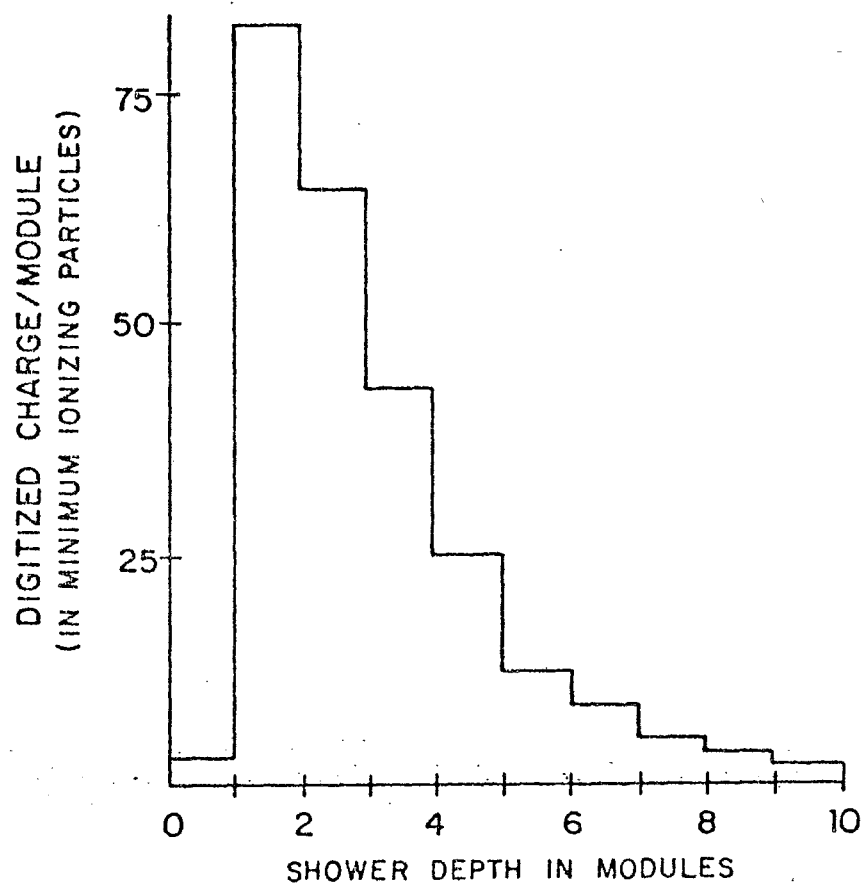


Figure A 9.8

IRON COLORIMETER

A) ENERGY/CHARGE COLLECTED VS. ENERGY

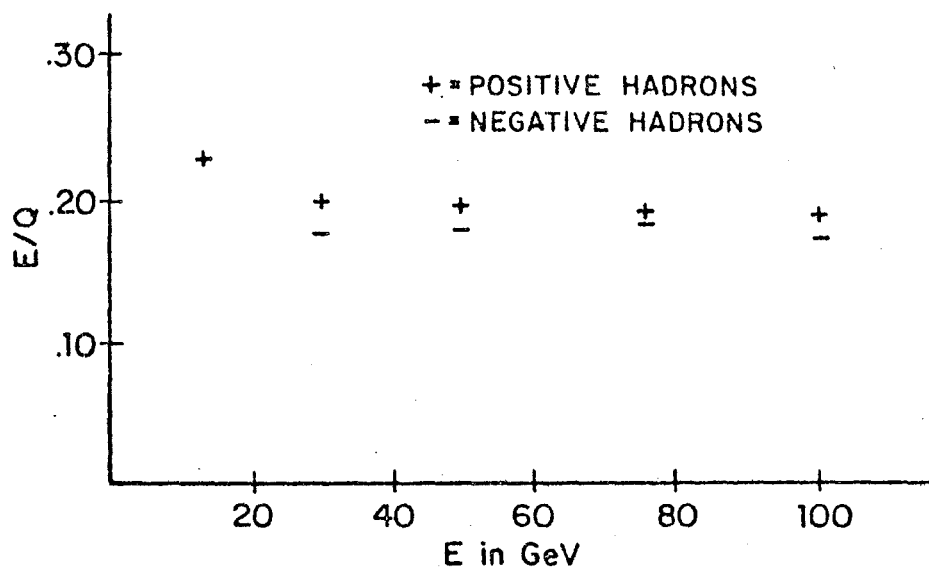


Figure A 9.9a

B) RESOLUTION VS. ENERGY

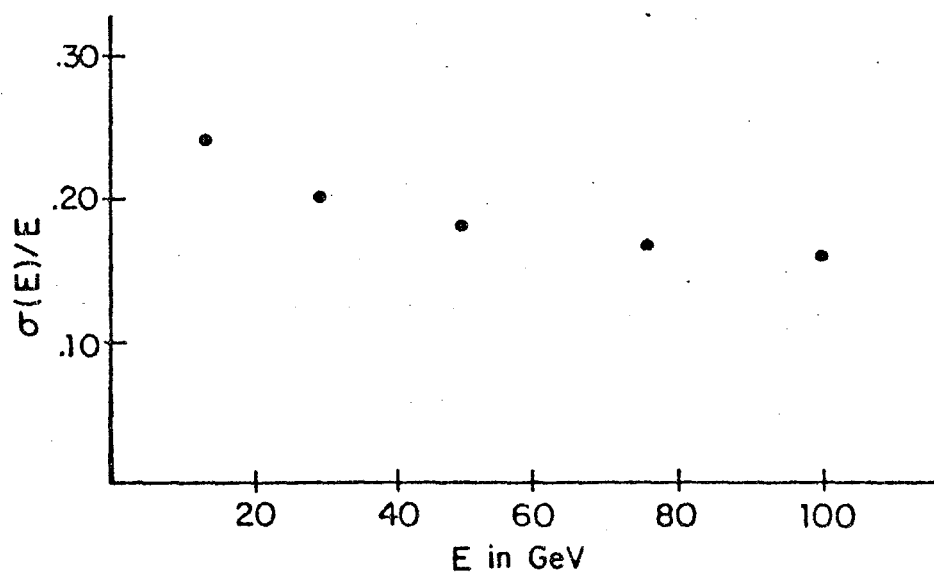


Figure A 9.9b

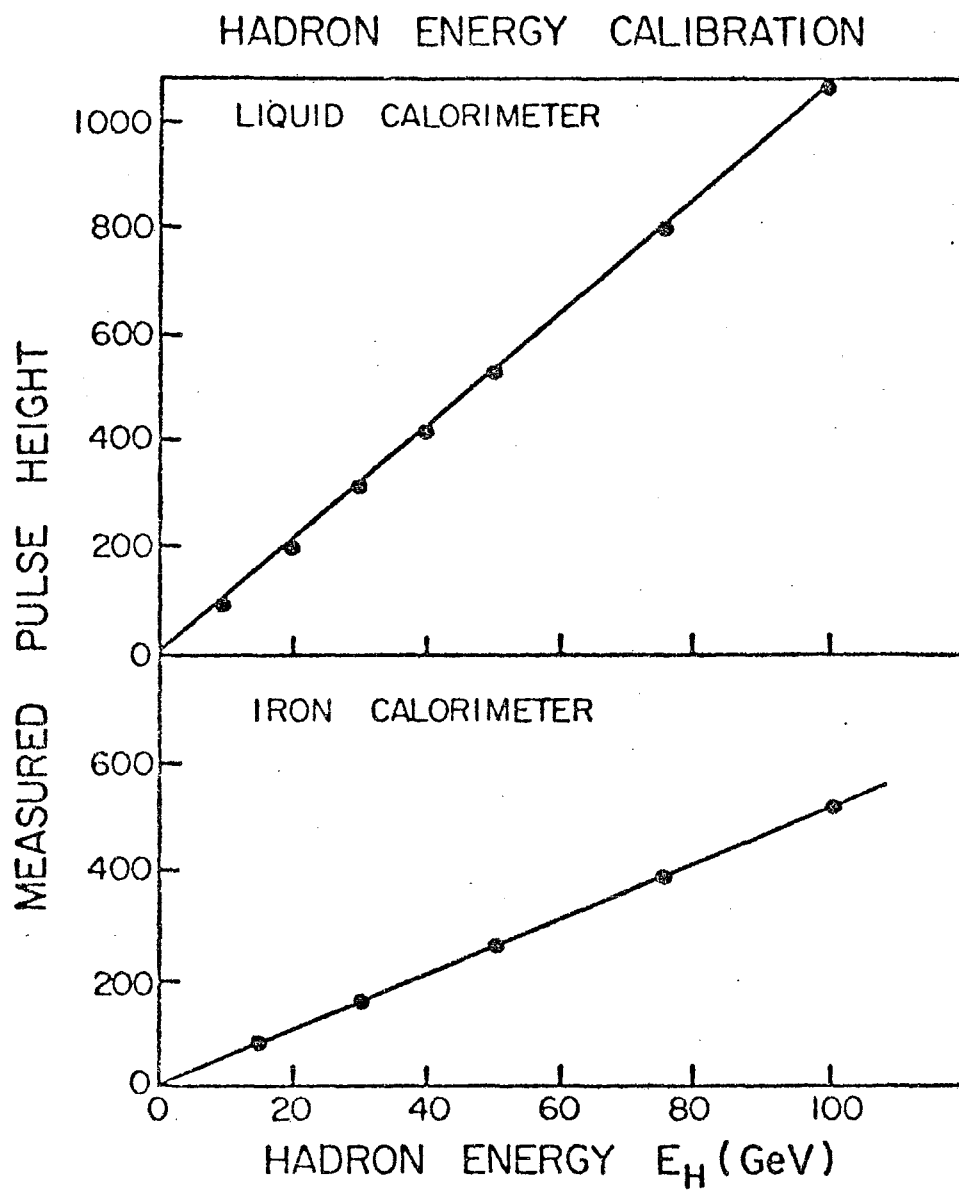


Figure A 9.10

APPENDIX X

Spectrometer Calibration

Monochromatic muons were transported to the apparatus by the calibration beam using a polyethylene absorber (Appendix IX). Figures A11.1a and A11.1b show the fitted momenta for 50 and 75 GeV incident muons, taking into account the range in the calorimeters.

By making a χ^2 cut of 6 per degree of freedom, the fits remained fairly stable. Below χ^2 of 6, the width of the momentum histogram did not decrease significantly, while above χ^2 of about 6, the width increased by more than 10%. This behavior was also checked before the calibration by examining the film and corresponding fitted single muon events. This χ^2 cut was then used for single muon events and thus the relative normalization for single and multimuons will be insensitive to the χ^2 per track. The average fitted momenta after this cut are 51.0 and 76.4, within 3% of the calculated values from the beam line. The half widths at half max are 12%, which is consistent with multiple scattering errors. The spectrometer momentum resolution expected from multiple scattering is

$$\sigma(p)/p = (2B R/L)^{-1}$$

where B is in kG, L is the muon path length in meters, R is the radiation length of iron in meters (0.018). For a 5 meter path and 18 kG, $\sigma(p)/p = 9\%$.

Appendix X

Figures

A10.1a, b Distributions in fitted momenta for 50 and 75
GeV muon beams.

MUON SPECTROMETER CALIBRATION

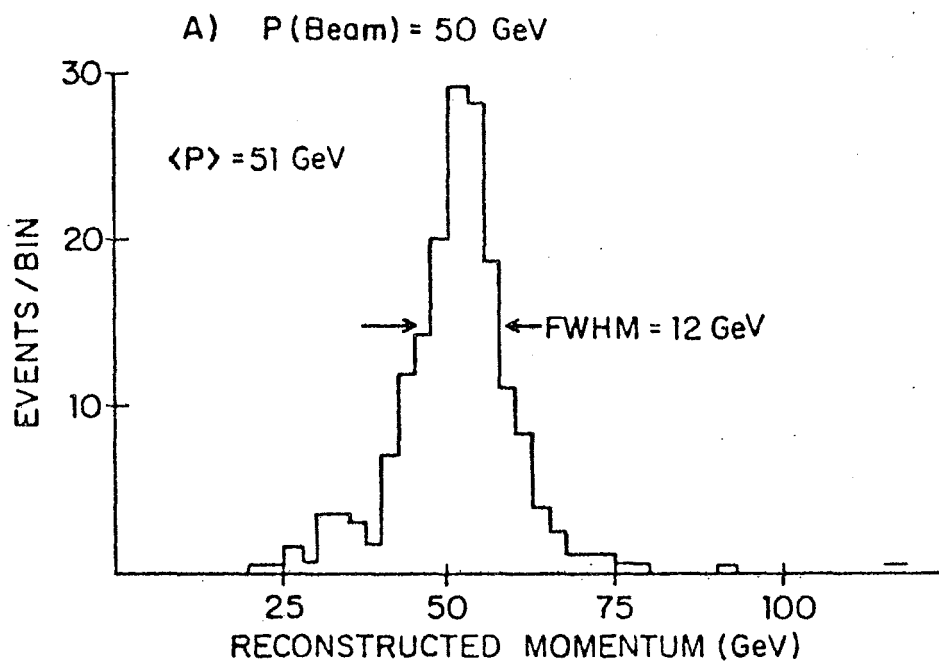


Figure A 10.1a

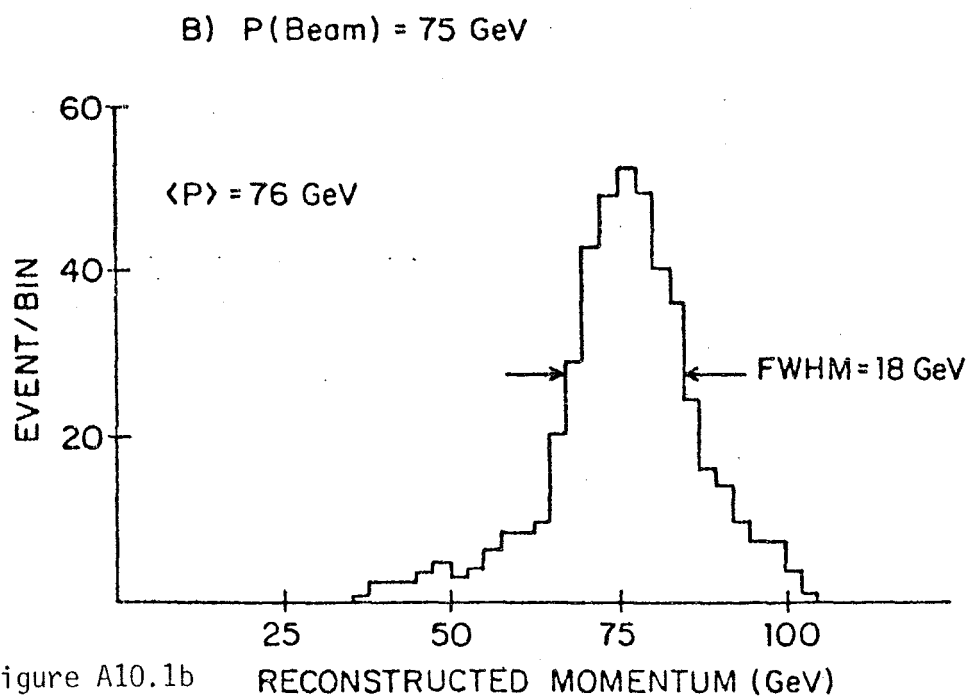


Figure A10.1b

APPENDIX XI

Single Muon Data

The single muon events were measured on an automatic machine SAMM at F.N.A.L. No events originating in the iron target were included. All sparks and fiducials in each view were digitized.

Since the event topologies for single muon events are relatively simple, an automatic procedure was set up to match sparks from chamber to chamber. This algorithm was 90% efficient.

After measurement, the events were then fit for momentum, using sparks from calorimeter chamber 7 on downstream. The coordinate of the vertex in the z (beam) direction was determined by the start of the hadron shower.

Events which failed to fit were inspected. Events with incorrect spark matches were corrected and refit. After this "massaging" procedure, the yield of good events with 2 magnet chambers was 72%, with 3 or more magnet chambers, 93%. About $\frac{1}{2}$ of these inefficiencies were due to events in the hole of the magnet or sparks missed by SAMM. Events with fewer than 2 magnet chambers were rejected as they had a very low efficiency.

Good events were required to pass several cuts:

1. verticize within 3 meters square in the iron calorimeter and 2.4 meters square in the liquid calorimeter
2. start after liquid module 1 and before iron module 7

3. muon track transverse the last calorimeter chamber and 2 magnet chambers
4. normalized chi-square less than 6

The events were then geometrically corrected using the counter efficiencies and the acceptance criteria when rotating and translating the events in the apparatus. For events in the calorimeters with EH above 6 and 12 GeV respectively, the efficiencies were above 90% for the energy triggers. Combining these with BCT triggers gives an overall efficiency of about 90% for all events with p_{\min} greater than 5 GeV in an unbiased fashion with respect to EH and kinematic quantities associated with it. These events were then compared to the number distributions in the scaling variables x and y predicted by scaling models. Figures A11.1 and A11.2 show the X distribution for ν and the y distribution for $\bar{\nu}$ together with simple fits over several energy ranges. Figure A11.3 shows the limit curves for acceptance in x and y .

To obtain the dimuon rates, the total corrected numbers of neutrino and anti-neutrino events for dimuon running are required. The number distribution as a function of energy for the anti-neutrino running is shown in figure A11.4. In the QT running, since the "spill" was split into multimuon (spill 1) and unbiased (spill 2) triggers, only events in spill 2 were measured for single muon data. Thus, to extrapolate to the entire spill the (protons on target in spill 2) = (SEM2) must be found, in order to compute

$$(\text{events/proton on target}) = (\text{events spill 2})/(\text{SEM2}).$$

The quantity SEM2 was found using the approximation:

$$\frac{(\text{Spill 1 triggers})}{(\text{Spill 2 triggers})} \approx \frac{(\text{Spill 1 triggers/SEM}) (\text{SEM1})}{(\text{Spill 2 triggers/SEM}) (\text{SEM2})} \quad (1)$$

where SEM1, SEM2 are protons on target in spill 1 or 2. Using the relation:

$$\text{SEM} = \text{SEM1} + \text{SEM2} \quad (2)$$

with the previous approximation, the SEM2 can be solved for in any given run by measuring the relative numbers of triggers. In spill 1 and spill 2 (LHS of (1)), and the total SEM, if the trigger rates per SEM of each spill are known. The trigger rates of spill 1 and spill 2 per SEM were measured independently early in the experiment by turning off spill 2 or spill 1 and taking the entire spill using one or the other trigger, thus measuring the rate per SEM directly during low intensity running. These rates are:

$$\begin{aligned} (\text{Events Spill 1})/(\text{SEM}) &= 0.25 \pm .05 \text{ events}/10^{13} \text{ p.o.t.} \\ (\text{Events Spill 2})/(\text{SEM}) &= 0.97 \pm .03 \text{ events}/10^{13} \text{ p.o.t.} \end{aligned} \quad (3)$$

Relations (1) - (3) are then used to find the SEM in spill 2 for a sample of runs in the QT. The number of corrected events per SEM can then be found for these runs from the measured spill 2 single muons. This is summarized in table A11.1 along with the spill splitting. Extrapolating this rate = $207.1/10^{16}$ p.o.t. to the entire QT dimuon data set (0.84×10^{17} p.o.t.) gives 17,400 single muon events. This is done as a function of energy in figure A11.5. Figure A11.6

shows the ratio of SEM1/SEM2 as a function of integrated total SEM from the start of the experiment. On average of all events there were about 40% spill 1 events, 60% spill 2 events, with an average (SEM1/SEM2) of $2.3 \pm .7$.

Appendix XI :

Figures

- A11.1 x distribution for neutrinos.
- A11.2 y distribution for antineutrinos.
- A11.3 lines of constant (60%) acceptance at $E=80$ and 100 GeV, and x-y resolution at $E=50$ GeV.
- A11.4 Number distributions as a function of energy for anti-neutrino events in BTSS running.
- A11.5 Number distributions for neutrino events in both spills in the QT, plotted as a function of energy.
- A11.6 Spill splitting in the QT; SEM 1 / SEM 2 as a function of energy.

Table A 11.1 Event Rates: Negative Muons in QT

Run	Events	SEM($\times 10^{16}$)	$\frac{\text{Events Spill 1}}{\text{Events Spill 2}}$	SEM 2	Events/ 10^{16} pot
118-119	367	3.6	0.69	0.96	383
127-31	161	2.7	0.60	0.96	167
132	359	3.6	0.36	1.49	241
138	414	8.4	0.46	2.96	140
139	448	7.4	0.58	2.23	201
140-3	379	5.8	0.63	1.65	230
144	271	4.4	0.74	1.11	244
148	373	7.8	0.70	2.0	186

Event rate = 207 per 10^{16} p.o.t.

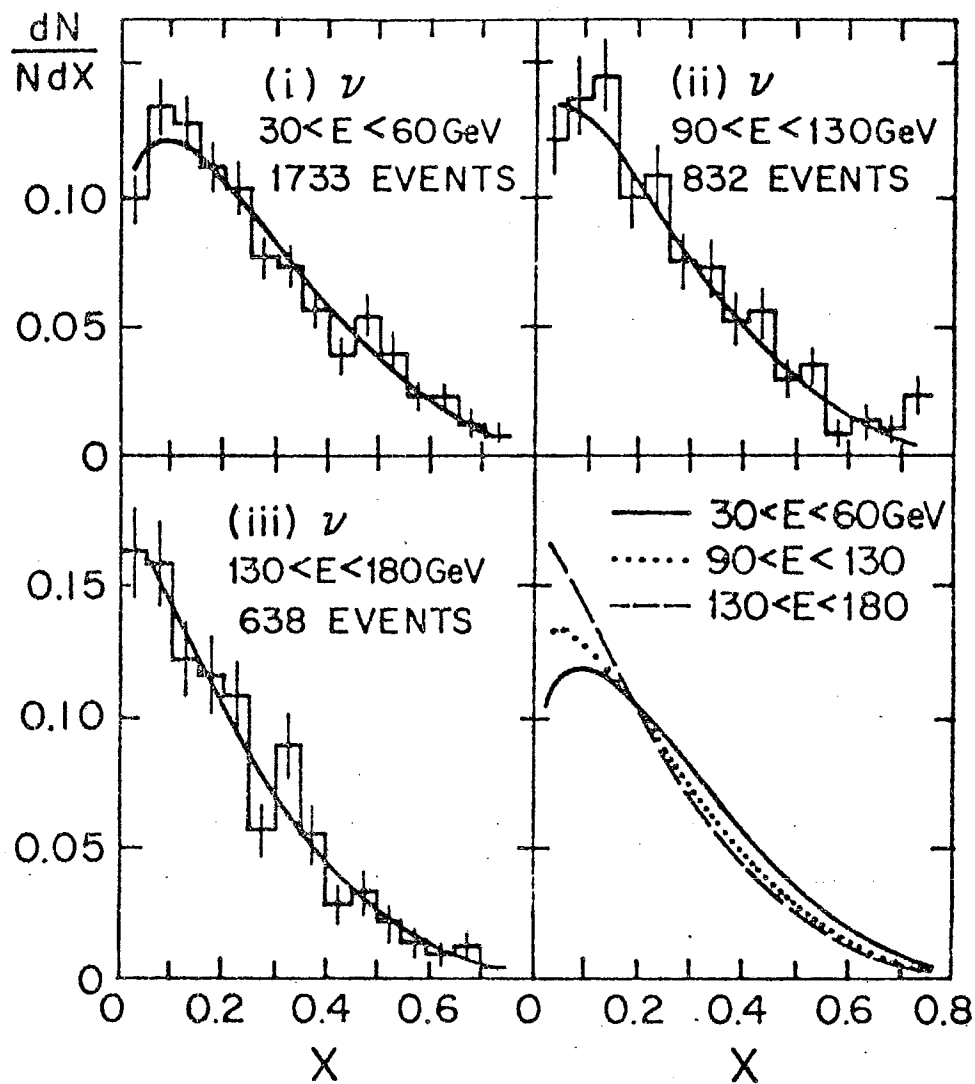


Figure A 11.1

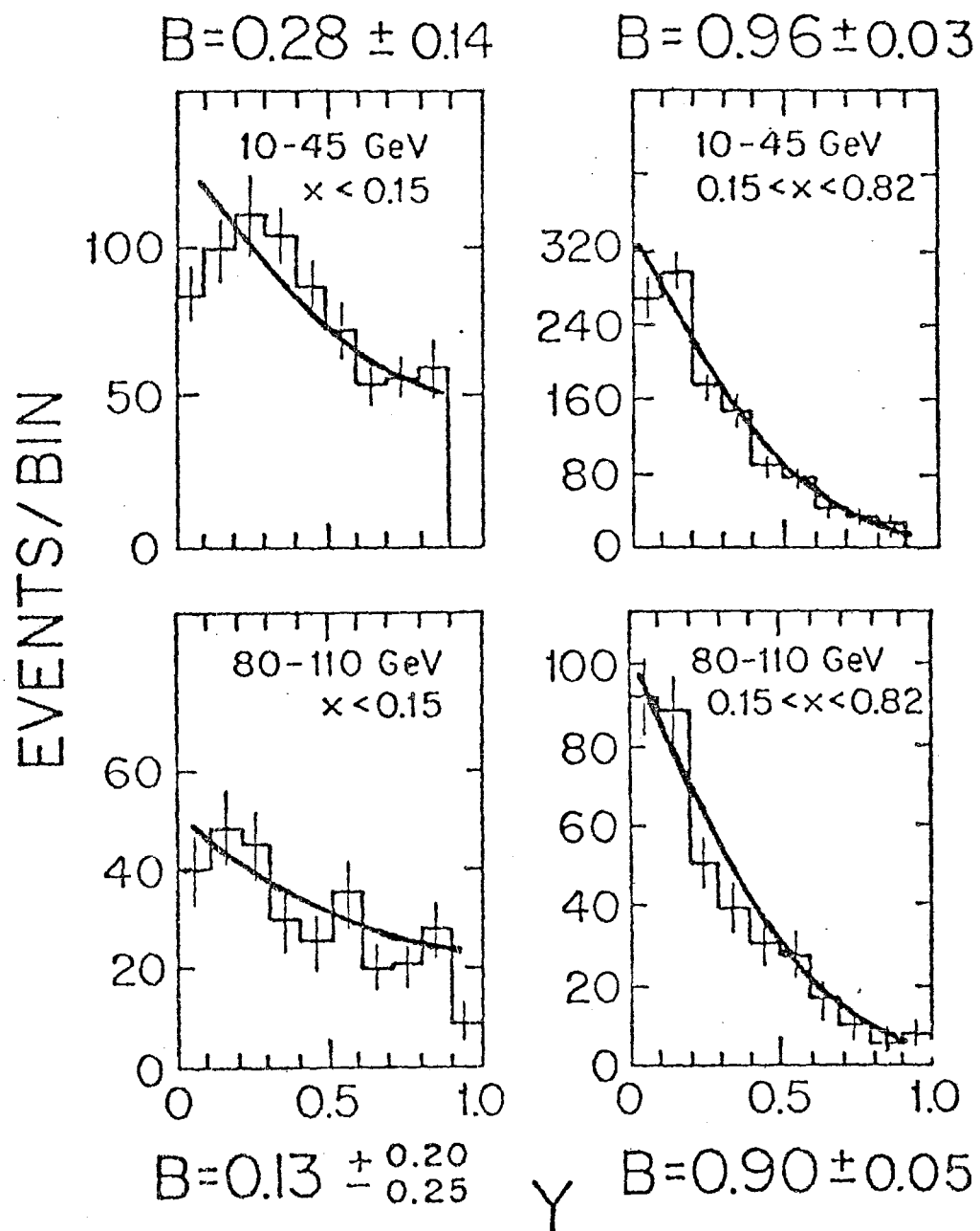


Figure A 11.2

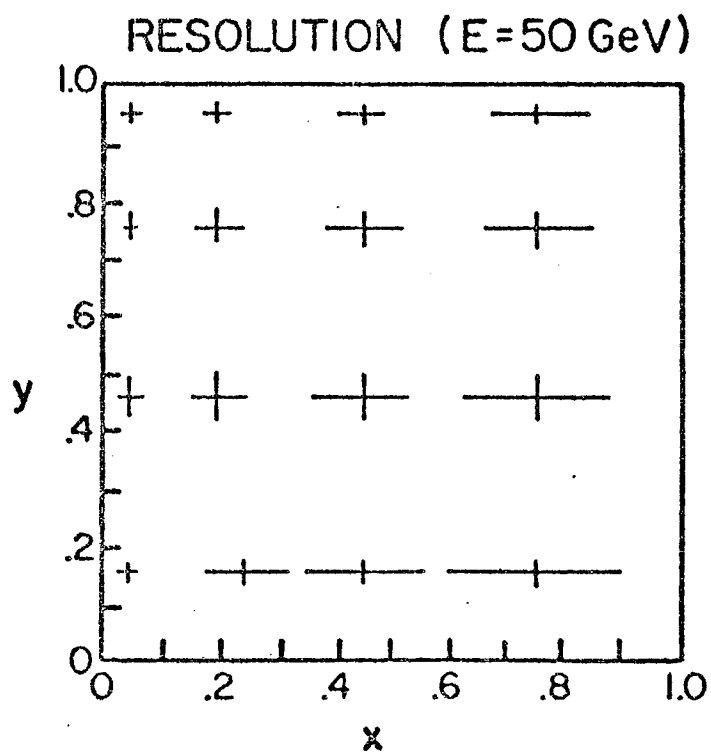
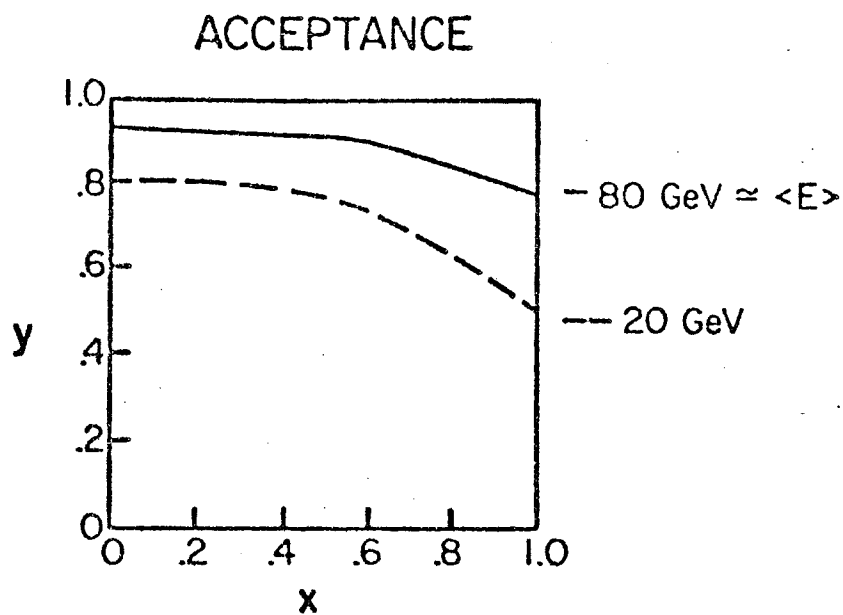


Figure A 11.3

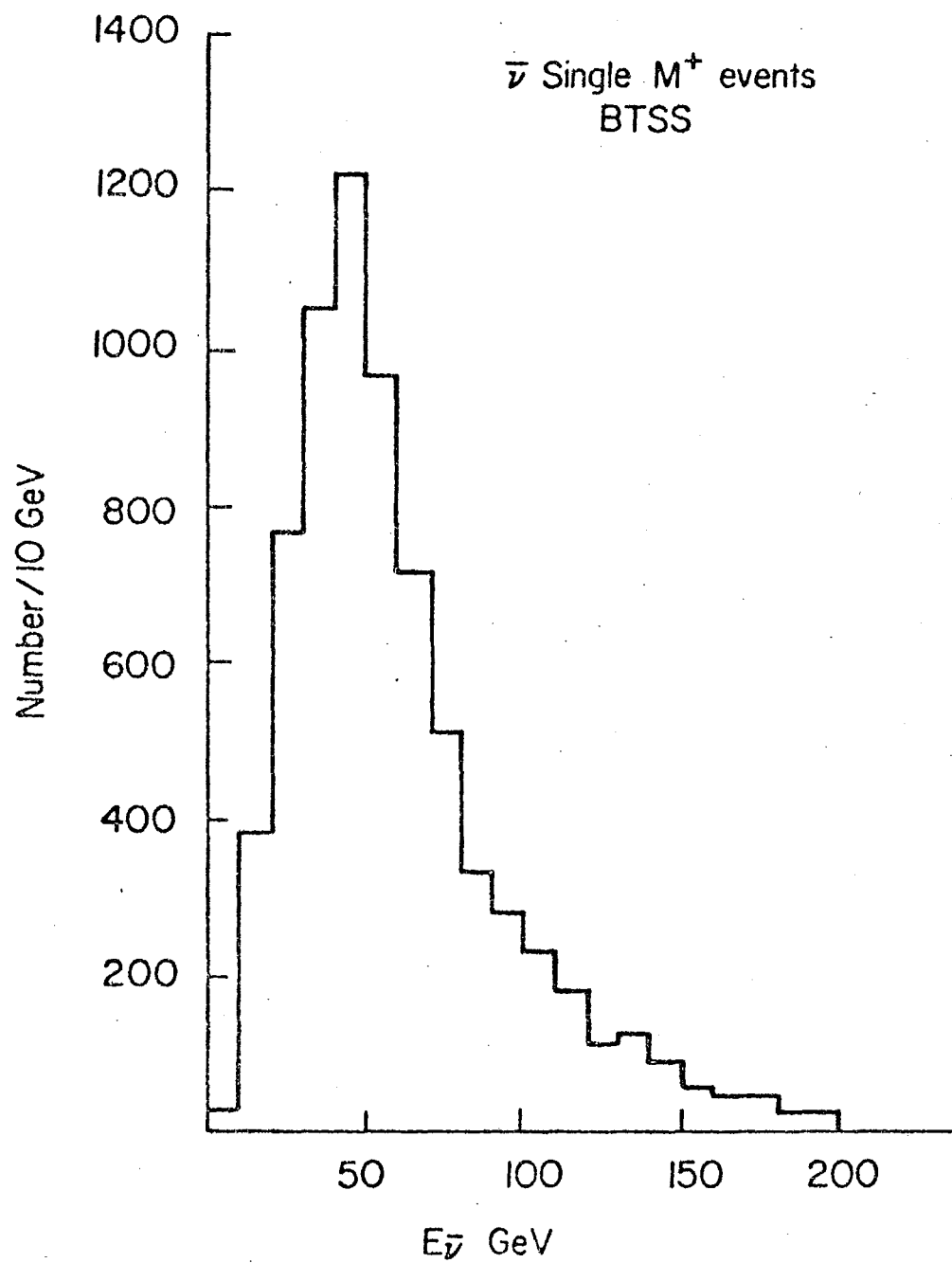


Figure A 11.4

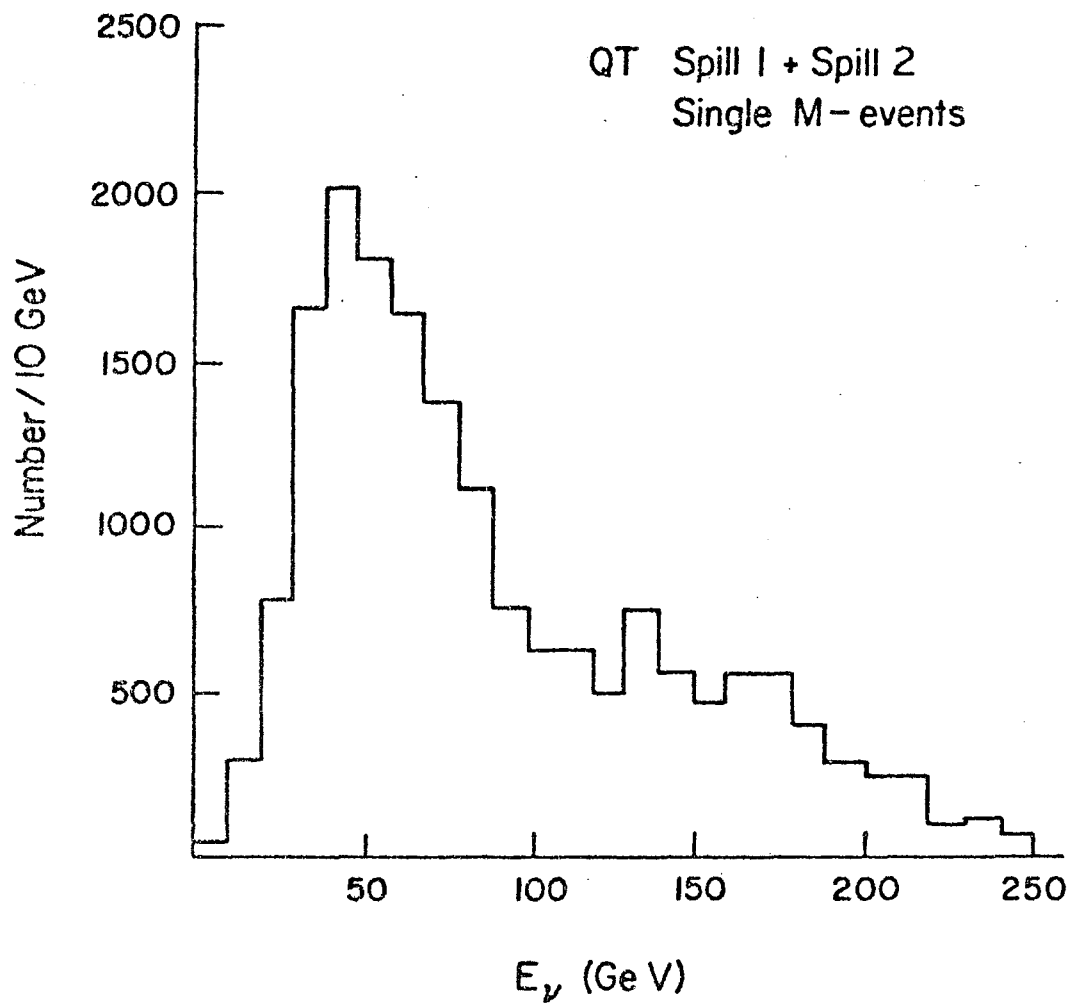


Figure A 11.5

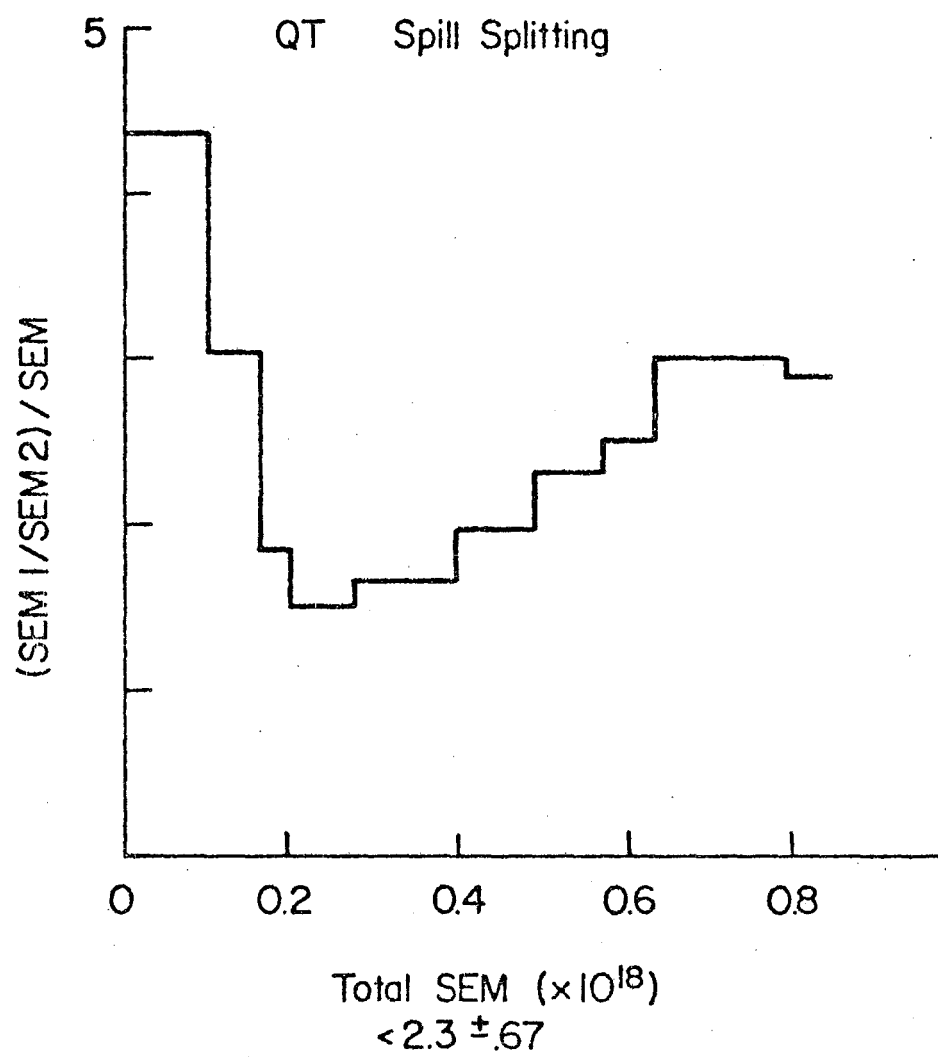


Figure A11.6

APPENDIX XII

DIMUON BACKGROUNDS

This appendix estimates dimuon rates relative to single muon events from background (uninteresting) sources. These are divided into two categories: accidentals, and pion and kaon decay.

Accidentals

A dimuon event may be simulated by a single muon event with a superimposed muon. This can occur by 2 single muon events occurring in the same vertization volume within the resolving time of the spark chambers. This gives a maximum dimuon rate of about 2×10^{-5} / single muon for calorimeter events and 5×10^{-5} / single muon event for iron target events. This is a conservative estimate, as it does not include counter timing cuts or any allowance for visual inspection. Iron target events have an additional source of background dimuons from entering single muons. This was measured by scanning for calorimeter events in the QT with an entering muon from the iron target, giving 8 muons per 2100 events. All of these events had out-of-time counters set. Assuming these are random in transverse position, this gives a rate inside a transverse 1 m^2 area of 4×10^{-4} before fiducial volume, triggering, pattern recognition

In addition, a further check on iron target events was performed by fitting the dE/dx of the muons as measured in the calorimeters for 1 muon and 2 muon hypotheses. Muons entering outside the 200 nsec resolution of the calorimeters should then cause false dimuons in the spark chambers which have only single minimum ionizing traces in the calorimeters. The results of these fits are shown in Figure A12.1 as the chi-squared per DOF of 1mu vs. 2mu hypotheses for each event. As can be seen, all iron target events have a lower chi-squared per DOF for the 2mu hypothesis except for one borderline event.

Pion and Kaon Decay

Dimuon events can occur by single muon events with a pion or kaon decaying into a muon. This background was calculated by monte carlo for neutrino and anti-neutrino beams. The monte carlo generated events according to the energy, x and y distributions, and then generated hadron showers from inclusive distributions. The showers were then propagated with the particles in the shower having probabilities to interact and produce more particles, or to decay into muons.

The showers were generated by using measured inclusive distributions for hadrons produced in bubble chambers by neutrinos. These are given in the variable z , the fraction of the hadron momentum along the shower direction to the total hadronic energy. For z above 0.2 at an average neutrino energy of about 100 GeV, these

distributions are well parametrized by the forms:

$$\frac{dN^+}{dz} = 16 e^{-6.7z}$$

$$\frac{dN^-}{dz} = 12.9 e^{-8z}$$

normalized to the total positive and negative multiplicity. For average E_ν of 50 and z above 0.2,

$$\frac{dN^+}{dz} = 12 e^{-5.3z}$$

$$\frac{dN^-}{dz} = 6.0 e^{-6z}$$

The difference in these two parametrizations contributes to the monte carlo error. Uncertainty in the very low z region also contributes to errors in the monte carlo; however, this is a small effect for muons above the momentum cuts. The z distributions are almost independent of E_ν , W , and Q^2 for $z > 0.1$. The multiplicity varies slowly with $\log W^2$.

The measured z distributions did not distinguish between pions and kaons, and so electroproduction data was used:

$$\begin{aligned} K/\pi &= 0.2 & z > 1/3 \\ &= 0.2 z^2 & z < 1/3 \end{aligned}$$

giving about 0.13 K/event, similar to observed K^0 production in

neutrino reactions.³ Since protons are at very low z ($z < 0.15$) the background calculation is basically not sensitive to subtracting them from the $+$ distribution.

Secondary hadrons were generated in the cascading by using the inclusive x distributions for secondaries in the reactions:⁴

$$\pi^+ p \rightarrow \pi^+ x = \pi^- p \rightarrow \pi^- x$$

$$\pi^+ p \rightarrow \pi^- x = \pi^- p \rightarrow \pi^+ x$$

$$K^+ p \rightarrow K^+ x = K^- p \rightarrow K^- x \quad ^5$$

where the R.H.S. is assumed from the L.H.S. data. Each secondary particle was assigned a weight equal to the product of the parent weight, the charge multiplicity and the flavor. The particles continued to interact until all were below the minimum momentum cutoff, or until they decayed into $\mu\nu$.

The secondary particles were assigned a p_t according to an exponential distribution with an average value of 300 MeV. This was used for generating distributions used in the comparison of charm.

Estimates of the contributions to the error in the monte carlo are:

$D(z)$	20%
$hN \rightarrow h'N$	10%
absorption lengths	10%

giving an error of about 25%.

The results in pure iron for a 4.5 GeV cut are summarized in Table A12.1 per 10^4 (anti) neutrino interactions. To compute the background in each target, the rates in iron are scaled by the absorption lengths in the target. In the calorimeters, the total background rate relative to all events was $25 \pm 7\%$ for neutrinos, and $16 \pm 9\%$ for antineutrinos. These rates fall to about 9% and 5.5% in the iron target. If the momentum cut is raised to 10 GeV, the rates fall by a factor of ≈ 3.5 .

Appendix XII:

References

1. R. Imlay, private communications and Rutgers preprints(1977);
 J. Rich, Ph.D. thesis, Harvard U. 1979 and private comm.;
 H. Rudnicka et al., VTL pub 53 (1978);
 T. Burnett et al., Phys. Lett. 77B,443 (1978);
 M. Derrick et al., Phys. Rev. D17, (1978);
 J. Bell et al., Phys. Rev. D19,1 (1979);
 P. Bosetti et al., Oxford-NP-58/78 (1978);
 D.D. Reeder, private communication (FNAL E28 data).
2. G.J. Feldman et al., SLAC PUB 2038(1977).
3. P.C. Bosetti et al., Nucl. Phys. B54, 141(1973);
 J.P. Berge et al., Phys. Rev. Lett. 36, 127 (1976) .
4. P. C. Bosetti et al., Nucl. Phys. B54, 141 (1973).
5. P. C. Bosetti et al, Nucl. Phys. B60, 307 (1973).
6. The absorption lengths were scaled from data on
 copper and carbon for incident pions, kaons, and protons:
 S.P. Denisov et al., Nucl. Phys. B61, 62 (1973); l_{abs}
 were for iron(liq. scint.) 21 cm(117 cm) for pions and
 25 cm(134 cm) for kaons.

Appendix XII:

Tables

A 12.1 Event rates from pion and kaon decay

Figures

A 12.1 1 muon vs. 2 muon hypotheses for dE/dx in calorimeters
from iron target dimuon events

Event Rate of Pion and Kaon Decay
in pure iron per 10^4 interactions
to give \pm dimuons, $p_{\min}=4.5$ GeV

Neutrino Energy(GeV)	QT+BTSS neutrino	BTSS antineutrino
20-50	1.9	.9
50-100	4.1	1.8
100-150	6.1	3.5
150-200	7.0	4.7
200-250	7.6	

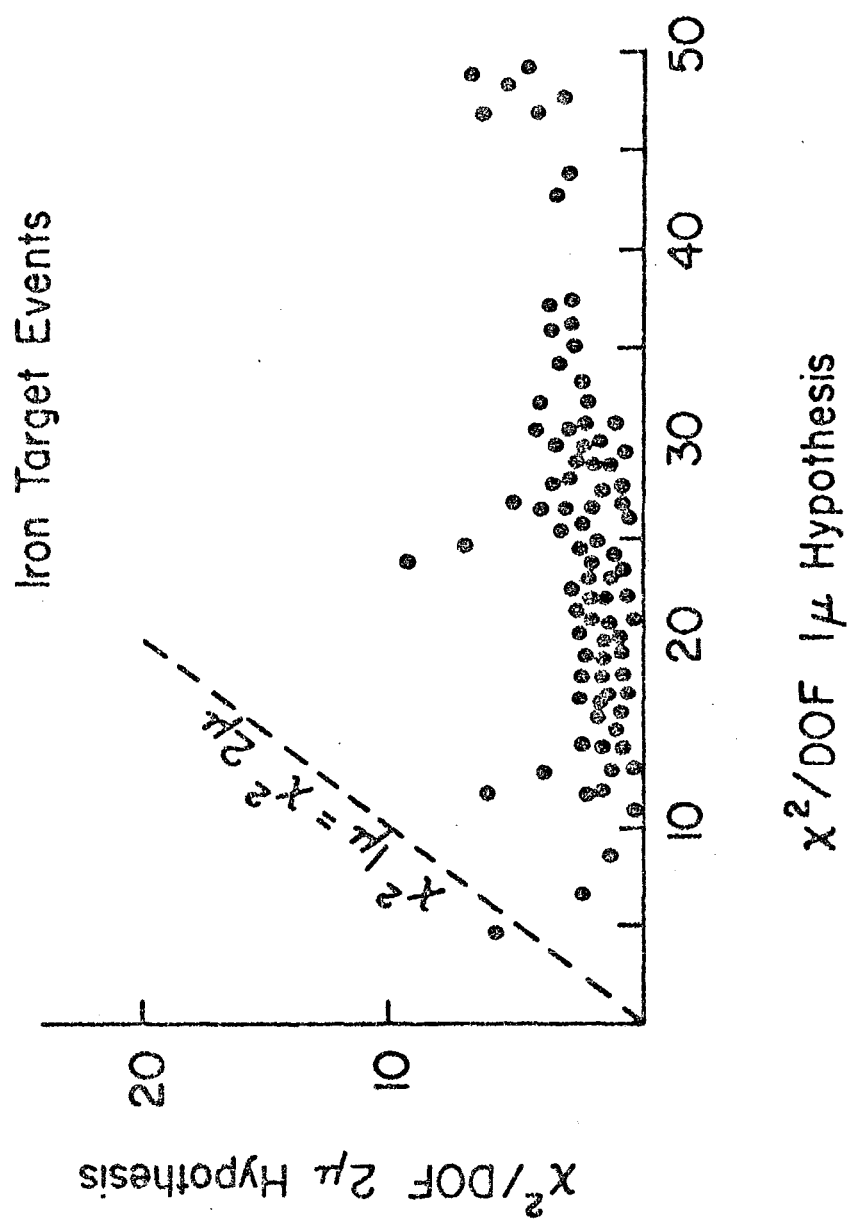


Figure A12.1

